DEVELOPING A NOVEL EXTRA-AORTIC CUFF WITH PERISTALTIC MOTION AND COUNTERPULSATION TO ASSIST HEART FUNCTION

Parn Naruenart Wangdee Jones

Master of Engineering

2017

DEVELOPING A NOVEL EXTRA-AORTIC CUFF WITH PERISTALTIC MOTION AND COUNTERPULSATION TO ASSIST HEART FUNCTION

Parn Naruenart Wangdee Jones

Primary Supervisor: Dr. Andrew Lowe

Secondary Supervisor: Jeffrey Kilby

A thesis submitted to Auckland University of Technology in fulfilment of the requirements for the degree of Master of Engineering

February 2017

School of Engineering

Faculty of Design and Creative Technologies

Abstract

The development of a prototype extra-aortic balloon cuff with peristaltic motion and counterpulsation system is explored to investigate the practical feasibility for potential future treatments for chronic heart failure. This concept is an extension of an existing clinical heart assisting device called C-Pulse® created by Sunshine Heart which is used to treat patients with New York Heart Association Class III and ambulatory Class IV heart failure. Both software simulation and hardware-based experimental work are undertaken.

The software simulation of a one-dimensional pressure wave propagation through an aortic segment and the influence of an external peristaltic movement are explored using Matlab® (MathWorks®, United States). Simulation results show characteristic differences between a normal pressure waveform and an augmented waveform. The hardware work was divided into three parts – development of a phantom aorta, cardiovascular simulation platform, and the peristaltic extra-aortic balloon cuff prototype. A phantom aorta was made from Dragon Skin® 10 with geometries and properties similar to that of the biological physiological human aorta. A devised cardiovascular simulation platform with the phantom aorta attached was constructed and utilised as a testing platform for the functionality of the peristaltic extra-aortic balloon cuff prototype. The prototype was developed using an Arduino based microcontroller which drives four pneumatic pumps that inflate and deflate extra-aortic balloon cuffs, attached to the descending aorta, in a counterpulsating manner to the natural heartbeat.

The peristaltic extra-aortic balloon cuff prototype was able to significantly increase the mean aortic pressure from ~92 mmHg to ~96 mmHg ($P<0.05$). The flow velocity waveform in the ascending aorta was also altered – increasing the mean diastolic flow from 13.47 cm/s to 17.73 cm/s ($P<0.05$).

Table of Contents

List of Figures

List of Tables

Glossary

Aorta		A major artery of the human body.
Arteries		Muscular-walled tubes forming part of the circulation system that blood flows through.
Ascending aorta	(AA)	Top part of the aorta (closest to the heart).
Cardiac Cycle	(CC)	A sequence of both electrical and mechanical events that repeats every heartbeat.
Cardiac Resynchronisation Therapy	(CRT)	A medical therapy that resynchronises irregular heartbeats with small electrical impulses.
Cardiac Output	(CO)	The amount of blood that the heart pumps out per minute. Usually expressed in L/min.
Counterpulsation		A medical technique that synchronizes the external pumping of blood with the cardiac cycle to assist circulation and reduce cardiac workload.
Chronic Heart Failure	(CHF)	Condition where the heart that cannot pump sufficient volume of blood around the body.
C-Pulse®		A heart assisting device created by Sunshine Heart.
Descending aorta	(DA)	Bottom part of the aorta (away from the heart).

External pneumatic compression	(EPC)	A device that is used to treat heart disease using counterpulsation.
Electrocardiogram	(ECG)	The measurement of electrical activity of the heart.
Extra-aortic balloon cuff	(EABC)	An inflatable balloon that attaches to the aorta exterior.
Hemodynamic		Flow of blood within the organs and tissue.
Intra-aortic balloon pump	(IABP)	A heart assisting device that uses an inflatable balloon implanted into the descending aorta.
Peristaltic		Progressive wave-like contractions.
Phantom		A synthetic analogue of a part of the human anatomy.
Pulse Wave Velocity	(PWV)	The measurement of arterial stiffness, or the rate at which pressure wave move down the vessel.
Stereolithography	(SLA)	A form of 3D printing technology that is used for rapid prototyping.
Ventricles		A hollow or cavity part of an organ, in this research, specifically referring to the heart.
Ventricle Assist Device	(VAD)	A mechanical pump that assists a weaken heart. (LVAD: to assist left ventricle, RVAD: to assist right ventricle).

Attestation of Authorship

I hereby declare that this thesis submission is a record of my original work produced from the best of my ideas and knowledge. It contains no material previously published or written by another person (except where explicitly defined in the acknowledgements) nor material which to a substantial extent has been submitted for the award of any other degree or diploma of a university or other institution of higher learning.

_____

Parn Naruenart Wangdee Jones

Date Signed: 19 June 2017

Acknowledgements

I would like to express my utmost sincere gratitude to my primary supervisor Dr. Andrew Lowe for providing valuable knowledge and assistance throughout the entire learning process of this master thesis. Furthermore, I would like to also thank my secondary supervisor Jeff Kilby for giving me the opportunity to publish a journal paper to support this thesis, as well as providing valuable advice for the thesis.

I would like to also thank the AUT Institute of Biomedical Technologies – the staff and students – for supporting my thesis throughout the journey. In addition, I would like to also acknowledge the help from the following company/people:

Gordon Fraser (AUT Textile and Design Technician)

Ross Jacobs (AUT 3D Print Technician)

Ross Jamieson and Jim Crossen (AUT Mechanical Technician)

Festo NZ Ltd

Bevin Bradley and Richard Keene (Providing materials for manufacturing of parts)

Lastly, I would like to sincerely thank my mum, dad and brother, who have supported me during the entire process, with them helping me put pieces together and keeping me focused.

Chapter 1

Introduction

Cardiovascular disease (CVD) is an expansive term that describes a range of medical conditions that affect the human heart. Conditions include atherosclerosis (narrowing of the arteries), congestive heart failure (CHF), heart arrhythmias and heart valve problems. According to the World Health Organization [1], it is estimated that 17.3 million people worldwide died from CVD in 2008 and these numbers are expected to rise to 23.6 million by 2030. CVD, in medical practice, is usually diagnosed when a person develops symptoms of the disease and heart attack is unfortunately the first sign that occurs [2]. There are multiple treatments that medical professionals can give to lower the risk of suffering a heart attack. However, if the damage to the heart muscle is too severe or medications fail to assist, then invasive surgery may be necessary. This can involve surgical coronary bypass, implantation of a heart assisting device and even full heart transplant.

CHF remains one of the biggest unsolved healthcare issues worldwide. According to statistics, CHF affects more than 5 million people in America alone with approximately 550,000 new cases diagnosed each year [3-4]. A new portable heart assisting device by Sunshine Heart Inc. called C-Pulse® is used to treat patients with CHF using an inflatable extra-aortic balloon cuff (EABC). The cuff was designed to increase cardiac output (CO) that could halt or reverse the progression of CHF. The results from clinical trials proved its design could assist CHF patients [4]. This research poses the question: what if you could improve the device's function by applying a peristaltic model – like the locomotion of a worm – to the EABC to further assist heart function? The hypothesis is that peristaltic counterpulsation in an EABC would increase aortic flow and diastolic pressure that could assist the function of diseased hearts. This novel peristaltic extra-aortic balloon cuff (PEABC) could become a viable alternative to cardiopulmonary bypass surgery or full heart transplant as a method of assisting heart function [5] to treat CHF.

1.1 Background of Study

1.1.1 Overview of the Cardiovascular System

The cardiovascular system comprises of a heart that is an anatomical pump with its intricate arteries, veins, and capillaries that traverse the entire human body transporting blood [6]. The blood transports oxygen, nutrients, waste and immune components to support basic functionality of human cells and organs [6]. A normal adult human holds about 5 litres of blood and this amount is circulated through the heart about once every minute when a person is resting - this circulation output is referred to as cardiac output (CO) [6]. CO can be calculated as the product of stroke volume (the volume of blood that the heart pumps per beat) and the heart rate in beat per minute (bpm) [7]. During exercise, the body may require four times the normal CO due to the fact that the muscles need more oxygen and this means the heart will pump faster or the stroke volume will be increased so that more blood can circulate around the body [7].

A human heart is roughly the size of an individual's fist and is considered to be the strongest muscle in the body. The electrical activity in the heart controls the heart's pumping action of its muscles. On average, a healthy adult heart beats[1] 100,800 times every day or 2.94 billion times in its lifetime[2]. The human heart is an organ that serves as a pump to circulate blood around the body. It is typically located slightly to the left of centre in between the two lungs. A normal heart rate is approximately 70 bpm so that the cardiac cycle spans a 0.86 second period [6]. The heart muscle is made up of four chambers: upper two (atria) and lower two (ventricles). These chambers form two separate pumps on each side of the heart (left and right) which are divided by a muscle wall called the septum. The heart chambers have sealing valves that make the blood travel in one direction only, allowing blood to flow either from one chamber to another or out of the heart [8]. These walled sac muscles contract and relax in sequence to transport oxygenated and nutrient-loaded blood around the human body to organs and muscles. Not only does the heart pump blood around the body, but it also pumps blood back to the heart muscle walls via coronary arteries. These coronary arteries originate from the major blood vessel (aorta) and latch on the walls of the heart muscle [9]. The

[1] 70 beats per minute

[2] 80 years

aorta is the largest artery of the body's systemic circuit and starts from the left ventricle [10]. The aorta can be an inch in diameter and more than a foot long. It is subdivided into four major segments that are clinically important [10]:

- The ascending aorta is the part that rises up approximately two inches from the heart's left ventricle. The two coronary arteries branch off the ascending aorta and provide blood back to the heart muscles [10].

- The aortic arch curves and hugs around the top part of the heart and branches out to three smaller arteries – right common carotid artery, left common carotid artery, and brachiocephalic artery – that supply blood to the arms, head, and neck [10].

- The descending thoracic aorta is the longest segment that travels down the body that also branches out into small arteries in the chest structure [10].

- The abdominal aorta is the last segment that starts at the diaphragm and bifurcates into a pair of iliac arteries (left iliac artery and right iliac artery) in the lower abdomen. It provides blood to major organs around the region that branch off from the abdominal aorta [10].

Looking at the microscopic anatomy of the aortic wall, the aortic wall is made up of three layers: intima, media, and adventitia [11]. Intima is the inner layer that provides a smooth surface for blood to flow; media is the middle layer consisting of muscles and elastic fibres that allow the wall to contract and expand with each heartbeat; adventitia is the outer layer that provides additional structural support to the aorta [10]. In regards to a normal aortic geometry, the size of the aorta decreases with distance from the aortic valve to the abdominal aorta in a tapered manner [12]. A general human aorta size and shape that's relative to the human body is shown on Figure 1.1. The nominal geometry size, shape, as well as the biophysical properties of a human aorta, are examined and discussed in Chapter 2.

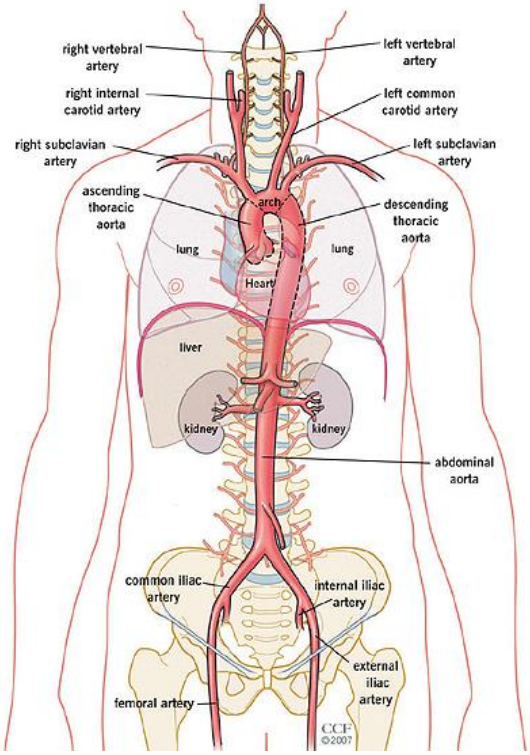

Figure 1.1: The human aorta geometry and its branching arteries [13].

The pumping of the heart (heartbeat) is caused by the alternating contractions and relaxations of the heart muscle wall (myocardium) [14]. The contractions are stimulated by electrical impulses from the heart's natural pacemaker (sinoatrial or S-A node) and these impulses cause the two atria to contract and force blood into the ventricles (see Figure 1.2) [14]. The contraction of the ventricles is caused by impulses from the atrioventricular (A-V node). As the ventricle relaxes, the pressure falls within, blood again flows into the atria, then an impulse from the S-A node initiates the cycle over again, and this is referred to as the cardiac cycle (CC) [14]. The contraction phase of the ventricles is termed systole and the relaxation phase is termed diastole. The diastolic period is the longest of the two phases and allows the heart to rest in between contractions [9].

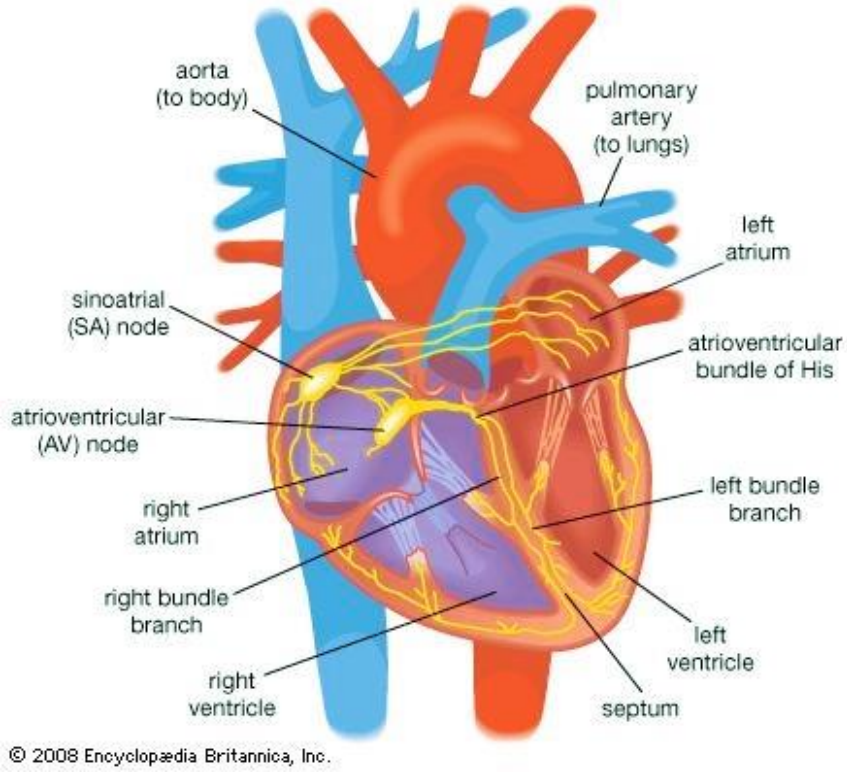

Figure 1.2: The four chambers and valves of the human heart [14].

The circulatory system has two pathways: the systemic circuit and pulmonary circuit. Within the systemic circuit, oxygenated blood leaves the body through the left ventricle to the aorta where it travels to arteries and capillaries to oxygenate body tissue [15]. The deoxygenated blood then returns via the veins, where it re-enters the heart's right atrium. In the pulmonary circuit, the deoxygenated blood travels out from the right ventricle via the pulmonary artery and travels up to the lungs where the blood can be oxygenated. This newly oxygenated blood then returns to the left atrium via the pulmonary vein and this cycle repeats every heart beat (see Figure 1.3).

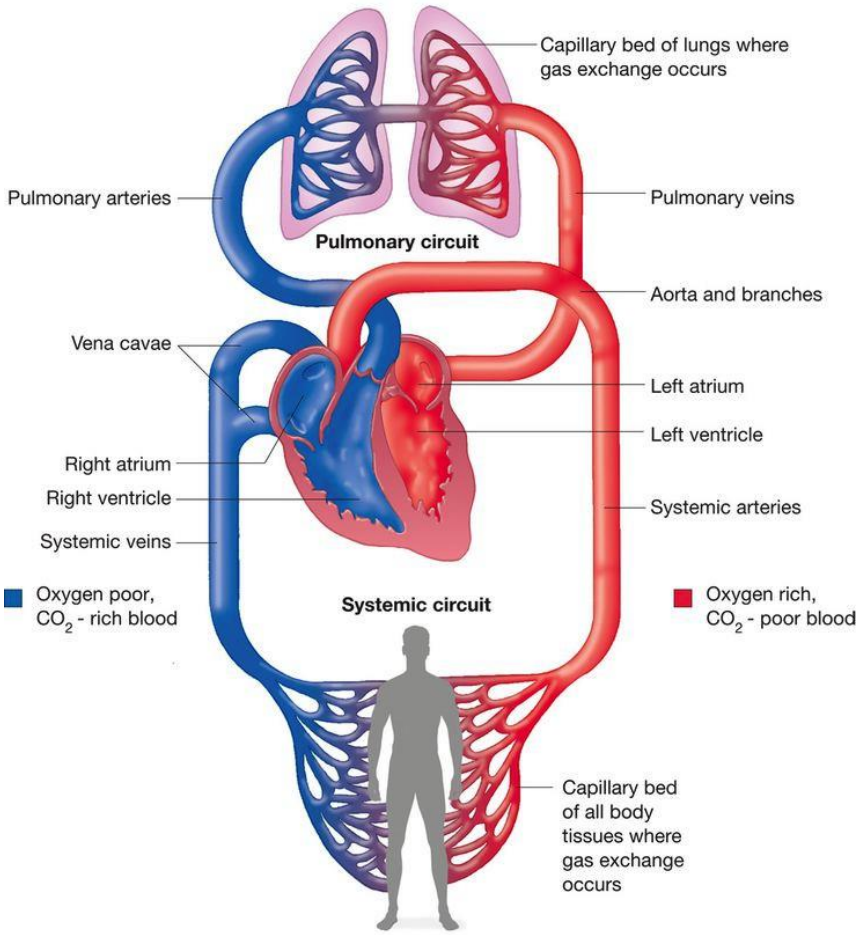

Figure 1.3: Overview of the human cardiovascular system [16].

The complexity of the cardiovascular system is highly vulnerable to damage from the things we do to it, such as smoking, unhealthy eating or stress. In some circumstances, a person can be born with a defective heart also known as congenital heart defect – according to the National Heart, Lungs and Blood Institute, more than 35,000 babies in the United States alone are born with congenital heart failure [17]. CVD is a broad term that covers various disorders to the system associated with the heart's functionality [18]. CVD directly affects the heart itself as well as the brain and peripheral circulatory system [19]. Below are three classifications of CVD and some of the associated types outlined by the World Heart Federation [19]:

Heart-related cardiovascular disease

- Angina
  Chest pain due to the lack of blood supplied to the heart muscle.

- Arrhythmia
  An abnormality of the heart rhythm.

- Heart failure
  A condition where the heart is unable to pump enough blood to supply the body's tissue and organs.

Brain-related cardiovascular disease

- Cerebrovascular disease (stroke)

  Blood flow to the brain is blocked or interrupted. This causes the cells in the brain to die due to oxygen and nutrient deprivation. There are two types of stroke – hemorrhagic and ischemic.

  - Hemorrhagic stroke
    A stroke that occurs when damaged blood vessels rupture and bleed onto the surrounding brain.

  - Ischemic stroke
    Occurs when the blood supply to the brain is blocked.

Circulatory system-related cardiovascular disease

- Deep vein thrombosis

  A condition where blood clots form in the veins (usually in the legs). These clots then break away and travel through the bloodstream to an artery in the lungs and block blood flow.

- Hypertensive heart disease

  Classified as heart damage that results from high blood pressure, heart failure and thickening of the heart muscle.

- Peripheral artery disease

  Refers to the narrowing of the arteries external to the brain or heart causing blood flow disruption that can lead to the death of tissue cells.

The specific type of CVD that is relevant to this study is the heart-related condition called heart failure. Heart failure is a condition in which the heart cannot sufficiently pump blood around the body. Heart failure is generally caused by heart attacks, high blood pressure, viral infection in the heart, cardiomyopathy or heart valve problems [20]. Heart failure can be categorised into three categories, left-side heart failure, right-side heart failure, and congestive heart failure (see Figure 1.4). Two types of left-side heart failure called systolic failure and diastolic failure can occur. Systolic heart failure occurs when the heart muscle does not normally squeeze due to a weakened heart muscle (cardiomyopathy) [21]. Diastolic heart failure, on the other hand, occurs when the heart squeezes well but cannot correctly fill with blood because the wall muscle has thickened and has lost the capability to relax [21]. Both systolic and diastolic heart failure results in the back up of blood to the lungs and other parts of the body (hands, legs, and feet). This backing up of blood is referred to as congestion, hence the term congestive heart failure. In some case a weak heart does not result in congestion [21].

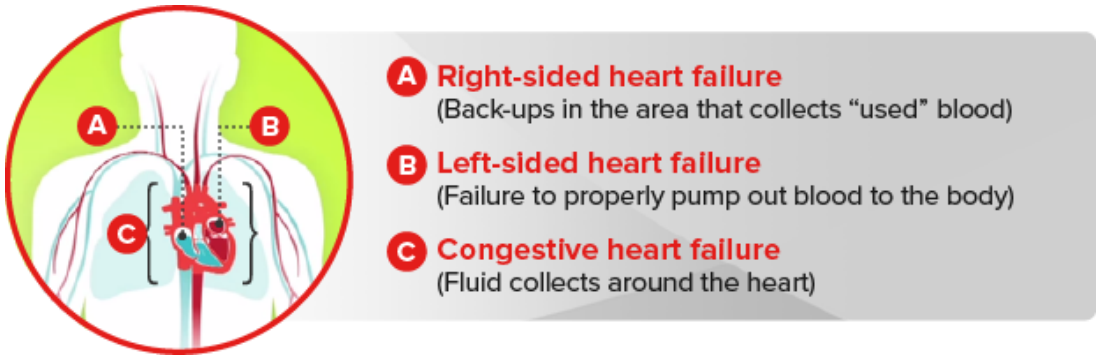

Figure 1.4: Three types of heart failure [22].

1.1.2 What is Congestive Heart Failure?

CHF presently affects about 5 million people in America alone with approximately 550,000 new cases diagnosed each year [21], [23]. CHF affects all ages in both genders although patients aged 59 and above have a higher risk of CHF. Along with the ageing population of the world [24], the number of patients diagnosed with CHF is increasing continuously [25-26]. More than half of diagnosed patients die within five years of diagnosis [21], [23]. The likelihood of developing CHF increases with age; at 40 years of age, the lifetime risk for both women and men is 1 in 5 [26]. It is a severe condition for which there is no cure. CHF is caused by numerous medical conditions that damage the heart muscle; associated conditions like heart attack, coronary artery disease and cardiomyopathy. These conditions make the heart struggle to keep up with the demands of the organs and tissue – the major symptoms that patients can experience are shortness of breath, reduced ability to walk and feeling tired and weak [26].

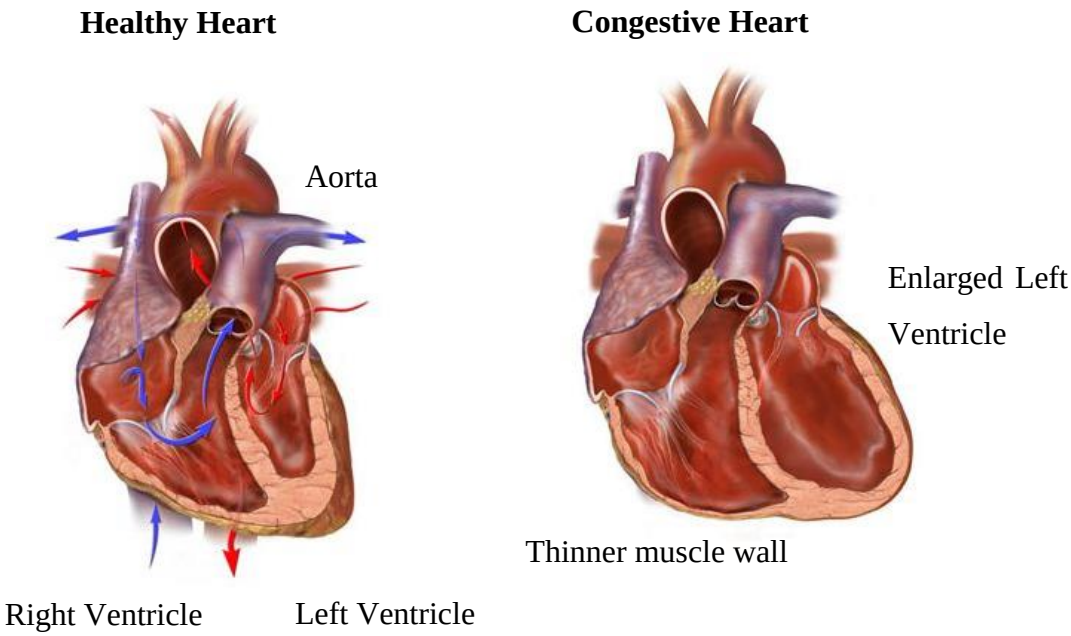

Figure 1.5: Healthy heart anatomy vs. congestive heart (modified) [27].

CHF is classified into four classes by the New York Heart Association (NYHA) standard. NYHA outlines the severity of how well the heart is still able to pump blood around the body indicated by how a patient with CHF limits their physical activities [28]. The following are definitions from the American Heart Association for the four NYHA classes [28].

- Class I (Mild)

  No limitations of physical activity. Ordinary physical activity does not cause undue fatigue, palpitation, and shortness of breath.

- Class II (Mild)

  Slight limitation of physical activity. Comfortable at rest. Ordinary physical activity results in fatigue, palpitation, and shortness of breath

- Class III (Moderate)

  Marked limitations of physical activity. Comfortable at rest. Less than ordinary activity causes fatigue, palpitations or shortness of breath.

- Class IV (Severe)

  Unable to carry on any physical activity with discomfort. Symptoms of heart failure at rest. If any physical activity is undertaken, discomfort increases.

CHF is a serious illness that can limit how long a patient can live for as well as their quality of life. With medical advancements today, proper treatment and thorough management, a patient can be managed to prolong their life [26]. Appropriate treatments for CHF are generally defined by the NYHA classification and the underlying medical conditions that the patient may have. As stated by Sunshine Heart [26] and American Heart Association [28] there are three major treatments that can manage CHF:

- Lifestyle Change

  Lifestyle change is usually the first option that is recommended for all patients. Changes such as healthier diet, exercise and other habits like quitting smoking can help alleviate symptoms, and decrease the rate of disease progression.

- Heart Medications

  Patients with CHF are often prescribed multiple medications to treat different symptoms or contributing factors of CHF. Various research studies show that medication is proven to be the best treatment of CHF. Types of medications can include blood thinners, anticoagulants, and statins, to name a few.

- Device and Surgical Procedures

  In some cases, patients with moderate to severe CHF require treatment further to the two mentioned above. Patients with severe damage to the heart muscle require an implantable device to either assist or replace the heart function. A Ventricular Assist Device (VAD) is an implantable device that is essentially a pump attached to the patient's own heart to aid the heart to pump blood around the body. In severe CHF cases where heart-assisting devices, medication and lifestyle change fails to slow down the progression, a heart transplant may be the only means to effectively treat the patient.

1.1.3 Heart Assisting Devices for CHF

Heart assisting devices with mechanical circulatory support are an essential treatment for patients with advancing moderate to severe CHF. Technological advances in this area have improved the overall survival rate and decreased the occurrence of complications [25].

Ventricle Assist Devices

For patients that are too ill to wait for a heart transplant or for the case that a heart transplant is not a viable option because of age or other medical complications, VAD offers a life-saving treatment [29]. VAD was initially designed as a temporary support to bridge CHF patients to heart transplant but they are now being used as lifetime support due to the technological advancements (see Figure 1.6) [29]. VAD's now allow some patients to return home and resume their normal daily activities. However, the VAD's pump design incurs invasive surgery and ongoing medical treatment which can result in a long-term risk of complications.

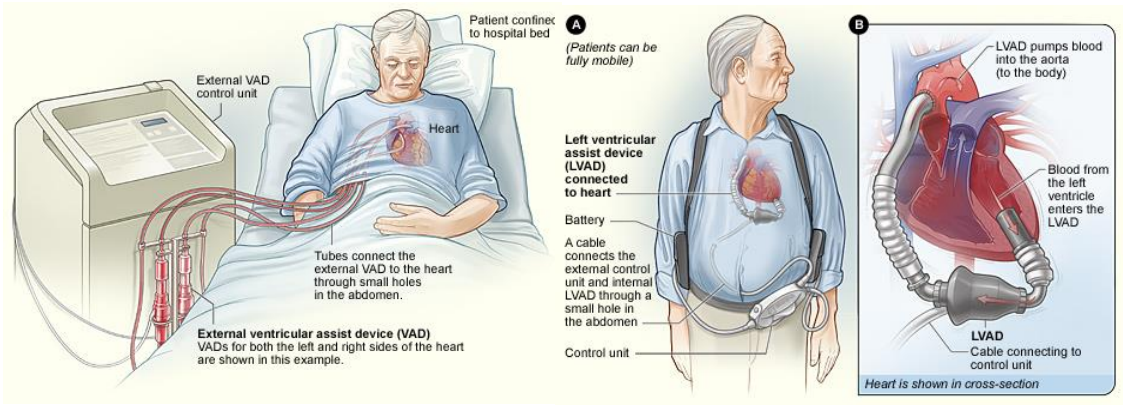

Figure 1.6: Transcutaneous VAD and an implantable VAD [30].

The main design functionality of VAD's is to assist the already damaged ventricle and maintain the normal flow of blood from the heart to vital organs [25-26]. There are two basic types of VAD's; left ventricle assist device (LVAD) and right ventricle assist device (RVAD). LVAD is the most common and is used to help the left ventricle pump oxygen-rich blood to the aorta [30]. The RVAD helps the right ventricle pump blood to the lungs via the pulmonary artery where the blood can be oxygenated [30]. Both LVAD and RVAD can either be transcutaneous or implantable. Transcutaneous VADs consist of an external pump and power unit located outside a patient's body. An implantable VADs

has the pump placed inside the patient's body with the power unit located externally to the patient's body.

Until recently, the hardware footprint of the VAD's systems was too large to be implanted into many patients, particularly women and children [30]. However, VAD's are now smaller in size and can fit most adult patients as well as older children [30]. Although VAD's offer life-saving treatment and improve the quality of life (QoL) for class IV CHF patients, complications will arise. These complications include internal bleeding from the chest, stroke, infection, kidney failure and even cause the right side of the heart to fail [29], [31].

Cardiac Resynchronization Therapy

Cardiac Resynchronization Therapy (CRT) is one of the few new treatments for symptoms associated with CHF caused by cardiomyopathy. Some patients with CHF have an abnormality of their heart's electrical system where the most common abnormality is the delay of the electrical conduction within the heart's muscle [32]. In approximately 40% of such patients this results in an uncoordinated ventricular muscle contraction [32]. This abnormal electrical delay that occurs along the pathway that electrical impulses travel to make the heartbeat is referred to as bundle branch block (BBB) [33]. BBB reduces the ability of the heart to efficiently pump blood through the circulatory system [33]. A CRT system is designed to restore the normal heart pumping action of the ventricles with small amounts of electrical charge applied to three sections of the heart [32]. The small electrical impulses are delivered from a common pacemaker via three leads which make CRT essentially a unique type of pacemaker (see Figure 1.7) [32], [34]. The small electrical impulses stimulate the heart muscle in sync with the natural heartbeat that results in an improvement in electrical delay. The CRT ideally treats patients with NYHA class III-IV CHF, cardiomyopathy and significant electrical delay across the ventricles [32]. According to Shea and Sweeney, scientific studies involving over 2000 patients worldwide have concluded that CRT consistently demonstrates a modest improvement in CHF class and QoL. However, only small numbers of CHF patients can actually benefit from CRT treatment [32]. Like the VADs, the treatment involves an invasive surgery of blood-contacting implants which could lead to device-related infectious complications [35].

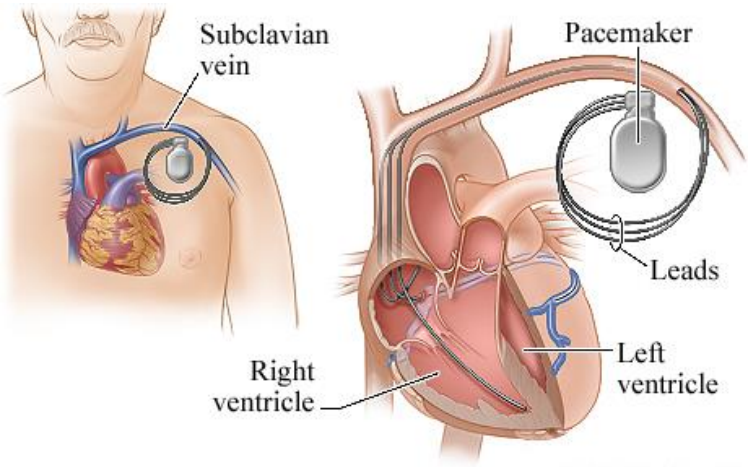

Figure 1.7: Cardiac Resynchronization Therapy [34].

Intra-aortic Balloon Pump

An Intra-aortic balloon pump (IABP) is a mechanical device that is surgically inserted into the descending aorta (DA) which is designed to help the heart pump blood around the circulatory system by reducing the heart's workload. The design of the IABP is a long, thin tube (catheter) with a balloon attached to the end [36]. The balloon at the end of the catheter inflates and deflates in synchrony with the heart, resulting in an improvement in function of the left ventricle [36]. The inflation of the IABP occurs after the contraction stage of the left ventricle which increases blood flow back to the heart and the rest of the body [36]. The deflation stage occurs as the left ventricle is about to pump out the blood for which the balloon creates extra space in the DA, allowing the heart to pump out more blood (see Figure 1.8) [36]. Like all invasive CHF treatments, IABP also comes with complications. These include infection in the bloodstream that can occur after prolonged usage of the IABP and aortic disruption (tearing of the aorta) caused by over inflation of the balloon [36]. The IABP device also requires the patient to be in the hospital with minimal or no mobility during the treatment which is considered inconvenient for the patients [36].

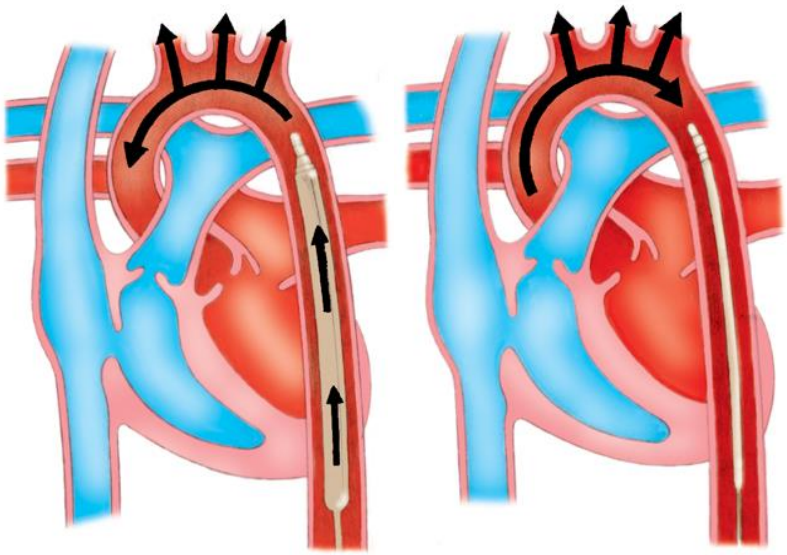

Figure 1.8: IABP System. Left: Inflation of the balloon during diastole. Right: Deflation of the balloon during systole [37].

Extra-aortic balloon pump

An extra-aortic balloon pump (EABP) is a CHF treatment that uses a balloon cuff that is attached to the aorta externally for the function of reducing the heart workload [38]. The system works by the process of inflation and deflation of the cuff in synchrony with the natural heartbeat [38]. The system uses the concept of counterpulsation – timed inflation in between heart beats. When the heart relaxes, the cuff inflation occurs which squeezes the aorta producing a blood surge to both the body and heart muscle [38]. Just before the heart starts to pump again, the cuff deflates and allows the blood to flow naturally around the circulatory system without disruption [38]. The EABP system is non-blood-contacting which means no risk of infection within the bloodstream and has been proven to be an effective treatment for NYHA class III and ambulatory class IV CHF patients [4]. However, EABP does again come with complications such as aortic rupture, lack of effectiveness and device failure [39]. More in-depth information on the EABP will be presented in Chapter 2.

1.2 Aims of the Research

The aim of this research is to study an extra-aortic balloon cuff that binds around the DA and applies peristaltic movement to the cuff with a pneumatic driver and a microcontroller; the objective is to determine if such a system could augment the pressure and flow waveforms in the DA – with the goal of increasing the coronary blood flow and decreasing cardiac afterload during a cardiac cycle (see Figure 1.9).

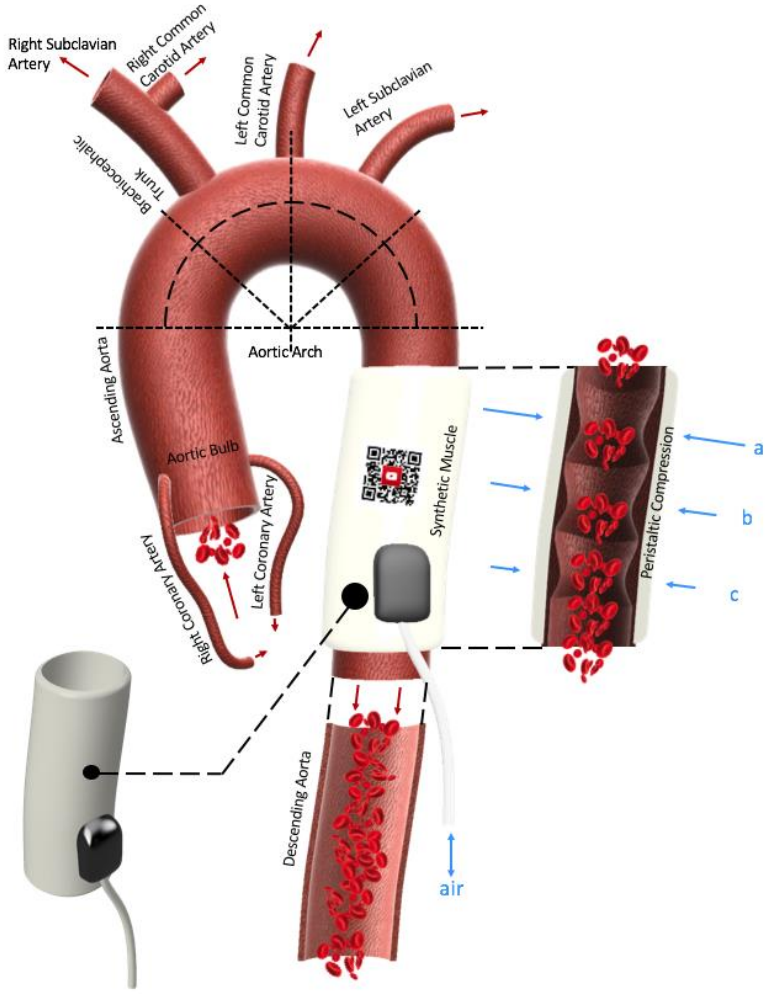

Figure 1.9: Concept of an extra-aortic balloon cuff attached to the descending aorta.

The study is based on a variation of the idea behind Sunshine Heart's C-Pulse® heart assist device. Their device uses a pneumatic balloon cuff that wraps around the ascending aorta (AA) and pumps in the rhythm of a natural heartbeat producing a thumbprint like depression on to the AA wall. The C-Pulse® system is a relatively new investigational clinic treatment option that treats patients with moderate to severe CHF. As Sunshine Heart has outlined, there is a gap for CHF treatment – late NYHA class III and NYHA

early class IV (see Figure 1.10) [40] and C-Pulse® is currently the only device that fulfils this gap. This treatment gap represents patients who are not responding well to optimal medical therapy, are severely limited in their daily activity or do not qualify for a full heart transplant [40].

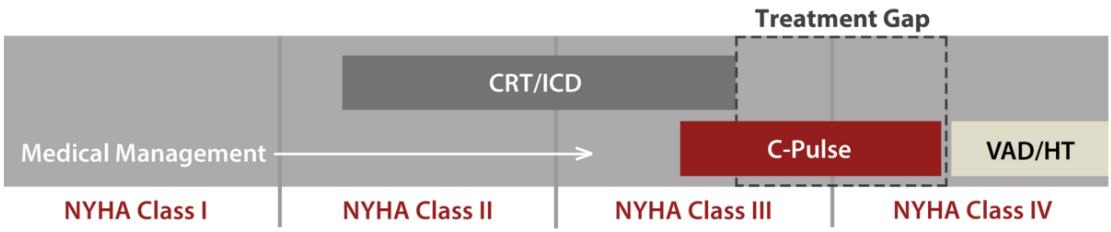

Figure 1.10: Heart failure treatment gap outlined by Sunshine Heart [40].

The C-Pulse® system has been designed to augment the diastolic pressure in the AA using counterpulsation. Clinical data published by Sunshine Heart has shown that the device does decrease left ventricular afterload (end-systolic wall stress) and increase coronary blood flow.

The idea of peristaltic actuation of pneumatic cuffs attached to the DA, that is the basis of this research, is supported by combining aspects of several areas of research. This idea is an adaptation of the fundamental design of the C-Pulse®. A second concept is that of peristaltic transportation of fluid. A study by Takagi and Balmforth [41] derived a model for a peristaltic wave that propagates down a fluid-filled elastic tube. Their mathematical model computes how a peristaltic wave behaves or is manipulated as it travels down the tube. Another similar study by Maiti and Misra [42] demonstrated the effects of peristaltic transport of fluid applied to a tube to study the hemodynamics.

Manipulation of the descending aorta to assist heart function was first discovered by the Kantrowitz brothers back in 1953 [43]. An experiment done by the Kantrowitz brothers demonstrated the benefits of using a diaphragm wrapped around the descending aorta which was stimulated to contract during diastole to decrease ventricular workload [43]. Their research lead to the creation of the IABP by Dr. Ardian Kantrowitz from which the concept of descending aortic augmentation was adapted.

1.3 Thesis Structure

This research was based on covering the areas that were relevant to support the hypothesis and conclude the feasibility of the overall project. The three major aspects – phantom aortas and cardiovascular simulation platform, pulse wave software simulation, and the PEABC Prototype – are described and examined in separate chapters. Each chapter is presented with its own individual introduction, methodology, results and discussion content. The introduction section briefly describes the functionality and purpose of the aspect. The methodology section explains the critical processes behind the work that was done based on work done by previous research. The result section shows the results obtained from testing procedures performed in that aspect. The results are then compared with related research – mentioned in the literature review chapter – in the discussion section. Once all of the aspects are presented separately, a result summary chapter describes the results as put together. The discussion summary then compares these consolidated results against what is reported in the literature. Chapter 3, Chapter 4 and Chapter 5 describe the development of a phantom aorta and cardiovascular simulation platform, software simulation of the aortic pulse wave and the hardware/software development of the PEABC respectively.

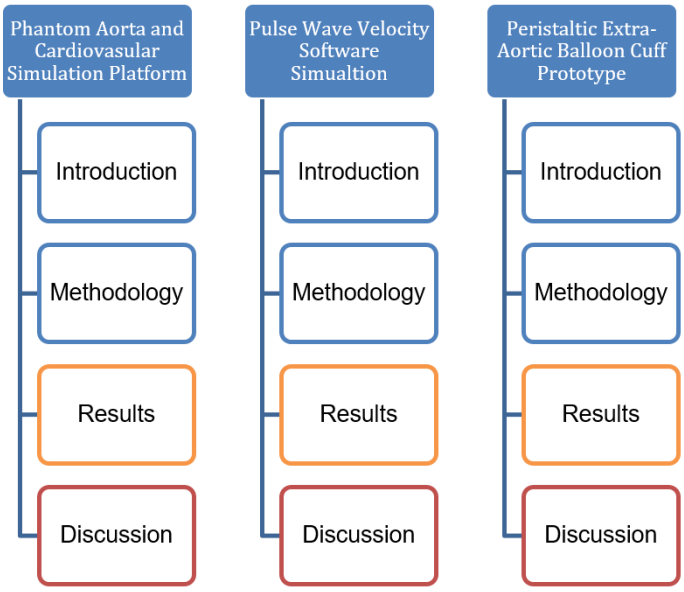

Figure 1.11: Thesis structure of the related topics, with each of the topic's result and discussion sections being summarised together in Chapter 6 and Chapter 7.

Chapter 2

Literature Review

The literature review presented here is intended to support this thesis by describing the feasibility of applying peristaltic counter-pulsation to an extra-aortic balloon cuff, to increase aortic flow and pressure that would result in reducing cardiac workload. Aspects of this review relate to the construction of a functional prototype that is capable of assisting heart function. This literature review is structured according to the following main themes:

- Extra-Aortic Balloon Cuff (C-Pulse®)

  Clinical trial device developed by Sunshine Heart Inc. that uses counter-pulsation to provide physiologic benefits (cardiac output and aortic diastolic pressure).

- Peristaltic Model

  The understating of peristaltic movement to transport viscous fluid in an elastic tube.

- Arterial Hemodynamic

  Knowledge of normal and abnormal hemodynamic statistics and waveforms in the human arterial system.

- Pulse Wave Velocity

  The understanding of pulse wave velocity, which is related to the experimental work undertaken in this research.

- Phantom Aorta

  The process of adapting anatomical geometry and biophysical properties of a human aorta to produce a phantom aorta.

2.1 Extra-Aortic Balloon Cuff - C-Pulse®

The C-Pulse® design revolves around implementing a proven balloon counterpulsation technology that assists the heart's cardiac cycle by reducing the workload of the left ventricle [26]. Stated by Sunshine Heart [38] the C-Pulse® is designed to improve heart function in the following ways:

- *"Increase coronary blood flow with more oxygenated blood flowing to the blood vessels and heart muscle."*
- *"Decrease cardiac afterload reducing how hard the heart has to work to pump blood through the body."*
- *"Increase cardiac function with more blood being pumped from the heart to the rest of the body."*

2.1.1 Design and Operation of the C-Pulse®

The C-Pulse® system consists of an internal extra-aortic balloon (EAB) and an epicardial electrocardiography sense lead that connect to an external battery-powered pneumatic drive (see Figure 2.1) [5]. The EAB was made from polyurethane fused with a polyester wrap that conformed to the ascending aorta (see Figure 2.2) [26]. The EAB is surgically attached to the ascending aorta and the epicardial sensor lead placed on the left ventricle [5]. The C-Pulse® pneumatic drive system pumps in counterpulsation to the natural heartbeat and results in the EAB deflating during systole and inflating during diastole [5].

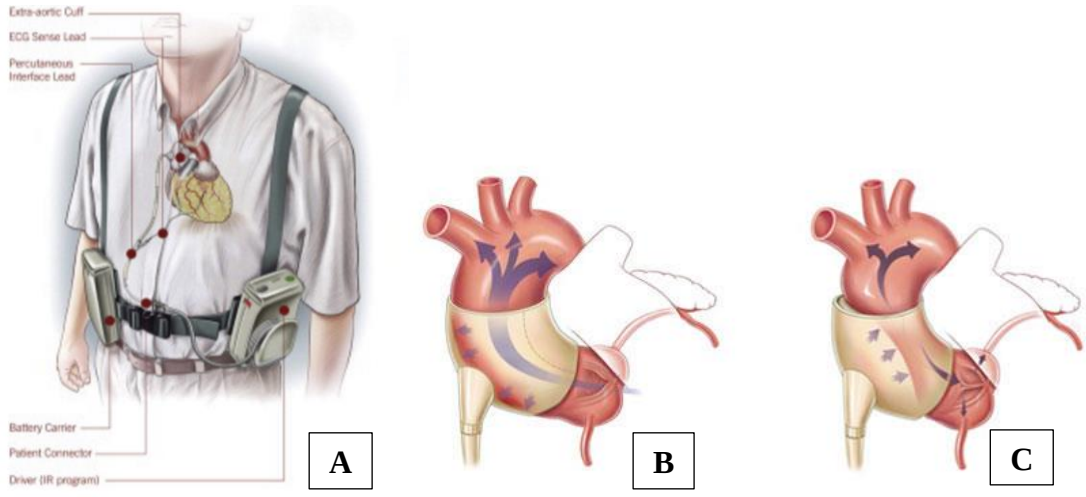

Figure 2.1: Extra-aortic balloon cuff (C-Pulse®) system attached to the ascending aorta. (A): C-Pulse® Device, (B): Cuff deflation, (C): Cuff inflation (modified) [5],[44].

The inflation and deflation timing of the EAB is programmed into the C-Pulse® system so that inflation begins directly after the dicrotic notch and deflation occurs during the ejection phase of systole [5] – the exact inflation and deflation timing data of the C-Pulse® system has not been disclosed publicly. The C-Pulse® device design allows the patient to detach the device for a period of time without complications as it is not a life sustaining device and therefore the patient is able to shower or undertake other activities. The implantation of the C-Pulse® EAB is performed using a minimally invasive surgical technique that takes around 90 min with no requirement for a cardiopulmonary bypass (stopping the heart) [4].

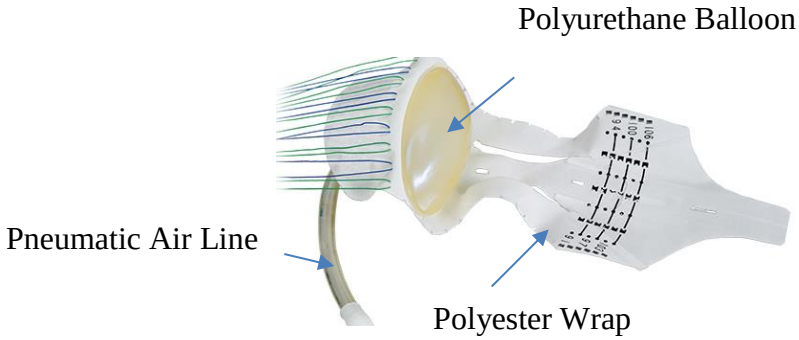

Figure 2.2: Material composition of the extra-aortic balloon cuff (C-Pulse®) (modified) [26].

2.1.2 Clinical Evidence by Sunshine Heart on C-Pulse®

There have been some publications by Sunshine Heart that outline the performance of the C-Pulse® in assisting patients with CHF [45]. These report evidence obtained in clinical trials that show an increase in coronary and diastolic carotid flow [44], [47-48], systolic and diastolic pressure wave augmentation [47], and improved cardiac output [48] which reflects a reduction in cardiac afterload [47]. Sunshine Heart's findings show that the C-Pulse® increases diastolic flow velocity by an average of 30% with a marked increase in net flow rate of +57% [47] (see Figure 2.3). In the same study, the forward and backwards pressure wave at the ascending aorta are also affected and the diastolic phase of the pressure waves are increased (see Figure 2.4).

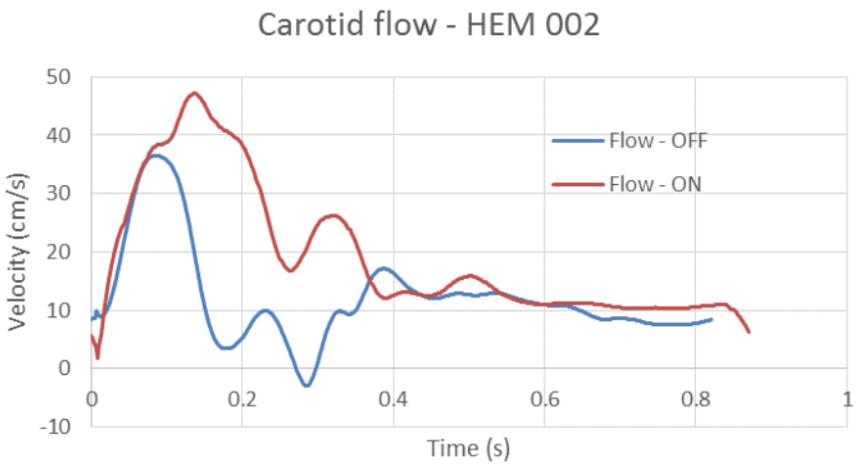

Figure 2.3: Carotid flow velocity. Blue: C-Pulse® off, Red: C-Pulse® on [47].

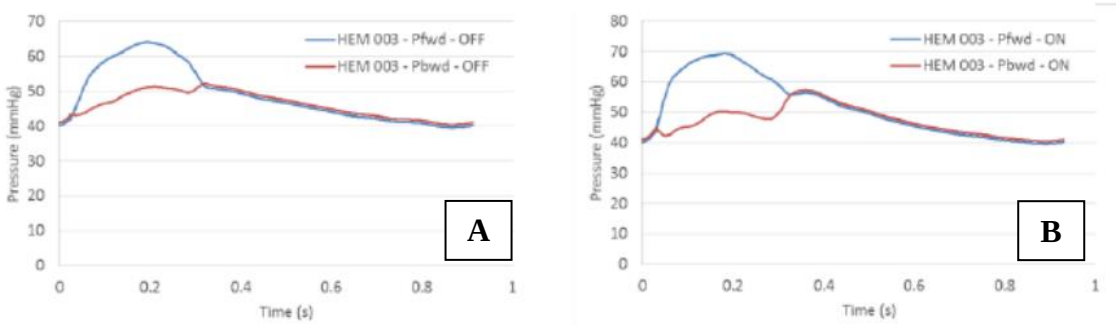

Figure 2.4: (A): Forward and Backwards pressure wave at the ascending aorta with the C-Pulse® off. (B): Forward and Backwards pressure wave at the ascending aorta with the C-Pulse® on [47].

A preliminary study by Legget et al. on an intraoperative feasibility study on EAB counterpulsation clinically tested EAB attached to the ascending aorta in 6 patients that were undergoing first-time off-pump coronary bypass surgical procedures [44]. Legget et al. stated that current methods of ventricular assistance have significant limb and vascular impediments on patients. Their study determined the safety and performance of the novel EAB. They concluded that EAB can augment coronary artery flow by 67% and reduces left ventricular workload [44]. A further study by Sales and McCarthy on understanding the C-Pulse® and its potential to treat heart failure reinforce Legget et al.'s statistical data on coronary artery flow [46]. They compared the hemodynamic augmentation of EAB (C-Pulse®) to an existing IABP device that also functions using aortic counterpulsation [46]. Their results showed that both of the circulatory support

devices could significantly increase diastolic arterial pressure and decrease left ventricular workload. Abraham et al. [5] also agree with the statement of physiological benefits of IABP and EAB stated by both Legget et al. [44], and Sales and McCarthy [46].

One of the key features of the C-Pulse® is inflation and deflation timing of the EAB. In another study by Sunshine Heart [49], C-Pulse® timing was investigated using plethysmography and concluded that timing of the EAB inflation and deflation has a significant effect on the efficiency of the C-Pulse®. Their use of plethysmographic waveforms provided a good approximation of the arterial blood pressure waveform in the tested patient with C-Pulse® [49]. In their documented technical bulletin, the initial test results shown in Figure 2.5, illustrates the optimised 1:2 operation (that is, C-Pulse activation every second cardiac cycle) with correct inflation timing.

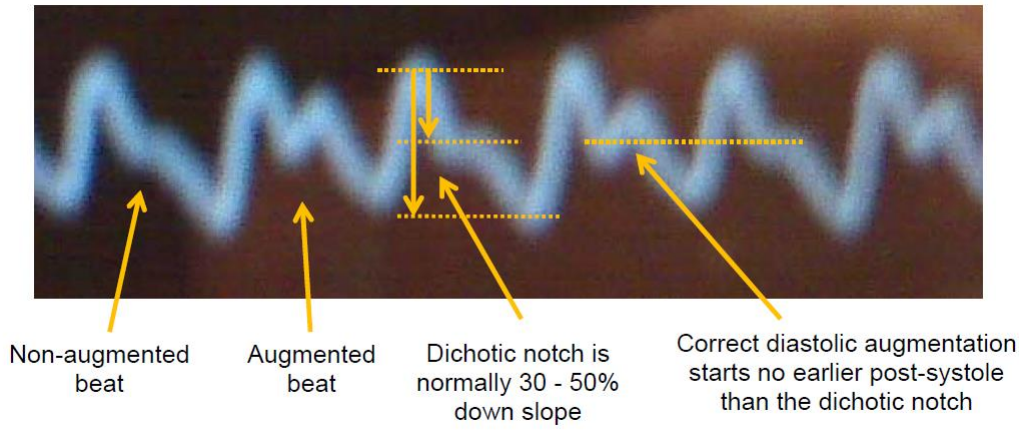

Figure 2.5: The effects on the pressure waveform with an optimised 1:2 operation of the C-Pulse® [49].

With the same 1:2 operation test of the C-Pulse®, the effects on the pressure waveform due to both late/early inflation and deflation timing were illustrated. The effects on the pressure waveform due to early inflation of the C-Pulse® – as stated on the technical bulletin – the diastolic augmentation will start up higher than the dicrotic notch [49] (see Figure 2.6). Early inflation time of the C-Pulse® was concluded to affect the cardiac performance negatively [49]. However, late inflation time was not considered unsafe but would reduce the effectiveness of counterpulsation [49].

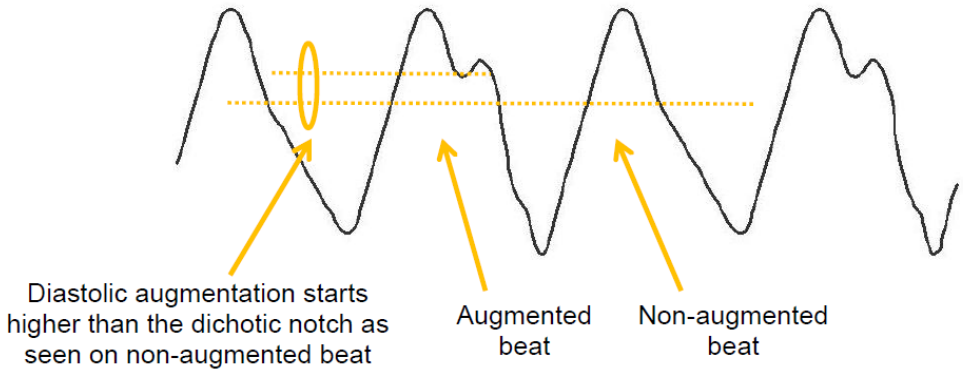

Figure 2.6:The effects on the pressure waveform due to early inflation timing of the C-Pulse®[49].

As for the deflation timing of the C-Pulse®, late deflation was also stated to affect cardiac performance negatively. An early deflation had the same effect on the outcome as late inflation – a reduction in effectiveness of counterpulsation (see Figure 2.7) [49].

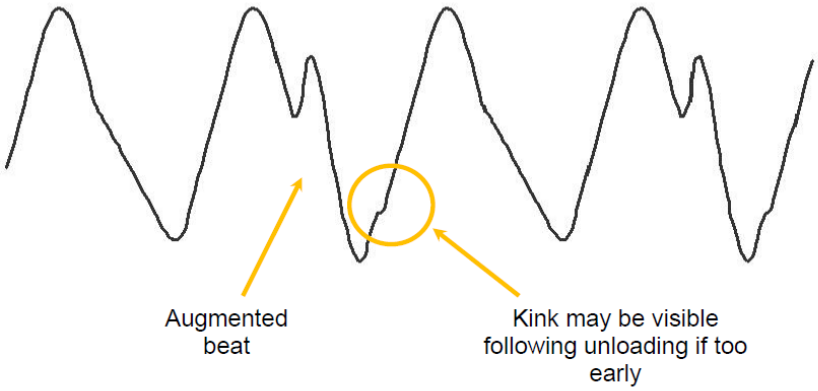

Figure 2.7: The effects on the pressure waveform due to early deflation timing of the C-Pulse®[49].

Their technical bulletin also documented the ideal inflation volume (depending on the C-Pulse® cuff size) and inflation slew setting of the C-Pulse®. C-Pulse® did not state the inflation volume of the cuff but they did state that the cuff was able to displace 20ml – 30ml of blood per beat [49]. The result of good inflation volume and slew rate was that the diastolic pressure waveform augmentation peaks would be close to the same height as the systolic peaks (see Figure 2.8). It was also specified that if the diastolic peaks were higher than the systolic peaks, reducing the slew rate would decrease the diastolic peak [49].

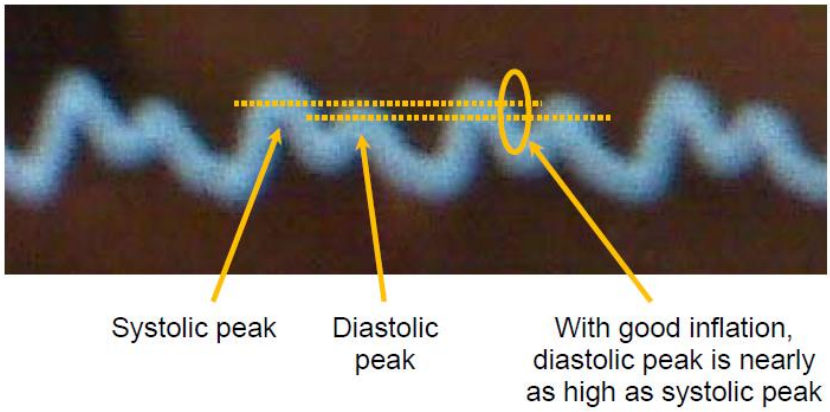

Figure 2.8: The effects on the pressure waveform due to a good inflation volume and slew rate[49].

2.1.3 Counterpulsation System

Counterpulsation therapy is one of the earliest and most common systems of mechanical circulatory support for patients with deteriorating CHF [1]. The foundation of aortic counterpulsation was discovered by Dr. Adrian Kantrowitz in 1956 [43]. The experiment involved using an animal model (dogs) in which the hemidiaphragm was wrapped around the descending aorta and with electrical stimulation, a contraction was made during diastole. His findings resulted in augmenting the diastolic pressure characteristics of the native cardiac cycle, improving coronary perfusion and reducing the cardiac afterload by 25% [50]. Today, counterpulsation techniques use a mechanical device to increase aortic pressure during the beginning of diastole which in turn, increases myocardial perfusion and decrease aortic pressure during the beginning of systole to decrease ventricular workload and cardiovascular afterload [3]. Both studies by Sunshine Heart [3] and Franco et al. [49] agree that the principle of effective counterpulsation operation requires

precise control of inflation and deflation timing and synchronisation of the counterpulsation device with the intrinsic cardiac cycle (see Figure 2.9). The triggering process of inflation and deflation of a counterpulsation device can be derived from an ECG signal and/or aortic pressure waveform [3], [29].

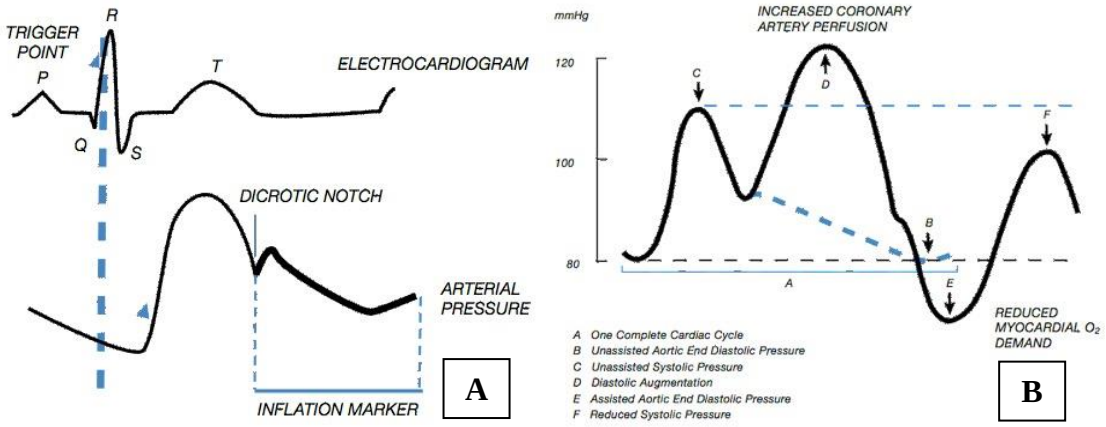

Figure 2.9: Counterpulsation timing during a cardiac cycle. (A): ECG and Pressure inflation trigger point. (B): Hemodynamic pressure augmentation during inflation and deflation [28].

There are multiple myocardial assisting devices that adopt the principle of counterpulsation. These counterpulsation devices include:

- Intra-Aortic Balloon Pump (IABP)
- Extra-Aortic Balloon Cuff (C-Pulse®)
- Extracorporeal Counterpulsation Device (ECP)

Counterpulsation therapy has multiple clinical benefits for not only the heart but also end-organs and peripheral circulation for patients with CHF. The therapy has been known to benefit patient's hemodynamic physiology, including[3]

Increased Cardiac Output	*0-20%*
Decreased heart rate	*0-10%*
Increased Coronary Perfusion	*0-100%*

[3] Statistics based on patients treated with an IABP [3]

Franco et al. also outlines that devices such as IABP's and C-Pulse® that adapts counterpulsation therapy have been shown to be most effective when the patient has systolic aortic pressures are between 40-70 mmHg, a heart rate between 80-110 bpm and has a high arterial stiffness [3]. In other corresponding statements between Sunshine Heart [49] and Franco et al. [3] the optimal performance of an IABP is achieved when the IABP balloon displacement volume equals the stroke volume of the native left ventricle [3]. The effectiveness of counterpulsation is also related to where the IABP device is located on the aorta with a preference for the device to be positioned close to the aortic valve [3]. Device placements of the IABP at the descending aorta and the C-Pulse® at the ascending aorta have become the standard of care because these locations avoid the risk of obstruction and/or embolization of the aortic arch vessels [3-4].

2.2 Peristaltic Model

Peristalsis is defined by the Merriam-Webster medical dictionary "as a *successive wave of involuntary contraction passing along the walls of a hollow muscular structure"* [52]. The peristaltic transport phenomenon occurs in various physiological activities like the flow of urine fluid from the kidneys to the bladder, the movement of food along the digestive tracts (large and small intestines) [42] and the transport of blood through small blood vessels (see Figure 2.10) [53].

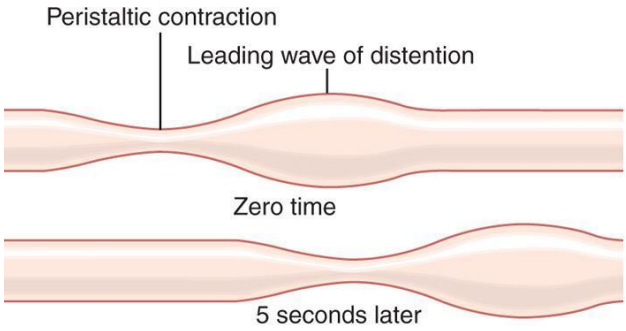

Figure 2.10: Peristaltic contraction and distension through an elastic tube within a 5 second period (modified) [54].

The dynamics of peristaltic augmentation can also be found in biological locomotion of worms [55], swimming of micro-organisms and snails [41]. This mechanism has been adapted for biomedical devices such as heart-lung machines, dialysis machines and blood

pumping machines [42]. Studies of peristaltic modelling have been receiving growing interest for scientific researchers [42]. An interesting research article by J. D. Glenn et al. [56] examined the circuitry system of a mosquito and how it transports blood through a peristaltic contraction in the dorsal vessel which consists of a thoracic aorta and an abdominal heart. Their findings concluded that the hemolymph flow at an average velocity of 8 mm/s is dictated by the anterograde and retrograde direction of the peristaltic muscle contractions of the heart which is made of segmental muscle fibres (see Figure 2.11) [56].

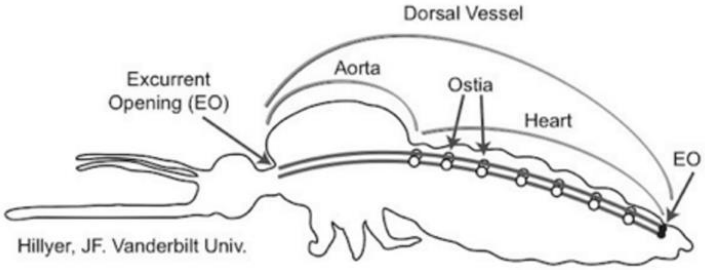

Figure 2.11: A Circulatory system of a mosquito [57].

It is a natural mechanism of pumping that is observed in many cases of physiology [42]. During peristaltic pumping, the physiological fluid is driven by periods of propagating waves of contraction and expansion that advances along a medium [42], [53]. There are numerous studies that investigate the peristaltic transport of blood using analytical, numerical and experimentation methods [42], [53], [59-61]. An analytical and numerical study by S.Maiti et al. theoretically investigated the peristaltic transport of blood in a porous channel [59]. S.Maiti et al. studied the effects of different physical parameters – amplitude ratio and reflecting permeability – on velocity and pumping action of blood by inducing a progressive wave of regional contraction and expansion along the length of the boundary of a fluid-filled distensible tube to observe the peristaltic transport of blood in a small blood vessel (see Figure 2.12) [59].

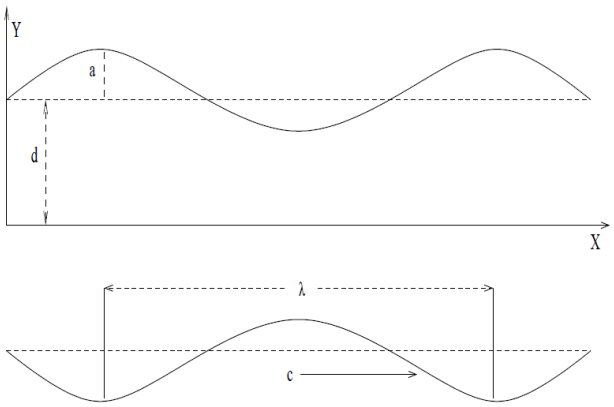

Figure 2.12: Peristaltic transport of blood wave schematic [59].

Another related study, similar to S.Maiti et al., conducted by Hariharan et al., explains the characteristics of peristaltic transportation of non-Newtonian fluid in a diverging medium with different waveforms [53]. Hariharan et al. modelled different waveforms – sinusoidal, triangular, trapezoidal, multi-sinusoidal and triangular – that limit wall motion [53]. Their study suggests that the best pumping waveform that increases pressure flow characteristics is a square wave, with a triangular wave having the worst characteristics [53].

A different study by Martin et al. employs the application of a peristaltic pulse to an external pneumatic compression device (EPC) that attaches to a patient's limb to observe the peripheral conduit and resistance artery function [60]. Their method involved the evaluation of the limb blood flow under the operation of a sequential EPC device with five inflation zones arranged linearly that inflates in a distal to proximal orientation along the lower limb [60]. The EPC parameters that were considered to have acute effects on the limb were treatment pressures, application sites and duty cycles [60]. From their findings that had the EPC inflation pressure set at 70 mmHg with treatment over 1 hour, the peak calf blood flow increased by 9% but the peak forearm had a negative effect with a reduction in blood flow of -10% [60]. The study of peristaltic pneumatic compression is also explored by Nicholas Kiefer et al., where an EPC device was attached to the leg – toe to groyne – with 12 overlapping chambers that inflate in a peristaltic matter resulted in an enhancement in hemodynamic stability (see Figure 2.13) [61]. The 12 chambers were inflated with different pressures; 60 mmHg in the first chamber (similar inflation pressure used by Martin et al.) and 38 mmHg in the last chamber [61]. The inflation process takes between 40-60 seconds and once the time elapses, the pressure is released

and after 4 seconds the cycle begins again [61]. Their conclusion states that the EPC device can increase an individual's mean systolic pressure from 85 mmHg to 92 mmHg [61].

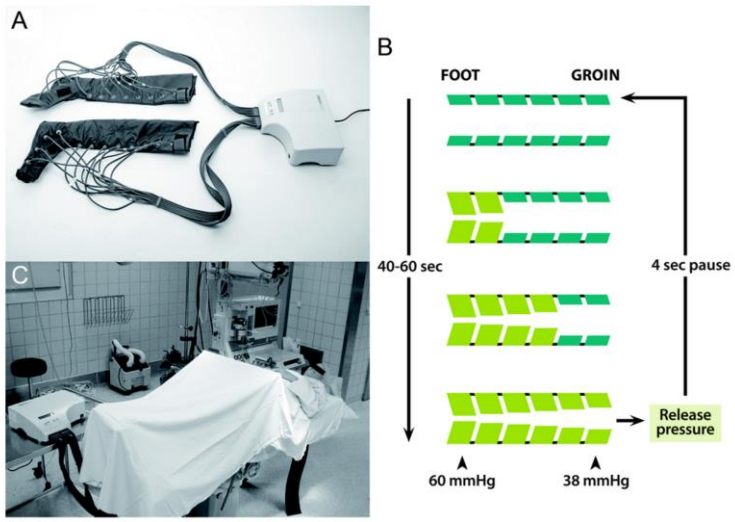

Figure 2.13: (A) EPC Device for the limb. (B) Compression cycle of the EPC device schematic. (C) Operation table with the surgery using the EPC device [61].

From the mentioned studies, one can assume that a practical application of peristaltic pneumatic compression can have a role in changing hemodynamic function. Although the reported studies differ from this research in the application, the principle of applying peristalsis to alter the hemodynamics is sound and thus this research explores the adaptation of that principle for a new purpose.

2.3 Arterial Hemodynamics

Hemodynamic studies blood flow in organic vessels in relation to the various internal and external factors that affect it. A fluid is a substance that continues to deform under a shear stress force and continues to deform even when the force is removed [62]. Fluids can be contained in an elastic material which deforms e.g. blood vessel which recovers its original shape after the force is removed [62]. Although a precise explanation of all cardiovascular system hemodynamic phenomena is complex, the cardiovascular system with the heart generating a steady flow through a series of pipes is similar to the flow of water through a city's water supply system (see Figure 2.14) [63]. Therefore, basic principles of fluid dynamics can be applied to understand the cardiovascular hemodynamic phenomena.

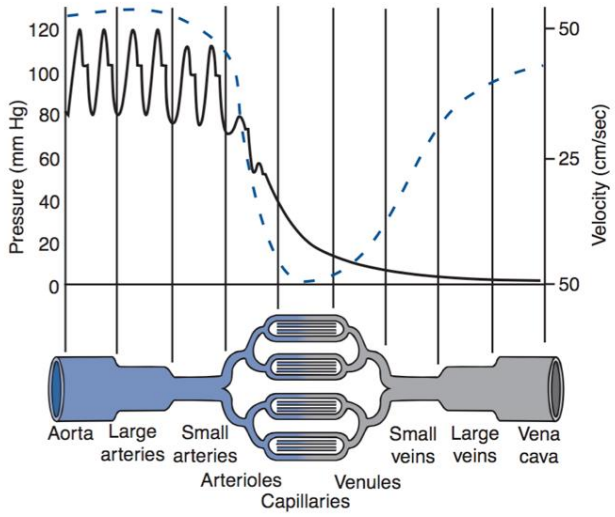

Figure 2.14: Hemodynamic pressure and flow profile [63].

For blood to flow through a vessel or across heart valves, a propelling force acting on the blood is required and is supplied in the form of fluid pressure. The arterial pressure that is explored in this research is the aortic pressure. During a cardiac cycle, the left ventricle ejects blood into the aorta thus the aortic pressure increases [63]. The peak aortic pressure that occurs subsequent to the ejection is defined as the systolic pressure [64]. As the left ventricle relaxes and replenishes with blood, the pressure in the aorta decreases. At the lowest aortic pressure point, before the cardiac cycle repeats, is the diastolic pressure [64]. For a young adult male, a normal systolic pressure is typically 120 mmHg, and 80 mmHg for diastolic pressure [63], [66]. The differences between systolic and diastolic pressure

are known as the aortic pulse pressure and normally ranges between 40-50 mmHg (see Figure 2.15) [64]. The mean arterial pressure is the average pressure during the cardiac cycle which can range between 70 – 100 mmHg [66]. There are several factors that alter the pressure waveform. For example, during exercise, according to Thore, the systolic and diastolic pressures can increase by 10-40 mmHg depending on the intensity [62].

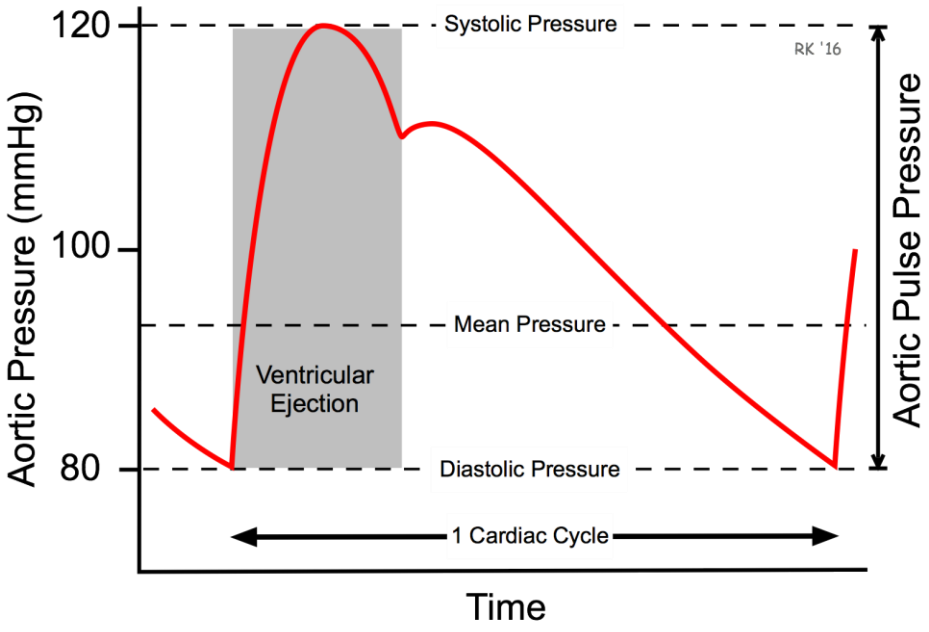

Figure 2.15: Arterial Pressure waveform during a cardiac cycle [64].

A study by Drummond aimed to model the hemodynamic flow and pressure characteristics of a segment of the cardiovascular system using a mechanical piston pump [67]. Drummond's study outlines the importance of creating a pulsatile pump system to model flow characteristics of pressure and velocity in the human aorta. The simulation platform uses a closed loop system constructed in LabVIEW (National Instruments™, United States) that utilises pulse width modulation (PWM) hardware and software to alter an aortic pressure set point via a linear actuator, water pump, and pressure sensors. His design allowed variable control of fluid displacement, velocity and acceleration through which the flow speed, volume flow rate and pressure in the artificial aorta could be made somewhat similar to physiological values. The maximum flow speed that was achieved in the experiment was 1.3 m/s, the volume flow rate in the artificial aorta during systole was 4.1 L/min, and a systolic and diastolic pressure of 83 mmHg and 20 mmHg respectively [67]. The flow and pressure measurements in the artificial aorta were obtained using an ultrasound machine and pressure sensors [67]. Drummond's work shown in Figure 2.16 allowed tests and observation of the cardiovascular hemodynamics of both pressure and flow data to be obtained in real time.

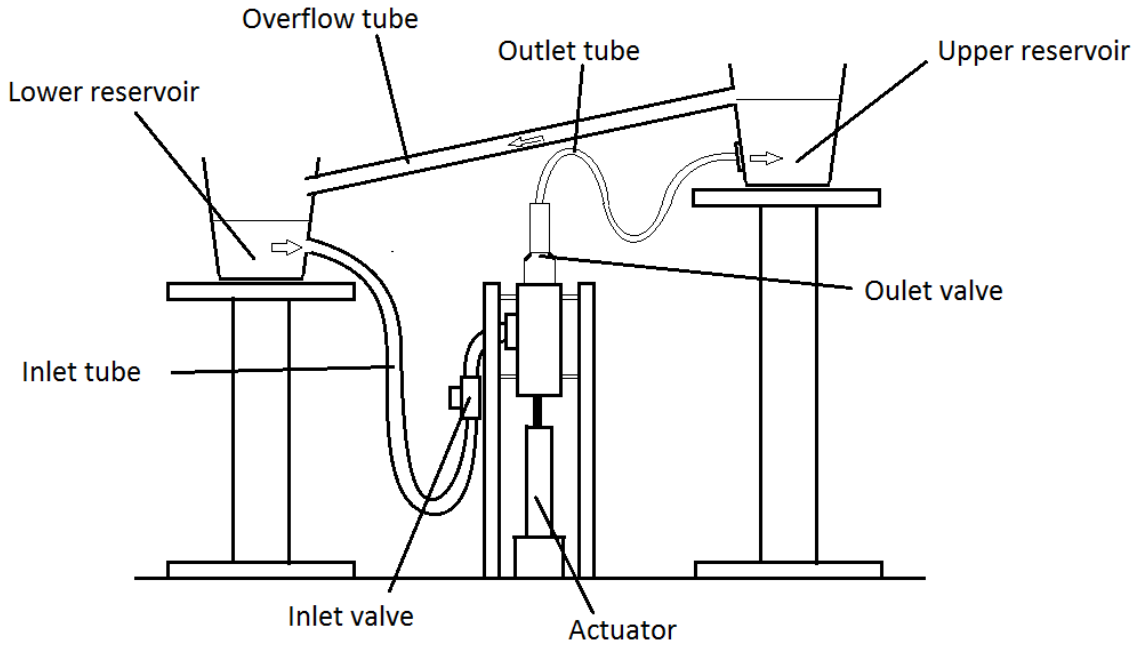

Figure 2.16: Drummond's left ventricle mechanism apparatus set up [67].

In Figure 2.17 and Figure 2.18, a comparison between approximate physiological and measured flow speed in Drummond's artificial aorta are illustrated. Both the measured flow speed and the ascending aortic pressure are lower than physiological values. However, the shape of the waveforms was similar [67].

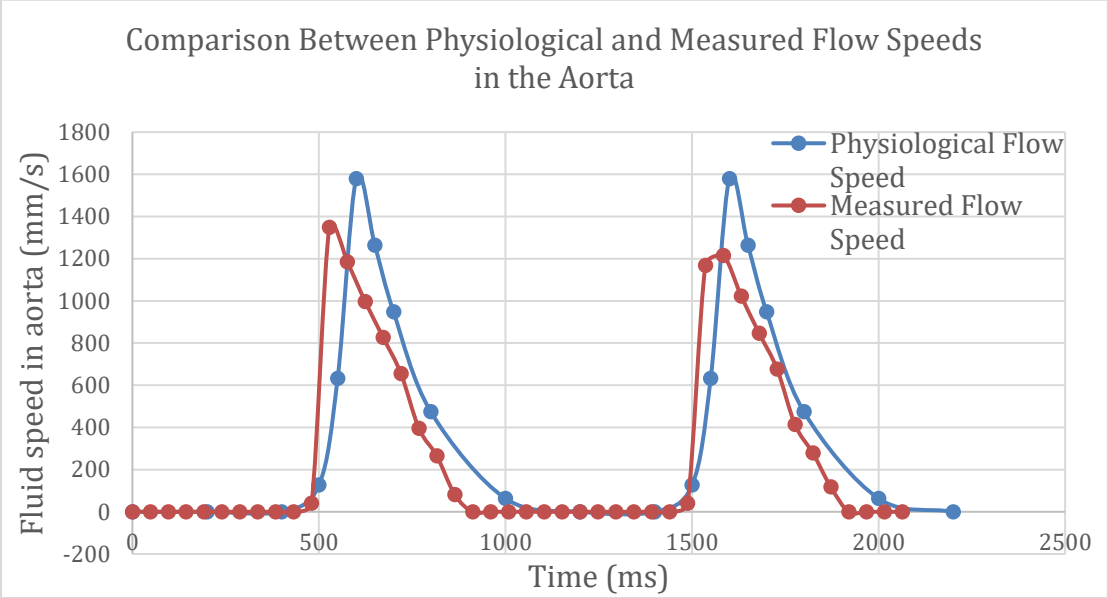

Figure 2.17: Comparison between physiological and measure flow speeds in the aorta [67].

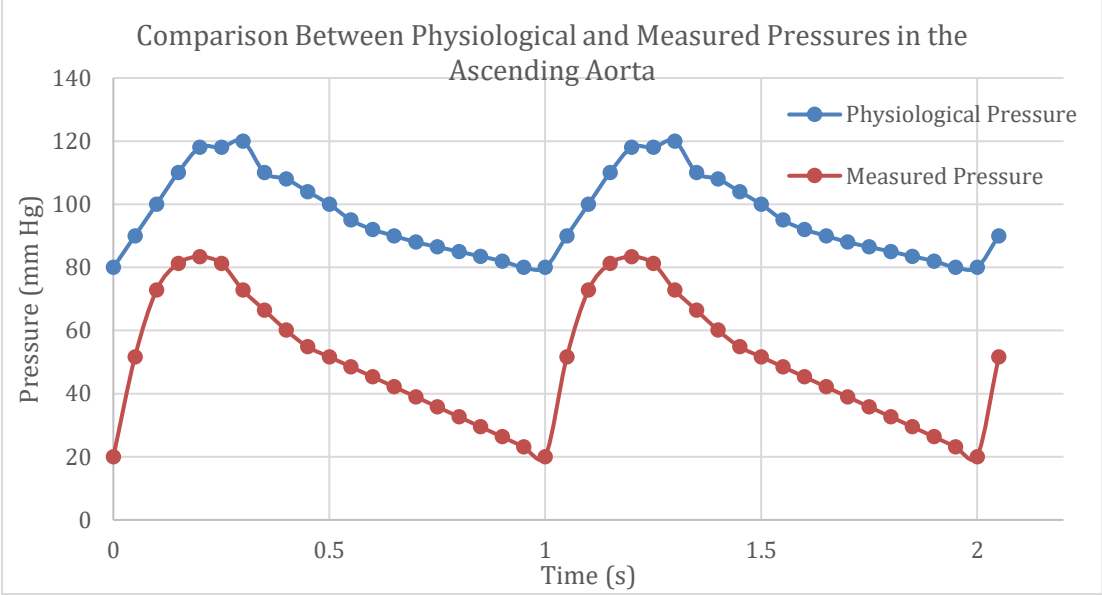

Figure 2.18: Comparison between physiological and measured pressures in the ascending aorta [67].

2.4 Pulse Wave Velocity (PWV)

Pulse wave velocity (PWV) is not the same as blood velocity, but instead relates to the transmission of energy through the arterial wall and not the displacement of mass through the blood filled artery [68]. PWV values vary with pressure and age [69-70]. According to London and Pannier, the PWV can range from 4 m/s to 12 m/s. In a large multi-centre study by Wentland et al., approximately 17,000 patients' carotid-femoral PWV were measured and the study reported a normal PWV value of ~6 m/s for healthy individuals aged <30 years old [69]. Wentland et al. also documented that individuals aged >70 years had a PWV of about 10 m/s. PWV can be obtained by measurements based on the change in the time it takes for the pulse wave to travel a known distance through the artery [70] (see Equation 2.1).

$$PWV = \frac{\Delta x}{\Delta t} \qquad \textit{Equation 2.1}$$

A common method for calculating PWV using a mathematical model is by using Moens Korteweg's equation (see Equation 2.2). This equation assumes no significant changes in vessel area and wall thickness. Moens Korteweg's equation computes PWV using the Young's Modulus (E), wall thickness of vessel (h), radius of the vessel (r) and blood density (ρ).

$$PWV' = \sqrt{\frac{Eh}{2\rho r}} \qquad \textit{Equation 2.2}$$

Another relevant study by Vappou et al. examined the variance of PWV values in an *in vivo* study of 11 patients against phantoms. The average *in vivo* PWV and Young's modulus were measured as 4.4 m/s ± 0.6 m/s and 108 kPa ± 27 kPa respectively [71]. These measurements were based on average abdominal aorta parameters that were obtained using ultrasound. The average inner diameter was 12.7 mm ± 0.8 mm, and the average artery wall thickness was 1.8 mm ± 0.1 mm. Arterial phantoms were constructed using polyacrylamide with an inner diameter of 9.7 mm and a wall thickness of 2 mm.

2.5 Phantom Aorta

Phantom modelling of certain common vascular structures of human anatomy allows experimenting with related medical treatments in a controlled environment [72]. Phantom aortas are made to simulate both vessel-like structures and biophysical properties that can be comparable to a real human aorta. One of the most commonly used materials that are suitable for modelling vessel-like phantom structures is silicone. Russ et al. explain the development of rapid prototyping of silicone-based phantom aorta models that could be viable for stent simulation validation [72]. Another study that developed phantom aorta using silicone was described by Savrasov et al. [73] (see Figure 2.19). In order to create a phantom aorta model comparable to other developed phantom aortas and real human aorta, the nominal aortic geometric size, shape, and biophysical properties had to be obtained and applied.

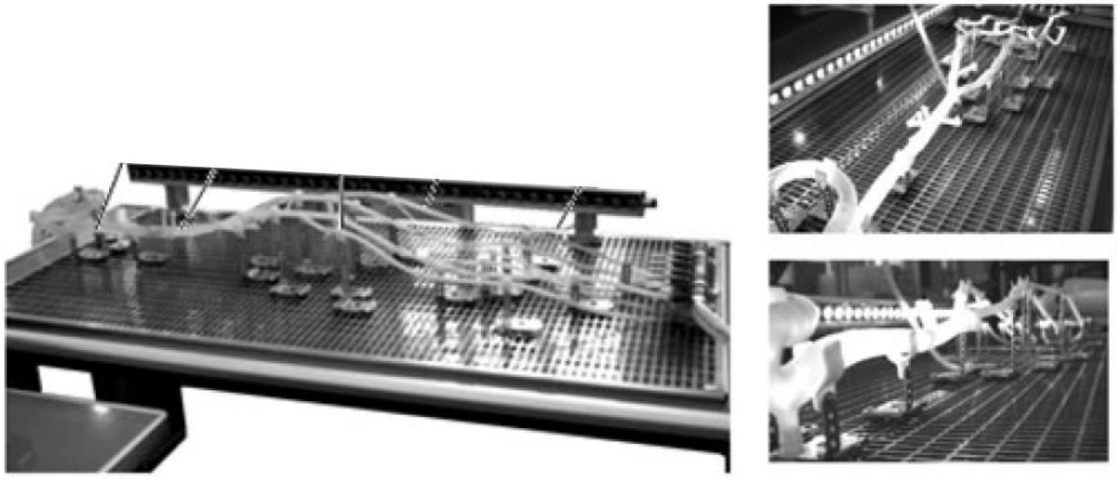

Figure 2.19: A Phantom model of the arterial system (modified) [73].

2.5.1 Aorta Geometric Size and Shape

The human aorta represents a complex organ that is variable in size and shape depending on an individual's age and gender [12]. A study of aortic dimensions and the risk of dissection published by Erbel and Eggebrecht stated that a normal diameter of the ascending aorta is <2.1 cm/m^2 (indexed to body surface area), the descending aorta as <1.6 cm/ m^2, and aortic wall thickness of <4 mm is considered as normal [12]. However, the normal range has to be corrected for all ages and gender. During a person's life through childhood and young adulthood the size of the aorta increases at a rate of 1-2

mm/year [12]. Another study by Evangelista et al. also describes aortic geometry but in a more detailed context. Evangelista et al. used echocardiography to establish measurements and record normative data of the aorta geometry and mentions that aortic size is strongly related to body surface area and age [74]. Evangelista et al. consider that in adults (based on body surface area), the upper normal diameter of an ascending aorta is 2.1 cm/m^2 [74] which is also stated by Erbel and Eggebrecht [12]. An illustration is shown in Figure 2.20 by Evangelista et al. shows the nominal aortic diameter range limits of the different segments.

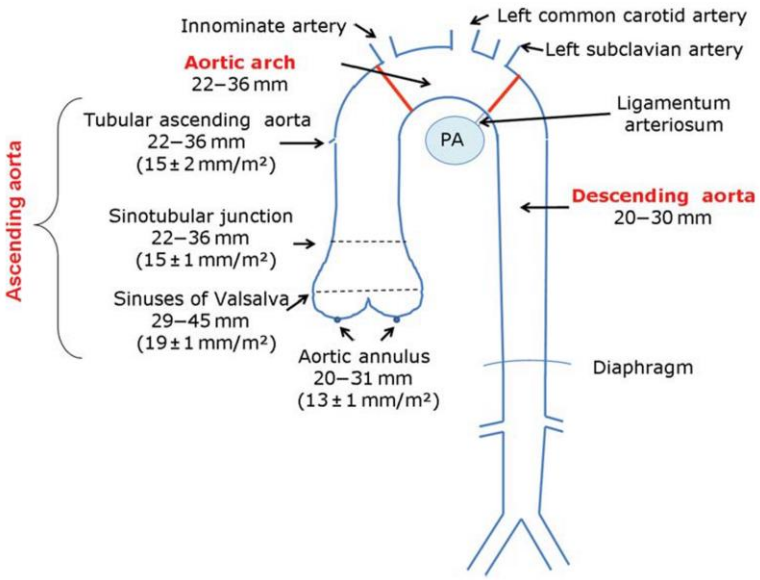

Figure 2.20: Normal size of the categorised aortic segments [74].

A research paper by Vasava et al. [75] also outlines detailed computational geometries of the aorta and reconstructed an idealised model of a human aorta based on an aorta model used by Shahcheraghi et al. [76]. Vasava et al. also divide the aorta into three segments – ascending aorta, aortic arch and descending aorta – with geometries within normal limits conforming to that of Evangelista et al. (see Table 1). The length of each aortic segment is also specified by Vasava et al. : the overall length of their modelled aorta from the top of the aortic arch down to the descending aorta was 120 mm and 148 mm with the inclusion of the left common carotid artery length [75].

Table 1: Computational geometries of the aorta by Vasava et al. [75].

Aortic Segment	**Geometry**	**Size (mm)**
Ascending aorta	Diameter Length	25.0 18.0
Aortic arch	Diameter Arch Radius	25.0 32.5
Descending aorta	Diameter Length	20.0 75.0
Brachiocephalic Artery	Length Diameter	28.0 8.8
Left common carotid artery	Length Diameter	28.0 8.8
Left subclavian artery	Length Diameter	28.8 9.9

A study by Savrasov et al., modelled phantom human arterial system using mean size geometries. Their phantom arterial system geometries are shown in Figure 2.21 and include the diameter, length and wall thickness from the ascending aorta to the abdominal aorta and its major branching arteries of lower extremities [73]. The phantom human arterial system has an overall length of 1258 mm [73] which was longer than used by Vasava et al. and Shahcheraghi et al. Aortic wall thickness is also specified in some studies in modelling phantom aortas. Savrasov et al. defined their wall thickness to be uniformly 2 mm but 1.5 mm at common iliac artery [73]. A study by Mensel et al. quantified the mean thoracic wall thickness using magnetic resonance imaging (MRI) across a population of 50 volunteers (24 men, 26 women; mean age 50.2 ± 13.1 years)

[77]. Their findings resulted in specifying the mean aortic wall thickness to be 1.89mm ± 0.21mm for the ascending aorta and 1.60mm ± 0.22mm for the descending aorta.

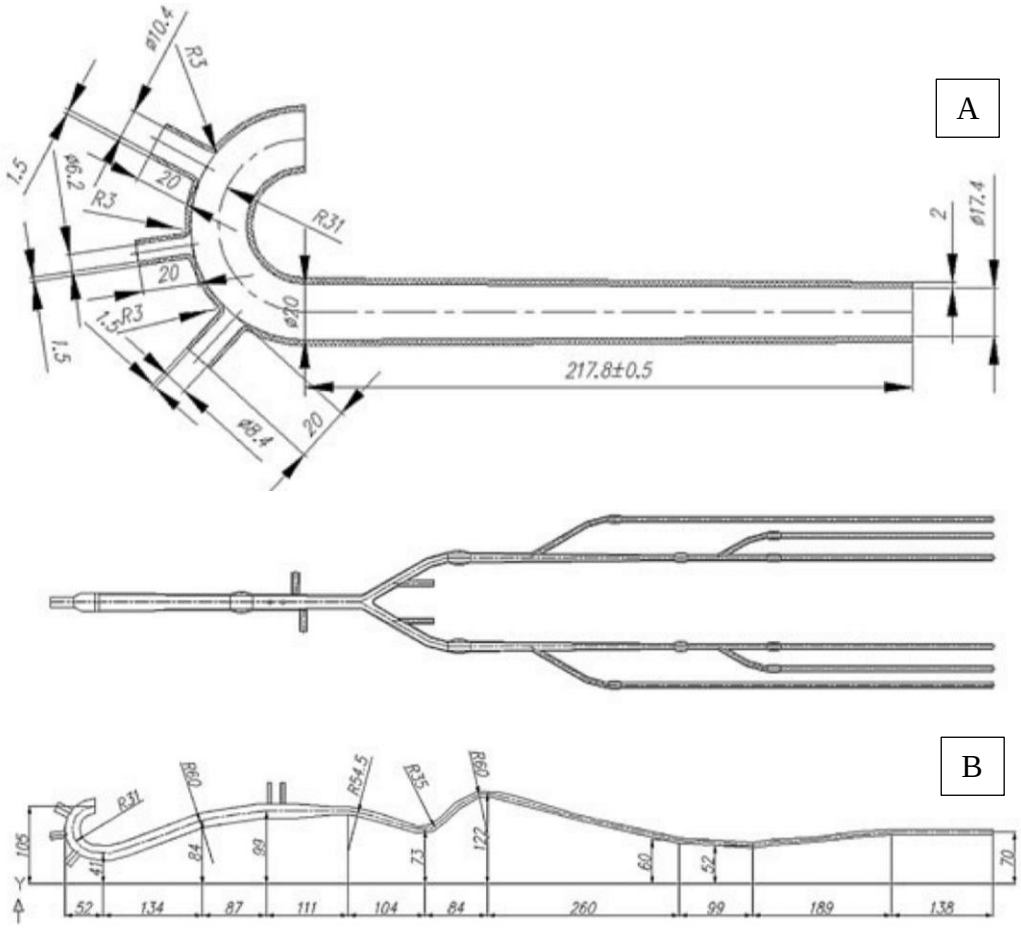

Figure 2.21: Geometries stated by Savrasov et al. (A): Cross-sectional geometries of an aorta; (B): Arterial system geometries. (modified) [73].

The structural shape of a human aorta is also variable with a form factor similar to a walking stick. The aorta first extends from the heart's left ventricle via the aortic valve [10], [76], [78]. It then branches off into three arteries – right common carotid artery, left common carotid artery, and brachiocephalic artery – that supply blood to the head and arms [10], [76], [78]. It then descends through the chest and abdomen and bifurcates into the left iliac artery and right iliac artery that supply the leg and abdominal organs [10], [73], [78]. Vasava et al. simplifying the geometry by ignoring the complex curvatures that are present in real abdominal aorta and torsion of the ascending aorta [75]. Most modelling of aortic structural shape is derived from observations of an actual human aorta using computed tomographic (CT) imaging or MRI [79] but are usually simplified

due to anatomy complexity that features curvatures, distal tapering and branching [76-77]. Caballero and Laín describe the technique of obtaining MRI data of a patient, then translating that data to create a patient-specific 3D model of an aorta with structural complexity (see Figure 2.22) [80].

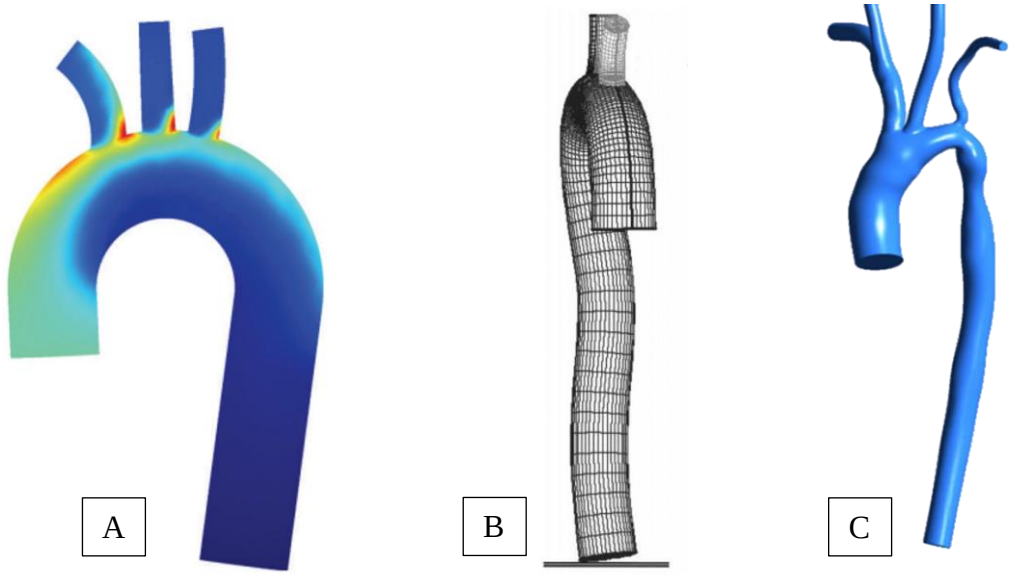

Figure 2.22: Different models of the aorta. (A): Simplified model of the thoracic aorta by Vasava et al. [75]. (B): The undermining curvature of the abdominal aorta modelled by Shahcheraghi et al. [76] (C): A patient-specific complex aortic anatomy modelled by Caballero and Laín [80].

2.5.2 Aortic Biophysical Properties

The aorta plays a key role in modulating left ventricular performance and arterial system function throughout the entire cardiovascular system [74]. The most important biophysical property that is considered widely across multiple studies modelling aorta or the arterial system is elasticity [72], [75], [84-85]. The elasticity of the aortic wall varies with blood pressure and the change in aorta diameter during systolic and diastolic phases [82]. A measurement of elasticity in an aortic tissue can be quantified by Young's Modulus (E) or Modulus of elasticity and is determined by the ratio of stress vs. strain [83]. For modelling a phantom aorta, both Russ et al. and Savrasov et al. have considered the modulus of elasticity for selecting an appropriate material (see Table 2).

Table 2: Table of materials for making phantom aorta that is used by some studies involving hardware experimentations.

Phantom Material	Young's Modulus (MPa)	Source
Dragon Skin® (02,10,20,30)[4]	1.1143 (20)[5]	Russ et al. [72] Atieh [84]
Polyurethane	1.8	Savrasov et al. [73]
Poly-Di-Methyl-Siloxane (PDMS)	1.68-2.51	Gülan et al. [85]
Aortic Tissue[6]	0.46 - 1	Bia et al. [86] Lantz et al., [87]

Utilising the aorta geometric data and defining the aortic biophysical properties from the mentioned sources is essential for fabricating a phantom aorta that can produce results similar to those of a real human aorta.

[4] Different Shore Hardness grades

[5] Sourced from Atieh [84]

[6] Non phantom material

Chapter 3

Phantom Aorta and Cardiovascular Simulation Platform

3.1 Introduction

In this chapter, the development of both the phantom aorta and an experimental cardiovascular simulation platform are explained. These two components work together as the platform for experimentation with the PEABC prototype. Such phantoms and simulation platforms have been created and used widely in testing and validation in cardiology based research such as evaluation hemodynamics [85], [88] and testing reliability of VADs [93-94].

The following sections in this chapter describe the development of two phantom aortas. Testing of phantom aorta 1 produced results that were used to guide the development of phantom aorta 2. This chapter also compares both phantom aortas against works mentioned in the literature review chapter. Phantom aorta 2 was utilised to complete the cardiovascular simulation system. This system is also compared to some key related studies in the literature review chapter.

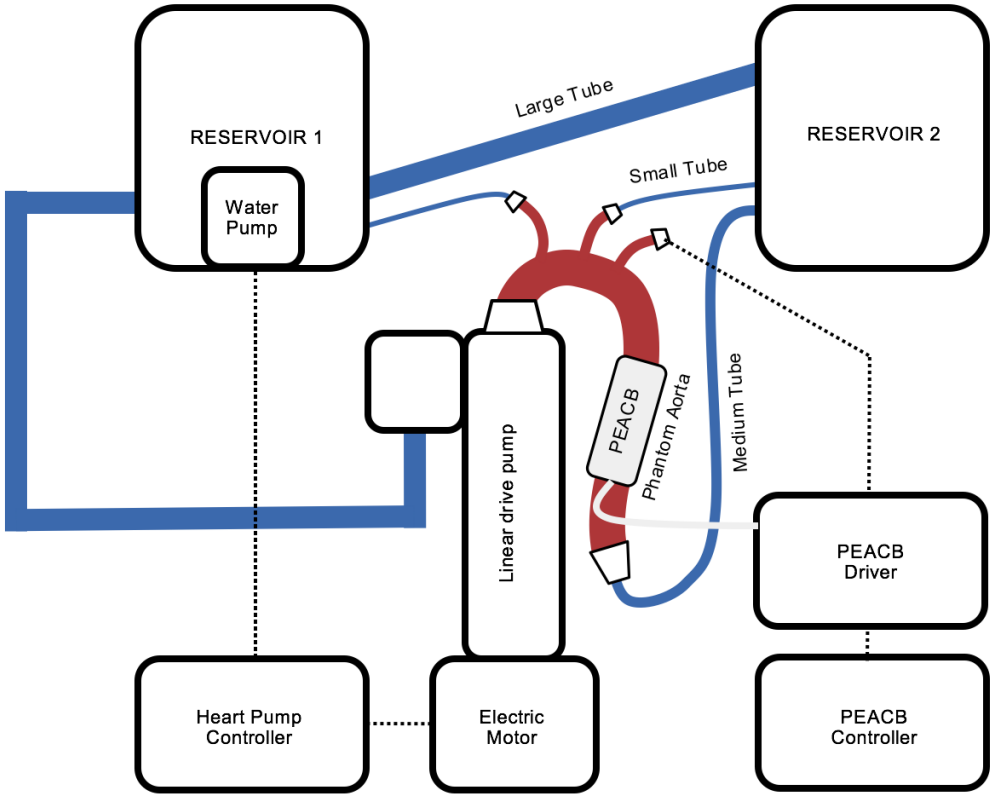

Figure 3.1: Left Ventricular Mechanism designed by Drummond with the phantom aorta and PEABC attached.

3.2 Methodology

3.2.1 Phantom Aorta 1 Development

In this section, we explain the processes that were involved in the development of the first phantom aorta, including mimicking the anatomy of a real aorta using a rapid prototyping technique which is explained in section 3.2.3. The target structural and biophysical properties of the phantom aorta have been mentioned in Chapter 2, section 2.5. Structural properties such as aortic shape, size, and branching arteries of the aorta were considered. The phantom aorta was designed to look anatomically correct for an average size human. Elasticity properties were considered when finding the appropriate synthetic materials like silicone, which were formed into the required shape using a moulding method developed for this project.

To further verify that the shape of the modelled aorta is relevant in size in comparison with an average sized heart, a 3D model of a human heart sourced from GrabCAD was used. The developed phantom aorta is projected alongside and fused with the 3D model heart to validate geometric compatibility (see Figure 3.2).

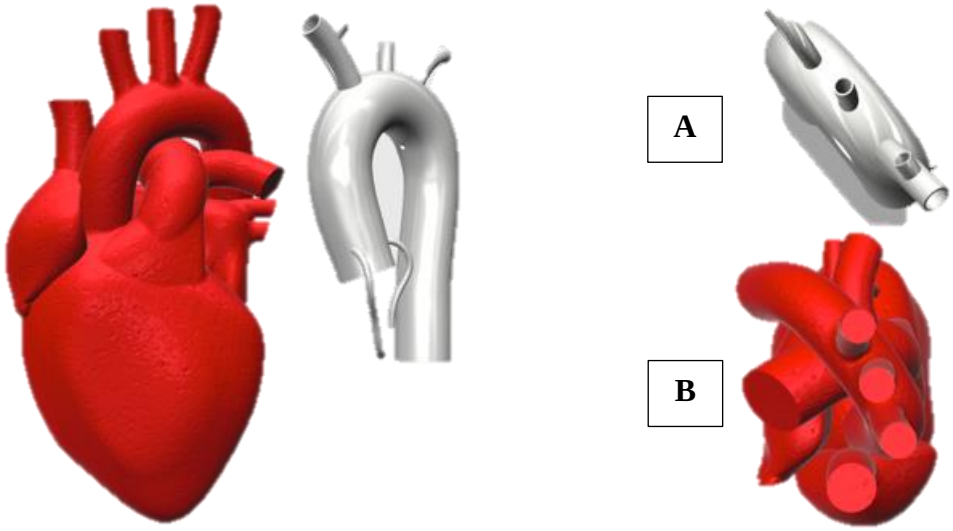

Figure 3.2 CAD models of the (A): phantom aorta 1 created for this research, compared to (B): an average sized human heart obtained through GrabCAD.

3.2.2 Research-specific Aortic Geometry and Biophysical Properties

As explained in the literature review chapter, the physical properties of a human aorta come in all shape and sizes depending on age and gender. To select an appropriate aortic geometry and biophysical properties for this research, relevant geometry and biophysical data mentioned in Chapter 2 are applied to the modelling of the phantom aorta. The aortic geometry selection for the phantom model that was created initially is shown in Figure 3.3 and Table 3.

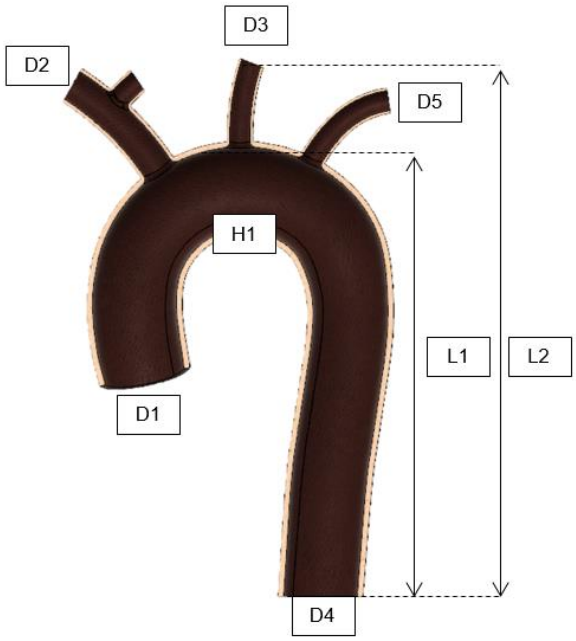

Figure 3.3: Cross section of the 3D CAD model of the aorta.

Table 3: Dimensions of the 3D CAD model of the aorta shown in Figure 3.3

Aorta Geometry	Size (mm)
Wall thickness (H1)	1.89
Diameter (D1)	30
Diameter (D2)	13.11
Diameter (D3)	8.7
Diameter (D4)	28
Diameter (D5)	8.7
Length (L1)	153.737
Length (L2)	180.552

These dimensions were utilised in the process of creating a 3D CAD model using the Fusion 360 (Autodesk®, United States) software. The model consisted of a hollow aorta profile that starts from the aortic valve and terminates in the descending aorta. The model incorporated three main branching arteries from the aortic arch and two coronary arteries at the ascending aorta.

3.2.3 Rapid Prototyping Technique

To fabricate the aorta modelled in CAD, the lost wax moulding technique was adapted. This type of moulding technique was chosen as it is repeatable and low cost. It is particularly suitable because the aorta is a hollow curved tube and it was desired to produce it in one whole piece. The moulding process was to first make an internal wax core mould using metal moulding plates that could be separated after the wax core had been poured. The mould plates allow the fabrication of an internal wax core that represents the interior lumen of the aorta. The process of producing the mould plates for the wax casting is described in section 3.2.3.2. Once the wax was poured in and had hardened, silicone rubber was applied to the wax core by brushing it on, left to cure and then the wax was melted away – explained in section 3.2.3.3, 3.2.3.4 and 3.2.3.5 – leaving an aortic form close to the 3D CAD model (see Figure 3.4).

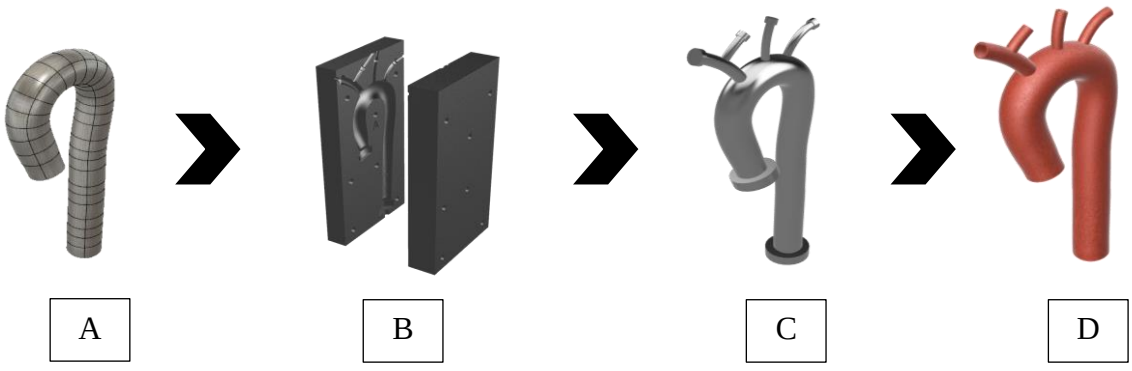

Figure 3.4: Process of developing the phantom aorta, (A): 3D CAD design model. (B): Development of the mould plates. (C): Wax mould of the internal profile of the aorta. (D): Silicone mould after the removal of the wax.

3.2.3.1 Materials

The rapid prototyping technique for this research involved the selection of appropriate materials for the different parts of the mould and the mould plates. The lost wax moulding process of fabricating the phantom aorta required the following four materials:

1. **Wax**

For the internal wax core, the wax had to melt at a practicable temperature so it could be poured and harden at room temperature to retain its solid shape during the process of silicone rubber application. This project used Ferris Mould-A-Wax® No. 5. Ferris Mould-A-Wax® is a uniquely malleable wax used to produce free-form shapes using the lost wax process [90]. Two grades of hardness were available – Soft (No. 6) and Regular Hardness (No. 5) – of which No.5 was chosen as it can maintain its shape at room temperature (melts at 76°C). No. 6 was not appropriate as the wax was malleable at room temperature.

2. **Aluminium Mould Plates**

Because of the fact that the Mould-A-Wax® No. 5 melts at 76°C, moulding the wax core required mould plates that could withstand at least this temperature during the moulding process. Aluminium is used for the mould plates because it can tolerate the hot wax being poured into it. Moreover, the mould plates could also be heated before and while the wax was being poured to ensure the wax did not set prematurely.

3. **Silicone Rubber**

To create the phantom aorta for this research, biophysical properties had to be considered in order to obtain statistical results that can be validated in comparison to a real aorta. From the list of potential materials mentioned previously in Chapter 2 section 2.5.2, silicone rubber was chosen to fabricate the phantom aorta. Smooth-On Rebound® 25 is a platinum-cured brushable silicone rubber with a mixing ratio of 1:1 by volume [91]. The material has a Shore hardness of 25A which makes it soft and flexible.

4. Mould Release Agent

The use of a mould release agent is an important material that aids the demoulding process of the wax core. Marbocote® 227CEE is a mould release agent designed for releasing all types of epoxy, polyester resins from steel, aluminium or composite moulds [92]. Using the Marbocote® 227CEE was found to be effective in releasing the No. 5. Ferris Mould-A-Wax from machined aluminium plates, and significantly better than oil, Vaseline and CRC for this purpose (mention in section 0).

3.2.3.2 Mould Plates Design for Casting

The aluminium alloy mould plates were to be fabricated using CNC machining. A 3D model of the mould plates was created from the internal profile of the 3D model phantom aorta. Some modifications to this internal body were made to make the process of pouring in the wax easier. These modifications called sprue were larger cylindrical profiles extruded out at the ends of the four main branches (see Figure 3.5).

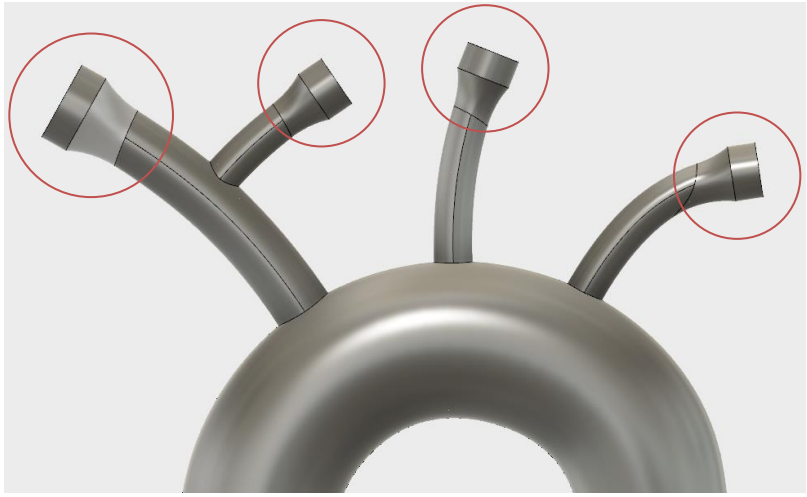

Figure 3.5: Sprues on the inner wax core (circled).

Once the inner core body was finalised, a new body was constructed from the bottom of the inner core. The extruding of the new body was configured to intersect the inner core and produce a cut-out of the inner core as shown in Figure 3.6.

Figure 3.6: Extrusion of the new body thought the inner wax core.

The newly created body with the cut-out core was then split into two along the side, resulting in two bodies that represent the mould plates (Plate A and Plate B). To keep the two plates joined tightly during the wax pouring process, holes were put in place for nuts and bolts. Apart from joining to the two mould plates tightly, the plates also need to align to avoid imperfections of the wax core during moulding. To assure that these mould plates aligned properly, several interlocks were put in place on the mould plates – Plate A: male interlock, Plate B: female interlock (see Figure 3.7). After finalising the 3D CAD design of the mould plates for any deficiencies, the CAD file was sent away to the mechanical workshop at AUT University for CNC machining. The machined plates once assembled together with nuts and bolts, results in a mould cast that wax can be poured into to form a wax core.

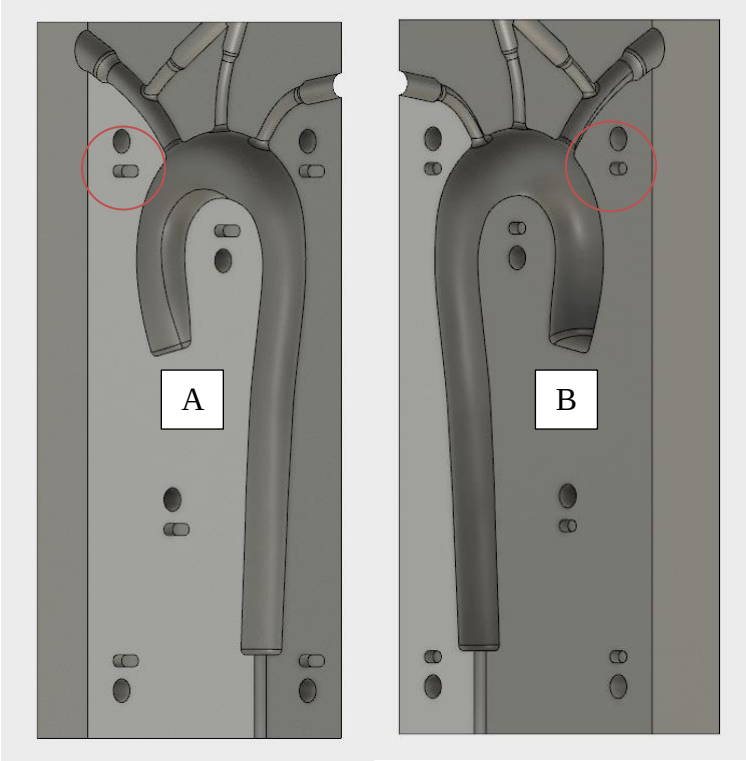

Figure 3.7: (A): Wax mould plate A with male interlocks. (B): Wax mould plate B with female interlocks (circled).

3.2.3.3 Wax Mould Process

The method of moulding the wax using the developed mould plates required some preparation before the wax could be poured into the mould cast. These preparations were developed after several unsuccessful mould attempts explained in section 3.3.1.

The first task of preparation involved the use of the mould release agent. To aid the demoulding process, three layers of the Marbocote® 227CEE mould release agent were applied to the mould plates with a brush. Each layer of Marbocote® 227CEE was applied at 15-minute intervals to allow each application to dry properly. As the Marbocote® 227CEE is highly flammable in liquid form with a flash point less than 21°C, it was applied in a well-ventilated place with no exposure to spark or open flames.

Once the third layer was properly dried, a solid 450g block of Mould-A-Wax® was melted down to a liquefied form in a glass jug by putting it into an oven set at 110°C for 1-1.5 hours. During that time regular stirring was conducted to break up lumps that remained partially melted. At the same time, the mould plates were also put in another heating oven subjected to 80-100°C heat. The two plates were then aligned and joined together tightly with six M10x7.5 stainless steel hex nut and bolts. To prevent the wax from pouring out during the wax pouring process, a dell was inserted at the bottom of the cast.

After all the wax was liquefied, it was then slowly and carefully poured into the sprue holes at the top of the cast via a polymer funnel. Using a polymer funnel over a metal funnel avoids rapid cooling of the wax during the initial pouring. To confirm that the cast was correctly filled from the bottom to the top, the wax was poured into the cast to the point where overfilling occurred at all four holes at the top. The cast was then set aside at room temperature to cool down for 24 hours before demoulding.

3.2.3.4 Demoulding Wax Process

Before splitting the cast, overfilled wax present on the top and sides of the cast was removed. All six nuts and bolts were then removed and the mould plates split. Care needed to be taken when separating the cast as if not done correctly the branches would break at weak points. To avoid this, plate A was laid flat on its side and all four corners pried in turn with a metal wedge. Once the two plates were loosely separable, plate B was slowly removed to expose the wax core resting on the other mould plate. The wax core was then carefully removed from plate A and preparation was made for application of silicone rubber.

3.2.3.5 Silicone Rubber Mould Process

The application of the Rebound® 25 silicone rubber first required mixing the two pots together at room temperature with a one to one (1A:1B) mixing ratio by volume. The volume of the aorta obtained on CAD – 77.88 ml – was used as the minimum volume of Rebound® 25 required for the application. Typically, as some volume was lost during the process an additional ~30% of the required volume was mixed thus 1A = 60 ml, 1B = 60 ml.

Rebound® 25 has a pot life of 20 min which provided adequate time for brushing it on to the wax core. Before applying the Rebound® 25, a small metal shaft was inserted at the bottom of the wax core to allow it to be suspended upside down (see Figure 3.8).

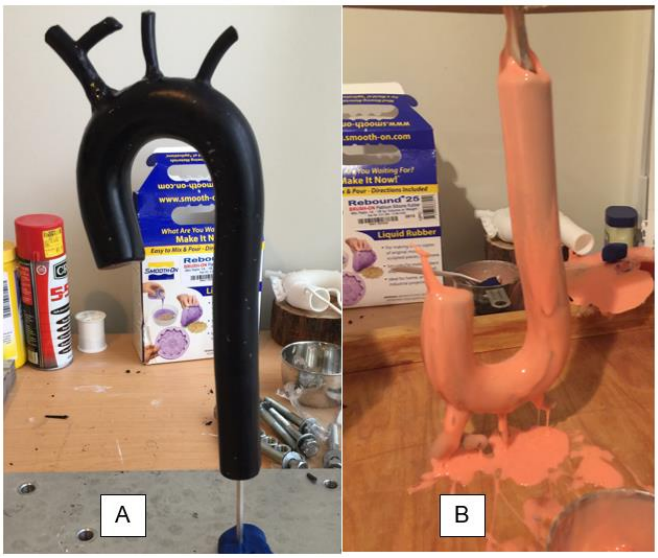

Figure 3.8: (A): Wax core with a metal shaft inserted at the bottom of the mould. (B): Wax core suspended upside down for the application of the Rebound® 25.

The Rebound® 25 was applied onto all surfaces of the wax core using a horsehair bristle paint brush. Due to the viscosity of the substance, layers were applied in turn after waiting for the previous layer to cure. To achieve the specified aortic thickness previously mentioned in section 2.5.1, the thickness of each layer was checked until the correct thickness was achieved, which was on the third layer. The Rebound® 25 was then cured for 6 hours at room temperature. The ends at points shown in Figure 3.9 were then cut off for the purpose of removing the wax core.

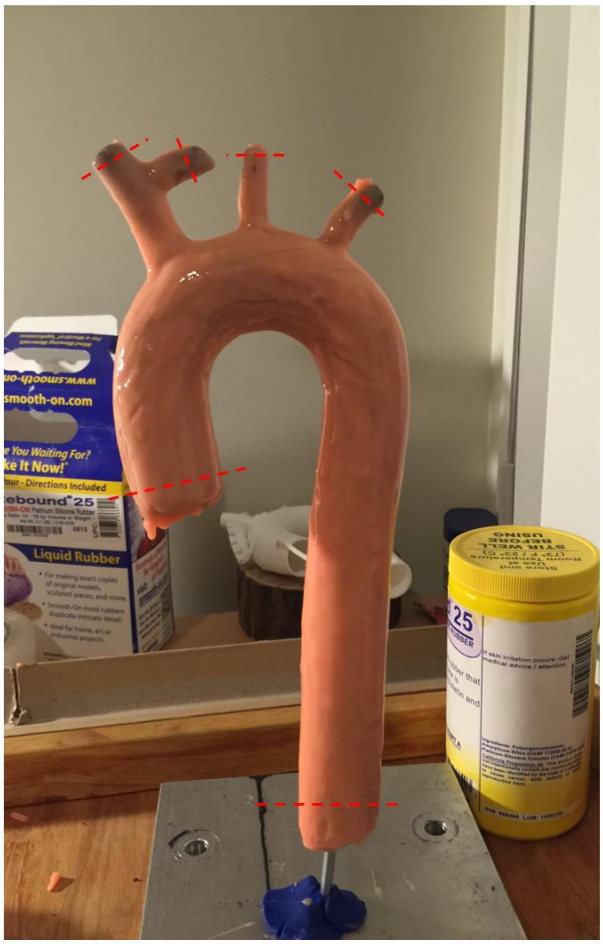

Figure 3.9: Cured Rebound® 25 silicone rubber ready for internal wax removal. Points marked with a dashed line indicate where the cut outs were performed to remove the inner wax core.

The removal of the inner wax core was done by submerging the whole mould in hot water. The mould was introduced into a container filled with 5 L of water at 100°C for 20 min. After this time the wax was soft enough to be bent and removed from the newly moulded phantom aorta. The phantom aorta was then removed out of the water and dried. The phantom aorta was then ready for use with the cardiovascular simulation platform.

3.2.3.6 Testing Procedure

The methodologies for moulding a phantom aorta stated in section 3.2.3 were the result of examining failures and finding an appropriate solution to solve/improve on preceding moulding attempts – these moulding challenges are fully explained later in section 3.3.1. The final product of the silicone rubber phantom aorta resulted in a similar aorta form

factor as the 3D CAD version but had some geometries variances due to the moulding techniques performed and the validation of the silicone rubber led to adaptation of an another student's work development of a phantom aorta using PDMS which is explained in section 3.3.2. The silicone rubber aorta, however, was useful for obtaining the preliminary results (see section 3.3) when implemented into the left cardiovascular simulation platform.

3.2.4 Phantom Aorta 2 Development

With the help of Johnson's work [93], phantom aorta 2 was devised as an improvement on the first phantom aorta. Johnson chose to use PDMS as a phantom material. This project carried on from Johnson work and the material section was changed to using Dragon Skin® 10 due to reasons mentioned in section 3.3.2. Phantom aorta II was developed and adopted over the first phantom aorta. The following sections explain the context of both Johnson's and this research's work.

3.2.4.1 Aortic Geometries

Johnson adapted aortic geometries from sources that specified the ascending aorta to be around Ø25 mm and the descending aorta to be around Ø20 mm [93]. This linear tapered profile followed the length of the aorta from the aorta valve to the iliac bifurcation and this distance was stated to be 750 mm [93]. The thickness of the aorta model was set at 1mm thick for reasons of manufacturing practicality [93]. The geometry was simple (see Figure 3.10 and Table 4) and similar to this research and Savrasov et al. [73].

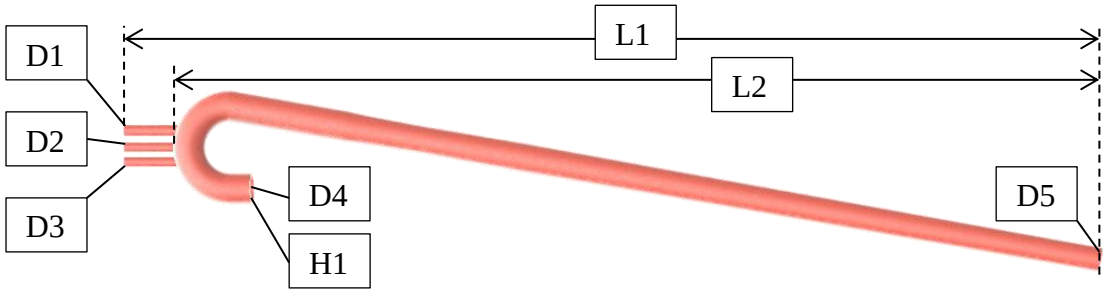

Figure 3.10: Johnson's phantom aorta shape.

Table 4: Dimensions of the 3D CAD model of the aorta shown in Figure 3.10.

Aorta Geometry	Size (mm)
Wall thickness (H1)	1.6
Diameter (D1)	9.9
Diameter (D2)	8.5
Diameter (D3)	8.8
Diameter (D4)	25
Diameter (D5)	21
Length (L1)	820.61
Length (L2)	772.258

3.2.4.2 Materials

For phantom aorta 2 other silicone rubber types such as PDMS and Dragon Skin® 10 were explored (other materials that were used for making the phantom aorta 1 were still used i.e. wax, aluminium mould plates and Marbocote® 227CEE mould release agent):

1. **Poly-Di-Methyl-Siloxane (PDMS)**

Polydimethylsiloxane (PDMS) is a mineral-organic polymer that was initially used for fabricating the phantom aorta 2 that was performed by Johnson [93]. The material required a mixing ratio of both curing agent and PDMS based on desired material characteristics. The mixing ratio applied by Johnson's method was a 10:1 ratio that creates a suitable material characteristic for a phantom [93]. The curing process required the PDMS mould to be placed in an oven set at 45°C for 12 hours.

2. **Dragon Skin® 10 (Silicone Rubber)**

Smooth-On Dragon Skin® 10 is a platinum cured silicone rubber. The preparation of the material also requires mixing a 1:1 ratio of the Dragon Skin® 10 Silicone rubber and a FAST Platinum cured agent by weight or volume for the curing process to start. Dragon Skin® cures after 75 min at room temperature of 23°C. With a pot life of 8 min, the preparation process and application time were adequate for the moulding process of the phantom aorta 2.

3.2.4.3 Moulding Technique

Johnson's work produced two sets of mould plates that would mould the wax core as well as the walls of the phantom aorta. His moulds were also derived from modelling the aorta

on CAD (Solidworks) and then translation to the mould plates. His technique of moulding the phantom aorta using two separate sets of moulding plates was designed to better control the thickness of the walls of the phantom aorta during the process of moulding the PDMS. Johnson also adapted the lost wax technique and the same process of moulding the wax was performed as for phantom aorta 1. However, a larger oven was required to prepare the mould plates for wax pouring due to the fact that the plates were 830 mm x 60 mm x 200 mm. Being this large it took more time for the plates to heat up to the desired temperature (1.5 hours for the mould plates to achieve 60°C). The mould plates were joined together with nuts and bolt with additional external guiding dells. The melted wax was then poured into the wax cast – following the same procedure as mentioned in 3.2.3.3. The wax core was then taken out from the wax cast and was transferred to the PDMS cast. This process also required the use of demoulding agent Marbocote® 227CEE of which three layers was applied to the PDMS cast. To assure that the wax mould was correctly lined up properly with the PDMS cast, four brass M5 screws were inserted at the ends of three branches – one for each branch – and one for the bottom of the aorta (see Figure 3.11).

Figure 3.11: M5 brass screws moulded into the wax.

The process of moulding the PDMS layer onto the wax core was achieved by pouring the material through the filling holes in the second set of mould plates. The PDMS mould required mixing a ratio of PDMS and its curing agent, with the ratio that was adapted by Johnson being 10:1. According to Johnson, this is the ratio which, once the PDMS is cured, mimics the characteristic properties of an aorta. To cure the PDMS, the mould was exposed to a radiant heat of 45°C for 24 hours. The mould plates of the PDMS cast

were then carefully separated. The phantom aorta II was then placed in hot water to remove the inner wax core.

Due to difficulties that resulted in mould imperfections for the PDMS, an alternative material was used in this research. The alternative material was Dragon Skin® 10 as mentioned by Russ et al. [72]. Dragon Skin® 10 requires mixing two parts in a 1:1 ratio by volume/weight – same as the Rebound® 25 – and the viscosity allowed application flexibility by either pouring, injecting or brush on. Since Dragon Skin® 10 has a curing time of 75 min at room temperature 23°C, an oven is not required to cure the Dragon Skin® 10. A total of 150g of Dragon Skin® 10 was mixed for moulding the aorta. Dragon Skin® 10 has a pot life of 8 min and it required 2-3 min of mixing before applying to the mould, thus the working time for applying the Dragons Skin® 10 onto the wax core was approximately 5-6 min. In order to achieve these times, although Johnson's cast mould plates were used, the Dragon Skin® 10 was simply brushed on to one of the mould plates first followed by the second mould plate (see Figure 3.12) rather than being poured.

Figure 3.12: Dragon Skin® 10 applied to the second mould plate.

Once both mould plates were covered with Dragon Skin® 10, the wax core was placed on one of the horizontally rested mould plates and positioned correctly to ensure proper fixture. The other mould plate was then carefully placed on top, resulting in the full closure of the cast. The mould was allowed to cure for the time that was required and the same demoulding procedure as mentioned previously was performed. Any imperfections of the phantom aorta 2 e.g. air bubbles were fixed by mixing and applying small batches of Dragon Skin® 10 with a brush. The outcome of the phantom aorta 2 mould using Dragon Skin® 10 is described later in section 3.3.2.

3.2.5 Cardiovascular Simulation Platform

In order to test and validate the conceptual idea of using PEABC hardware to augment aortic pressure and flow, a testing platform that could simulate parts of the cardiovascular system was to be used. In particular, the system simulated the left ventricular pumping mechanism. This project was based on a system first described by Drummond [67]. However, this platform was redesigned and remade to overcome issues of the original problem and serve the purposes of this research. This lead to the creation of making a Cardiovascular Simulation Platform hardware that integrated the phantom aorta 2 to complete the setup. The cardiovascular simulation platform was redesigned on CAD but the same concept of simulating the left ventricle and the connection links and software integration were kept. As part of solving issues of friction with the original piston pump, a bellows system was designed and implemented as shown in Figure 3.13 (marked B). Additional hardware was also added to simulate the capillaries for which the effects are described in section 3.3.3.

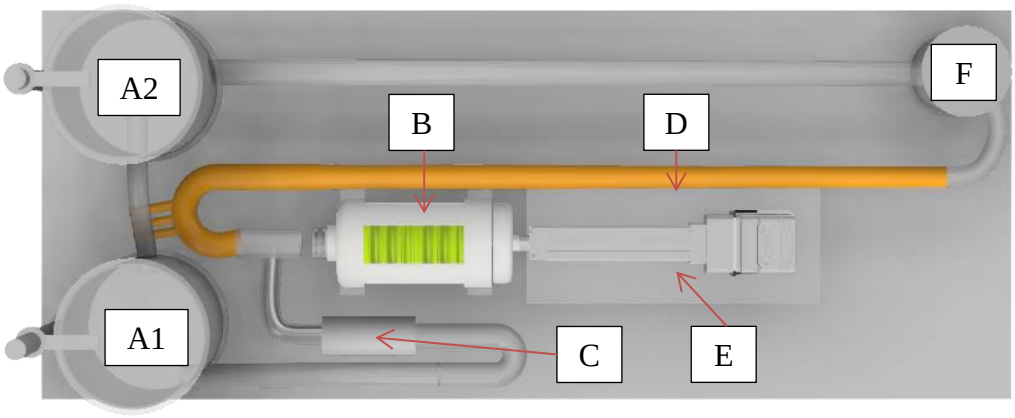

Figure 3.13: (A1): Reservoir 1. (A2) Reservoir 2. (B): Bellow system. (C): Valves. (D): Phantom aorta 2. (E): Linear actuator. (F): Capillaries.

3.2.5.1 Design and Operation

The orientation of the platform was also changed from being vertically orientated to being horizontally orientated. This setup allowed flexibility of mounting hardware components as well as avoiding over-current problems of the SmartMotor™ (MOOG Animatics, United States) actuator, as less force was required to actuate the linear drive.

Using bellows type actuation required less actuation force for the SmartMotor™ (MOOG Animatics, United States) compared to the original piston design of the left ventricle mechanism. The piston originally had two wiper seals and required sufficient lubricant to avoid the jamming of the piston pump during operation. Bellows, by contrast had negligible frictional force during operation. The bellows type that was selected is essentially a suction cup with a six-folded bellows by piGrip®. The piGrip® bellows (shown in Figure 3.14) is 124.8 mm in build height with a vertical movement of 73.2 mm and has a lip diameter of 70 mm.

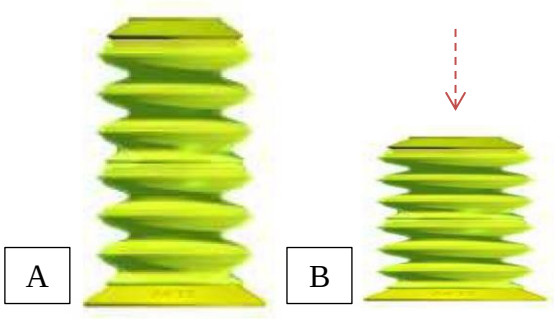

Figure 3.14: (A): piGrip® bellows uncompressed. (B): piGrip® bellows compressed.

The piGrip® bellows have an internal volume of 211.3cm^3 and a shore A hardness of 87 which provides excellent wear resistance. The configuration of this piGrip® bellows was selected to replace the left ventricle piston pump as it could produce comparable liquid volume output per actuation.

The integration of the piGrip® bellows to the SmartMotor™ (MOOG Animatics, United States) required designing and manufacturing of the mounting hardware. The three mounting hardware components were the coupling for the connection between the SmartMotor™ (MOOG Animatics, United States) drive and piGrip® bellows, the frame for fixation and support of the piGrip® bellow, and a bush for frame and piGrip® bellows connection (see Figure 3.15).

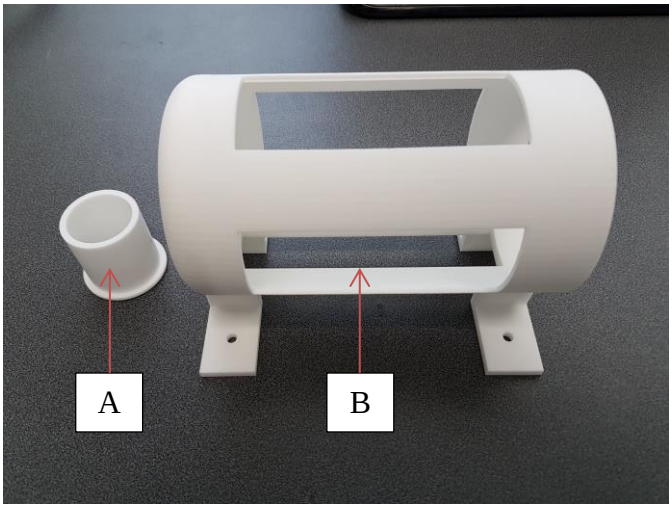

Figure 3.15: (A): 3D printed bush. (B): 3D printed frame for the piGrip® bellows.

This mounting hardware were designed on CAD and 3D printed with a Stereolithography (SLA) technique. The fixation between the coupling and the piGrip® bellows was done by pouring Pinkysil® silicone rubber with a shore A hardness of 30 into the cavity that once cured, formed a strong and air/water tight bond (see Figure 3.16).

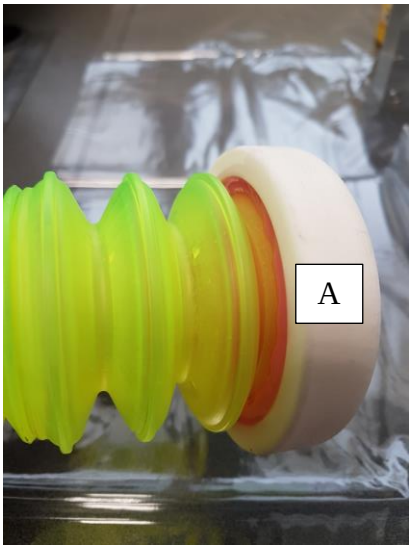

Figure 3.16: (A): Coupling attached to the piGrip® bellows via silicone rubber.

The bush was used as a mount for the piGrip® bellows to connect to the mainframe. The main frame was simply designed to hold the whole piGrip® bellows components onto the base (see Figure 3.17).

Figure 3.17: Assembled piGrip® bellows with bush and coupling.

The two 1.5 litre containers served as reservoirs, both of which have the ability to move up and down for the purpose of changing the calibration pressures. As shown in Figure 3.18 all of the hose connections to and from the reservoirs were Ø12 mm.

Figure 3.18: One of the reservoirs with the 12 mm hose connections.

Two one-way valves were attached to the entry and exit of the bellows system that represented the left ventricle. A brass check valve (entry) and prosthetic aortic valve shown on Figure 3.20 (exit) were connected into PVC pipe connections shown Figure 3.19.

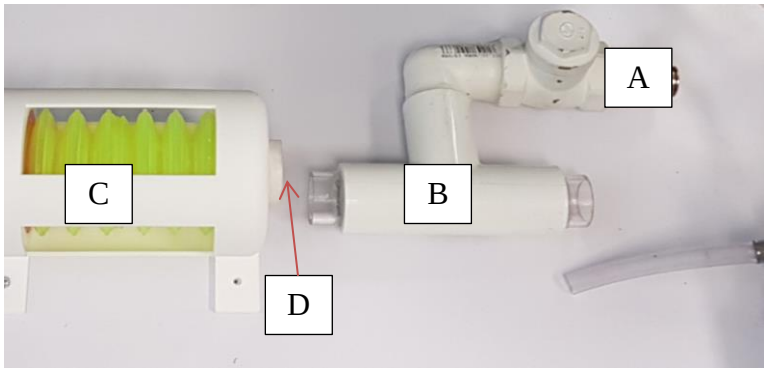

Figure 3.19: (A): Brass check valve. (B): PVC piping. (C): Bellow system. (D): Aortic valve.

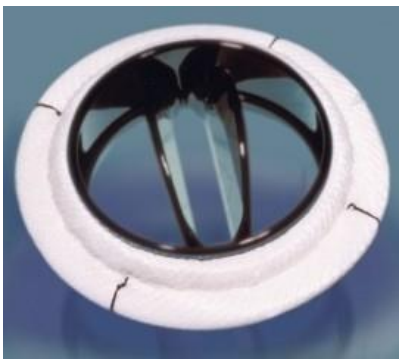

Figure 3.20: Prosthetic aortic valve (CardiaMed Rotating Heart Valve) supplied by OBEX®

A water pump and its controller were also added to allow controlled increases of mean aortic pressure but for reasons discussed later in section 3.4.3 were not utilised. An additional component is shown in Figure 3.21 was made to simulate the capillaries. This artificial capillary bed was designed to restrict the flow of water and increase the pressure in the phantom aorta 2. The cylindrically shaped sponge (Ø30mm x 20mm) was inserted into a tube that joins the end of the phantom aorta 2 to reservoir A.

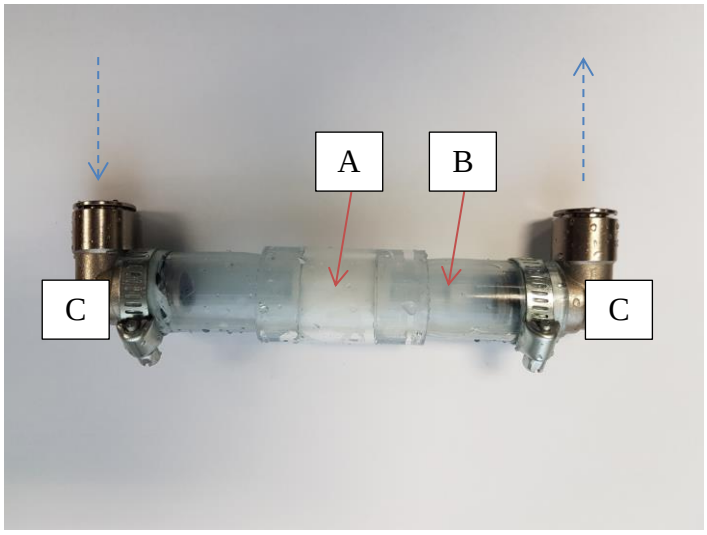

Figure 3.21: Artificial capillary. (A): cylindrical sponge. (B): PVC pipe. (C): 12 mm push fitting.

The left ventricle pump mechanism was controlled using a camming profile that was loaded on the SmartMotor. As shown in Figure 3.22 the profile was designed to mimic the output flow and pressure of the left ventricle at a cycle rate of 60 bpm that compresses the piGrip® bellows by 34mm. Another camming profile was created which was utilised and uploaded on to the SmartMotor as the original camming profile did not result in the output pressure waveform being sufficiently similar to the normal aortic waveform.

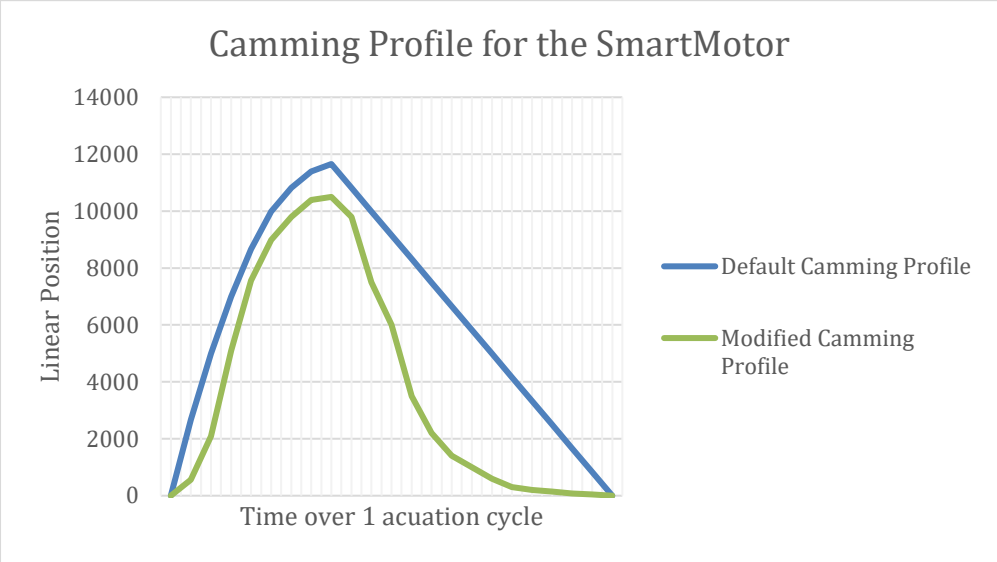

Figure 3.22: Drummond's default camming profile Vs. Modified camming profile that was uploaded to the SmartMotor™ (MOOG Animatics, United States).

Once all of the hardware components were assembled and the software instructions uploaded correctly, testing was performed to ensure proper functionality and reliability of the cardiovascular simulation platform. The testing procedures involved measuring the pressure and flow at various points in the phantom aorta and operating the system for a long period of time to ensure stability and reliability of the hardware to ensure valid results of future experiments could be obtained.

3.3 Mould Fabrication

3.3.1 Phantom Aorta 1

Creating the phantom aorta using a moulding technique that would be repeatable was essential for the reason of assuring multiple moulds could be performed if the first attempt resulted in a failure. The process of moulding the wax core resulted in multiple attempts before it was right for the silicone rubber application. As each attempt of moulding the wax core was made, review on why the mould resulted in a failure was examined and solutions to improve were implemented. The first attempt made towards moulding the wax core resulted in the wax cooling fast as it was poured in. This produced non-uniform surfaces (ripple like surfaces) and large air pockets which were not desirable for the steps that followed. As a solution, heating up the mould plates before pouring dramatically slowed down the cooling of the wax and allowed proper formation of the mould. The demoulding step that followed failed as the wax core broke in large pieces during separation of the mould plates. The cause of the wax core breaking into pieces was the result of the wax core sticking to the mould plates. The material properties of the Mould-A-Wax® also contributed to the failure because even though the wax itself is hard at room temperature, it is also brittle. In an attempt to avoid the wax core from sticking to the mould plates mechanical oil was applied to the mould plates but still resulted in the wax sticking to the mould plates. Further attempts were made using CRC and Vaseline but were also unsuccessful. The solution to the problem was found using a commercial mould release agent 227CEE. The 227CEE was applied to the mould plates on the fifth moulding attempt and resulted in the wax core being separable during the separation of the mould plates. During the separation of the mould plates, the wax core was taken out but the three branches weren't strong enough as to hold its form. The fracture lines that occurred during the process of separating the wax core from plate B were present where the branches joined the main aorta profile. These dismounted branches were fixed by applying heat to each piece to melt and fuse it to the main aorta profile.

The application of the Rebound® 25 silicone rubber encountered no complications but once the final layer was cured, the surface of the material was somewhat rough with contours formed around some areas as shown in Figure 3.23. This was expected as the "brush-on" technique of the Rebound® 25 was adapted and although the 1:1 mixture of the Rebound® 25 creates a viscosity that allows the material to be brushable, the consistency is quite thick and the material once brushed on would drip due to gravity.

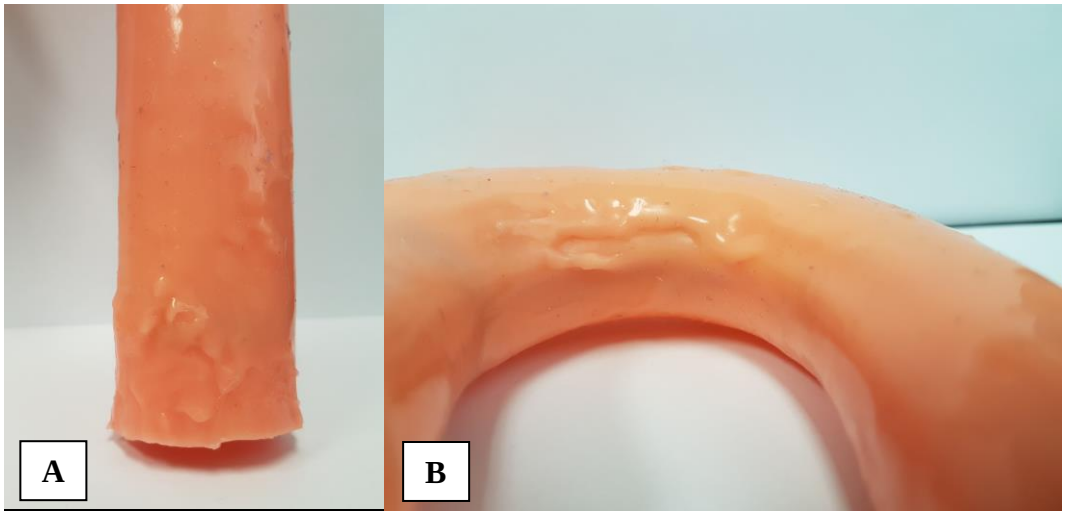

Figure 3.23: Rough surfaces of the phantom aorta occurring at the bottom of the (A): descending aorta and the (B): aortic arch.

However, over the duration of the curing time, it would begin to solidify. The removal of the internal wax core produced a smooth internal wall that had no air bubbles. Visually examining at the phantom aorta's thickness geometry, the thickness was not uniform. As shown in Figure 3.24 the phantom aorta wall was thicker on one side than the other. This thickness variance that occurred from the ascending to the descending part of the phantom aorta was the result of using the brush on technique for the Rebound® 25 which makes it very difficult to get the exact desired thickness geometry as designed on 3D CAD.

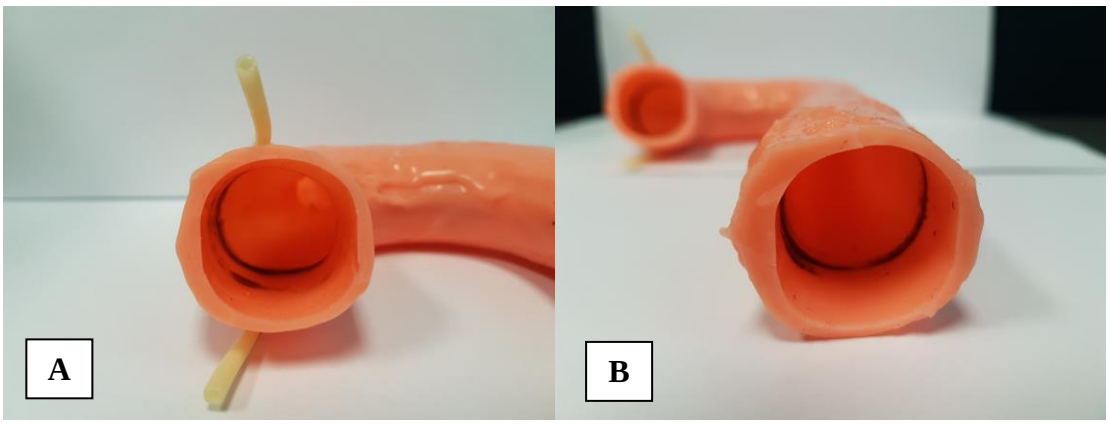

Figure 3.24: Thick geometry variances of the phantom aorta. (A): View of the ascending aorta; (B): View from the descending aorta.

The thickness of the ascending part (A) varied from 4 mm to 2 mm, whereas the descending part (B) ranged from 5 mm to 2 mm. The internal lumen diameter of the phantom also varied: ascending part (Ø 29 mm to Ø 25 mm), descending part (Ø 27 mm to Ø 24 mm).

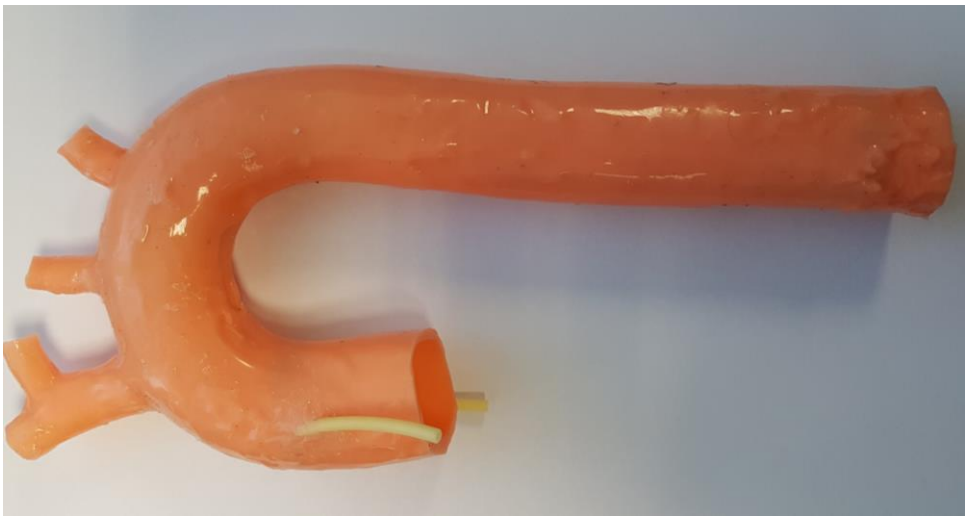

Figure 3.25: Phantom aorta 1 fabricated using brush-on silicone rubber.

The preliminary testing of the phantom aorta 1 that was performed was to check the structural integrity and characteristics when subjected to pressure and flow. The tests used the left ventricular pump mechanism and LabVIEW (National Instruments™, United States) software to examine the behaviour of the phantom aorta 1 [67]. The first test performed was to check for any leaks. The phantom aorta 1 was initially filled with

water in the absence of pressure and flow being generated by the left ventricular pump mechanism. No leaks were present under this condition. However, once the left ventricular pump mechanism started to operate, leaks were found in the systolic phase where peak pressure and flow were experienced inside the phantom aorta. This peak pressure and flow expanded the phantom aorta wall which opened small holes/cuts that were present and caused the water to shoot out. These holes were patched with a small batch of Rebound® 25, as the material does bond to already cured surfaces. Once all the holes were patched, more tests were performed to obtain the pressure and flow readings inside the phantom aorta. The initial testing involved measuring the pressure using the Freescale™ MPX5100AP sensor. The Freescale™ MPX5100AP sensor was attached to one of the branching arteries. Initially, the Freescale™ MPX5100AP sensor was connected to Drummond's LabVIEW (National Instruments™, United States) software via the National Instrument (NI) Analog/Digital converter where pressure wave was obtained. The LabVIEW (National Instruments™, United States) software provided a graphical user interface (GUI) for setting the desired mean pressure, pressure difference and the heartbeat. The software was used to set the conditions for the obtaining the pressure that the phantom aorta experiences during the operation of the left ventricle pump mechanism. The pressure was measured under two conditions of operating the left ventricular pump mechanism. The first condition was to operate without the assistance of water pump and the second was to operate it with the water pump used to simulate and increase the mean aortic pressure to physiological values [67]. The results as shown in Table 5, shows the difference in pressure between the two conditions when the phantom aorta was tested at 60 bpm. Moreover, the second test condition result was achieved by setting the mean aortic pressure to 80 mmHg on the LabVIEW software.

Table 5: Aortic pressure results from two testing conditions performed.

Aortic Pressure	**Pump Unassisted**	**Pump Assisted**
Systolic Pressure ($P_{systolic}$)	80 mmHg	100 mmHg
Diastolic Pressure ($P_{diastolic}$)	20 mmHg	65 mmHg

The pressure test setup involved obtaining the pressure readings by using a pressure catheter inserted through one of the branching arteries. The pressure readings from the catheter were coupled to the PowerLab (ADInstruments, Australia) device connected to a PC where the pressure readings were visualised on LabChart 8 software. This testing method provides the versatility of being able to measure the pressure inside the phantom aorta at different locations.

The flow rate that the left ventricle pump mechanism produces was obtained using COnfidence Flowprobes (Transonic Systems Inc.®, USA) placed in one of the reservoirs submerged in water where the end of the phantom aorta was connected to (see Figure 3.26). The flow reading obtained during pump assisted operation of the left ventricle pump mechanism was 3.2 L/min at the descending aorta. As observed on the transonic flow module, the flow was not constant and would occasionally fluctuate approximately ±0.3 L/min, possibly as result of flow turbulences present in the reservoir.

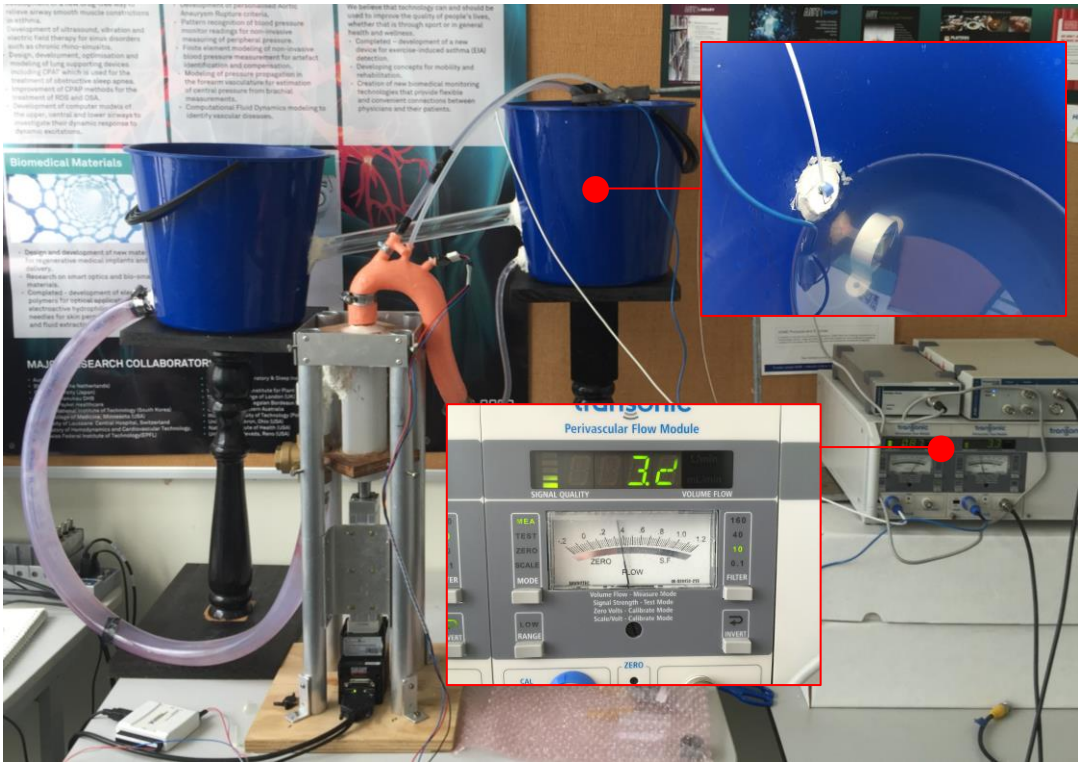

Figure 3.26: Location of the flow sensors on Drummonds left ventricle mechanism.

3.3.2 Phantom Aorta 2

The outcome of Johnson's attempt of modelling the phantom aorta using PDMS was not altogether successful. As documented by Johnson, the first PDMS mould resulted in an incomplete filling due to some of the PDMS leaking out at the bottom of the mould during the pouring stage – the second batch of PDMS was poured in to fill the mould. During the process of removing the PDMS mould from the mould plates, uneven thickness throughout the profile of the aorta resulted in the phantom aorta ripping during the separation of the mould plates. In areas of the phantom aorta 2, the rip was predominant along the profile shown in Figure 3.27. A further problem was encountered when the wax core was removed, as since some areas of the phantom aorta was thin, more ruptures occurred. This problem did not occur with the silicone phantom aorta, possibly due to the characteristics of the material being more tear resistant than PDMS. Moreover, the PDMS phantom aorta's wall thickness was thinner than the silicone phantom aorta 1.

Figure 3.27: Phantom aorta 2 using PDMS. The red circle marks the ripping area due to thin wall thickness.

In contrast, when using Dragon Skin® 10, during the demoulding process no rips occurred, however, a couple of large air bubbles were present as marked in Figure 3.28.

Figure 3.28: Phantom aorta 2 with Dragon Skin® 10 mould with arrows marking the air bubbles.

Another problem that occurred that exposed the flaws of the phantom aorta was an aneurysm-like effect observed in the descending aorta when the phantom was tested on the cardiovascular simulation platform pumping liquids at 60bpm (see Figure 3.29).

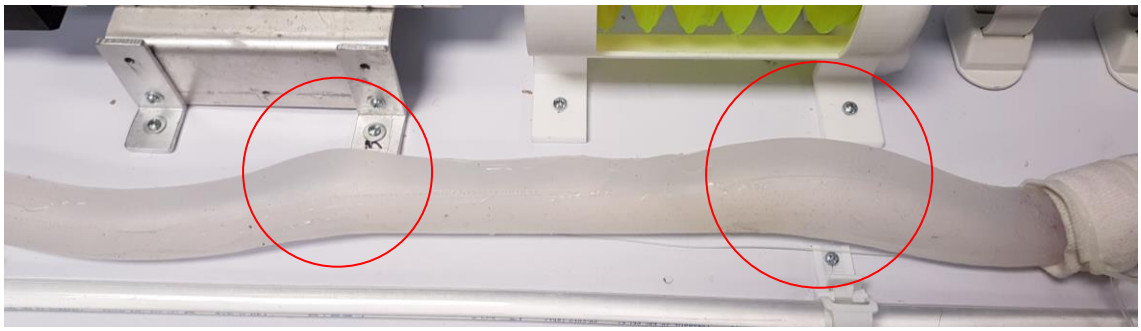

Figure 3.29: An aneurysm like effect occurring along the descending aorta.

The solution was further patching the phantom aorta 2 at the points at which an aneurysm occurred using an additional layer of Dragon Skin® 10, brushed on (see Figure 3.30).

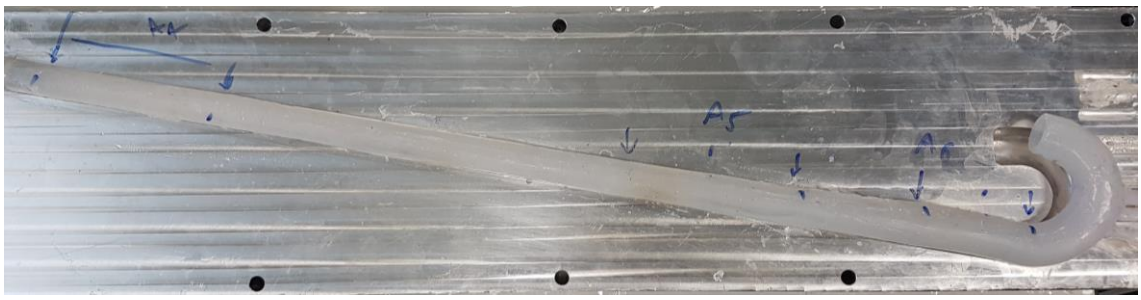

Figure 3.30: Patching points (marked with blue dots) on the phantom aorta 2.

With the addition application of the Dragon Skin® 10, the phantom aorta 2 wall thickness was measured near the ends of the phantom aorta 2 to compare the dimension parameters with the intended 3D CAD design (see Table 6). Two areas of the aorta were subjected to this measurement – ascending aorta and descending aorta. An ultrasound machine was used to measure the wall thickness over a scan area of 30 mm (see Figure 3.31).

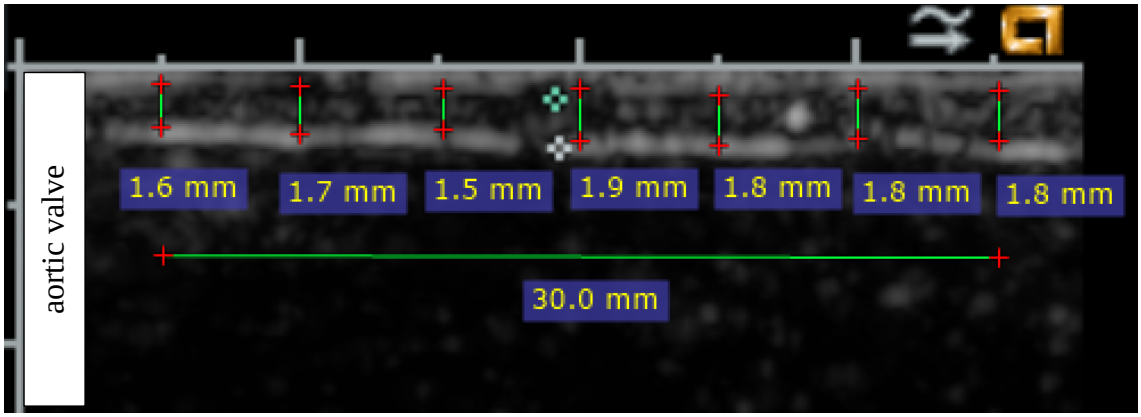

Figure 3.31: Aortic wall thickness at the ascending aorta obtained from the ultrasound machine.

Table 6: Aortic wall thickness comparison between 3D CAD measurement and ultrasound measurement.

Aortic Wall Thickness	Ascending Aorta (near aortic valve)	Descending Aorta (end of the phantom)
3D CAD Measurement	1.6 mm	1 mm
Ultrasound Measurement	1.6 mm	1.1 mm

The lumen diameter at the same measuring locations was also obtained and compared to the 3D CAD and the ultrasound machine (see Figure 3.32 and Table 7).

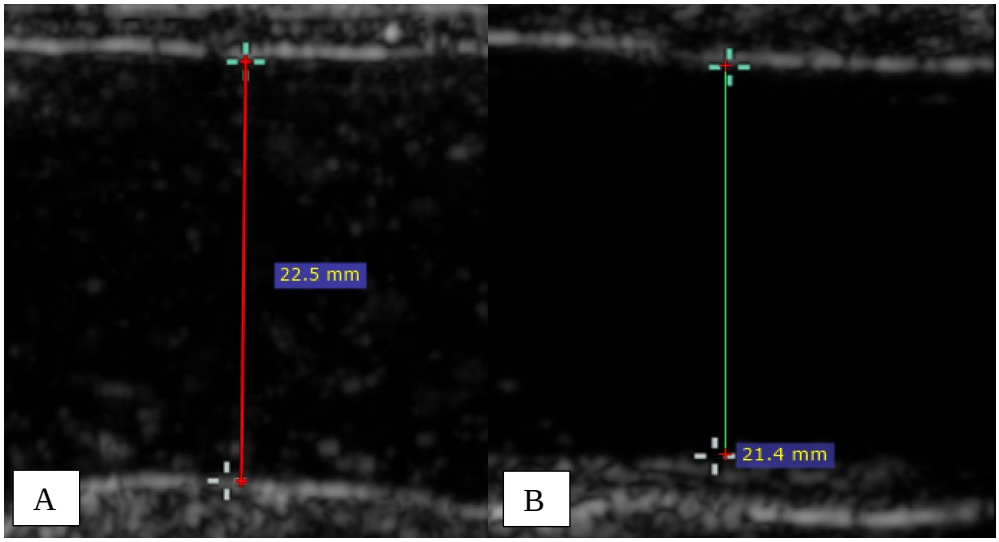

Figure 3.32: (A): Diameter at the ascending aorta. (B:) Diameter of the descending aorta.

Table 7: Aortic lumen diameter comparison between 3D CAD measurement and ultrasound measurement.

Aortic lumen diameter	Ascending Aorta (near aortic valve)	Descending Aorta (end of the phantom)
3D CAD Measurement	23.4 mm	19 mm
Ultrasound Measurement	22.5 mm	21.4 mm

The elasticity and Young's modulus was also obtained from the phantom aorta 2 made from Dragon Skin® 10 using a tensile test. With the same testing technique documented by Johnson [93], a ring sample of the Dragon Skin® 10 was moulded and tested on the Texture Analyzer (TA.XT+, UK) under stretching. The test stretched the Dragon Skin® 10 ring sample over 35 mm at 0.5 mm/sec and a force over distance profile was obtained (see Figure 3.33).

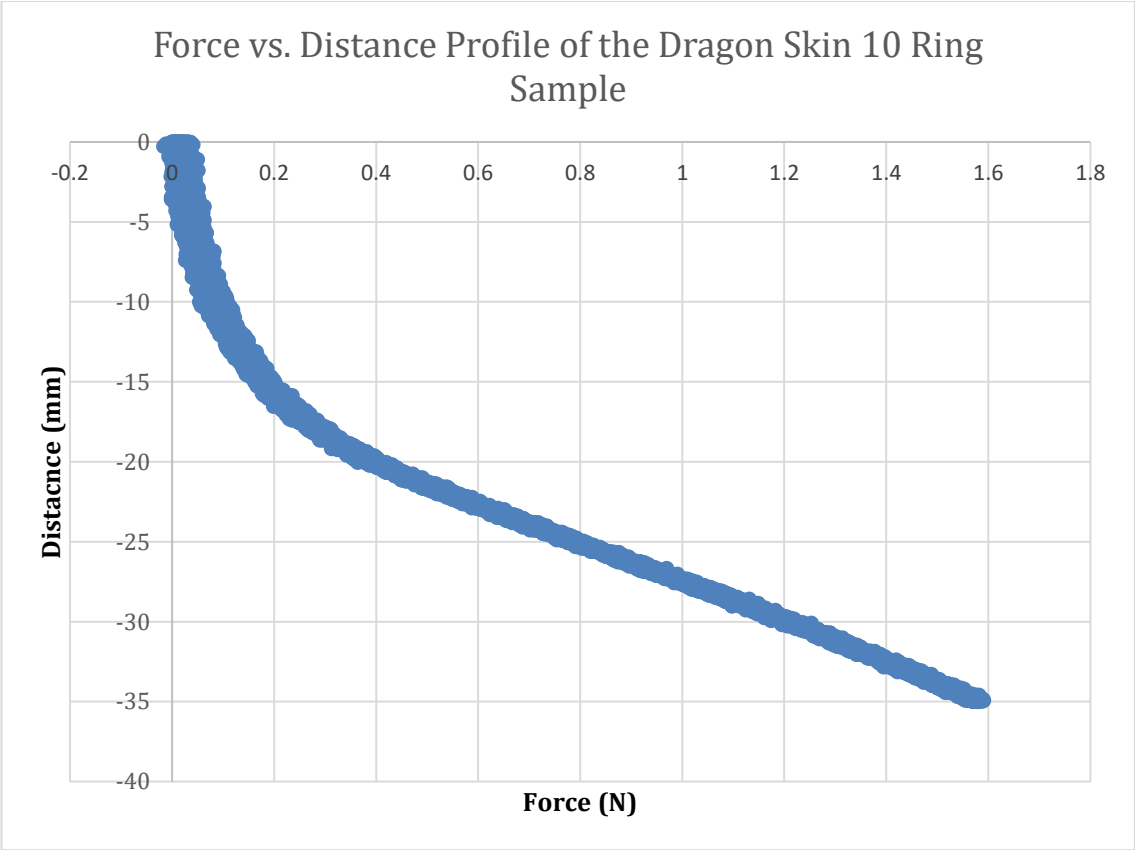

Figure 3.33: Distance vs. force profile of the Dragon Skin® 10 ring sample.

The force and distance profile was then converted to stress over strain (see Figure 3.34) from which the Young's modulus was calculated. For the conversion from force to stress, Equation 3.1 was used:

$$Stress = Force/Area$$

$$\sigma = F/A$$

$$Stress = \frac{1}{(2 \times 4 \times 4) \times 1000000)} \qquad \textit{Equation 3.1}$$

$$Stress = 31{,}250\ Pa$$

As for the distance to strain, Equation 3.2 was used:

$$Strain = \frac{change\ in\ length}{original\ length}$$

$$\varepsilon = \frac{\Delta l}{l}$$

$$\varepsilon = \frac{27mm}{53mm} \qquad \textit{Equation 3.2}$$

$$\varepsilon = 0.5094$$

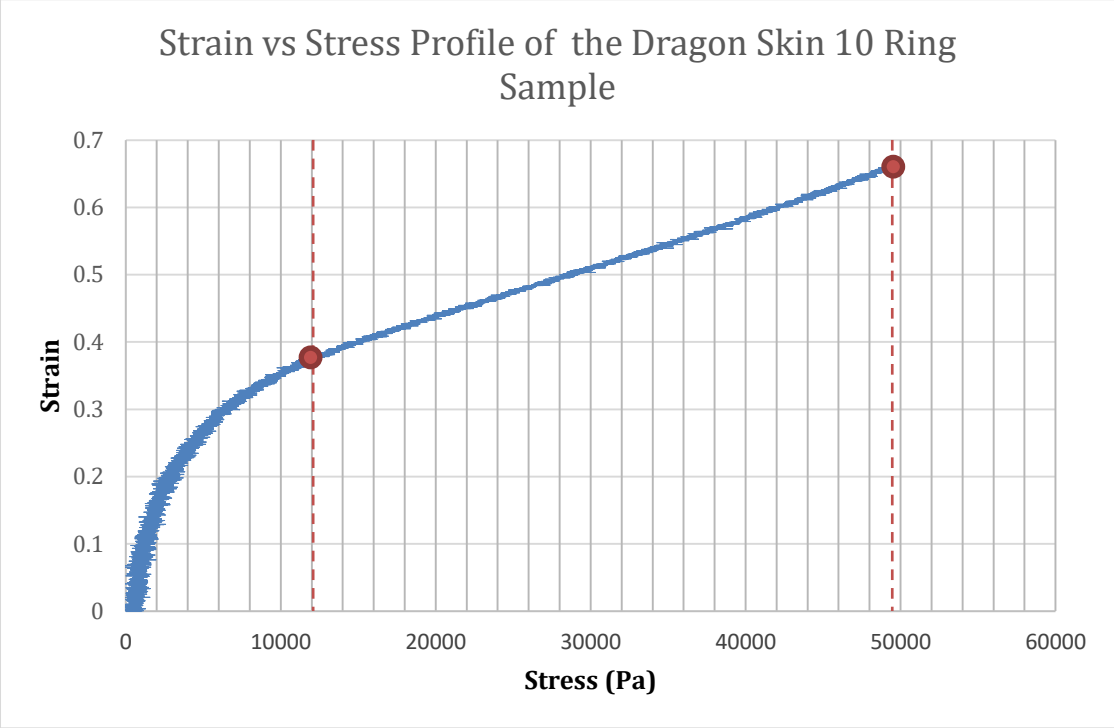

Figure 3.34: Strain vs. stress profile of the Dragon Skin® 10 ring sample.

From the given stress and strain values obtained and calculated from the linear part of the profile, the Young's Modulus was calculated using Equation 3.3.

$$Young's\ Modulus = \frac{Stress}{Strain}$$

$$E = \frac{\sigma}{\varepsilon}$$

Equation 3.3

$$E = \ E = \frac{50000 - 12200}{0.65 - 0.37}$$

$$E = 0.135\ MPa$$

3.3.3 Cardiovascular Simulation Platform

During the initial testing stage of the phantom aorta's functionality, the left ventricular pump mechanism encountered a major hardware malfunction that resulted in the motor that actuates the piston becoming unusable. The problem was analysed and it was concluded that the motor experienced an overcurrent caused by the piston jamming. A voltage shunt was obtained and connected to the motor and power supply as illustrated in Figure 3.35, along with a new motor, to prevent reoccurrence of this problem.

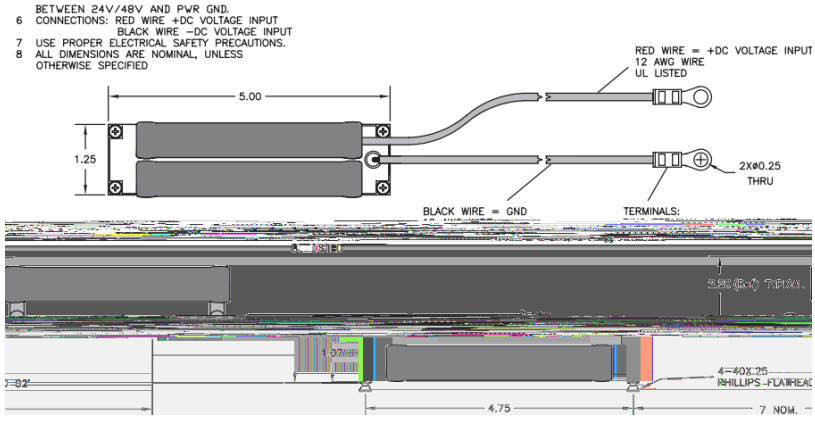

Figure 3.35: A 42V 200W shunt for the SmartMotor™ (MOOG Animatics, United States).

Other hardware complications to the left ventricular pump mechanism soon followed, including the piston starting to leak caused by a split O-ring (see Figure 3.36).

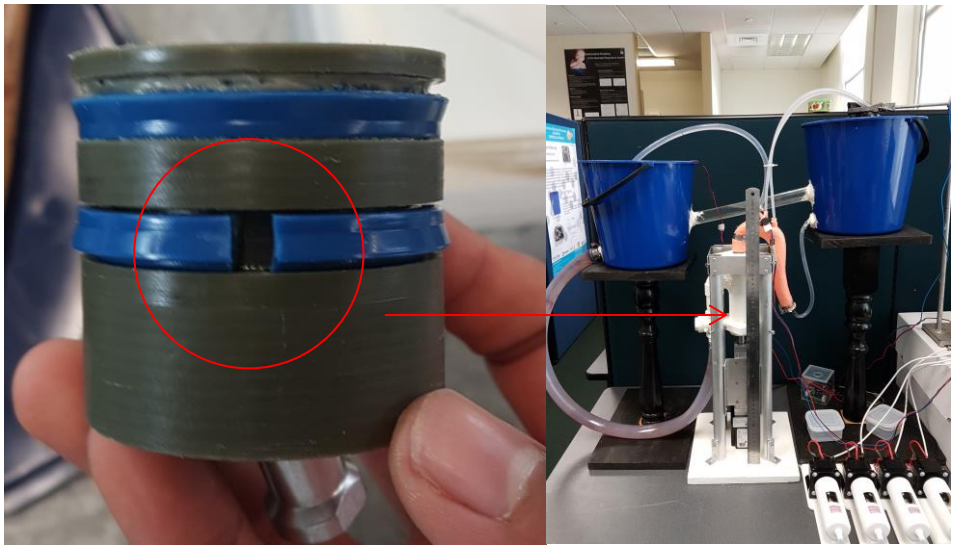

Figure 3.36: Splitting of the O-ring inside the piston drive of Drummond's left ventricle mechanism.

This problem caused the piston to jam and irregular actuations caused the overcurrent problem to show up again. With multiple problems occurring to the left ventricular pump mechanism, a redesign of the mechanism was undertaken for better reliability and to obtain the necessary results needed for validating this research (see Figure 3.37). The redesign has been explained back in section 3.2.5 and a functional platform was achieved for which further results were obtained.

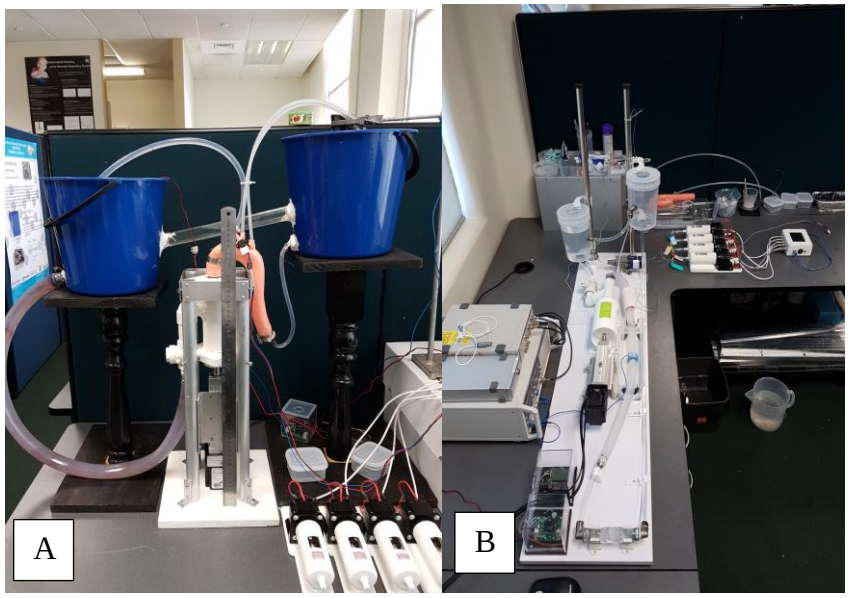

Figure 3.37: (A): Drummond's left ventricle mechanism. (B): Redesigned cardiovascular simulation platform.

The native pressure and flow waveform from the cardiovascular simulation platform were acquired using the PowerLab (ADInstruments, USA) and Transonic flow measurement devices. With pressure catheters' placed inside the aorta and the flow sensor on the exterior of the aorta, the waveforms illustrated in Figure 3.38 were obtained in LabChart

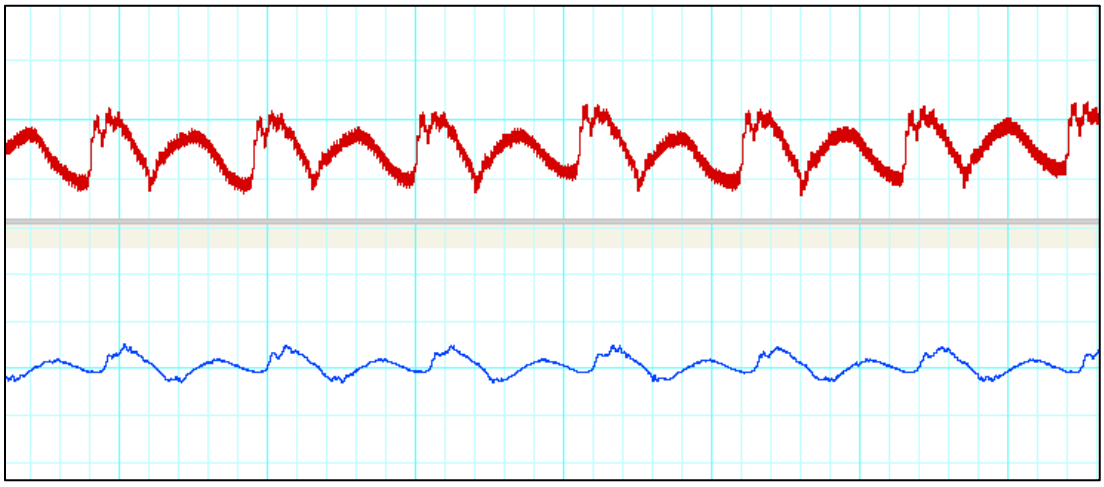

Figure 3.38: Uncalibrated Pressure waveform (shown in red) and Flow waveform (shown in blue).

The synthetic capillary bed changed both the pressure and flow waveforms. As shown in Figure 3.39 the implementation of the synthetic capillary reduced the rapid decreasing of the diastolic pressure wave when compared with Figure 3.28. Moreover, the synthetic capillary was able to increase the systolic flow wave.

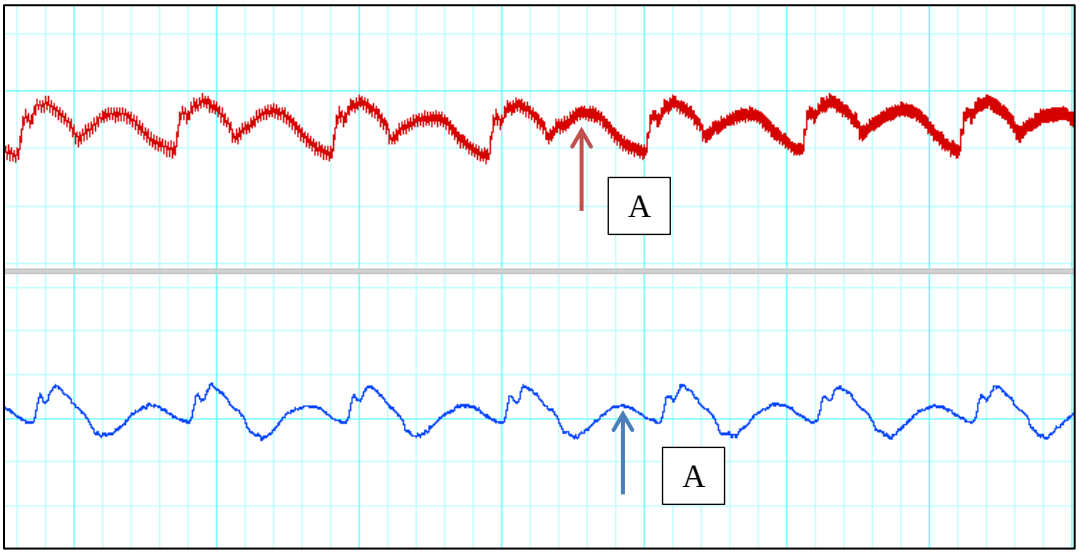

Figure 3.39: The effects to the pressure and flow waveforms with synthetic capillaries implemented. (A): Second parabola.

Looking at the pressure waveform shown in Figure 3.39, both seem to have a secondary parabola during the diastole phase, which is non-physiological. This secondary parabola artefact of the pressure waves was reduced by creating a tapered tube using the same material used for the phantom aorta 2 and added to the end of the phantom aorta (see Figure 3.40).

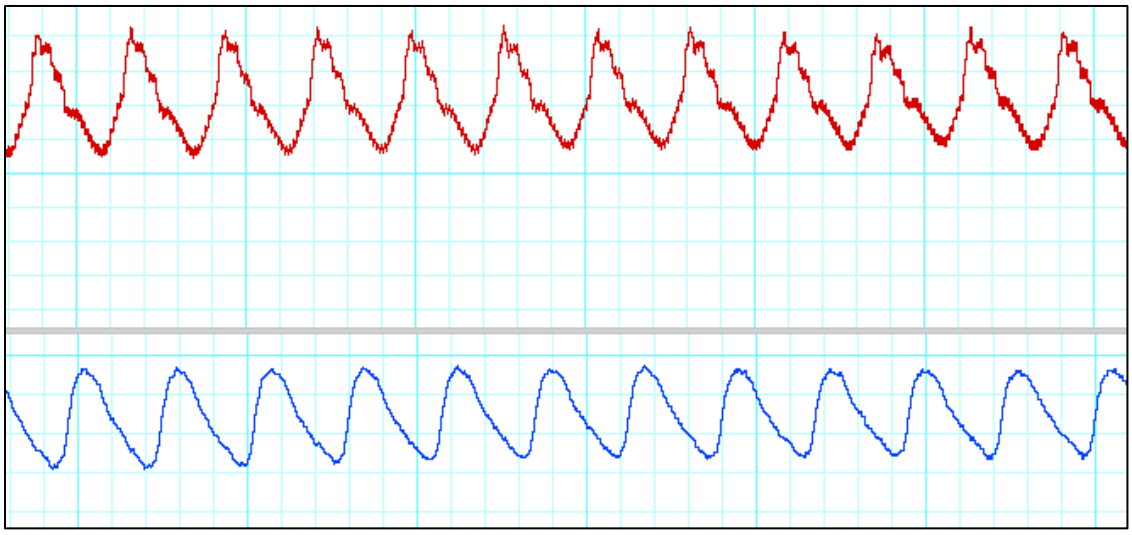

Figure 3.40: Reduced secondary parabolic artefact with the attachment of the tapered tube to the phantom aorta 2.

Further modifications to the cardiovascular simulation platform were made to refine the pressure and flow waveform. As explained above, the SmartMotor™ (MOOG Animatics, United States) actuation profile was modified. With this change the waveform also changed and is shown in Figure 3.41 (Real pressure scales shown in Table 8 are reported after calibration).

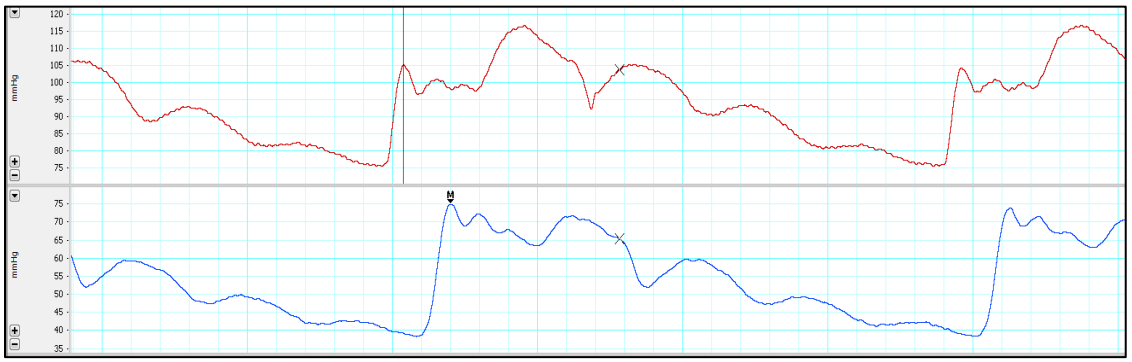

Figure 3.41: Calibrated ascending aortic pressure (red waveform) and descending aortic pressure (blue waveform) obtained from LabVIEW (National Instruments™, United States).

Table 8: Systolic and diastolic pressure measured at the ascending and descending aorta.

Aortic Pressure	Systolic Pressure	Diastolic Pressure	Mean Arterial Pressure
Ascending Aorta	117 mmHg	75 mmHg	88 mmHg
Descending Aorta	75 mmHg	39 mmHg	51 mmHg

Knowing the point of measurements of pressure along the phantom aorta 2 and phase shift between the two waveforms, a PWV was calculated using Equation 3.4.

$$\text{PWV} = \frac{\Delta x}{\Delta t}$$

$$\text{PWV} = 0.7 \text{ m} / 0.16 \text{ s} \qquad \textit{Equation 3.4}$$

$$\text{PWV} = 4.375 \text{ m/s}$$

This aortic wall displacement was visually observed and was compared to the pressure wave shown on the LabVIEW (National Instruments™, United States) to which it can point that it is the material related characteristics that's causing the various parabolas on the pressure wave shown previously in Figure 3.41. To further prove this speculation, more tests was performed to remove the unwanted waves by changing the SmartMotor™ (MOOG Animatics, United States) actuation wave profile. The alterations were to change the frequency and displacement settings that were programmed into the SmartMotor™ (MOOG Animatics, United States) and thus – in relation to physiological terms – modify the cardiac cycle and blood volume output. These settings were in the form of camming programming software on SmartMotor™ Interface (SMI) and by changing code that represents the displacement/frequency multiplier [67], alterations to the pressure/flow wave and the amount of cardiac output was archived. Based on the technical data, the piGrip® bellows has a total volume of 211 cm^3 with an effective compressible length of 73.2 mm and with the displacement length of 30 mm generated by the SmartMotor™ (MOOG Animatics, United States), the volume displacement of the liquid was approximately 86 cm^3 per stroke. With the SmartMotor™ (MOOG Animatics, United States) cycling at 1 second or 60 bpm, the cardiac output was calculated using Equation 3.5:

Stroke Volume (SV) = 86.475 cm^3

(86.475ml)

Therefore, CO = x HR (bmp)

Equation 3.5

Cardiac Output (CO) = 86.475ml x 60

CO = 5.188 L/min

The initial setting of the SmartMotor™ (MOOG Animatics, United States) represented 60 bpm that equates to a cardiac cycle of 1 second. The cardiac cycle was changed to 1.33 seconds or 45 bpm to make the cardiovascular simulation platform and phantom aorta 2 operation more stable. With the change in cardiac cycle, the cardiac output also changed to CO = 3.901 L/min at 45 bpm.

The major instabilities that were present when running at 60 bpm were the following:

- The ballooning up (an aneurysm like effect) in some areas of the phantom aorta 2 as a result of the wall thickness being thin and increase in internal pressure.
- The backflow from reservoir 1 to reservoir 2 – volume flowing into the reservoir 2 is greater than the volume of liquid flowing out into reservoir 1 caused by leaking one-way valves.

A better approximation of the cardiac output was obtained by testing the cardiovascular simulation platform using an ultrasound machine (see Figure 3.42). The cardiac output was measured using the ultrasound transducer with the measuring point at the ascending aorta part of the phantom aorta 2. Under the same testing condition (45 bpm), a good pulse wave reading was obtained for determining the measured cardiac cycle (see Figure 3.43). The average flow velocity was also measured and the cardiac output was calculated (see Equation 3.6 and Equation 3.7).

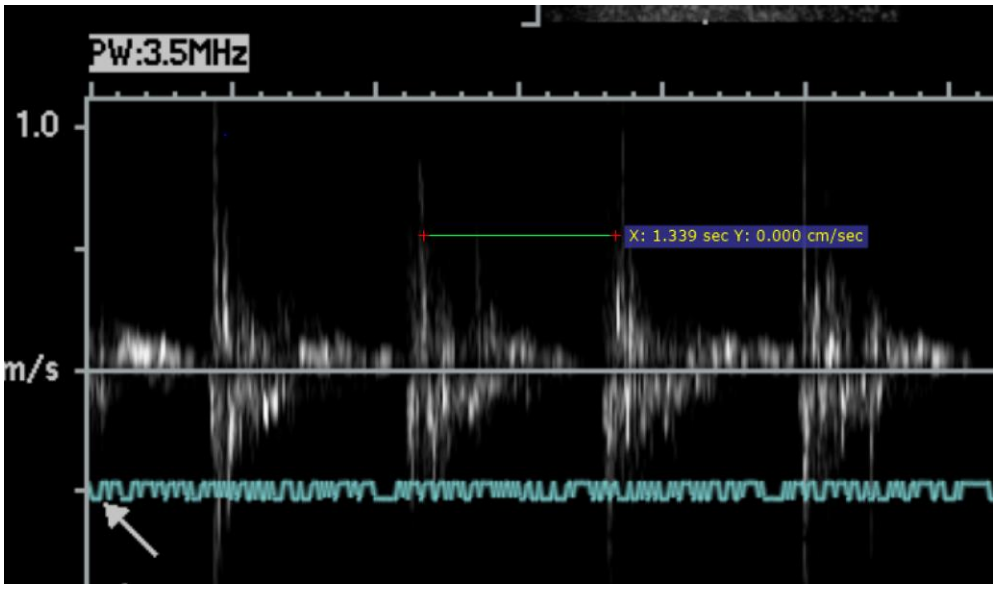

Figure 3.42: Flow pulse wave measured on the ultrasound machine. The cardiac cycle corresponded to the cycle set on the SmartMotor™ (MOOG Animatics, United States).

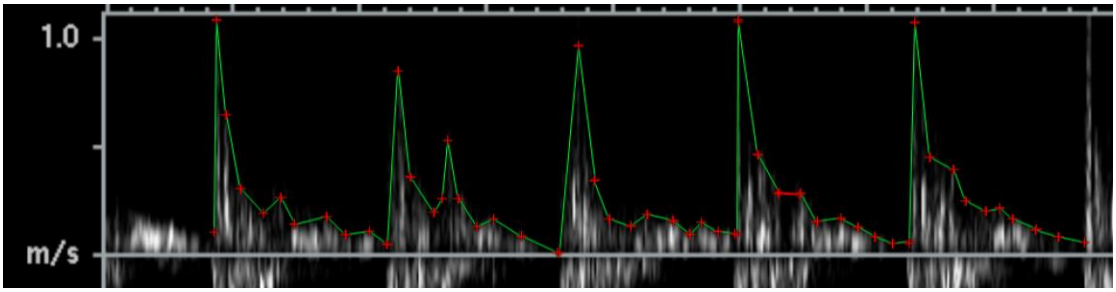

Figure 3.43: Tracing of the pulse wave to determine the mean flow velocity.

Average Velocity (V_{avg}) = 20.465 cm/s

Cross sectional area of the ascending aorta = 3.976 cm^2

Volume Metric Flow Rate (Q) = Velocity (V_{avg}) x Area (A) *Equation 3.6*

$Q = 20.465 \text{ cm/s} \times 3.976 \text{ cm}^2$

$Q = 81.368 \text{ cm}^3/\text{s}$

SV = 81.368ml / beat

Therefore, CO = SV x HR (bmp)

CO = 81.368 ml x 45 bmp *Equation 3.7*

CO = 3.661 L/min

3.4 Discussion

3.4.1 Phantom Aorta 1

To a significant extent, phantom aorta 1 did follow the desired spline profile designed on 3D CAD. However, the aortic thickness was not uniform and varied throughout the phantom aorta. Non-uniform cross-sectional thickness can have an effect on hemodynamics due to the fact that a thicker aortic wall thickness can increase pulse wave velocity. Both Gülan et al. and Willemet and Alastruey imply that the aortic wall stiffness affects the hemodynamic pressure's magnitude and velocity as a result of a minimal loss in kinetic energy of the waveform [85], [94]. It is noted that the brush-on technique makes it difficult to control the thickness when applying the Rebound® 25 that takes 2 hours to cure. This made the outside diameter of the aorta larger than intended but the lumen diameter of the aorta was measured to be close to the intended geometry within <2mm. The overall length of phantom aorta 1 was also an issue for taking measurements as the phantom aorta was physically 215 mm long (aortic arch to the descending aorta (DA)). This length is similar to Savrasov's et al. work where their phantom had an aortic arch-

DA length of 256 mm [73] but is short compared to the real aorta. On a related note, Savrasov et al. did also lengthen their arterial model by another ~985 mm that included renal arteries and iliac bifurcations that were unified with a connecting bushing. Having a longer aorta makes it easier to obtain pulse wave velocities and pressure/flow waves at different locations of the aorta and thus better validation of results when testing the PEABC prototypes. Joining arteries is not ideal as the connection points can create sites for wave reflection.

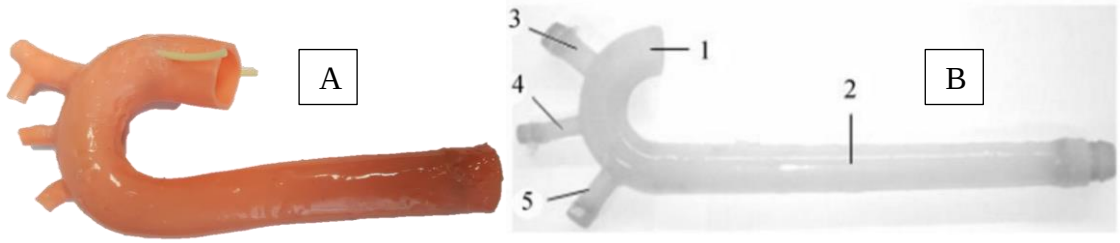

Figure 3.44: (A): Phantom aorta developed for this research; (B): Phantom aorta developed by Savrasov's et al. [73].

When it comes to comparing the phantom aorta with other phantom artery research work, silicone has been prominent as the most widely used material for phantom experiments [75-76], [88]. Research work that uses PDMS as phantom materials relate to the fact that the physiological characteristic is similar. However, as pointed out back in section 3.3.2 complications were encountered which led to using an alternative phantom material – Dragon Skin® 10 – for rapid prototyping the phantom aorta. An alternative material such as polyurethane has been used by other researchers [73].

Phantom aorta 1 was used for testing the initial operation of the PEABC prototypes and was useful for obtaining the preliminary results, shown in Chapter 5. However, although making the phantom aorta 1 have the characteristics similar to a real aorta was desirable, it was not that critical for validating the overall outcome of this research. As noted earlier, another phantom aorta – the phantom aorta 2 – was connected to the left ventricle pump mechanism and used to obtain test results with the PEABC applied externally to it.

3.4.2 Phantom Aorta 2

Comparison was made between the tensile strength of PDMS obtained by Johnson's work and the Dragon Skin® 10. Johnson performed tensile tests of PDMS by moulding a ring and using a TA.XT+ Texture Analyzer (Stable Micro System, UK)) and his results suggest that the PDMS can closely mimic actual human aorta when comparing biophysical properties. However, in this study Dragon Skin® 10 was chosen to mould the phantom aorta 2, instead of trying to perfect the PDMS mould technique that caused problems for Johnson. Dragon Skin® 10 compared to PDMS has a faster cure time (75 mins vs. 1440 mins). Moreover, Dragon Skin® 10 could be applied by injection, pouring or brushed on, and could also be cured at room temperature without applying heat which aided the process speed of rapid prototyping the phantom aorta. The grade of Dragon Skin® 10 that was selected for this research was also used in the tensile strength evaluation by Russ et al. shown in Figure 3.45 Dragon Skin® 10 was utilized as it can be seen to have comparable tensile strength to aortic tissue being ~3 MPa vs. ~2.6 MPa [72].

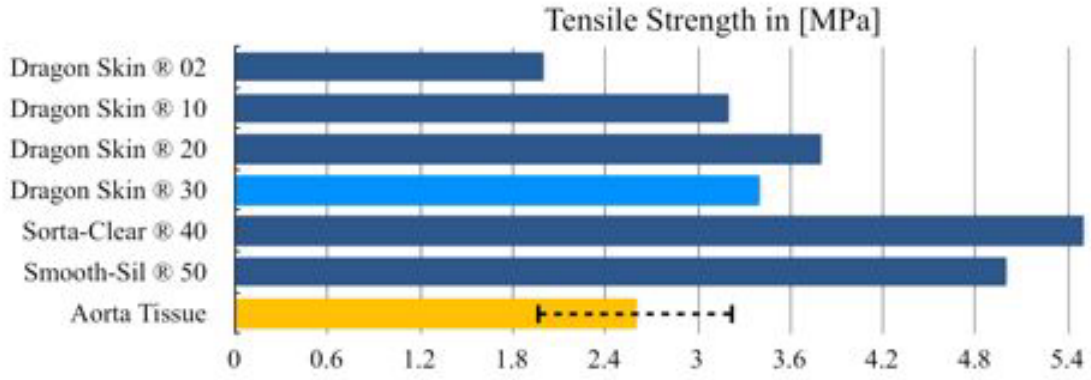

Figure 3.45: Tensile Strength of silicone based material by Smooth-On Inc. in comparison with aortic vessel tissue [72].

In addition, the Young's modulus of Dragon Skin® 10 obtained through tensile testing (0.135 MPa) is comparable to that of Vappou et al.'s Young's modulus of the aorta (0.108 MPa ±0.027 MPa) [71]. As shown in Table 9, the Young's modulus of Dragon Skin® 10 is actually closer to the biophysical properties of aortic tissue than PDMS with standard mix ratios. Thus Dragon Skin® 10 is suitable for fabricating the phantom aorta 2.

Table 9: Table comparing Young's modulus of studied materials.

Material	Young's Modulus (MPa)	Source
PDMS	1.68-2.51	Gülan et al. [85]
Dragon Skin® 10	0.135[7]	-
Aorta Tissue	0.46 0.108	Bia et al. [86] Vappou et al. [71]

Demoulding, however, proved to be the most difficult part of the fabrication process. As mentioned previously in section 3.3.2, the air bubbles could have been avoided if the batch of Dragon Skin® 10 was poured into the mould – following the same technique that Johnson performed. However, this could use up valuable curing time. Another moulding technique that could have been implemented is injection moulding, although this would also have required more complicated equipment. In addition to the moulding improvements, a longer phantom incorporating the gradual tapering section added on to the original phantom aorta 2 in this research could also change the overall pressure waveform by reducing multiple reflection artefacts from the location of the join.

One can criticise that the overall length of the phantom aorta 2 is also too long for a tapering profile i.e. the lumen diameter of the descending aorta should be smaller at length 700 mm from the aortic root. Savrasov et al. reported that the lumen diameter at length 700 mm was approximately 11 mm. Furthermore, the bifurcation started at length 384 mm and not 700 mm. Indeed, the diameter should be around 17.4 mm at length 384 mm and not 19 mm at length 700 mm. Nevertheless, the phantom aorta 2 was able to provide a sufficient experimental setup that along with the cardiovascular simulation platform was crucial for running experiments with the peristaltic extra-aortic balloon cuff.

3.4.3 Cardiovascular Simulation Platform

Since the cardiovascular simulation platform is an additional component to this research for testing the PEABC prototype, the pressure and flow generated by the platform didn't

[7] Obtained from stress/strain experiment of the Dragon Skin® 10

need to exactly match physiological characteristics. However, achieving repeatable results for the validating the PEABC prototype was the main focus. The decision that was made to redesign the left ventricle mechanism of the cardiovascular simulation platform was essential as without it, the effects on the hemodynamics could not be adequately explored with the PEABC prototype in operation. Moreover, the cardiovascular simulation platform was also required to implement the longer geometries of the phantom aorta 2 as it would have otherwise been more difficult for the PEABC to be attached to the left ventricle mechanism.

The pressure waveform results that were obtained from the cardiovascular simulation platform did differ with Drummond's pressure waveform profile [67] which were more similar to physiological than the cardiovascular simulation platform. However, the systolic and diastolic pressures that were obtained from the cardiovascular simulation platform were closer to physiological than that obtained by Drummond [67]. These variances can be explained in several ways:

- The orientation of the cardiovascular simulation platform affected the valves used in the left ventricle pump mechanism, as Drummond's system was orientated vertically.

- The use of a larger and longer phantom changed the site and timing of wave reflection.

- Implementation of capillaries increased the mean aortic pressure to physiological values.

- The use of a bellows type pump system instead of a piston pump system could have changed the turbulence and effectiveness of flow.

With the development of the cardiovascular simulation platform, tweaks were made in an attempt to mimic the physiological aortic pressure and flow. The implementation of the tapered tube that was attached to the phantom aorta 2 to improve the pressure waveform profile was concluded to reduce the second parabolic artefact but it was still present. It is thought that one cause could be attributed to the material characteristics of the Dragon

Skin® 10. Being more elastic than PDMS (10:1), this allows the phantom aorta 2 to have more aortic wall displacement oscillations during the diastolic phase in areas between the closed aortic valve and the end of the phantom aorta 2. Another speculation was that this waveform feature was due to the sudden change in lumen diameter and change in material properties where the phantom aorta 2 with a lumen Ø25 mm – silicone is connected to a polyurethane Ø12 mm hose via a push-in fitting at the end of the phantom aorta 2. As the pulse wave travels down the phantom aorta 2, the wave would hit the junction with the terminating fitting creating a large reflective wave that travels back and forth several times during the diastole phase. This situation was also observed in the pulse wave simulation software explained in Chapter 4 where a terminal point or large reduction in aortic radius can alter the pressure wave due to the propagation of reflected waves. To possibly improve the pressure and flow waveform to point where the waveform can represent physiological characteristics, a better tapering of the aortic diameter is suggested. Also, bifurcations added to the phantom aorta recommended in the works of Savrasov et al. shown in Figure 3.46 could potentially alter the waveforms.

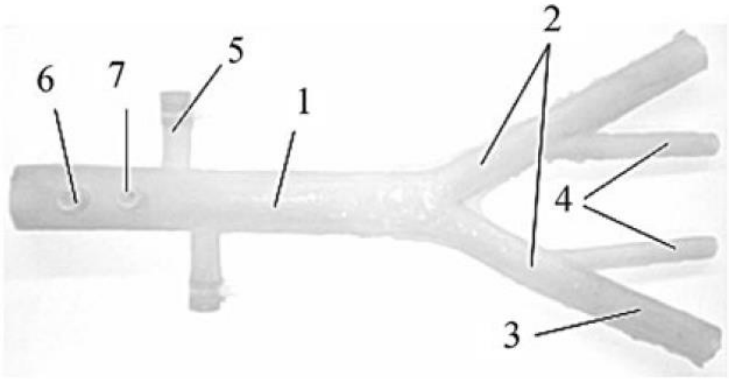

Figure 3.46: Savrasov et al. abdominal and bifurcations to other arteries phantom [73].

The variance of pressure and flow waves observed during operation of the cardiovascular simulation platform can also be related to many other mechanical properties that could possibly affect the hemodynamics within the phantom aorta 2. The first crucial factor is the air bubbles that were present in the cardiovascular simulation platform. It is known in medical studies that air bubbles present in the arteries, also known as venous air embolism can change blood pressure and cause disturbance of hemodynamics [95]. Air bubbles were present inside the piGrip® bellows and would be pushed out of the aortic valve and around the aortic arch section of the phantom. This

reduces the effectiveness of the aortic valve which produced tiny oscillations that represent the multiple opening and closing of the prosthetic aortic valve after peak systolic pressure. Air bubbles were also thought to disrupt attempts at measuring flow using ultrasound probes near the aortic valve, although results of measurements show reasonable agreement between cardiac output calculated from ultrasound measurements, using the displacement of the bellows, and physiologically reasonable values.

Discontinuities could be defined on the cardiovascular simulation platform whereby the phantom aorta is connected to the rest of the set up with different materials and thus could explain the dissimilar pressure waveforms between physiological and the simulation. Another variable that may be the cause of undesired pressure and flow waveform points towards an aortic aneurysm link effect that was present at the end of the phantom aorta 2. This aortic aneurysm was simply a big bulge that expanded on one side of the phantom mainly related to the non-uniform thickness of the phantom aortic wall. It has been observed in the medical study by Swillens et al. [96] that having aortic aneurysm can dramatically effect on the pressure waveform, due to pulse wave reflections. Nevertheless, the PWV that was obtained from the cardiovascular simulation platform when comparing to Vappou et al. study was very similar – 4.3 m/s vs. 4.4 m/s respectively – considering that in both cases that the aortic thickness was also similar. Wall thickness of phantom aorta 2 measured using ultrasound was very similar to the designed values.

Chapter 4

Pulse Wave Software Simulation Using Matlab®

4.1 Introduction

A software simulation of pulse wave propagation in the aorta was created to test the concept of applying an external peristaltic motion to a segment of an aortic wall. The peristaltic movement is determined by the cardiac pressure and flow output in synchronisation with a counterpulsation system. Modelling the peristalsis movement to efficiently move blood in an aorta requires factoring in the pulse wave produced by the heart. The pulse wave model uses a 1-D wave equation to create a pressure waveform that would determine when each air chamber inflate and deflate during a cardiac cycle. The simulated pressure and flow wave profiles are then augmented with peristaltic wave motion profile to simulate what would happen if a PEABC is applied to the descending aorta. To investigate this concept, a Matlab® (MathWorks®, United States) simulation software was written to illustrate how the pulse wave characteristics propagate through an aorta. The data obtain from the simulation will then be utilised for comparison against the results obtained from the peristaltic extra-aortic balloon cuff prototype. The purpose of creating a pulse wave simulation for this research is to obtain simulation data that could be compared with the experimentation so that any similarities or differences between the two can be validated.

4.2 Methodology

4.2.1 Simulation Overview

The pulse wave simulation was created and simulated using Matlab® (MathWorks®, United States) to illustrate a moving pulse wave in one-dimension (1-D). The total pulse wave propagating through an aortic segment was represented as being composed of forward and backwards waves (see Figure 4.1). Parameters relevant to the simulation

include the aorta's geometry, material properties, boundary conditions and aortic pressure wave profile and external peristaltic movement applied to an aortic segment.

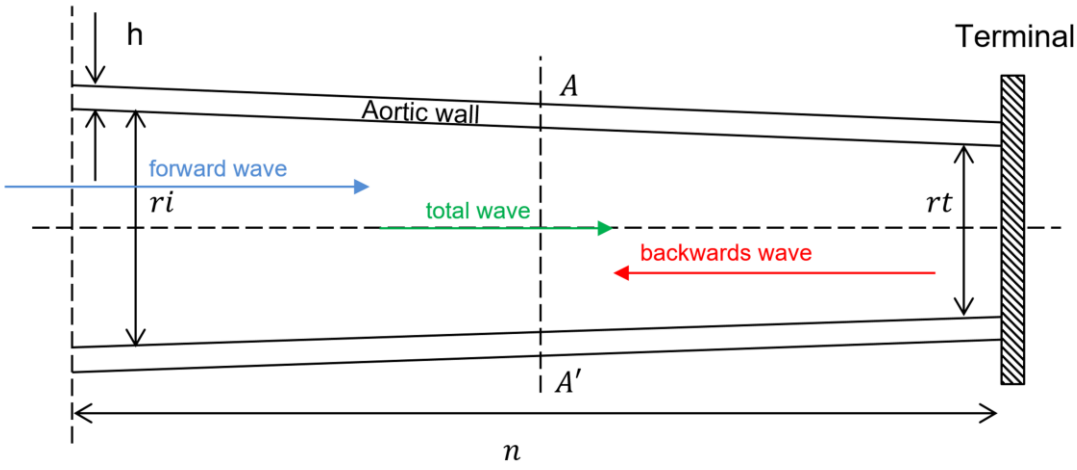

Figure 4.1: 1D wave propagation and boundary conditions used to simulate the pulse wave.

4.2.2 Mathematical Models

Several mathematical models were used in combination to produce the simulation, which is described below.

4.2.2.1 Modified Pulse Wave Equation

For this simulation, Moens-Korteweg's PWV equation was modified to compute the pulse wave propagation over the change in aortic radius which in itself is a dynamic variable that is used to calculate other simulation parameters such as the area and admittance that defines the boundary conditions.

Referring back to the aortic geometries that were stated in section 3.2.2, the radius dimensions in the 3D CAD model of the phantom aorta were utilized to calculate the radius difference (dr), radius at initial point (ri) and radius at terminal point (rt) (see Equation 4.1) with the consideration of the gradient defined by the length of segment (nx). The time segment (n) is related to the cardiac cycle (T) that is based on the time increment (dt) for which dR's is set over the nx and simulation time (nt). Equation 4.1 was create to factor the tapering aortic radius profile based on the adaption of Watanabe et al.'s change in aortic radius variable [97].

$$dr = ri - rt$$

$$grad = dr/nx \qquad \textit{Equation 4.1}$$

$$dR = (ri - (n \times grad))$$

Pulse wave velocity is calculated using Equation 4.2 with the variables defined below:

- $E = Young's Modulus$
- $dR = Change\ in\ aortic\ radius$
- $\rho = Rho$
- $v = Poisson\ Ratio$

$$PWV'' = \sqrt{\frac{Eh}{2dR\rho(1 - v^2)}} \qquad \textit{Equation 4.2}$$

4.2.2.2 1-D Wave Propagation Equation

For the simulation of the forward wave, backwards wave, and the total wave, a wave profile had to be defined. The wave profile considers the time domain, amplitude and shape of the pressure waveforms that were simulated (see Figure 4.2).

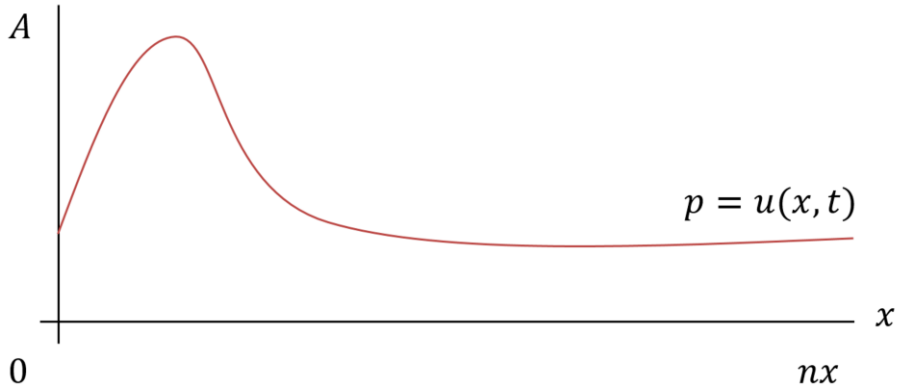

Figure 4.2: Simple 1D pressure wave based on number of x segments (nx) and time

Suppose that the function $u\,(x,t)$ represents the amplitude of the pulse wave at position x and time t. For 1-D wave propagation u satisfies the differential equation (see Equation 4.3, Equation 4.4, Equation 4.5 and Equation 4.6).

$$\frac{\delta^2 u}{\delta x^2} = \frac{1}{c^2}\frac{\delta^2 u}{\delta t^2}$$

Equation 4.3

$$\frac{\delta^2 u}{\delta x^2} = \frac{1}{\frac{Eh}{2dR\rho(1-v^2)}}\frac{\delta^2 u}{\delta t^2}$$

Equation 4.4

To adapt the 1-D wave equation for implementation in Matlab, the central finite difference update rule was utilised and thus second derivatives were defined for the approximation of both x and t:

$$\frac{\delta^2 u}{\delta t^2} \approx \frac{u(x, t+\Delta t) - 2u(x,t) + u(x, t-\Delta t)}{\Delta t^2} \qquad \textit{Equation 4.5}$$

$$\frac{\delta^2 u}{\delta t^2} \approx \frac{u(x, t+\Delta t) - 2u(x,t) + u(x, t-\Delta t)}{\Delta t^2} \qquad \textit{Equation 4.6}$$

Using the above approximations, the wave equation can be rewritten as:

$$\frac{u(x, t+\Delta t) - 2u(x,t) + u(x, t-\Delta t)}{\Delta t^2} \ldots = c^2 \frac{u(x+\Delta x, t) - 2u(x,t) + u(x-\Delta x, t)}{\Delta x^2} \qquad \textit{Equation 4.7}$$

Note that time $(t + \Delta t)$ represents the next time step, $(t - \Delta t)$ is the previous time step, and the t is the current time step. A similar definition is applicable to x. Rearranging the equation above to calculate the wave at the next time step gives:

$$\begin{aligned} u(x, t+\Delta t) = c^2\big(&u(x+\Delta x, t) \ldots \\ &+ u(x-\Delta x, t)\big) \ldots \\ &+ 2(1-c^2)u(x,t) \ldots \\ &- u(x, t-\Delta t) \end{aligned} \qquad \textit{Equation 4.8}$$

To define the pressure waveform profile (P) that considers the initial amplitude (A) and time period based on T, Equation 4.9 was used in place of the $u\ (x, t)$ function:

$$P = A \sin\left(\frac{2\pi}{T}\right), 0 \leq t\ \leq T/2 \qquad \textit{Equation 4.9}$$

The 1-D wave profile of all three waves – forward, backwards and total – is represented by Equation 4.10, Equation 4.11, and Equation 4.12 respectively, for pressure wave (P). This defines P waves to be the following, where f and g are univariate functions:

$$P_{forward} = f(x + ct) \qquad \textit{Equation 4.10}$$

$$P_{backward} = f(x - ct) \qquad \textit{Equation 4.11}$$

$$P_{total} = P_{forward} + P_{backward} \qquad \textit{Equation 4.12}$$

4.2.2.3 Boundary Conditions

The pulse wave simulation involved creating a pulse wave that is produced every cardiac cycle (T = 0.8 seconds) as a dynamic boundary condition. Since the simulation is based on a narrowing aorta, coefficients had to be calculated for every segment (nx). The dynamic boundary conditions that make up the aortic segment involved defining the length of the aorta, the initial and terminal point boundaries, and the coefficients that represent the narrowing of the aortic radius at each n segment based on the change in PWV. These boundary conditions specify the behaviour of the pulse wave as they enter and exit or reflect within the aorta segment [97]. The equation for defining the waveform's (u) boundary condition is represented by Equation 4.13 (initial boundary) and Equation 4.14 (terminal boundary) for which was it was defined on the pulse wave simulation for initiating the Matlab® (MathWorks®, United States) software.

$$u(0, t) = 0 \qquad \textit{Equation 4.13}$$

$$u(nx, t) = 0 \qquad \textit{Equation 4.14}$$

Since the descending aorta that is being modelled has a tapered diameter, the pulse wave will endure wave reflections at nx segment based on the changing in diameter (dx). It is assumed that dx for this simulation is set to 0.1 mm over the nx segment and the coefficients are defined at every instance of nx. The coefficients were calculated for forward and backwards waves of the initial, reflective and transmitted waves. The coefficients were calculated based on the admittance (Yn) which was derived from the c and cross-sectional area at which the diameter changes over the segment of nx (see Figure 4.3).

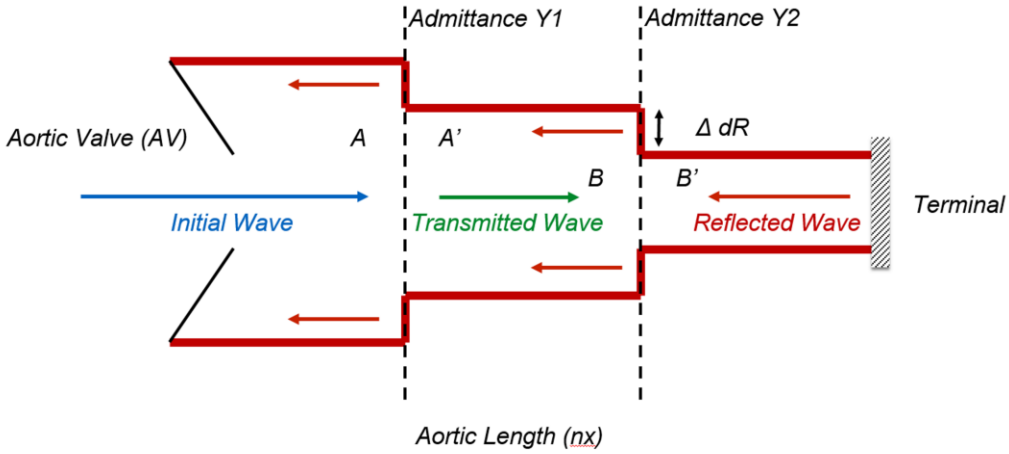

Figure 4.3: Boundary conditions for a tapered aorta.

The calculations for defining reflection coefficients over the phase of current t and nx are as follows:

$$An = \pi(dR^2) \qquad \textit{Equation 4.15}$$

$$Yn = An/\rho c \qquad \textit{Equation 4.16}$$

For Reflective Forward Coefficient:

$$PrfCoe(t, nx) = \frac{(Y(t, nx) - Y(t, nx + 1))}{(Y(t, nx) + Y(t, nx + 1))} \qquad \textit{Equation 4.17}$$

For Transmitted Forward Coefficient:

$$PtfCoe(t,nx) = \frac{2(Y(t,nx))}{Y(t,nx) + Y(t,nx+1)} \qquad \textit{Equation 4.18}$$

For Reflective Backwards Coefficient:

$$PrbCoe(t,nx) = \frac{(Y(t,nx) - Y(t,nx-1))}{(Y(t,nx) + Y(t,nx-1))} \qquad \textit{Equation 4.19}$$

For Transmitted Backwards Coefficient:

$$PtbCoe(t,nx) = \frac{2(Y(t,nx))}{Y(t,nx) + Y(t,nx-1)} \qquad \textit{Equation 4.20}$$

The effects of the waves under the influence of an aortic valve opening and closing during a cardiac cycle are defined by changing the boundary condition at the initial point. This is defined as the aortic valve coefficient with the coefficient set to 1 to simulate a closed aortic valve for the time of 0.6 seconds. The aortic valve coefficient affects any reflective wave that is travelling left (see Figure 4.4) to reflect back at full size. For the event that the propagating wave reaches the end of the aorta, bifurcation coefficients are assigned to allow some waves to continue on and some to reflect back. The bifurcation coefficient is applied to the propagating wave at the terminal point, with the coefficient set to 0.5 [94]. This means that half the amplitude of the wave that's travelling right is reflected back.

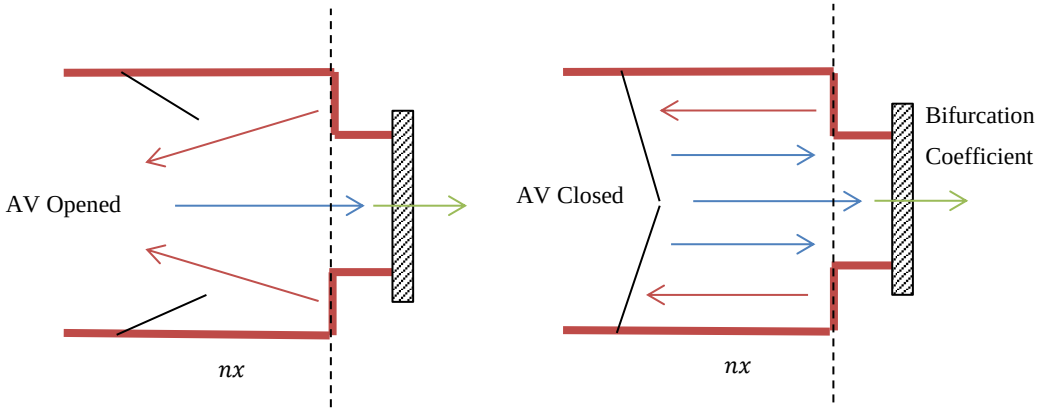

Figure 4.4: The effects of the initial (blue arrow), reflecting (blue arrow) and transmitting (blue arrow) waves travelling through the aorta.

The propagation of the pulse waves over nx and t was subjected to the summation of the product of coefficients and the other waves that transmit and reflect with the boundary conditions that were mentioned. Referring back to Figure 4.3, the 1-D pressure wave is represented by the following:

$$Pf(t+1,nx) = (PfLeft \times TfCoeLeft) \ldots + (Pb(t,nx) \times RbCoeLeft) \quad \textit{Equation 4.21}$$

$$Pb(t+1,nx) = (PbRight \times TbCoeRight) \ldots + (Pf(t,nx) \times RfCoeRight) \quad \textit{Equation 4.22}$$

$$Pt(t+1,nx) = (Pf(t,nx) + Pb(t,nx)) \quad \textit{Equation 4.23}$$

4.2.2.4 Peristalsis and Counterpulsation Augmentation of the Aortic Wall Model

The peristaltic motion of the aortic wall was represented by changing the aortic radius during the simulation. This direct indentation to the aortic wall from extra-aortic cuff would increase the PWV according to the Moens Korteweg's equation. However, elasticity decreases at low strains, which acts to decrease the PWV. Overall, the main effect on the pulse wave is through changes in reflection coefficients, which are related to both PWV and cross-sectional area. The desired changes in aortic radius due to peristalsis were implemented using the following equation (see Equation 4.24).

$$B1(x1,t1) = -\mathrm{A}\ Sin\left(\left(\frac{2\pi}{\frac{1}{T}}\right)(t-i)\right)^{-\left(\left(\frac{\frac{-nx-lN}{N}}{40}\right)\right)^{6}}, 0 \le t \le T/2$$

Equation 4.24

Referring to Equation 4.24, i is a phase delay from the start of the cardiac cycle and l is the inflation location along the direction nx. Four cuff wave equations were derived with different inflation time and inflation location to create the peristalsis motion along the aortic wall (see Figure 4.5).

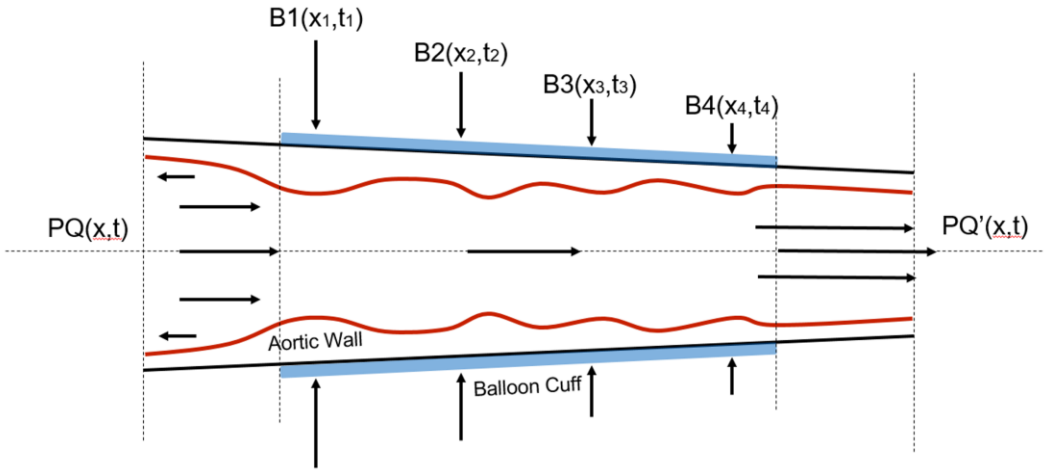

Figure 4.5: Balloon cuff augmentation location along the aortic wall.

The inflation and deflation timing of balloon cuff waves were specified to perform a peristaltic motion to the aortic wall – changing the aortic wall radius at different locations (x_{1-4}) and times (t_{1-4}). An example of the timing of inflation of the four cuffs is represented in Figure 4.6.

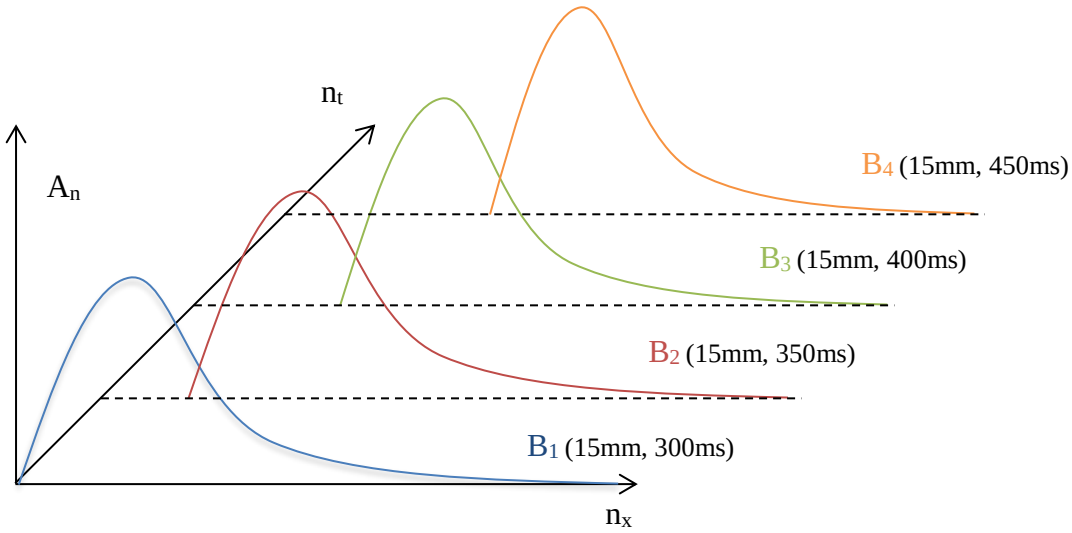

Figure 4.6: Four cuff wave profile at different location (n_x) and time (n_t).

4.2.3 Pulse Wave Simulation Development on Matlab®

The first stage of developing the software simulation was setting up the parameters for obtaining the change in PWV along the segment of aorta. These include defining parameters for Moens Korteweg's equation, initial boundary conditions, time and length constraints for the simulation and the initial waveform for both pressure and flow. It is then followed by a series of calculations that calculate the difference in aortic radius (dR), PWV (c), cross-sectional area (A) and admittance (Y) over a table of t and nx. The inflation time and location variables for modeling the peristaltic movement to the aortic wall is also defined in the initialization part of the software.

The next set of software instructions performs the calculations for forward wave coefficients of reflecting and transmitting waves. This is followed by a similar calculation of the backwards wave coefficients of both reflecting and transmitting waves. The peristaltic movement is also calculated in the same loop. The final set of calculations is performed to calculated the three waves – forward, backwards, and transmitting – for both pressure and flow based. All of the waveforms are then plotted on multiple figures. The following diagram (see Figure 4.7) illustrates this process.

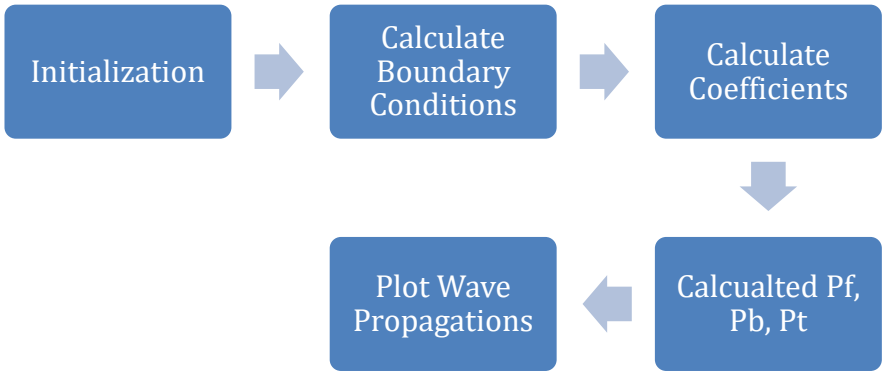

Figure 4.7: Structure diagram of the pulse wave simulation on the Matlab® (MathWorks®, United States) software.

Boundary conditions for the overall simulation were calculated and these include the following:

- Input pressure waveform.
- Reflection coefficients representing the aortic valve and aortic bifurcation.

- Tapering profile of the aorta based on the change of the aortic radius.
- Time and aortic segment constraints.
- Initial and termination boundaries.
- Location of the cuff waveform.
- Pulse wave velocity.

4.3 Results

A set of tests was performed on the pulse wave simulation to see if the propagation of the pulse wave would create a pressure wave that is similar to that of pressure inside a human aorta. The second set of tests was performed to observe the behaviour of the pressure wave when an external peristaltic movement is introduced. Comparison between these two sets of data clarifies the initial feasibility of the concept. Moreover, these sets of data would also be compared to the data obtained from the cardiovascular simulation platform, which is discussed in Chapter 7.

4.3.1 Initial and Normal Condition Test Results

Figure 4.8 shows the linear decrease in aortic radius along its length at initial conditions. The initial radius and terminal radius values used in the simulation are taken from the measurement of the phantom aorta 2.

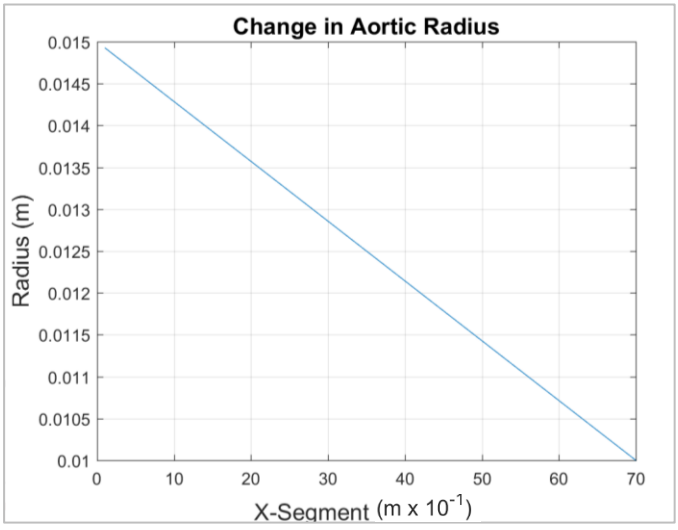

Figure 4.8: Change in aortic radius over the aortic segment.

Calculated PWV under initial conditions is shown in Figure 4.9. It was observed that changes in c along the length of the aorta increases as the aorta radius gets smaller. It was also observed that an increase in aortic thickness increases c.

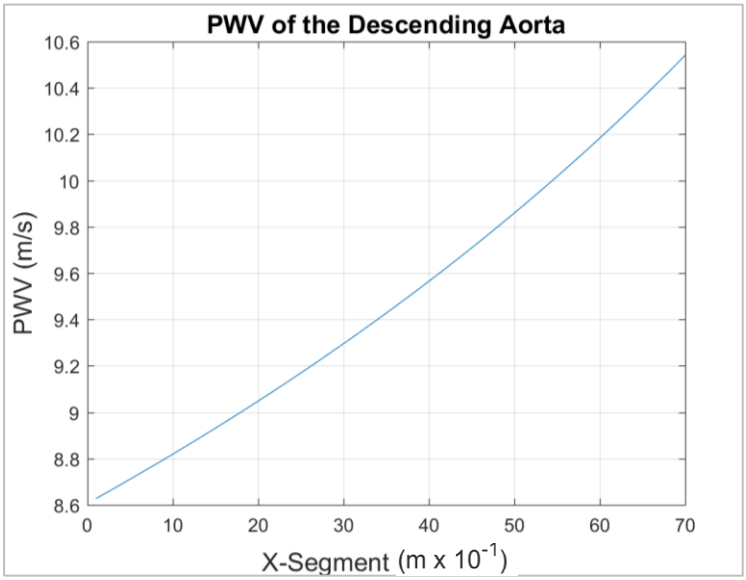

Figure 4.9: Calculated pulse wave velocity along the aortic segment.

The propagation of the input, forward and backwards pressure waves along the length of the aorta were examined. The systolic time (with the aortic valve open) was set to 0.3 seconds. Backwards waves that were propagating towards the valve did not experience reflection during this time. However, when the aortic valve is closed for 0.5 seconds, any waves propagating towards the valve would experience a reflection. The aortic valve reflection coefficient profile is represented in Figure 4.10.

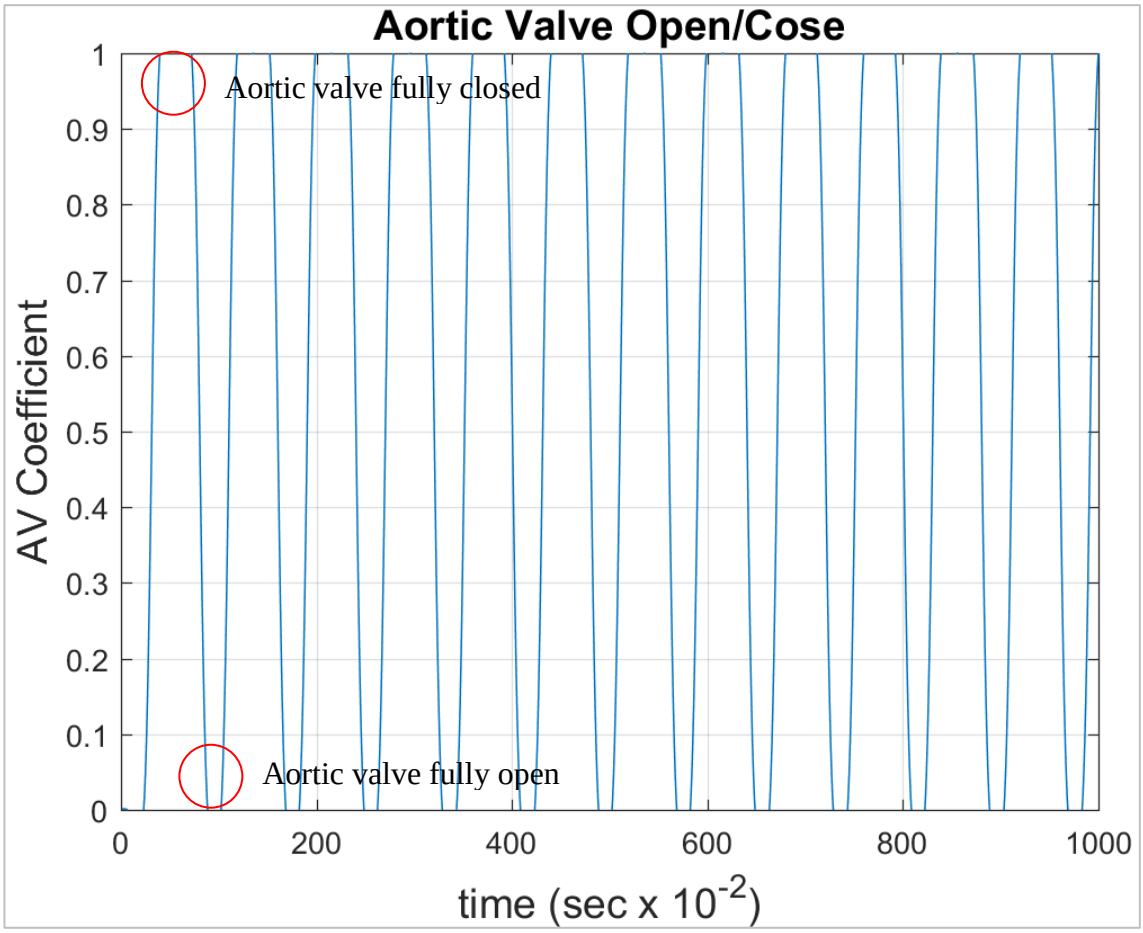

Figure 4.10: Aortic valve opening and closing coefficient waveform

The forwards, reflecting and total waveforms were also observed at the terminal point where bifurcation occurs. As shown in Figure 4.11, the incident wave resulted in the reflecting wave amplitude with a positive reflection being halved due to the fact that the bifurcation reflection coefficient was set at 0.5.

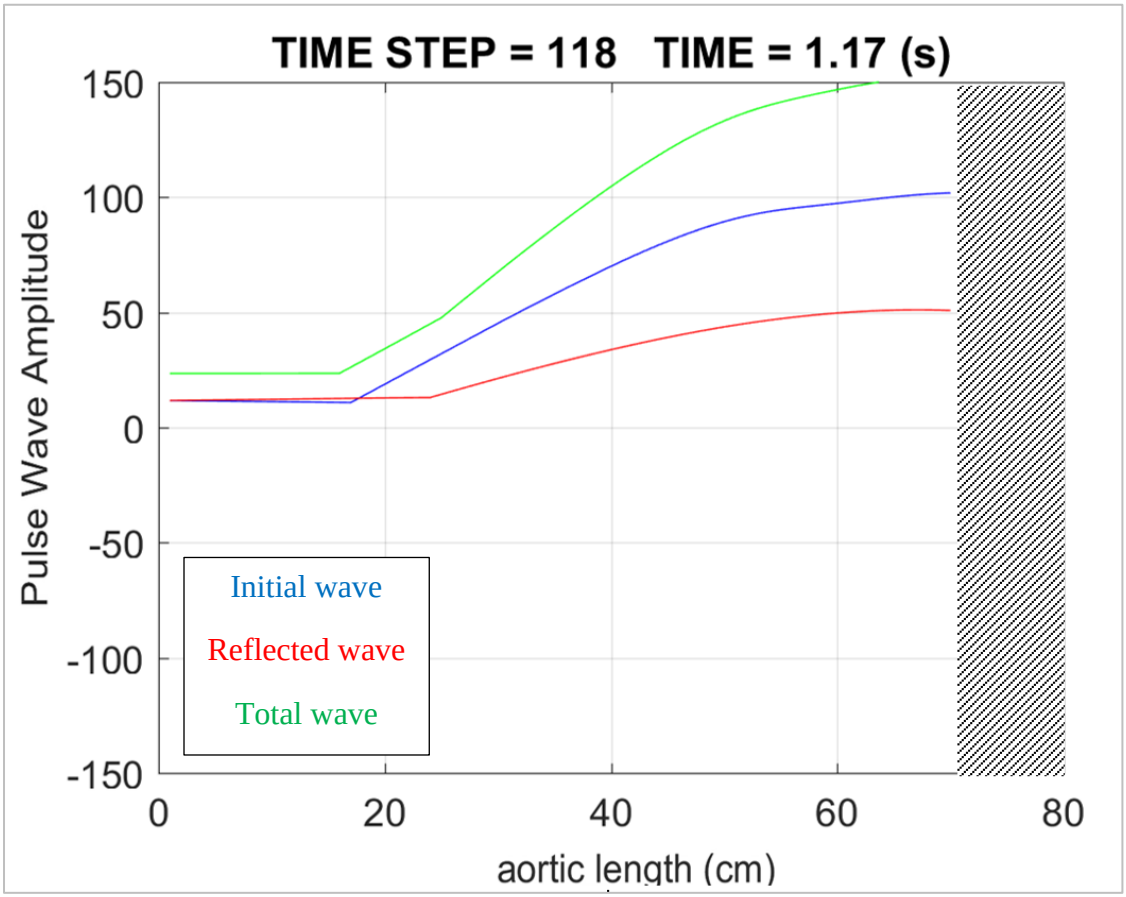

Figure 4.11: Three pulse waves simulated along the aortic segment after 1.1 seconds.

As for the total waveform, the wave is simply the sum of the forward waveform and the reflecting waveform (see Figure 4.12).

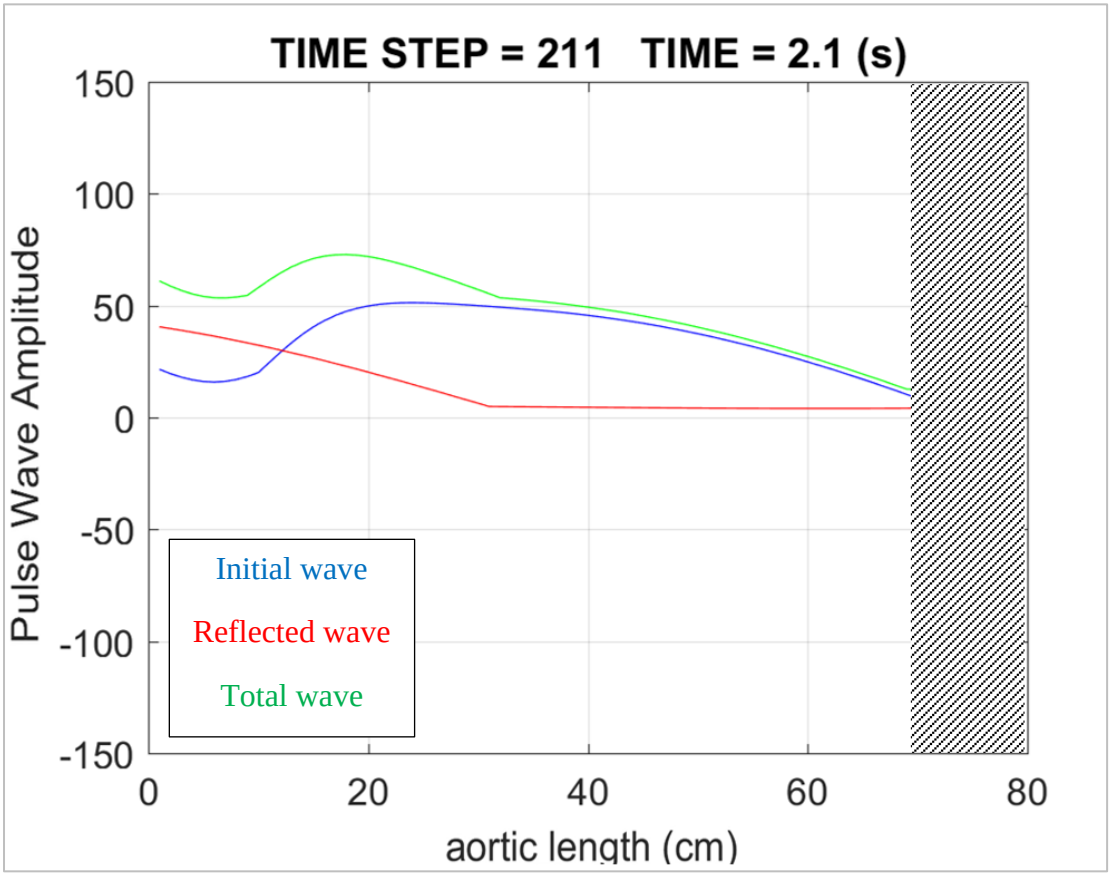

Figure 4.12: Three pulse waves simulated along the aortic segment after 2.1 sec.

With the waves propagating through a narrowing aortic radius with a uniform aortic thickness, the forward wave's amplitude was observed to increase over the aortic length whereas the reflected wave's amplitude decreased. It was also observed in the propagation simulation, as expected, that small reflection waves occurred at the boundaries of each x-segment. After an elapsed simulation time of 10 seconds, the total pressure waveform at the beginning of the aortic length is shown in Figure 4.13.

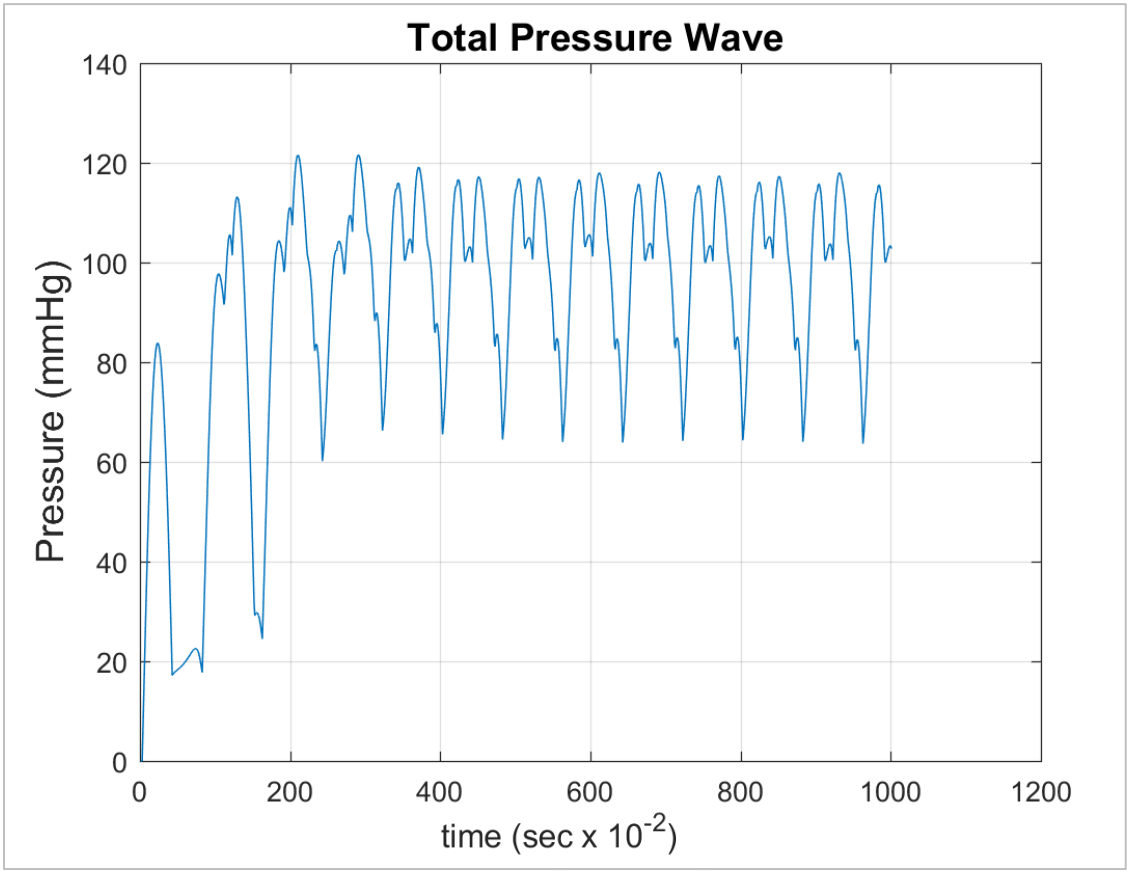

Figure 4.13: Total pressure simulated for 10 sec.

Figure 4.14 represents the same wave propagation simulation that was performed but also shows behaviour along the aorta (pressure, time and x-segment). Looking at both Figure 4.13 and Figure 4.14, the pressure wave is perceived to stabilise after 4 seconds has elapsed from the start of the simulation. Another aspect of analysing the total pressure waveform is the wave shape itself. Although the initial pressure wave peak amplitude was set at 80 mmHg, this increases to a stable peak systolic pressure of 117 mmHg and a diastolic pressure of 64 mmHg over the 4 sec due to the mechanism of wave reflection.

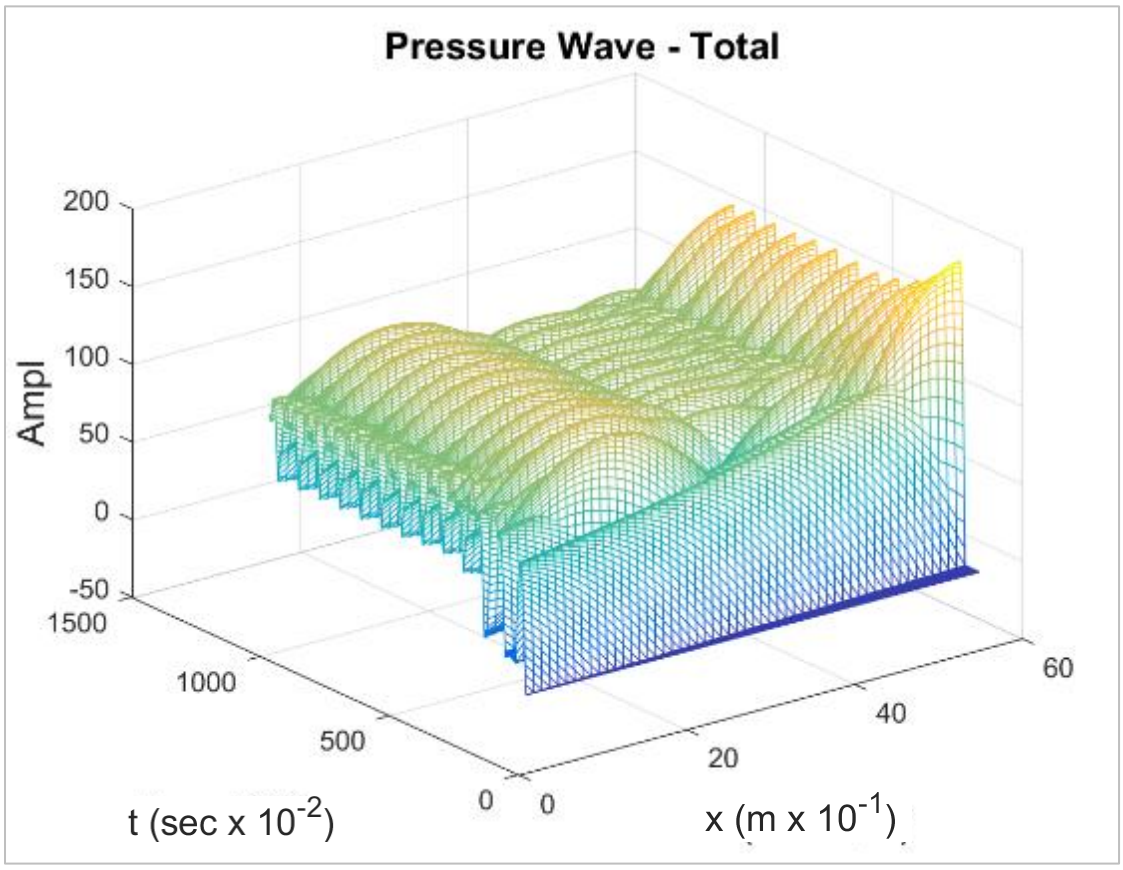

Figure 4.14: Total pressure wave represented in a 3D based on the amplitude, time and aortic segment.

Looking at Figure 4.15 the systolic pressure wave profile is affected by the opening and closing of the aortic valve. During systole, the pressure was observed to rise as normal. During diastole, the pressure drops but a secondary wave hump was present for approximately 0.2 seconds before dropping down to minimal diastolic pressure.

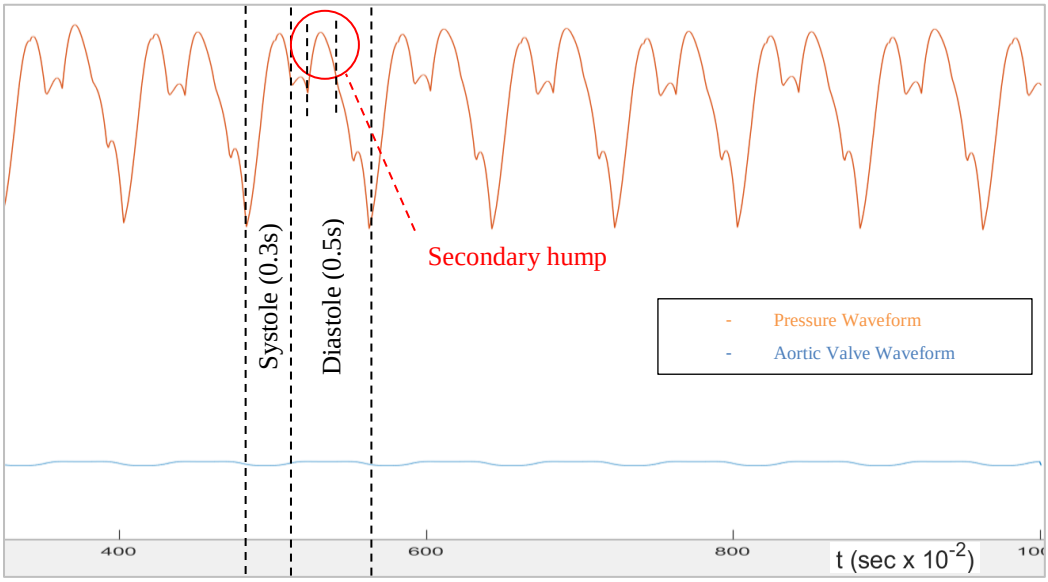

Figure 4.15: Relationship between the pressure waveform and aortic valve opening and closing.

One physiological explanation for this is the effect of aortic valve closure, also known as a dicrotic notch. In physiological terms, a dicrotic notch is a small descending inflection in the arterial pulse/pressure waveform that occurs immediately after the closure of the aortic valve and is used as a marker for the systolic phase. This reason was validated by altering the aortic valve closure coefficient in the simulation. Reducing the coefficient factor from 1 to 0.8 had the effect of reducing the dicrotic notch (see Figure 4.16).

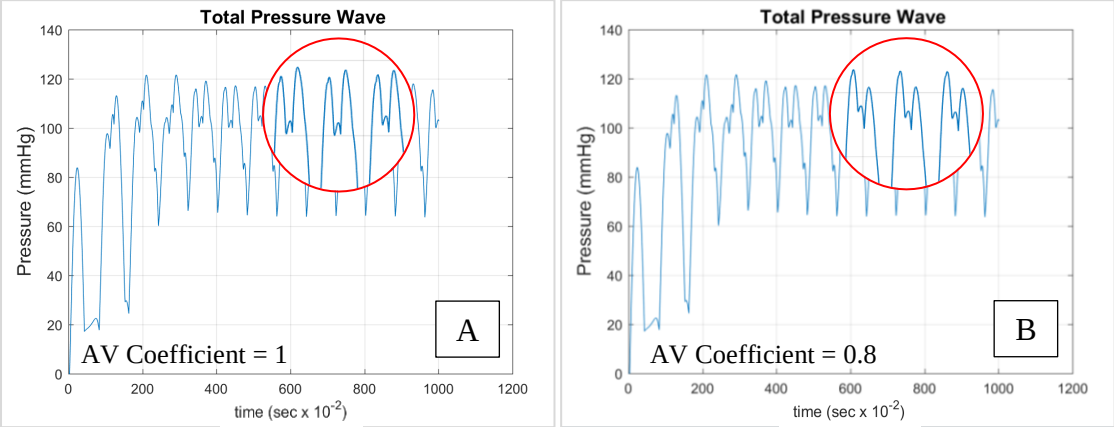

Figure 4.16: The effects of reducing the aortic valve coefficient on the total pressure wave. (A): AV coefficient set to 1. (B): AV coefficient set to 0.8).

4.3.2 Peristaltic Application Condition Test

Once the simulation was established to produce an aortic pressure waveform with features of a physiological waveform, the implementation of an external peristaltic movement applied to the aortic wall was added to the simulation to simulate the operation of the PEABC prototype. The simulation accounts for the location of the PEABC along the aortic length, the time at which each balloon is inflated and deflated, and the change in artery radius when PEABC is operation. Changes in wall stiffness or thickness were not accounted for as further work is required to factor in these variables. The balloon inflation profile was represented over the time, inflation amplitude and location (shown in Figure 4.17).

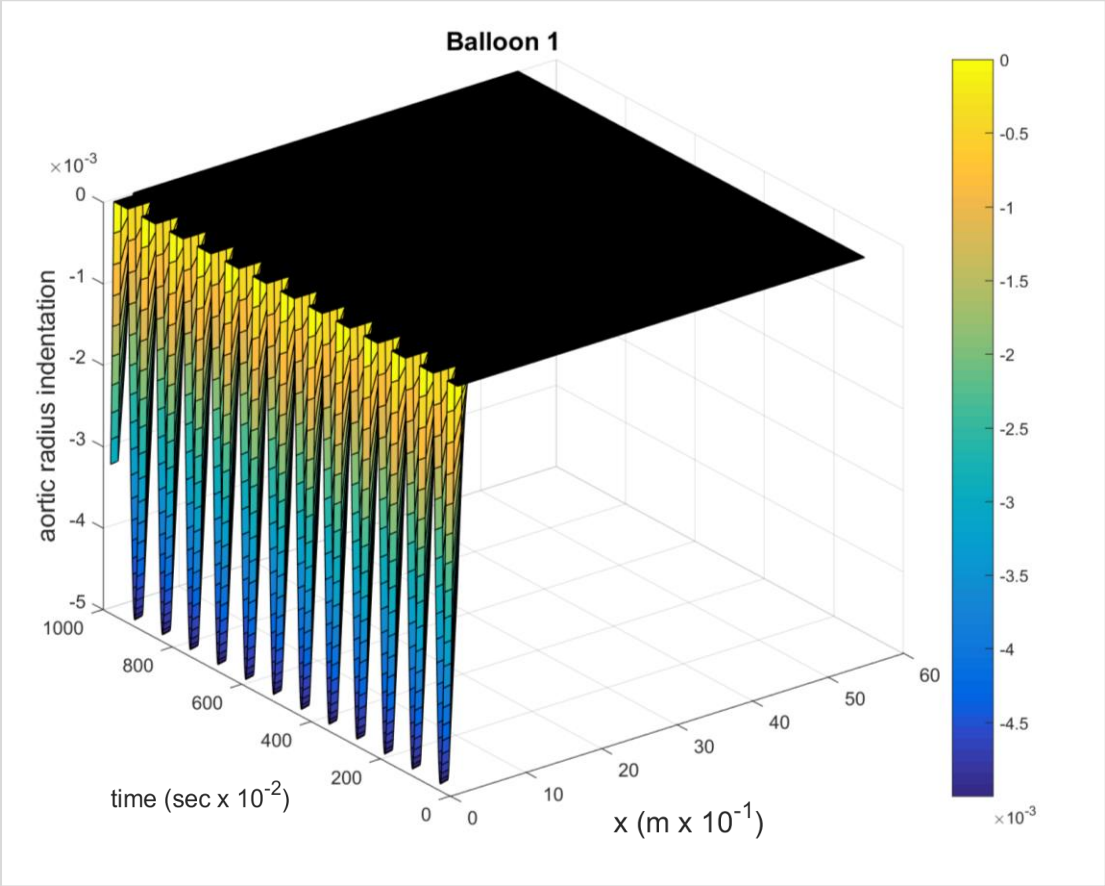

Figure 4.17: Balloon 1 inflation profile.

As shown in Figure 4.18, B1 was activated 0.1 sec directly after systole to imitate counterpulsation with a peak indentation of 5 mm to the aortic radius.

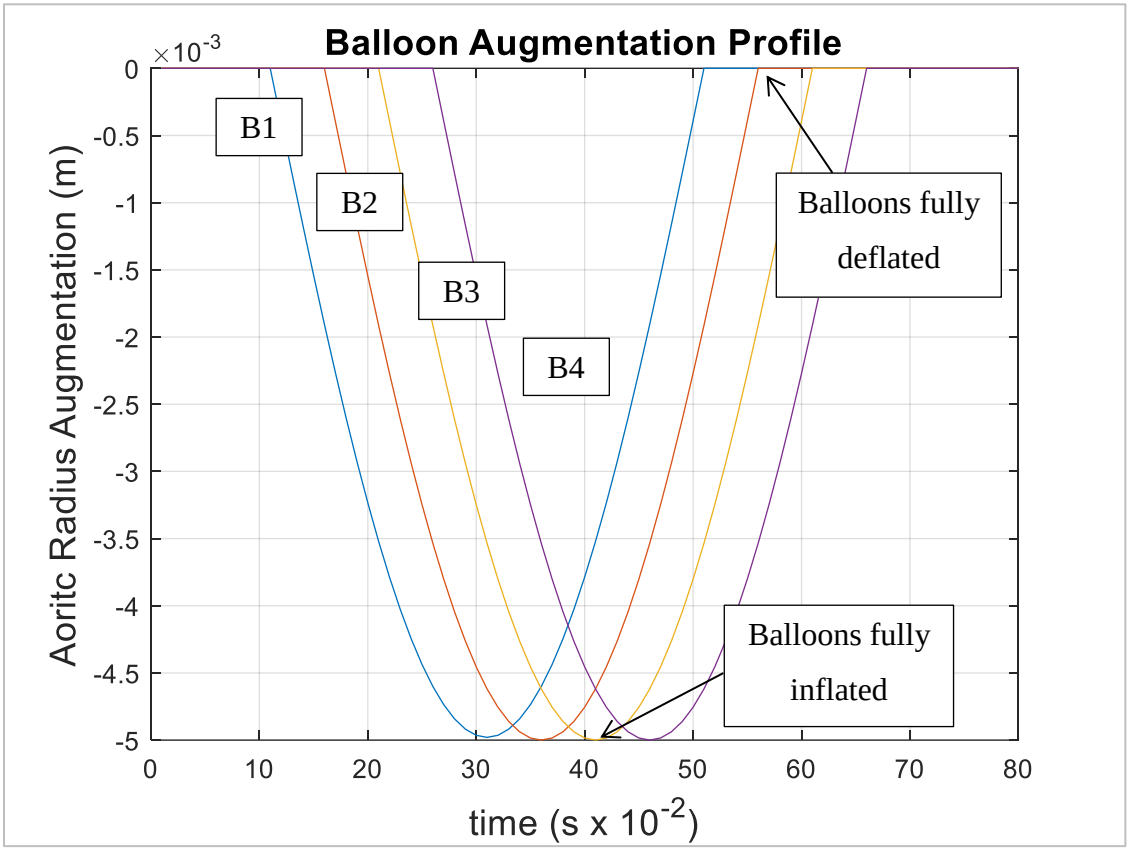

Figure 4.18: Balloon indentation over timing profile.

The deflation of B1 then occurs 0.3 seconds after it was activated. No aortic radius augmentation from B1 occurred after 0.5 sec. The time for each balloon to inflate and deflate was 0.4 seconds. The second balloon (B2) had a different start time where a small time delay of 0.05 sec phased after B1's activation, however the duration of the inflation and deflation is identical. The third and fourth balloons (B3, B4), both subjected to the same time delay with B3 activated after B2, and B4 activated after B3. The centres of each balloon were: B1 set at 15 mm (the start of the aortic length), B2 was located at 35 mm, B3 was at 55 mm and B4 was at 75 mm. The position gap between each balloon position of 20 mm matched the fabricated peristaltic balloon cuff described in Chapter 5, section 5.2.2.

The aortic radius changes over both time and distance along the aorta as each cuff balloon is activated. This changes the PWV and reflection and transmission coefficients in the affected segments. It is shown in Figure 4.19 that the PWV increases at the location of the inflated cuff balloons.

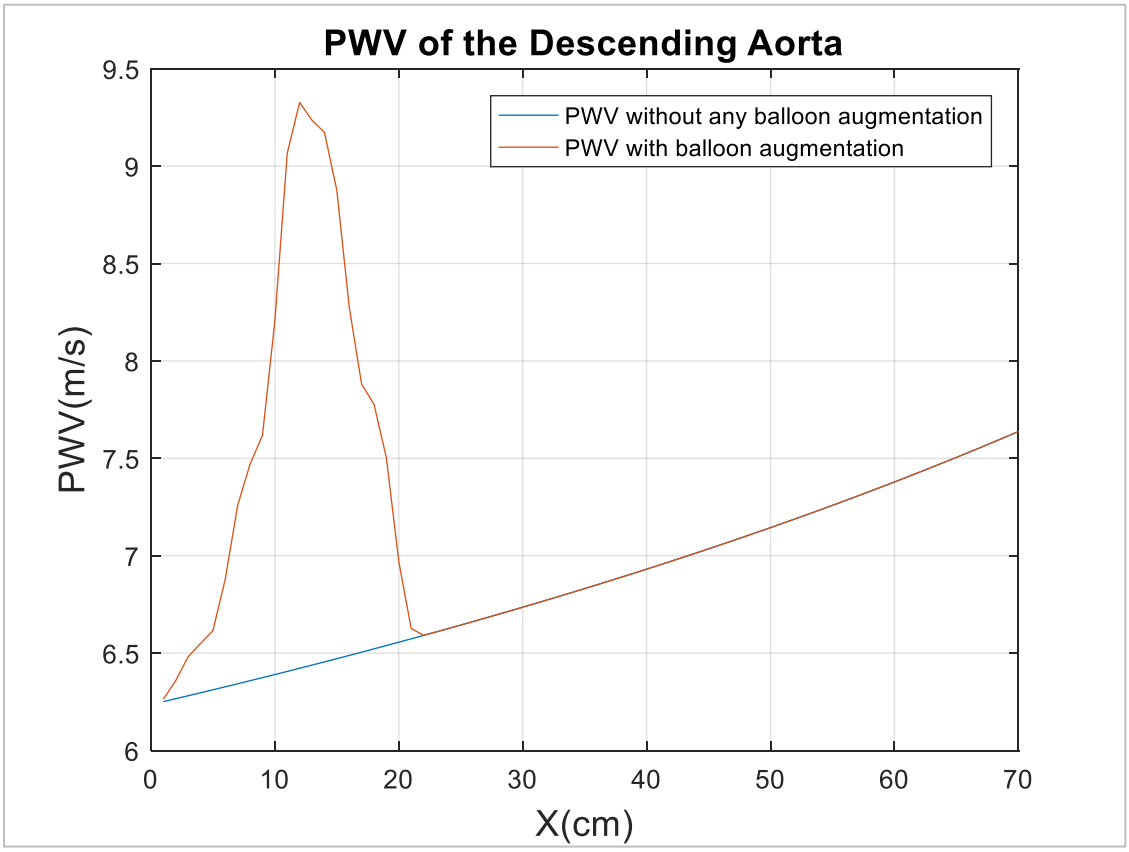

Figure 4.19: The effects of PWV along the aortic segment with and without the balloons inflating and deflating.

In the simulation, each balloon cuff was observed to alter the forward, backwards and total waves during the inflation of each balloon cuff. Looking at Figure 4.21, which shows pressures after 42 time steps (0.42 seconds), it can be seen that there is a reduction of the backwards wave's amplitude and an increase in the forward wave's amplitude around the segment of the first balloon cuff.

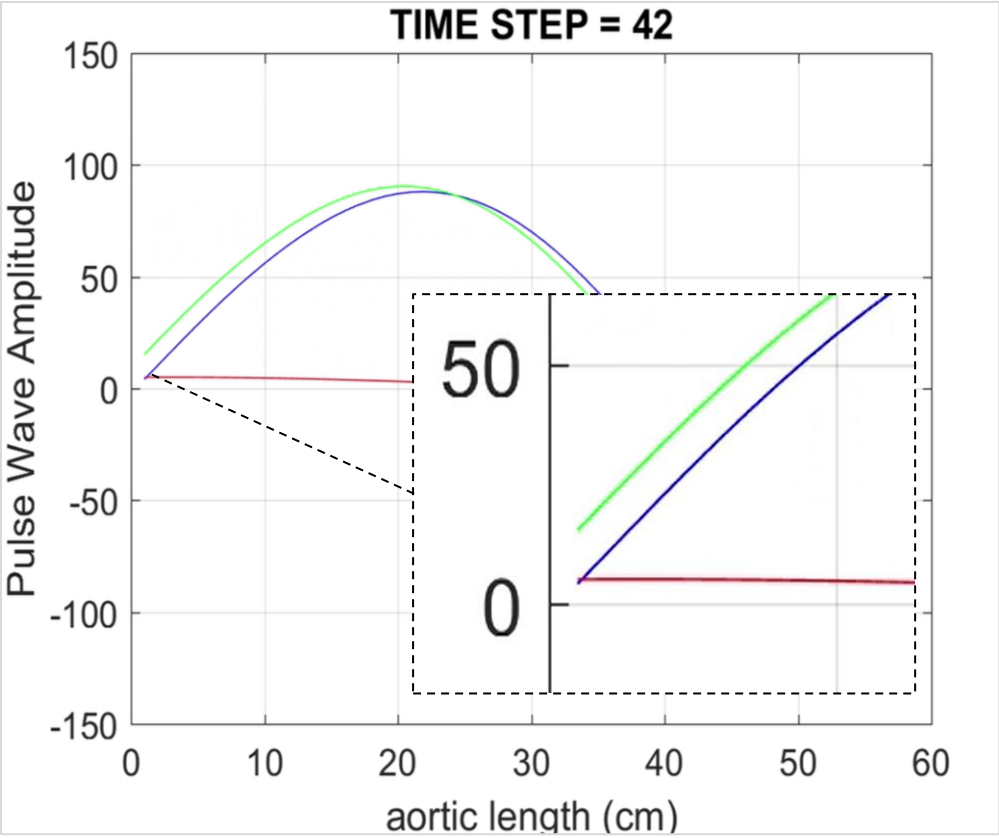

Figure 4.20: The forward (blue), backwards (red) and total (green) pressure waveform.

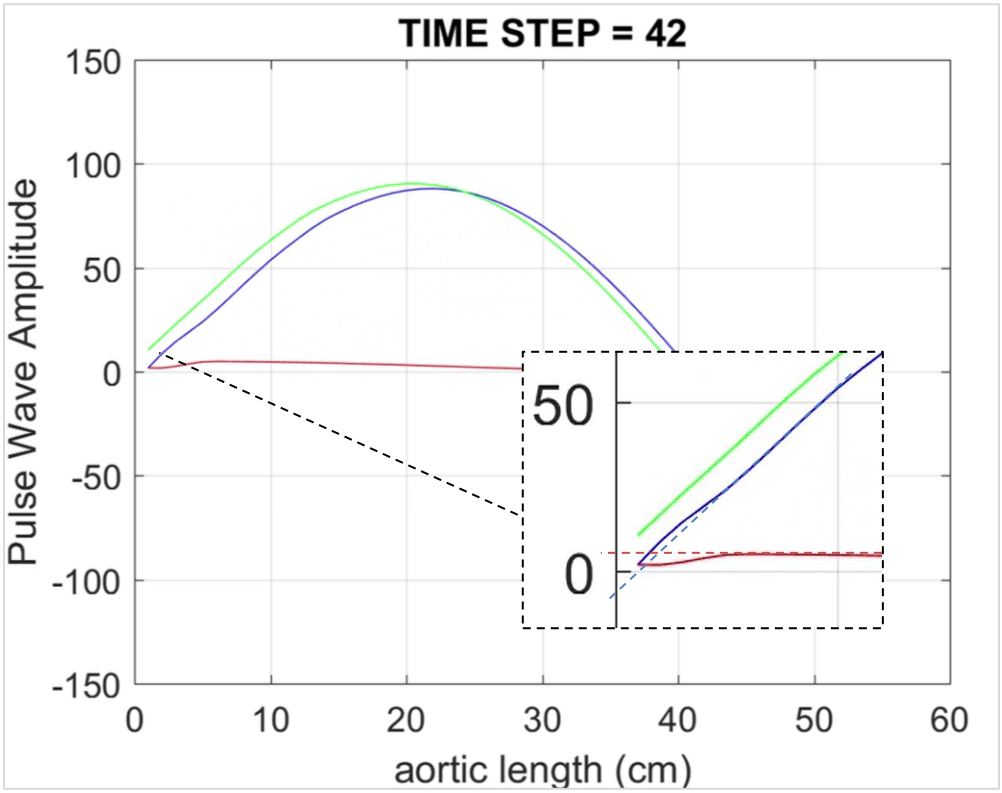

Figure 4.21: The forward (blue), backwards (red) and total (green) pressure waveform with balloon cuff inflation.

Continuing the simulation time over 10sec shows other differences. Figure 4.22 and Figure 4.23 show that the augmentation of the balloon cuff changes the peak dicrotic notch pressure to increase from 88.23 mmHg to 92.63 mmHg (Δ4.4 mmHg). However, both peak systolic pressure and end-diastolic pressure were essentially unchanged. The peak systolic pressure was reduced by 0.95 mmHg and the end-diastolic pressure was reduced by 1.59 mmHg as a result of balloon cuff augmentation.

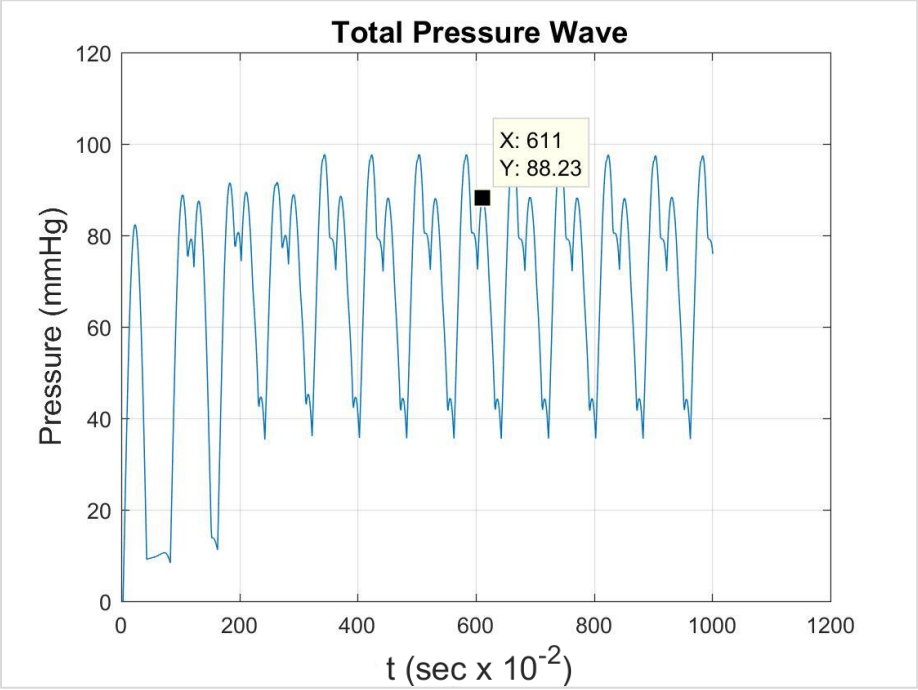

Figure 4.22: Total pressure waveform simulated for 10 seconds without balloon cuff augmentation.

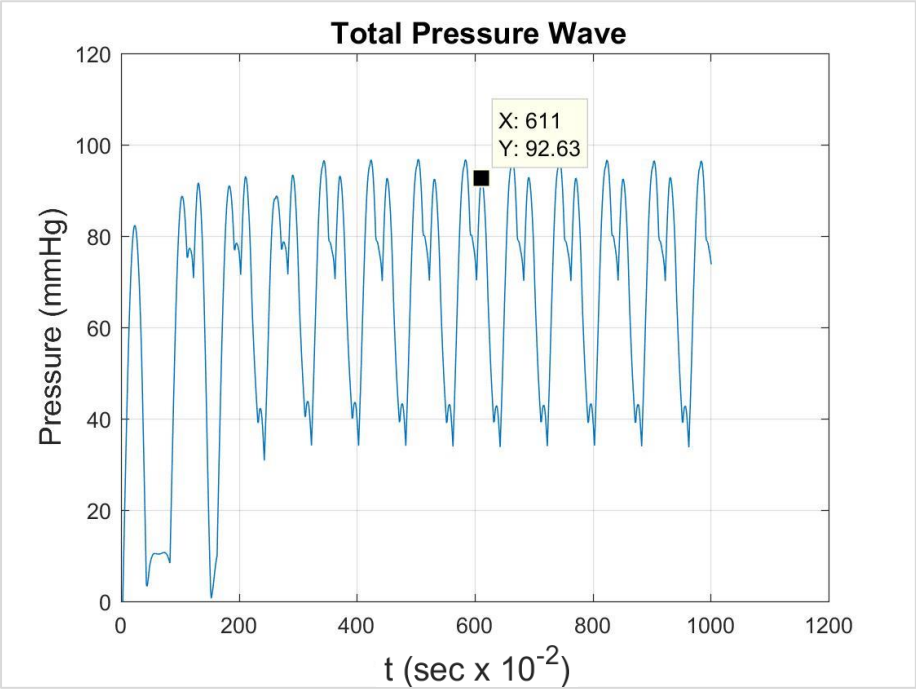

Figure 4.23: Total pressure waveform simulated for 10 seconds with balloon cuff augmentation.

The timing and location of the balloon cuff and the amount of aortic radius augmentation produced by the balloon cuff was explored to see the effects of the total pressure wave. Altering the time between each balloon inflation (from 0.05 seconds delay between the inflation of each balloon to a 0.10 seconds delay) produced the results shown in Figure 4.24. Examining the two waves on the same figure closely shows a small increase in both peak systolic pressure (Δ1 mmHg) and the end-diastolic pressure (Δ1 mmHg).

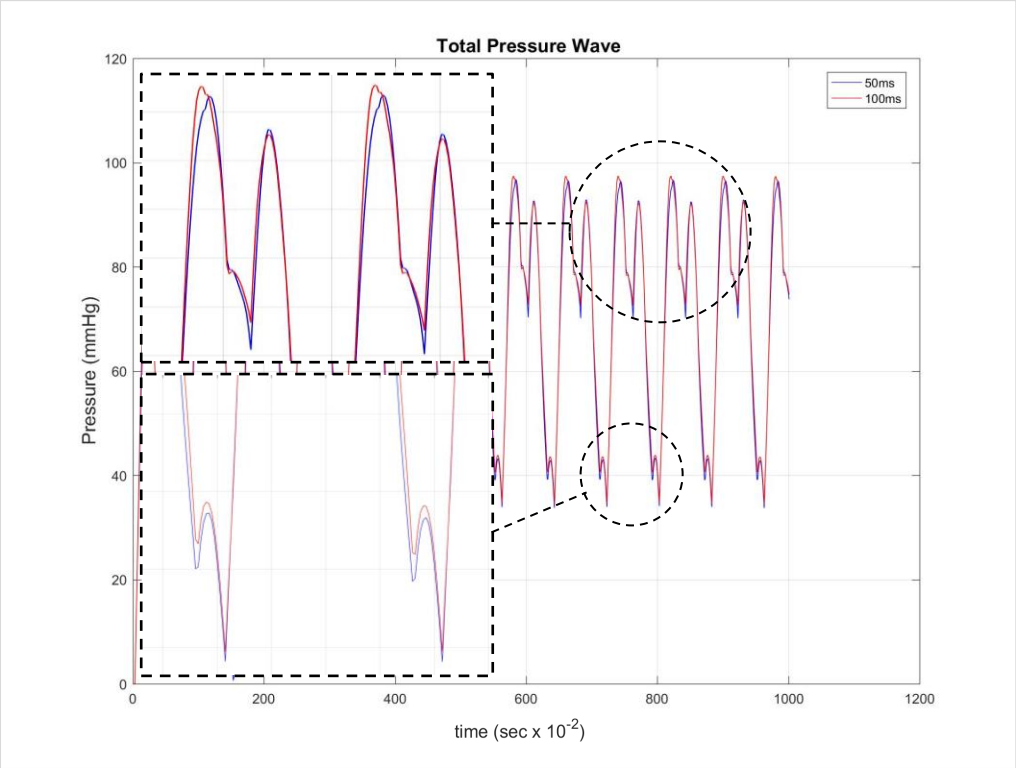

Figure 4.24:The effects on the total pressure waveform of altering the time between each balloon inflation waveform 0.05 seconds to 0.10 seconds.

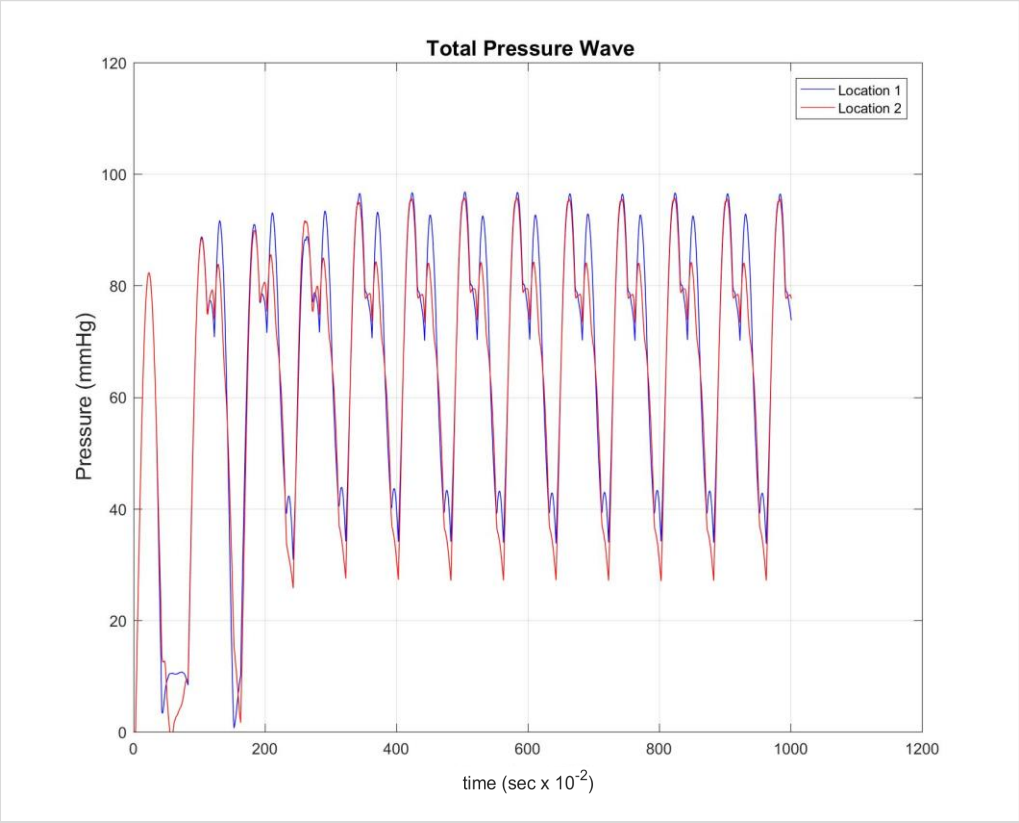

Figure 4.25: The effects on the total pressure waveform by changing the balloon cuff location.

Shifting the balloon cuff down the aorta by 85 mm (location 2) dramatically decreases the dicrotic notch pressure (see Figure 4.25). With the decrease in the dicrotic notch, the end-diastolic pressure also decreased by 6.79 mmHg (33.92 mmHg at location 1; 27.13 mmHg at location 2).

An increase and reduction of the indentation of the aorta of 1mm were simulated using the standard inflation and the location of the balloon cuff (location 1). Figure 4.26 shows that increasing the balloon inflation profile directly increases the dicrotic notch pressure by 1.52 mmHg and decreasing the balloon inflation profile directly decreases the dicrotic notch pressure by 1.78 mmHg.

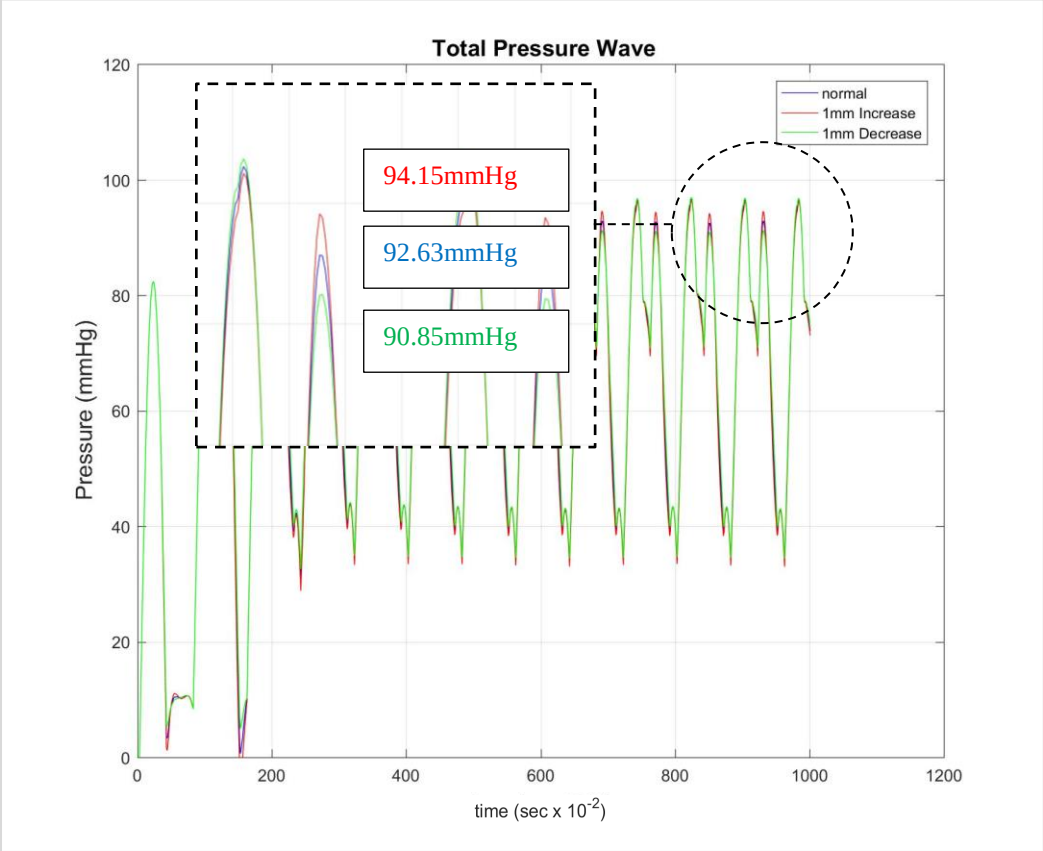

Figure 4.26: The effects on the total pressure waveform by increasing the amplitude profile of the balloon cuff.

The pulse wave simulation was adapted using parameters from the cardiovascular simulation platform that included the following alterations:

- Aortic radius tapering profile (larger tapering gradient)
- Length of the aorta (increased from 550 mm to 700 mm)
- The duration of the cardiac cycle (from 0.8 seconds to 2 seconds)

The parameters listed above dramatically change the shape of the pressure waveform without balloon augmentation (see Figure 4.27). This was done for the purpose of comparing the results from the numerical simulation with the results obtained from the cardiovascular simulation platform experiment – later presented and discussed in Chapter 6 and Chapter 7. Furthermore, cuff augmentation also produces dramatic changes in overall wave shape as can be seen in Figure 4.27.

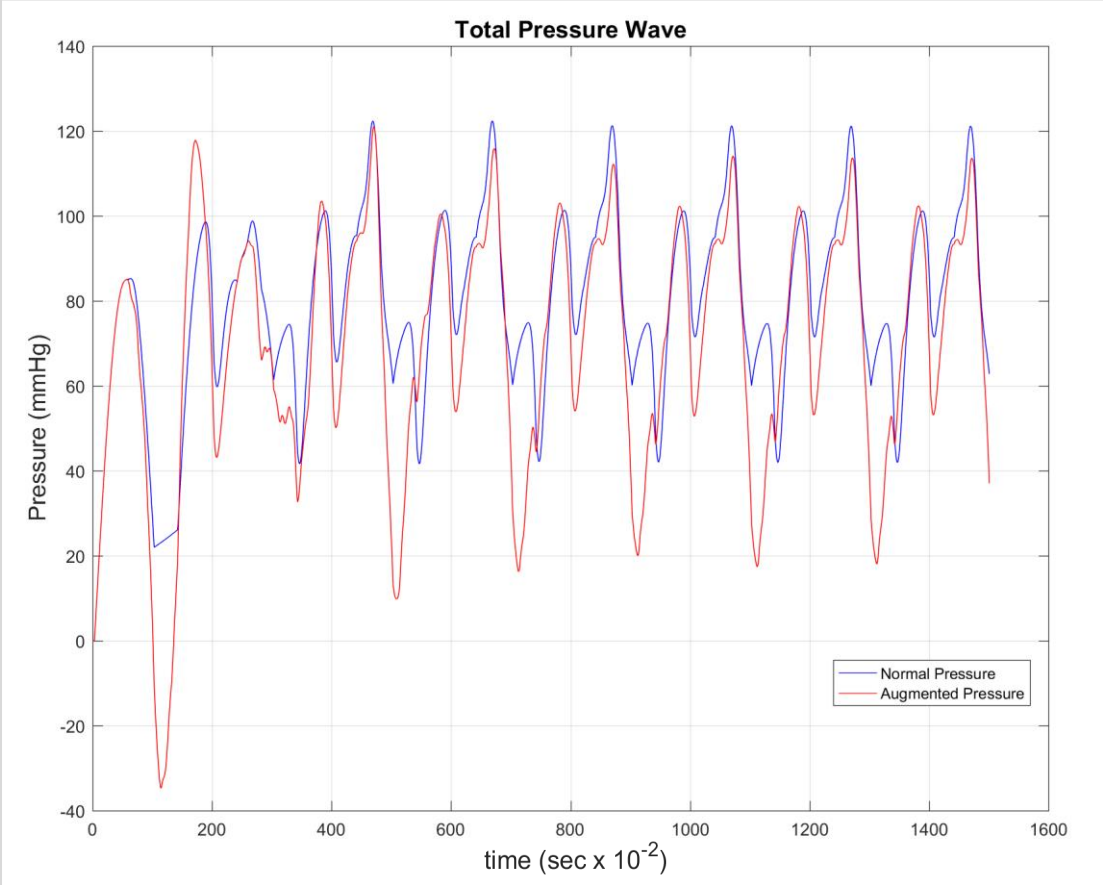

Figure 4.27: Comparison between normal (no augmentation) and augmented (peristaltic) total pressure waveform with a cardiac cycle of 2 seconds simulated for 15 seconds.

Table 10: Key pressure readings of normal and augmented conditions obtained from the pulse wave simulation shown in Figure 4.27.

Total Pressure	Normal Pressure	Augmented Pressure
Peak Pressure	121.2 mmHg	114 mmHg
End Diastolic Pressure	42.1 mmHg	48.8 mmHg

Non-peristaltic augmentation was also compared with peristaltic augmentation. As shown in Figure 4.28 the characteristic differences on the pressure waveform are minimal.

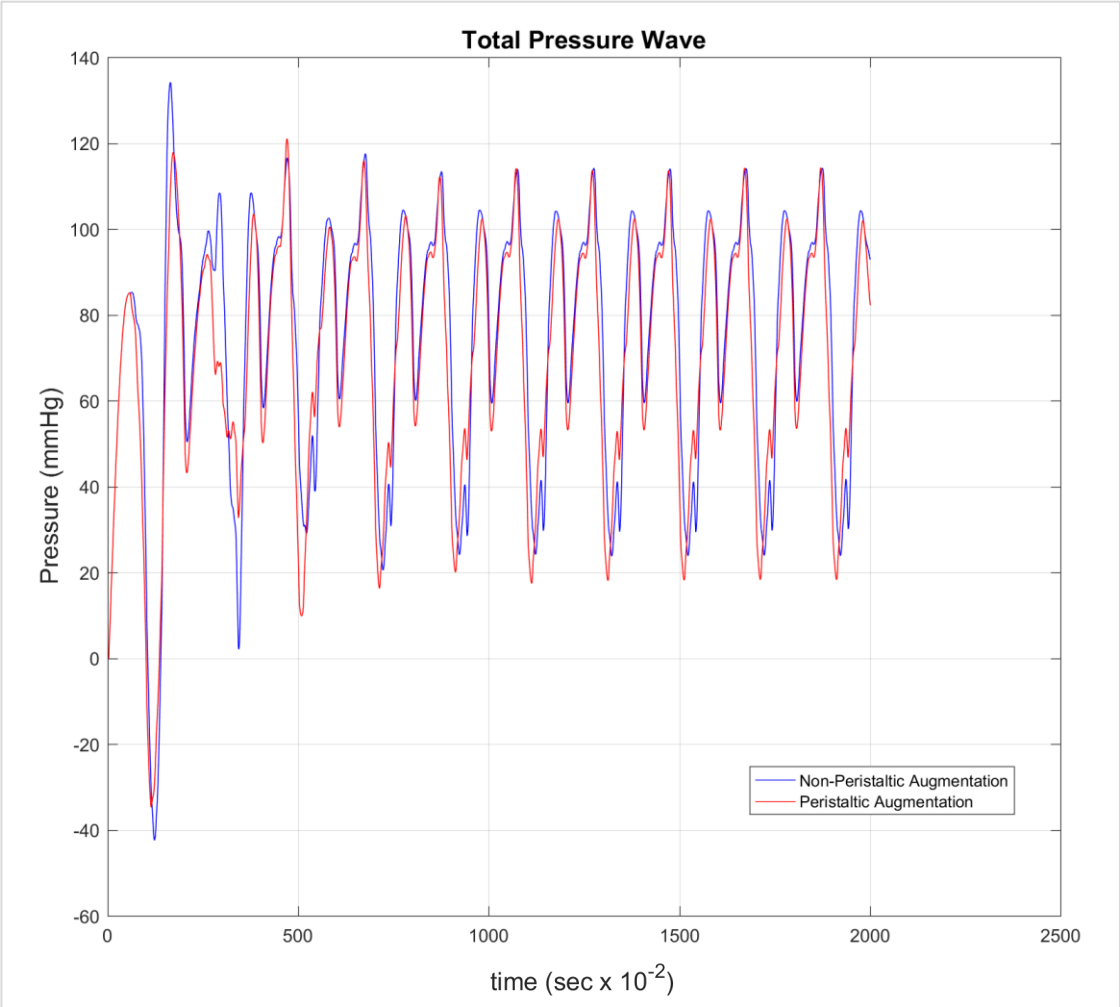

Figure 4.28: Comparison between non-peristaltic and peristaltic augmentation of the total pressure waveform with 2 seconds for the cardiac cycle.

4.4 Discussion

The pulse wave simulation created for this research was used to understand how a peristaltic augmentation can change the pressure waveform profile. The use of a modified Moens Korteweg's equation for calculating the PWV was adapted to simulate a speed at which the 1-D wave travels along the aorta. The PWV that was calculated using Moens Korteweg's equation were in the physiological PWV range that was obtained by London and Pannier [68]. The small increase of the PWV along the narrowing aorta also agrees with Moens Korteweg's equation – a narrowing aortic radius results in an increase in PWV. This meant that the PWV started at 6.25 m/s at the start of the aorta and increased to 7.63 m/s at the end. In relation to computational results by Fukui et al., their computational simulation PWV result – obtained over a length of 1 meter – conclude that the PWV values were not constant but varied around 10% when compared to Moens Korteweg's calculation. Their PWV computation was, however, based on a uniform radius boundary condition and did not have a tapering radius boundary condition which may explain the differences in PWV results. In comparison to physiological studies [71-72], the variance in patient's PWV is affected by the individual geometry of the aorta that associates to the gender and age of the patient, and the dissimilar methodologies that were performed to measure the PWV. However, the PWV values found for this research's simulation are somewhat similar to the mentioned studies.

The pulse wave that was created from simulation shared some features with real waveforms obtained experimentally. These include the pressure augmentation as a result of an incident wave propagating through the aorta and hitting a terminating point, which is agreed with Watanabe et al. [97].

Table 11: Arterial pressure comparison between physiological and pulse wave simulation data.

Aortic Pressure	Systolic Pressure	Diastolic Pressure	Mean Arterial Pressure
Physiological Data	<120 mmHg	<80 mmHg	<93 mmHg
Simulation Data	~92.63 mmHg	~35.51 mmHg	~55 mmHg

The aortic pressures from the simulation are noted to be on the low side compared to physiological data [63], [66] (see Table 11). This could be the result of the amplitude of the incident wave (which was 80 mmHg) – whereas actual left ventricular pressures

follow the aortic systolic pressure, and also the cardiac cycle time. The range of physiological pressures, in any case, is very wide.

In terms of the characteristic shape of the pressure waveform, the implementation of the opening and closing of the aortic valve boundary condition introduces a dicrotic notch which corresponds to physiological waveforms. With the aortic valve factor that was experimented with, the timing of the opening and closing was concluded to be a crucial part of simulating the pressure waveform as it can affect the reflected pressure waveform and thus change the total pressure waveform.

When it comes to augmenting the pressure waveform with an external peristaltic movement, the parameters that were chosen for the simulation had small effects on augmenting the total pressure waveform. This small augmentation that was based on realistic parameters – balloon size, augmentation profile (aortic wall indentation) and balloon's inflation/deflation timing – may have contributed to the limitation of pressure augmentation.

With the alterations to the pulse wave simulation's cardiac cycle from 0.8 seconds to 2 seconds, the normal total pressure waveform significantly changed and larger diastolic augmentation to the total pressure waveform was found. The other test condition – non-peristaltic and peristaltic augmentation – resulted in similar waveform profiles although some differences were observed. One of the key differences was that the diastolic pressure is higher due to non-peristaltic augmentation when compared to peristaltic augmentation. These simulation results are supported by experimentation involving the operations of the PEABC prototype tested with the same conditions.

The idea of applying an external peristalsis to augment pressure waveforms is a novel study, and cannot be validated fully against literature. Further validations of the pulse wave simulation against experimentation data from the PEABC prototype is given in Chapter 7.

Chapter 5

Peristaltic Extra-Aortic Balloon Cuff Prototype

5.1 Introduction

In this chapter, the development of a Peristaltic Extra-Aortic Cuff device or PEABC device is described. The PEABC device is designed to change the pressure and flow waveform in the aorta during the cardiac cycle by externally compressing the aorta. The PEABC system is similar to that of the C-Pulse® system by Sunshine Heart [38] however it is not designed to be ready for clinical trials, but instead to investigate the concept of the device.

5.2 Methodology

5.2.1 System Operation Design

The device is made up of three major hardware components: peristaltic balloon cuff, pneumatic cuff driver and the controller. The development of all components was performed concurrently with the design of each was dependent on the other. For instance, the peristaltic balloon cuff inflation volume was dependent on the volume output by the pneumatic cuff driver, and the control procedure needed to inflate the peristaltic balloon cuff via the cuff driver was based on software and hardware features (see Figure 5.1).

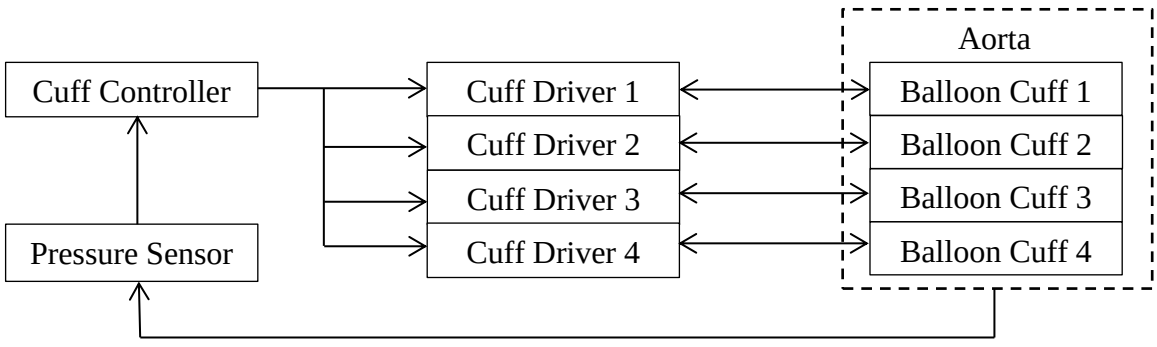

Figure 5.1: System Operation Diagram

5.2.2 Peristatic Balloon Cuff

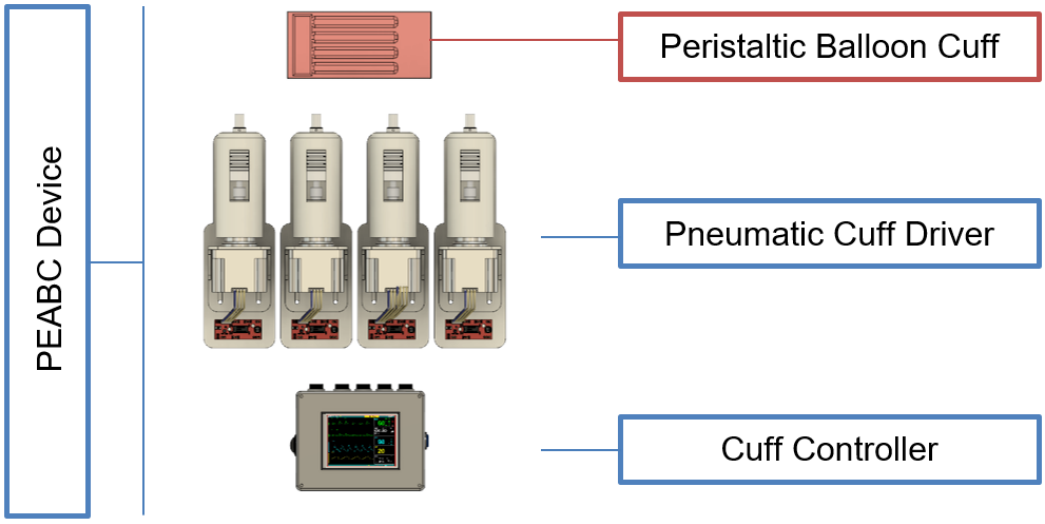

Figure 5.2: Peristaltic balloon cuff component.

The peristaltic balloon cuff contains no electronics (see Figure 5.2). It is attached to the descending aorta and consists of four separate air chambers that are inflated and deflated by the pneumatic cuff driver via an air hose. The composition of the balloon cuff is made up of two layers with the outer layer made from textile and the inner made from silicone rubber that fits both phantom aorta 1 and 2. The peristaltic balloon cuff when in operation, produces 4 independent radial-aortic wall indentations with or without peristaltic wave motion similar to the wave motion simulated on the pulse wave software.

5.2.2.1 Design Overview

Using the 3D CAD model of the phantom aorta 1 as a template, the balloon cuff was also designed and implemented on CAD. The overall size of the peristaltic balloon cuff was based on the size of the outer layer which wrapped around the phantom aorta with a small overlap. Firmly wrapping the peristaltic balloon cuff around the phantom aorta provides constriction of the peristaltic balloon cuff inflation and consequently can deliver more aortic wall indentation (see Figure 5.3).

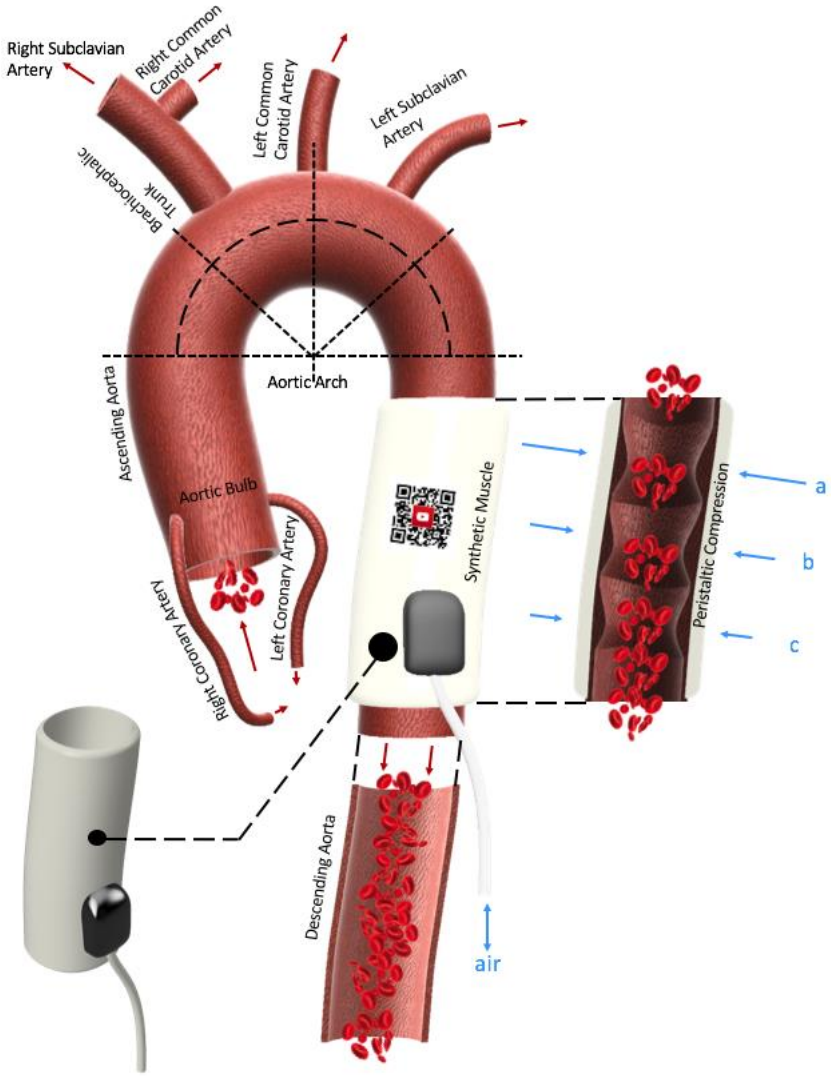

Figure 5.3: 3D CAD model of the peristaltic balloon cuff wrapped around the descending aorta phantom 1.

The balloon cuff was designed in two layers such that the outer layer restricts the outward expansion of the silicone bladder. This constrains the air chambers to inflate inwards and thus generates more aortic wall indentation.

The material that was chosen for the outer layer is Pemotex fabric, which when knitted using the interlocking method produces a piece of fabric sheet with minimal stretchability but good flexibility.

The inner layer material is made from Rebound® 25 – the same material used for phantom aorta 1. This silicone rubber layer is manufactured with 4 air chambers with air hoses connected to each of them to allow air flow in and out of the chamber. Furthermore, the silicone rubber is manufactured to have the side that is in contact to the phantom aorta much thinner than the side that is fused with the Pemotex fabric (Figure 5.4) to better indent the aorta when inflate.

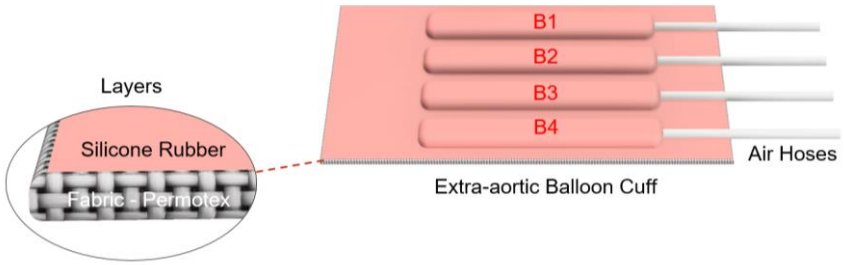

Figure 5.4: Peristaltic balloon cuff layers.

Figure 5.5 illustrates the cuff concept with a single-bladder cuff attached to a 30 ml syringe in place around a mock descending aorta.

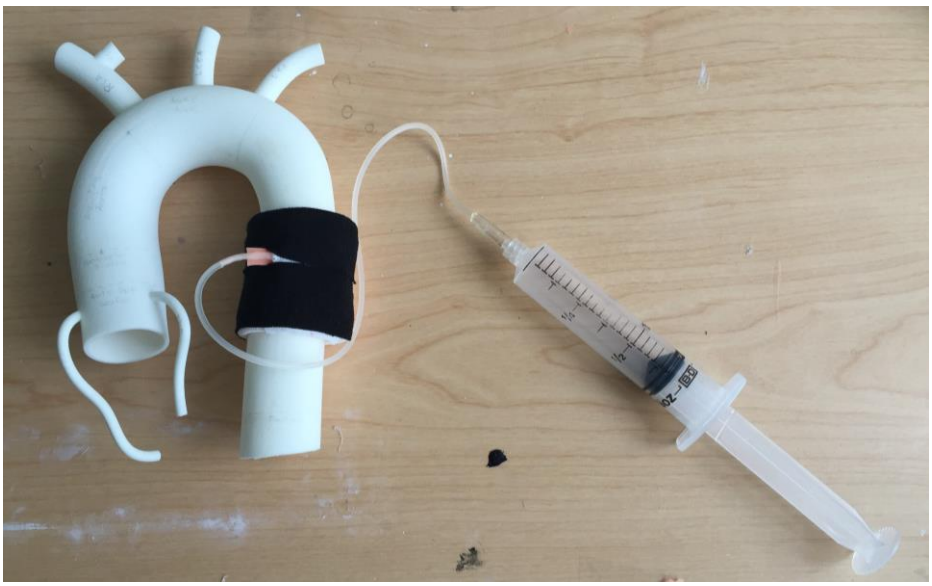

Figure 5.5: First prototype; syringe used to inflate and deflate a single balloon made from silicone rubber and fabric.

5.2.2.2 Manufacturing Process

A single 105 mm x 22 mm x 2.5 mm balloon cuff prototype was manufactured and tested. When wrapped and restrained with zip ties around the 3D printed descending aorta and then inflated using a syringe, the cuff expanded outwards significantly. Its profile expanded in height to 10 mm which equates to 7.5 mm of inflation height profile (see Figure 5.6 and Figure 5.7). This is considered a "worst case" scenario as the 3D printed aorta had a solid aortic wall and was not flexible, corresponding to an aortic wall with high stiffness.

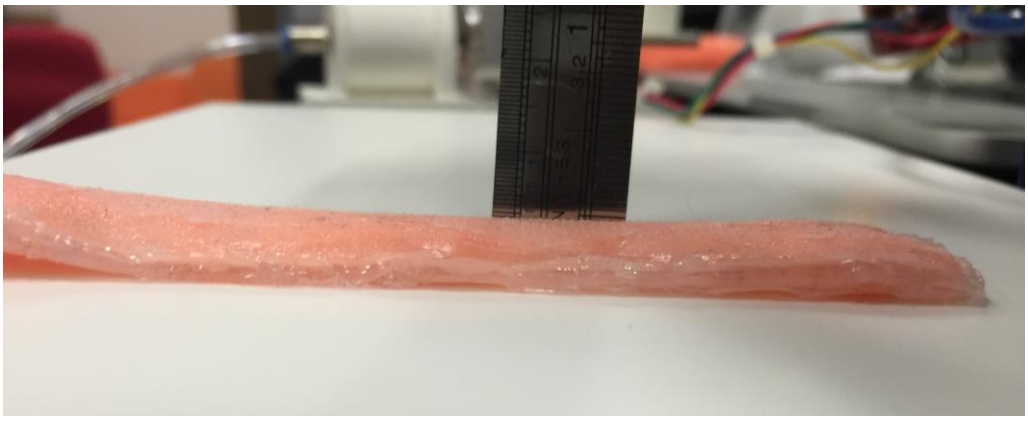

Figure 5.6: Deflated singular balloon prototype.

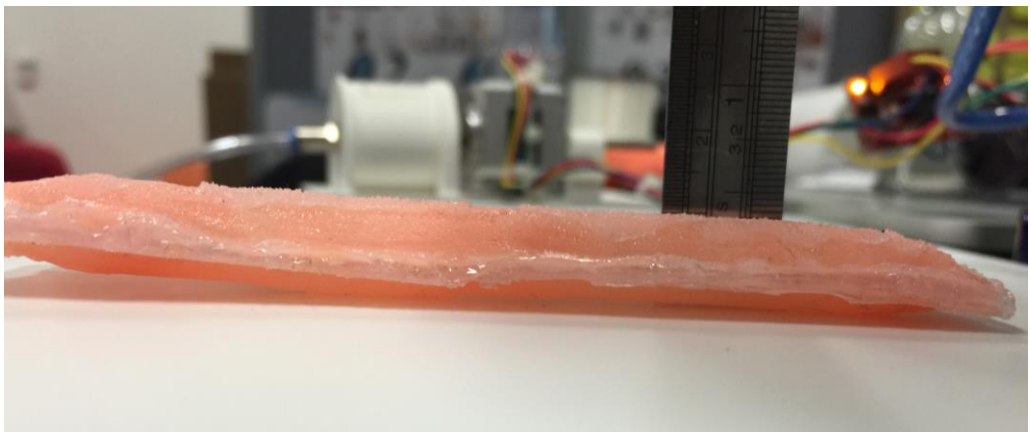

Figure 5.7: Inflated singular balloon prototype.

A textile layer was added in an attempt to restrain the outward inflation profile but as observed in Figure 5.8, when using a stretchable fabric, did not restrict the outward inflation profile. In contrast, a Velcro strap around the cuff was effective as most of the inflation profile was observably greater towards the inner side of the balloon (see Figure 5.9).

Figure 5.8: The result of the outer layer which resulted in an outward inflated profile when a stretchable fabric was used.

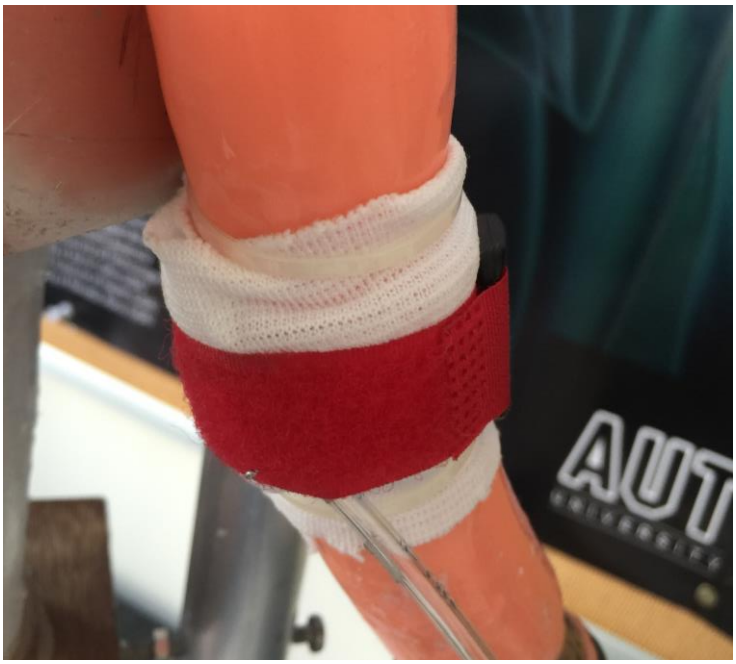

Figure 5.9: The use of a Velcro strap restricted the outward inflation profile.

The silicone rubber balloon layer of the cuff was manufactured first, followed by fabrication of the Pemotex layer. The first task was to mould two rectangular 150 mm x 100 mm sheets of Rebound® 25 silicone rubber. The same mixing ratio used for making the aorta phantom 1 (1A:1B) was used for both sheets. The peristaltic balloon cuff layers were formed on a rotating mould template as shown in Figure 5.10. The cylindrical form minimises the creasing of the balloon when inflated around the phantom aorta 1. Rotating the mould at approximately 50 RPM was found to ensure even distribution and thickness during curing and eliminates dripping.

Figure 5.10: Template/setup for the moulding of the peristaltic balloon cuff.

The first layer of the application was the thinner layer. As shown in Figure 5.11, a small amount of Rebound® 25 was applied to the rotating mould plate to just cover the template.

Figure 5.11: Moulding of the first layer of the balloon cuff on a rotating drill.

This mould was left to cure for 2 hours and preparation was performed for the second application. Four air chambers that make up the peristaltic balloon cuff were formed using 110 mm x 12 mm x 1 mm strips made from duct tape to separate the first layer from the second (see Figure 5.12). These separator strips were positioned evenly across the surface area of the first layer.

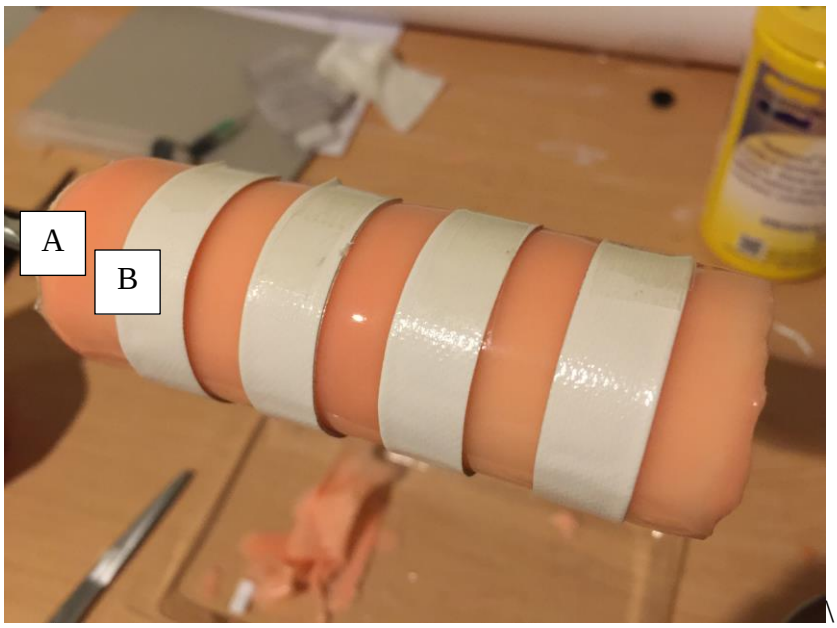

Figure 5.12: Separator strips applied onto the first silicone layer. (A): Silicone mould. (B): Duct tape separator strips.

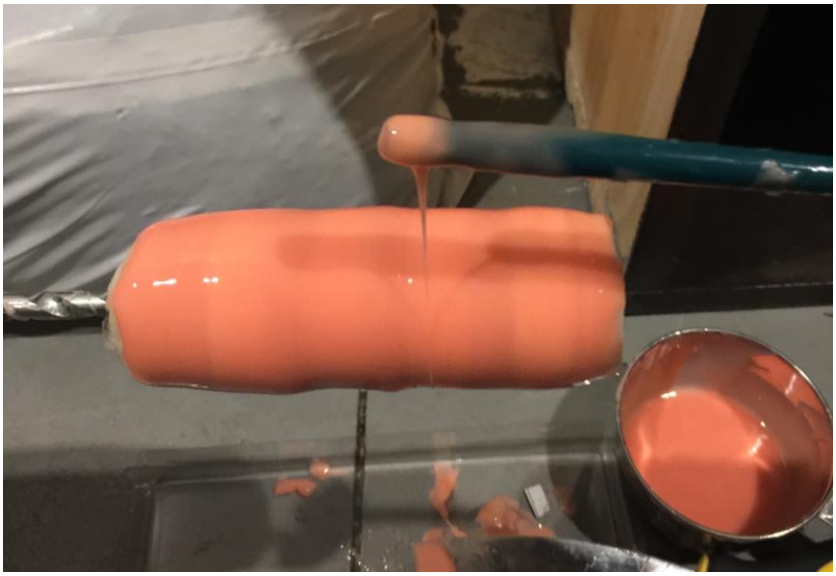

Figure 5.13: Application of the second layer of silicone.

The thicker outer layer was then applied on top of the first layer and the separator strips, with the mould template rotating at approximately 55 RPM and left to cure for another 2 hours. The mould was then separated from the moulding template by straight line incision across the mould from one end to the other.

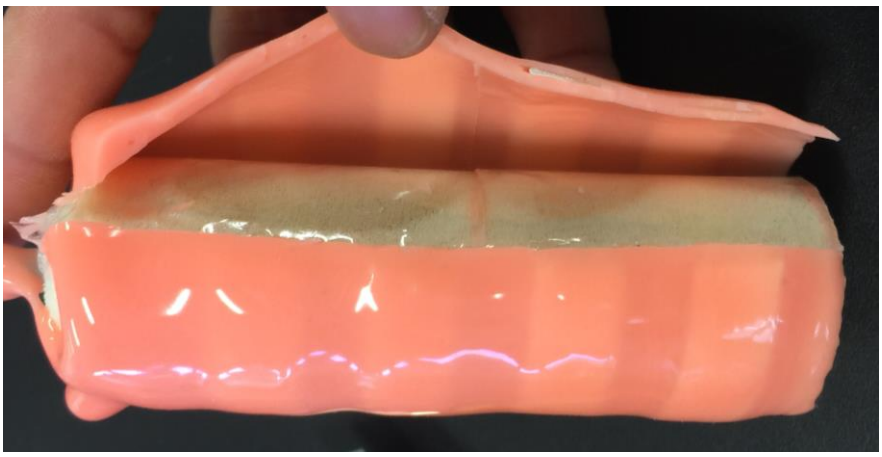

Figure 5.14: Removal of the cured peristaltic balloon cuff from the moulding template.

The separator strips were then removed from the mould and the four IV extension air hoses (84 cm long with 1 ml tube volume and Luer – Lock fittings) were inserted into each of the air chambers. The ends were then air tight sealed with marine silicone and left to cure for 24 hours.

Checks were performed to ensure that no air could leak out during inflation of the balloon cuff. Any air leaks that was present were patched with marine silicon. The final step in making the balloon cuff was to fabricate the Pemotex layer and attach it to the Rebound® 25 layer. The Pemotex layer was fabricated by AUT Textile and Design department. A simple template with specific design aspects – design footprint and material type – was provided to them for manufacturing.

Figure 5.15: Pemotex kitted with interlocking technique.

The template was simply a 150 mm by 100 mm paper sheet that was utilised as a footprint for the knitting software used to integrate the knitting process instructions on the knitting machine. In order for the Pemotex yarn to provide minimal stretchability when knitted and have ridged fabric properties, the interlocking knitting technique was used. The knitted Pemotex layer was then attached to the Rebound® 25 by the centre to centre alignment using some adhesives applied to both layers. Since the Rebound® 25 was moulded with a cylindrical mould template, the layer itself naturally curves when the material is in an unstressed state. Thus, the two layers were joined while wrapped around the moulding template. The adhesive took approximately 5 to 10 min to cure after which it was taken off the mould template and testing was performed to check for air leaks and functionality (see Figure 5.16 and Figure 5.17).

Figure 5.16: Pemotex fabric layer being fused with the silicone layer on the cylindrical mould template.

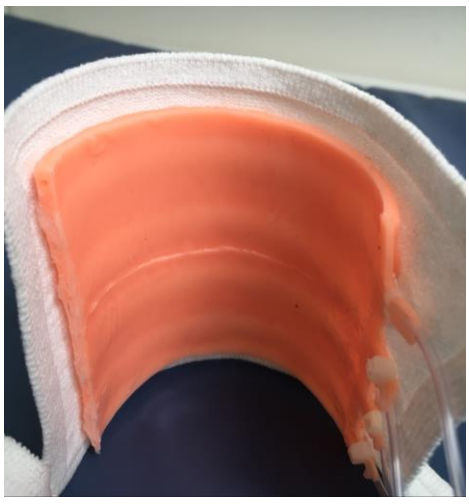

Figure 5.17: Peristaltic balloon cuff, once removed from the cylindrical mould template.

With the successful fabrication of the singular balloon cuff, Pemotex fabric was used as an outer layer to aid the effectiveness of the four-chamber peristaltic balloon cuff (see Figure 5.18).

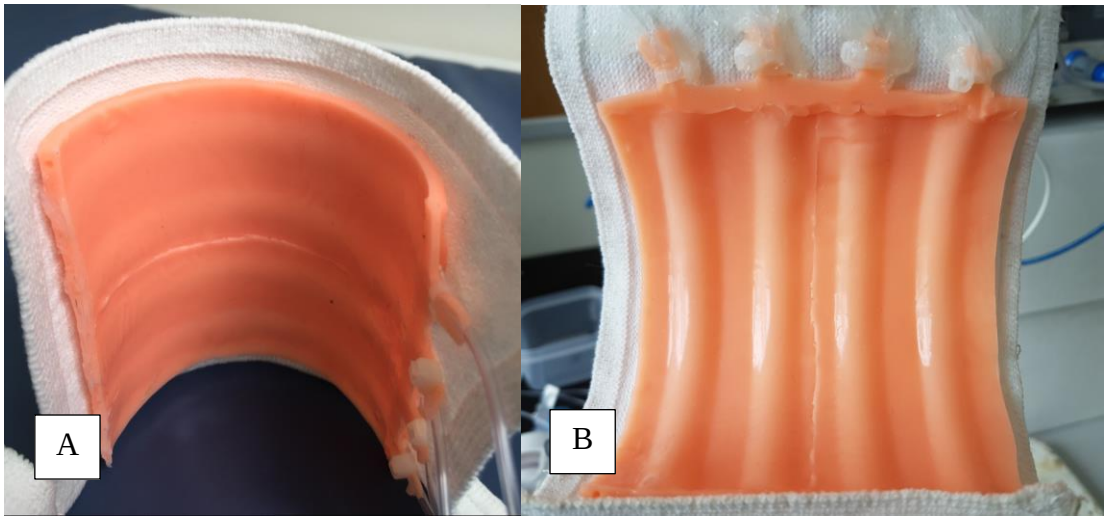

Figure 5.18: (A): Deflated peristaltic balloon cuff fabricated. (B): Inflated peristaltic balloon cuff fabricated.

Moulding the silicone rubber layers on a cylinder template and fabricating the Pemotex layer to the silicone rubber layer on a curved surface allowed the peristaltic balloon cuff to have minimal creasing when wrapped around the aorta when inflated (see Figure 5.19).

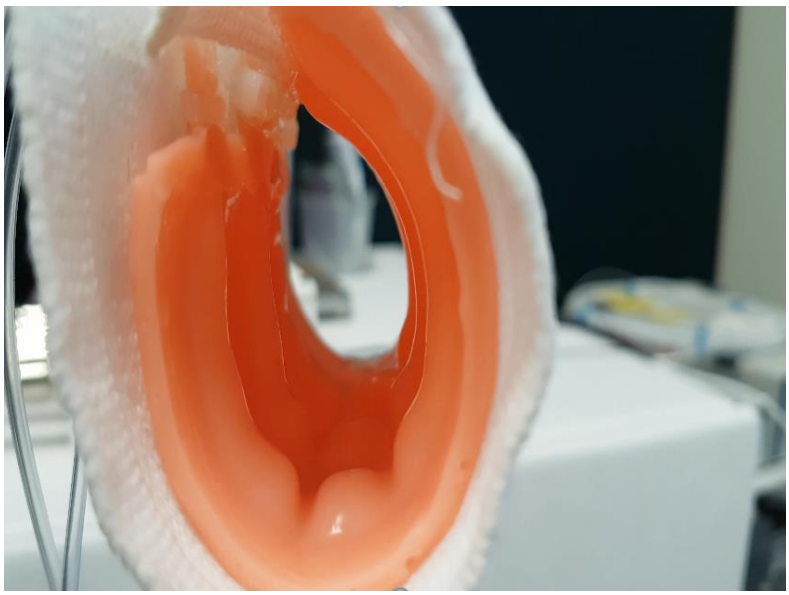

Figure 5.19: Peristaltic balloon cuff inflated with minimal creasing when in a wrapped formation.

5.2.3 Pneumatic Cuff Driver

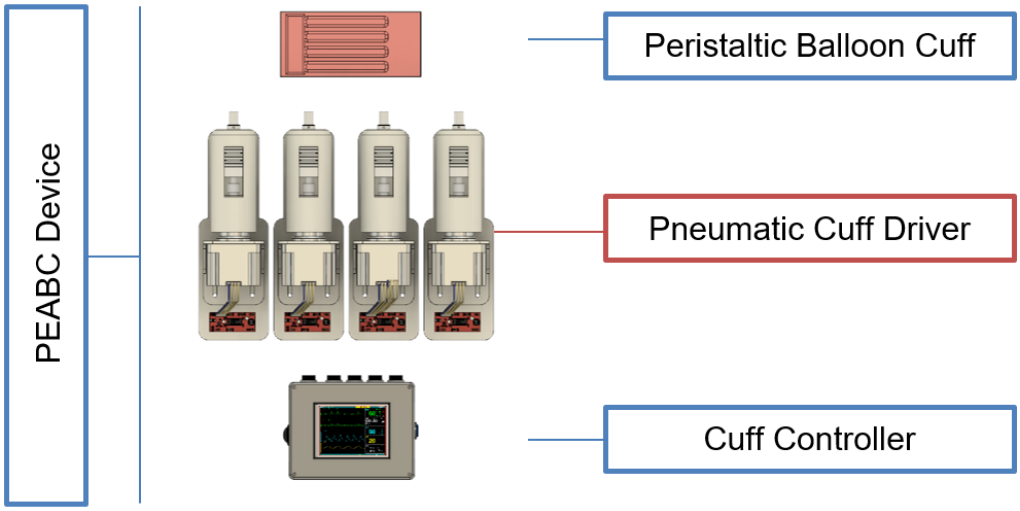

Figure 5.20: Pneumatic cuff driver component.

The pneumatic cuff driver component shown in Figure 5.20 physically inflates and deflates the peristaltic balloon cuff. To drive the four air chambers separately, four units are controlled individually to drive air in and draw out air when attached to the peristaltic balloon cuff via the air hose.

5.2.3.1 Design Overview

The inflation and deflation of each air chamber are driven by a stepper motor linear actuator that compresses and decompress a bellows which recycles air in and out of the air chambers.

5.2.3.2 Linear Actuator

The linear actuator is a Haydon & Kerk 57000 series size 23 captive stepper motor that has a stroke length of 38.1 mm with the linear travel of 0.0508 mm/step. The linear actuator is operated via a bipolar 4 wire system connected to the motor driver. This linear actuator was selected as it was suited to fully compress the air bellows (described in section 5.2.3.4) and perform adequate inflation and deflation timing sequence base on a

typical cardiac cycle (0.8 seconds to 1 seconds). The required performance (20 N force based on the required velocity with a safety factor of 3, and balloon cuff under the aortic pressure of 120 mmHg) is illustrated with a blue dot on Figure 5.21.

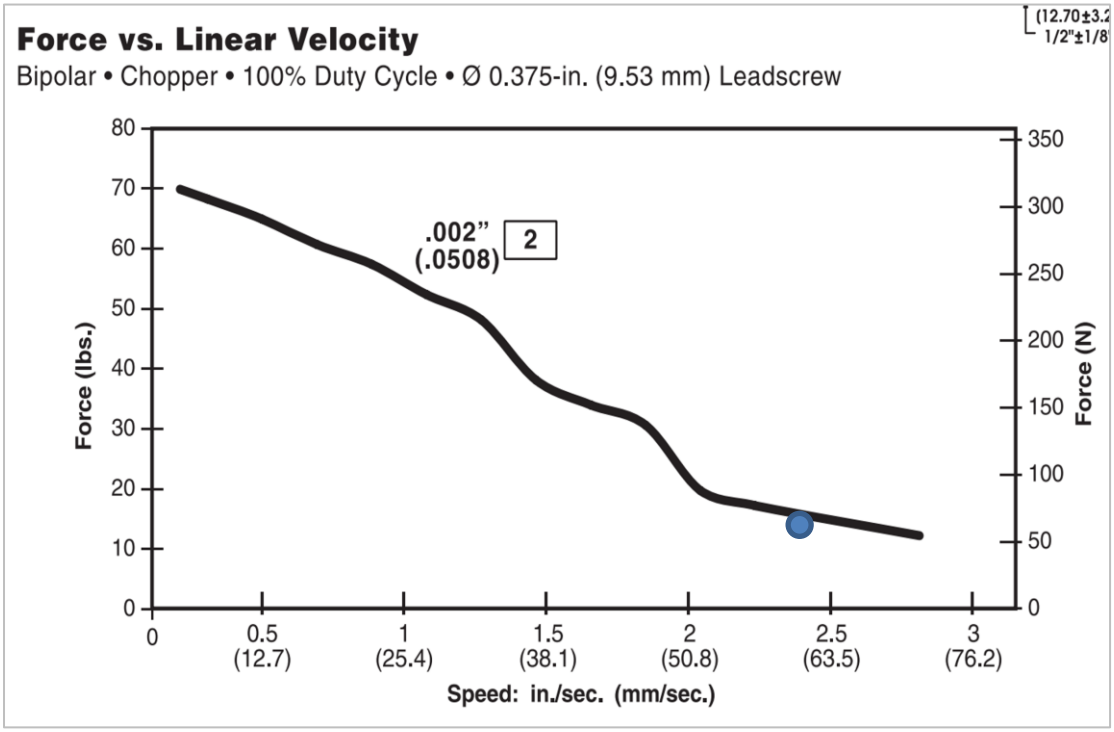

Figure 5.21: Stepper motor's force vs. linear velocity profile.

Table 12: List of constraints and parameters used for sizing the correct stepper motor.

Constraints and Parameters	Value	Units
Bellows Diameter	40	mm
Bellows Area	1256.64	mm^2
Required Displaced Volume	10000	mm^3
Required Stroke	7.95775	mm
Pressure (mmHg)	120	mmHg
Pressure (Pa)	15960	Pa
Force	20.0559	N
Velocity factor of safety	3	Units
Velocity	59.6831	mm/s
Power	1.197	W
Step size	0.0508	mm/step
Required step rate	1174.86	steps/second

5.2.3.3 Motor Driver

The motor driver is an electronic circuit that is used to take power and control signal from the cuff controller to produce the necessary signal to drive the linear actuator. This motor driver shown in Figure 5.22 is called the Big Easy Driver (BED) which uses an Allegro A4988 driver chip to step the 2A bipolar stepper motor linear actuator.

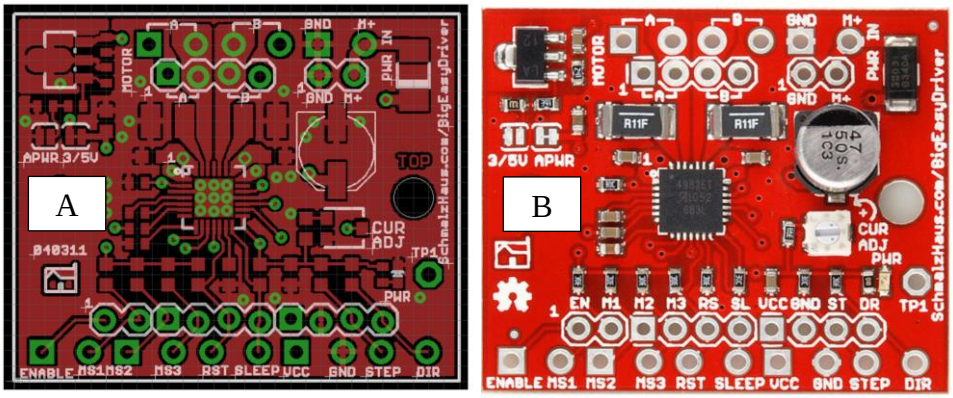

Figure 5.22: (A): Schematic of the BED. (B): Physical PCB of the BED.

The BED is connected to 4 wires of the linear actuator labelled A+, A-, B+ and B-. The stepper motor uses a bipolar 4 wire system shown in Figure 5.23. The bipolar system uses built-in H-bridge circuit to reverse the current flow through phases such that when the phases are energised with alternating polarity, the internal 2 groups of coils turn the motor.

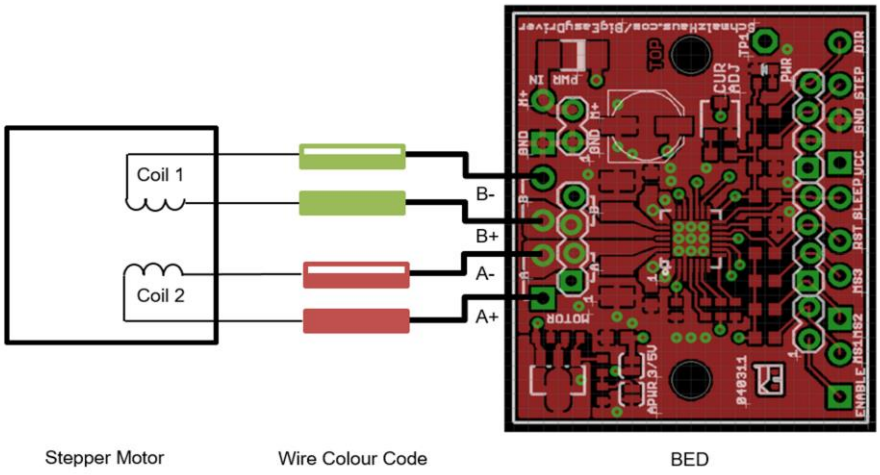

Figure 5.23: Wiring of the stepper motor to the BED.

Other connections to the BED were power (M+), ground (GND), microstep settings (MS1, MS2, and MS3), direction input (DIR) and step input (STEP). All of these pins were connected to the cuff controller powered by Arduino Mega 2560. The M+/GND pin draws 12 VDC from the Arduino Mega 2560 which was used to power both the BED and the stepper motor. The DIR pin is used to control the direction of the step instructed by the software in Arduino. When the DIR pin is set high, the stepper motor will step in a counter-clockwise rotation, and when set low, the stepper motor will step in a clockwise rotation. A rising edge of the STEP signal sent from the Arduino results in one step (linear moment of 0.0508 mm). Moreover, the rising and falling STEP signal must be high and low for 1μs respectively, for proper functionality. The pins MS1, MS2, and MS3 are used for microstepping the stepper motor which can be configured using Table 13. The microstepping configuration setting that was chosen for the stepper motor is also highlighted in Table 13. Pins were directly pulled down to ground with a wire and not via software instructions from the Arduino. All of the other pins were not necessary for connection and were left unused.

Table 13: Microstepping function set on the BED MS1, MS2, and MS3 Pins.

MS1	MS2	MS3	Microstep Resolution	Excitation Mode
Low	Low	Low	Full Step	2 Phase
High	Low	Low	Half Step	1-2 Phase
Low	High	Low	Quarter Step	W 1-2 Phase
High	High	Low	Either Step	2W 1-2 Phase
High	High	High	Sixteenth Step	4W 1-2 Phase

5.2.3.4 Air Bellows

The air bellows obtained from Festo is a mechanical element of the pneumatic cuff driver that accommodates most of the air volume displacement. It is fundamentally a 40 mm silicone suction cup bellows with 3.5 convolutions (see Figure 5.24). The end of the suction cup was sealed off to create the air cavity. The compression and decompression of the air bellows were actuated by the connected linear actuator. The air bellows were selected to displace the required volume of air given the linear travel of the actuator (see Table 14).

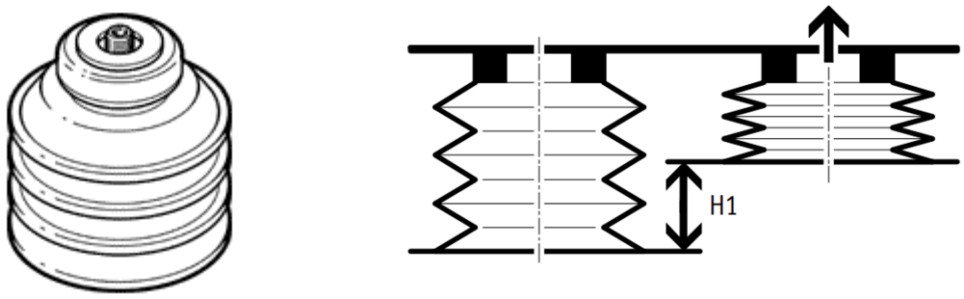

Figure 5.24: Festo's 3.5 convolutions suction cup used as air bellows.

Table 14: Specifications for the air bellows.

Parameters	Value	Units
Bellow Volume (total)	19720	mm^3
Bellow Volume (compensation)	8144.36	mm^3
Bellow Volume (compressible)	17176.12	mm^3
Height compensation (H1)	12.8	mm
Compressible Length	27	mm
Compensation factor	41.3	%
Compressible factor	87.1	%
Height of Bellow	31	mm
Required Volume for inflation	6000-12600	mm^3

The bellows were constructed from suction cups. The ends of all four bellows were sealed off with silicone rubber. Rebound 25® was poured into a small round moulding dish that

had a diameter of 71 mm to a thickness of 3 mm up from the bottom of the dish, with the suction cup placed in the moulding dish (see Figure 5.25). The mould was then left to cure for 2 hours. After the mould was cured, the suction cup was then removed and excess silicone was cut off by the lips of the suction up.

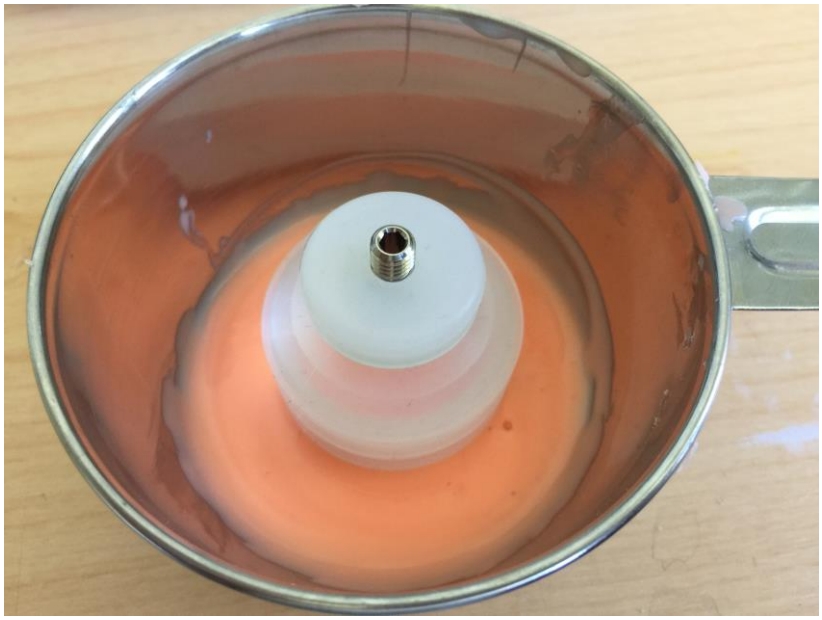

Figure 5.25: Suction cup placed in 3mm of Rebound 25 to seal off the ends.

5.2.3.5 Frame

The frame of the pneumatic cuff driver fixes the linear actuator, motor driver, and air bellows together. The frame itself was custom designed to suit the dimensions of the other hardware elements and 3D printed (see Figure 5.26).

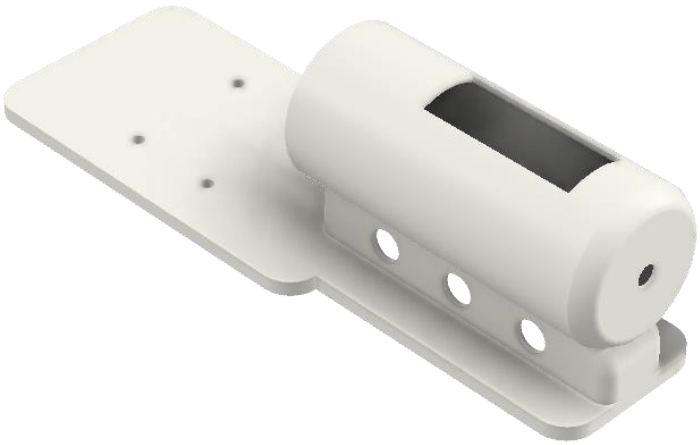

Figure 5.26: 3D CAD model of the frame used to mount all of the components for the pneumatic cuff driver.

The cylindrical section of the frame shown in Figure 5.27 constrained the air bellows to behave more linearly during actuations. A rectangular cut-out on the top of the frame was also put in place for the purpose of observation during experimentation.

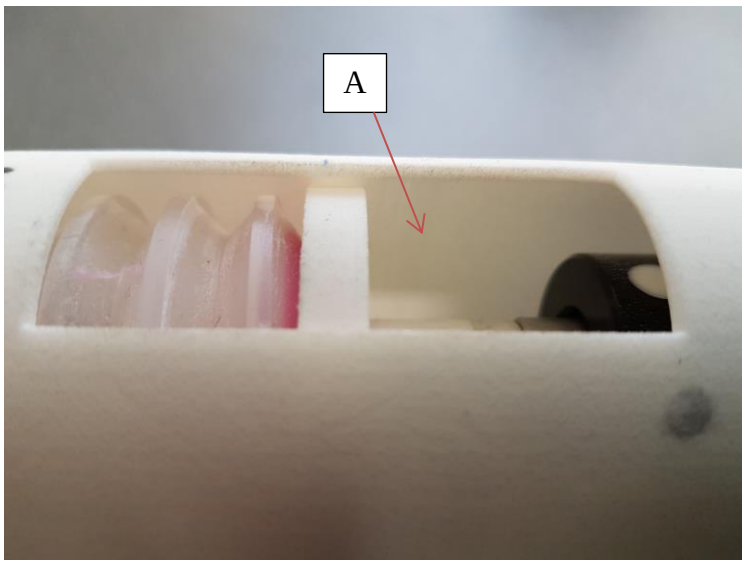

Figure 5.27: Assembled pneumatic cuff driver. (A) Cylindrical opening.

5.2.3.6 Fixation Parts

The fixation part that was required to allow a secure air-tight connection between the air bellows, the frame and the air hose from the peristaltic balloon cuff, is a custom made 3D printed female M6 x 1 fitting that was joined with a male luer lock head to make connections between the male M6 x 1 of the air bellows and the female luer lock ends of the air hose (see Figure 5.28).

Figure 5.28: 3D CAD Model of the M6x1 fitting for connecting to a male luer lock fitting.

Another fixation part was required for attaching the air bellows to the linear actuator. This fixation part was essentially a coupling similar to the one used for the cardiovascular simulation platform that provided a good link during constant linear actuator movement. This coupling was designed to seal off the end lips of the air bellows and have an M6 x 1 female thread to screw into the male threaded shaft of the linear actuator (see Figure 5.29).

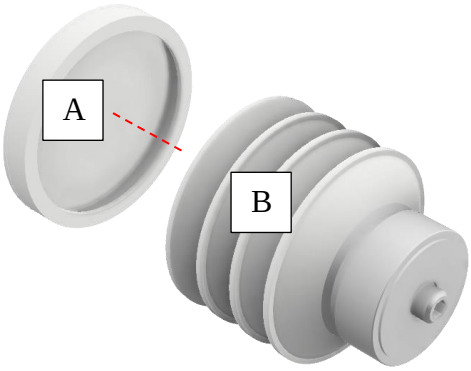

Figure 5.29: Coupling used to connect the linear actuator and air bellows. (A) Coupling. (B) Air bellows).

A NEMA 23 L bracket mount was used to secure the linear actuator to the frame (see Figure 5.30). It was made from coated steel and attached to both the linear actuator and frame via 8 stainless steel nuts and bolts.

Figure 5.30: NEMA 23 L bracket used for mounting the motor to the 3D printed frame.

An assembly drawing of the pneumatic cuff driver is shown in Figure 5.31. The assembly sequence required the air bellows and coupling be attached to the linear actuator first. The NEMA 23 mounts were then attached to the linear actuator and then this assembly secured to the frame by two sets of nuts and bolts. The male luer lock to female M6 x 1 fitting was then screwed into the air bellows thread. Lastly, the BED was attached to the frame by two screws and rubber spacers to secure it to the frame (see Figure 5.32). For dimensions of the 3D printed parts, please refer to the drawings show on appendix L.

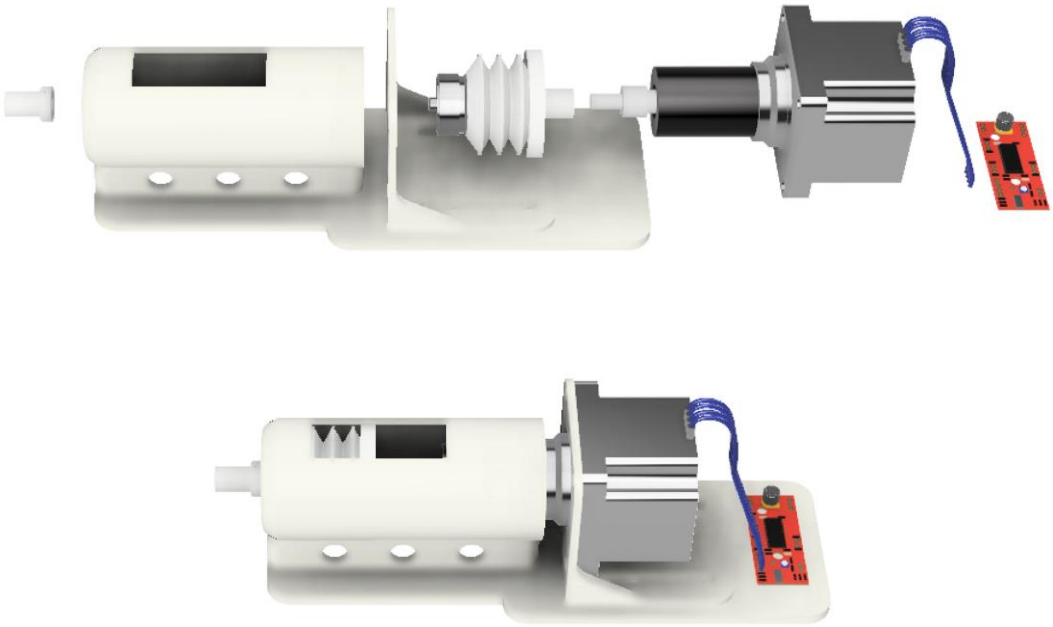

Figure 5.31: 3D CAD model assembly of the pneumatic cuff driver.

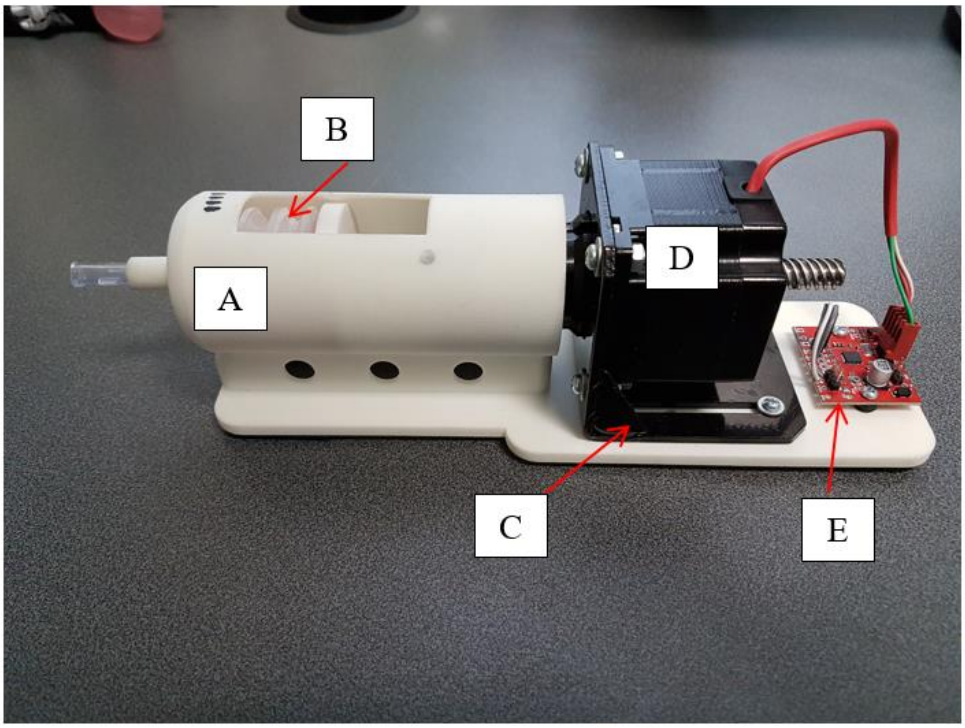

Figure 5.32: (A): 3D Printed frame. (B): Air bellows. (C): NEMA 23 L Bracket. (D) Stepper motor. (E): BED mounted.

5.2.3.7 Testing

Experiments were performed to test its hardware functionality and to investigate any flaws that were present. This included the verification of clearance between the coupling and the internal surface of the cylindrical opening, the structural integrity during operation of the linear actuator and the air tight connection between the male luer lock to female M6 x 1 fitting and the air bellows. Clearance tests using the manual movement of the linear actuator showed occasional brushing of the coupling against the inner wall in certain surface areas. The solution to this problem was to file down the edges of the coupling and a slight repositioning of the NEMA 23 mount within the frame. Slight bowing of the frame base was observed when the pneumatic cuff driver was inflating and deflating the peristaltic balloon cuff, particularly at maximum linear actuator travel. This contributed to the brushing of the coupling against the internal surface of the cylindrical opening. Future revisions should make the base of the frame thicker to eliminate this problem. A small air leak between the male luer lock to female M6 x 1 fitting and the air bellows during inflation was fixed by sealing the connections with marine silicone and no further leaks were experienced.

Figure 5.33: Pneumatic cuff drivers.

5.2.4 Cuff Controller

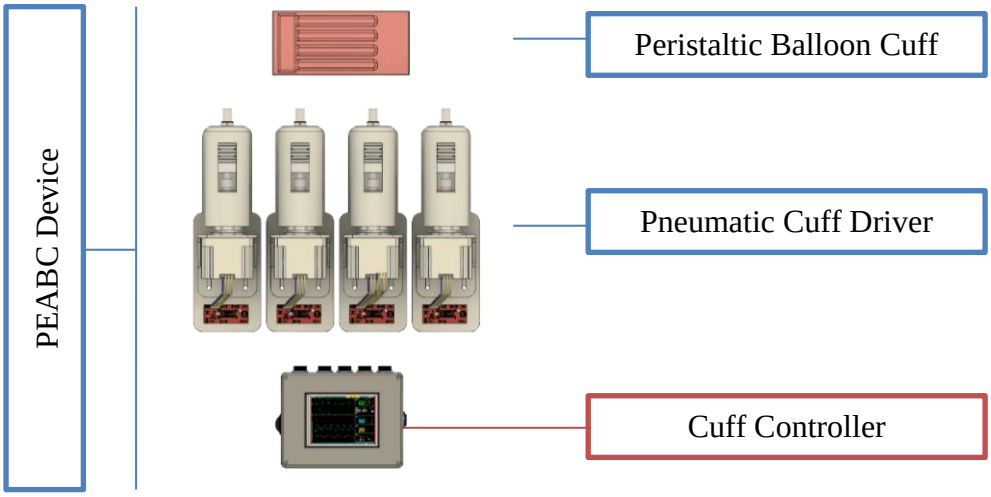

Figure 5.34: Cuff controller component.

The cuff controller shown in Figure 5.34 supplies power and software instructions to the pneumatic cuff driver. It has a touch screen interface to enable and disable the inflation/deflation cycle and is powered an Arduino base microcontroller. The cuff controller also takes readings from the pressure sensor probe in the phantom aorta 1 and 2, to control the amount of inflation volume in synchronisation with the cycle time produced by the cardiovascular simulation platform.

5.2.4.1 Design Overview

The cuff driver consists of both hardware and software. The hardware aspect is made up of electronic circuitry, hardware inputs and outputs and an enclosure. The software aspect is code programmed on the Arduino that controls the travel of each linear actuator base on the pressure in the aorta. In the following sections, more in-depth information is given about both the hardware and software aspects of the cuff controller.

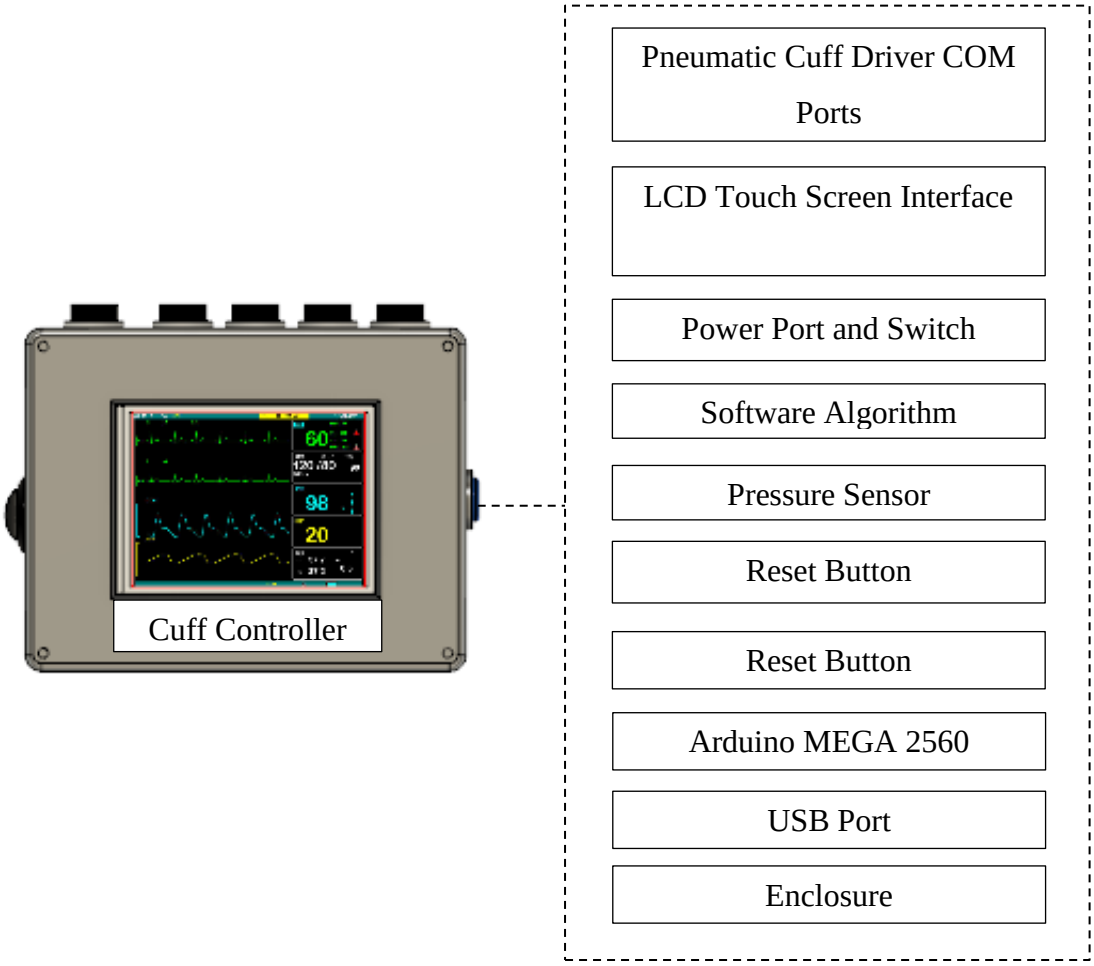

Figure 5.35: Component aspects of the cuff controller.

5.2.4.2 Hardware

The main control system that operates the PEABC device consists of two interacting electronic modules. The first module controls the four linear actuators and is powered by Arduino Mega 2560 (see Figure 5.36). The second electronic module is a UTFT 3.2-inch touchscreen LCD module stacked on top of the Arduino Mega 2560. It provides the user interface to enable/disable the actuation process, as well as displaying real-time aortic pressure readings obtained by the pressure sensor (see Figure 5.37).

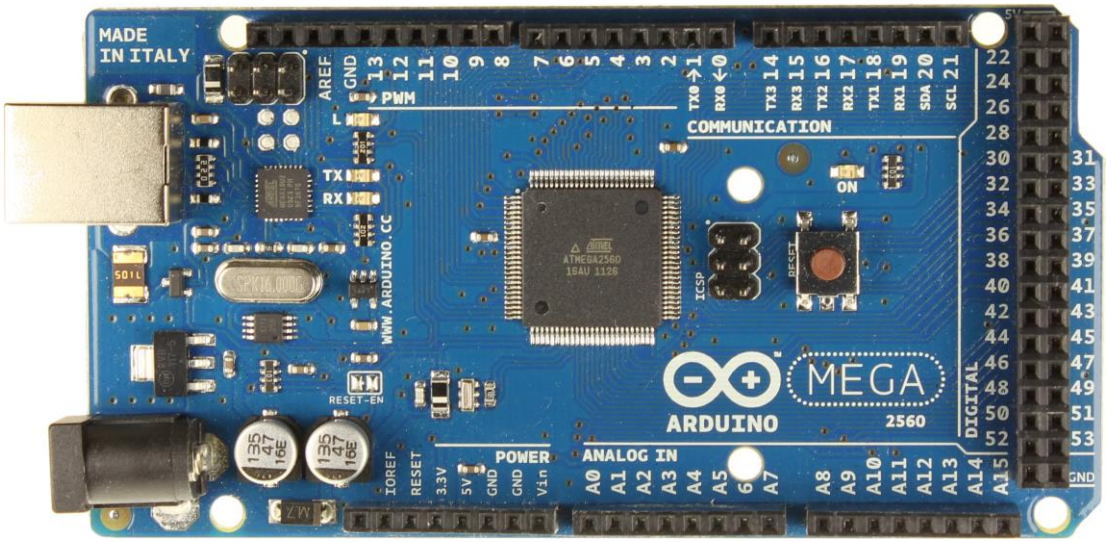

Figure 5.36: Arduino MEGA 2560 development board.

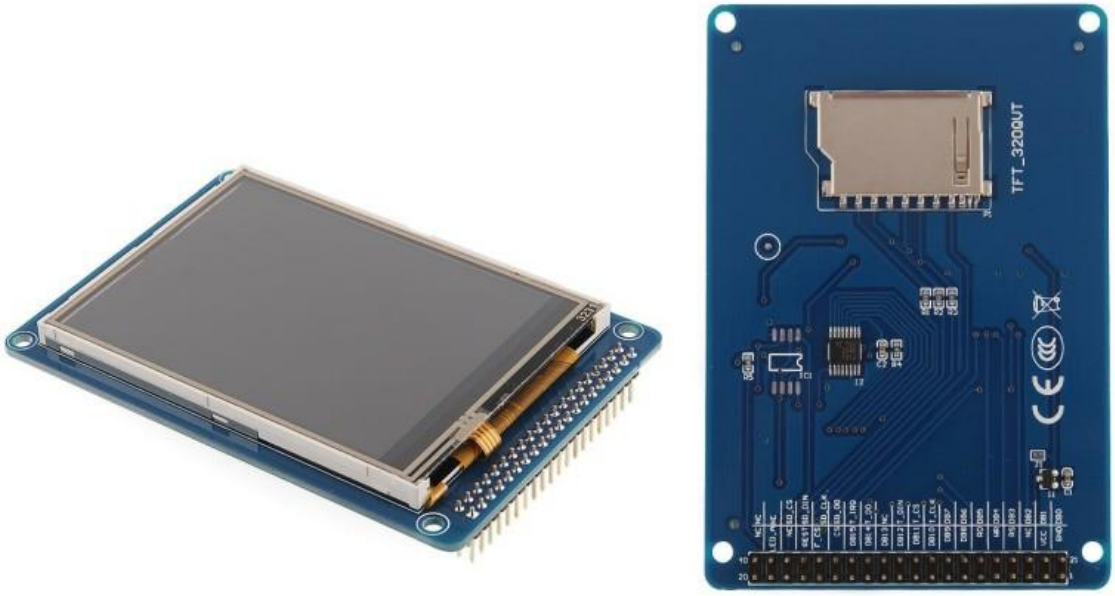

Figure 5.37: UTFT 3.2" Touchscreen module.

The Arduino-based control system of the PEABC device provides the digital control information to each of the linear actuators that make up the pneumatic cuff driver. Since the BED requires two input variables – STEP and DIR pins – to control the linear actuator, a total of 8 digital output pins were utilised on the Arduino Mega 2560 I/O. The VCC pins and GND pins from the Arduino Mega 2560 also supplied the necessary voltage of 12 VDC at 200 mA to each of the BED (see Figure 5.38).

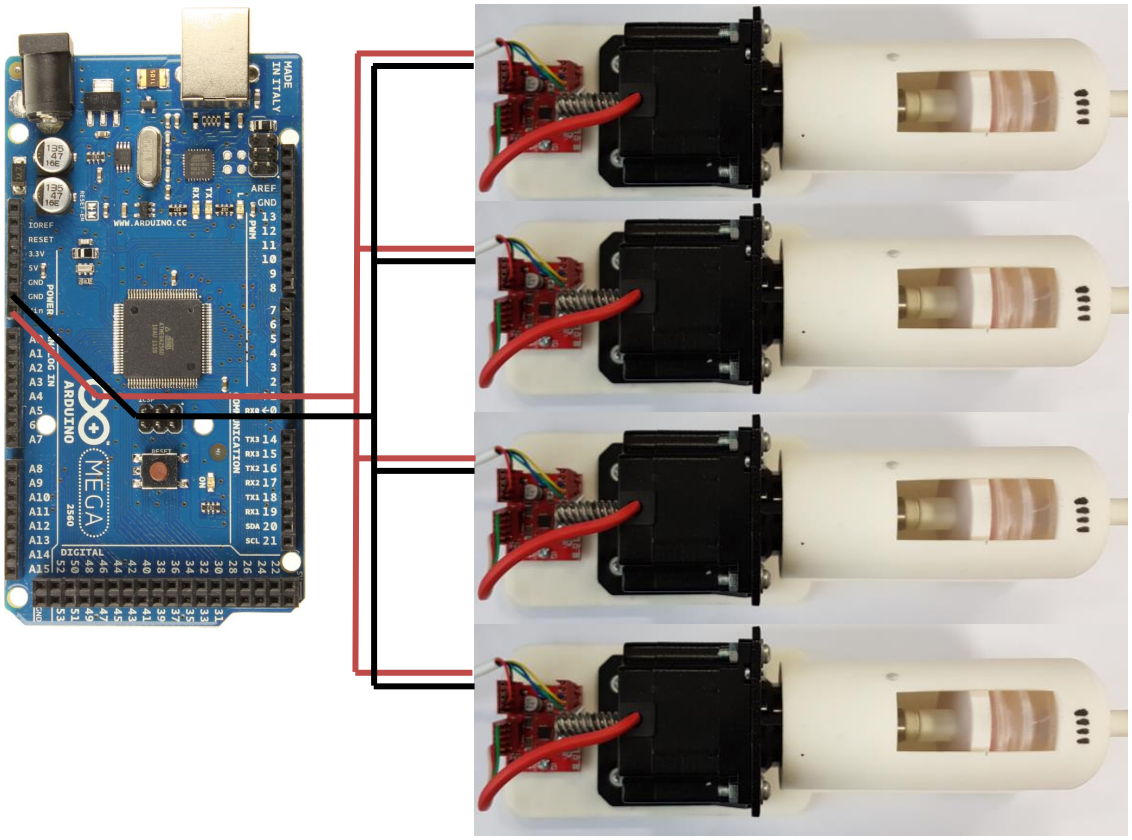

Figure 5.38: VCC and GND wiring from the Arduino MEGA 2560 to each of the BED that drives each stepper motors.

To sense the absolute pressure readings inside the phantom aorta with the Arduino Mega 2560, the MPX5100AP sensor used previously for testing the phantom aorta was adapted as an input sensor for the control system. The MPX5100AP sensor is connected to the Arduino Mega 2560's analogue input pin, 5 VDC pin, and GND pin (see Figure 5.39).

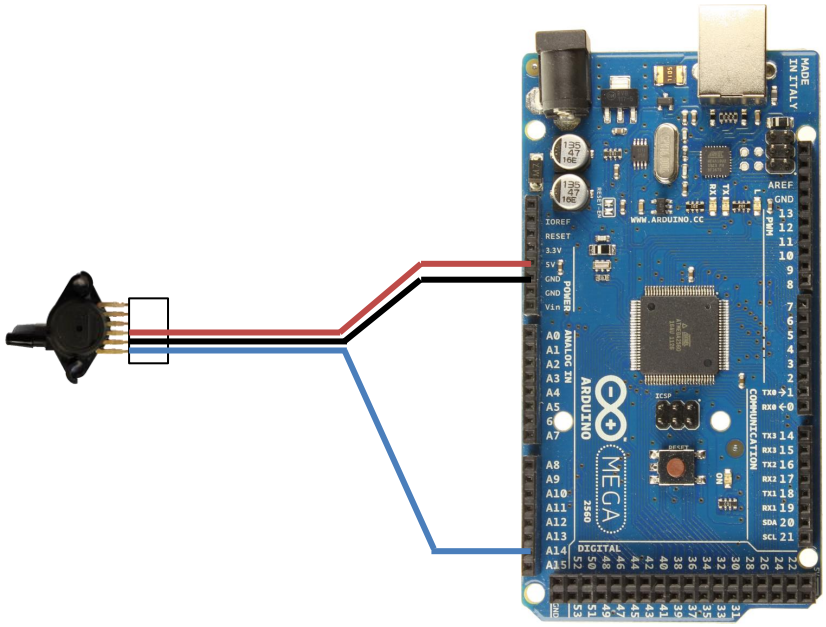

Figure 5.39: Wiring of the MPX5100AP to the Arduino MEGA 2560.

The Arduino Mega 2560 itself is supplied by an external power supply that provides a constant output of 12 VDC at 1A via the 3.1mm power jack connector. Programming the Arduino Mega 2560 with the Arduino software (described more in section 5.2.4.3) was performed by serial communication using the USB type B interface. The fitting for the BED to Arduino Mega 2560 was an 8 pin male/female connector and the MPX5100AP sensor to the Arduino Mega 2560 was a 3 pin male/female mic connector (see Figure 5.40).

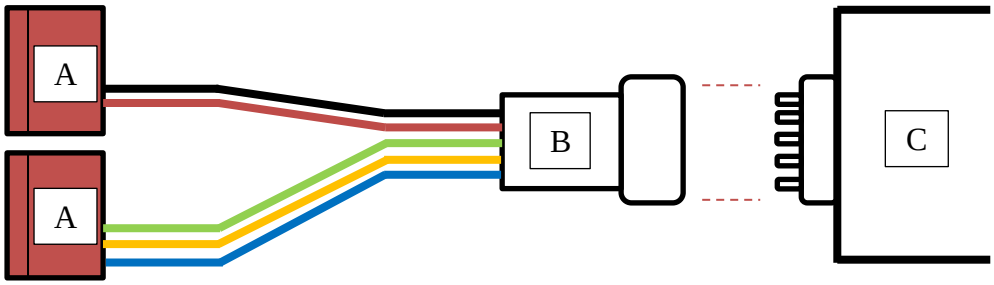

Figure 5.40: Pin connections between the cuff controller and the BED. (A): Connectors to the BED Pins. (B): 8 Pin Female connector. (C): Cuff controller.

An enclosure was made to house all of the electronic circuits, wirings, and connections. The enclosure is a two-piece case that contained components in the base and lid section. The base piece contains the Arduino Mega 2560, TFT LCD Mega Shield and all the connecting fittings. The lid section of the case fixes the UTFT LCD touch screen and is screwed onto the base section of the case. The cuff controller enclosure was designed specifically for this research in AutoCAD (see Figure 5.41).

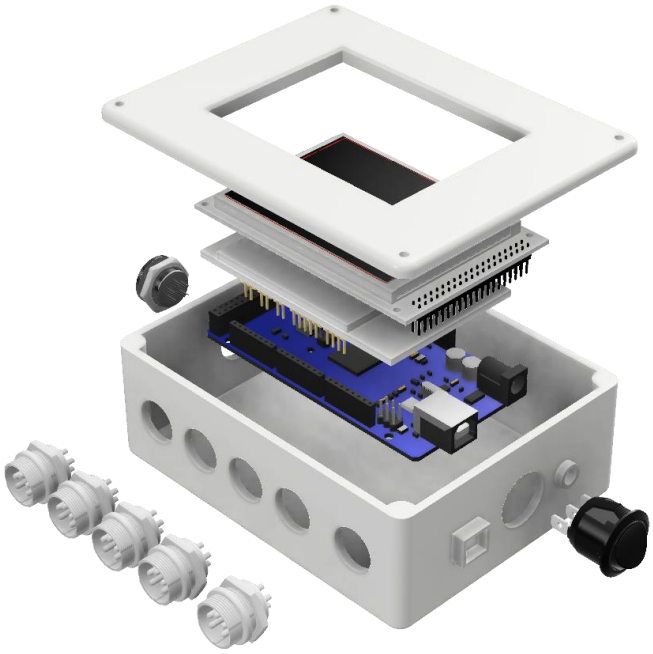

Figure 5.41: Exploded 3D CAD view of the cuff controller.

The enclosure base was designed with holes for connectors, switches etc. The location of these hole cut-outs is shown in Figure 5.42. The cuff controller enclosure parts were 3D printed with SLA separately.

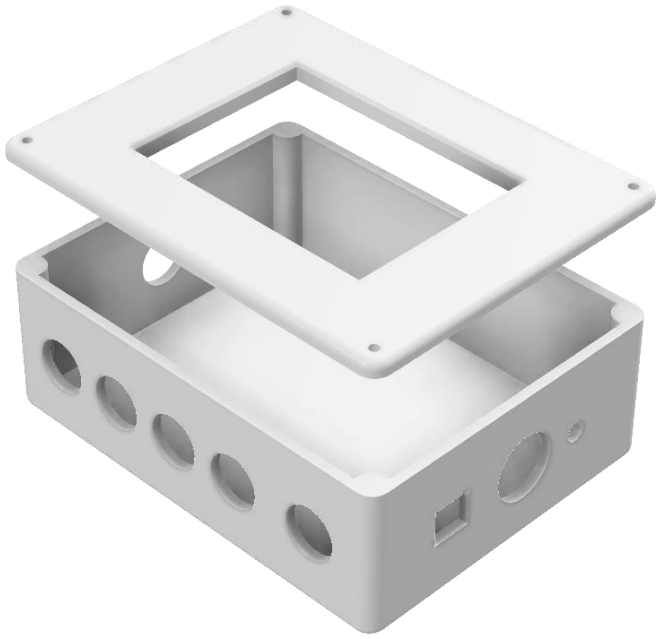

Figure 5.42: Exploded 3D CAD view of the cuff controller frame.

The physical placement of the of the Arduino Mega 2560 and TFT LCD Mega Shield was achieved using plastic standoffs glued to the enclosure base to mount the Arduino Mega 2560 board. The TFT LCD Mega Shield was simply connected on top of the Arduino Mega 2560 board via a 40 pin header as this module was designed to be compatible with Arduino Mega 2560 board. Before the four 8 pin connectors, 3 pin connector, reset button, power switch, and power port was mounted to the hole cut-outs on the enclosure, the wiring had to be soldered to them first. The process was then followed by attaching the wires soldered to the connectors to the appropriate pins allocations on the Arduino Mega 2560 board.

The enclosure top is where the UTFT LCD touch screen is housed in the allocated slot specifically designed to firmly secure the screen with high strength adhesives. The connection between the required TFT LCD Mega Shield model and the UTFT LCD touch screen was made with the use of a 40 pin ribbon cable. The two pieces of the enclosure were then assembled together with 4 screws to secure them on each four top corners of the enclosure.

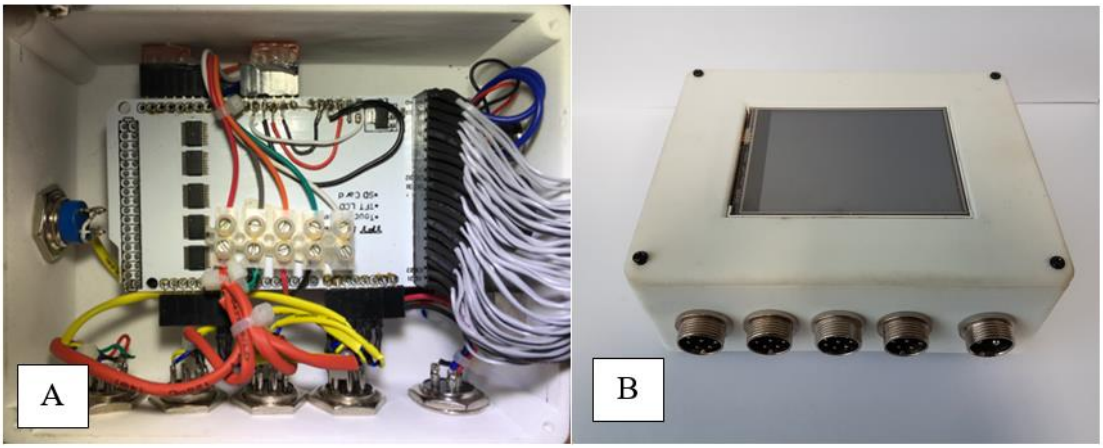

Figure 5.43: (A): Components inside the cuff controller. (B): External of the cuff controller.

5.2.4.3 Software

The motion control software of the peristaltic balloon cuff causes it to be inflated and deflated in response to the cyclic pressure readings obtained from the cardiovascular simulation platform. The start/stop operations and the displaying of the absolute pressure readings, as well as other calculated variables, are also programmed into the software to create the desired user interface. The software for the Arduino's cuff controller called the extra-aortic cuff driver or EACD was written in the C programming language. Open source software libraries were utilised for the UFTF touch screen, the BED, and a timer function. The counterpulsation and peristaltic motion of the cuff balloons via the cuff drivers are driven by the software algorithm programmed into the cuff controller. Counterpulsation was achieved by detecting the peak systolic pressure via a pressure sensor and initially inflating the first cuff balloon. Each of the four balloons is subjected to their own time delay which was achieved using a finite impulse response (FIR) filter algorithm. The FIR filter creates an output (motor position over time) based on the

frequency and amplitude that the pressure sensor outputs from the ascending aorta (see Figure 5.44) that becomes the input to each cuff driver.

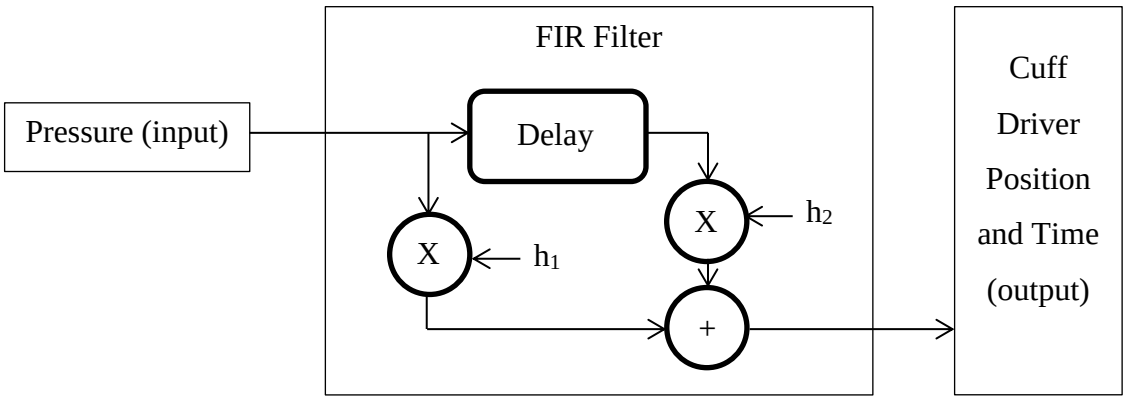

Figure 5.44: FIR filter structure diagram.

The software algorithm was created as a combination of several functions that allow the cuff controller to communicate to the cuff driver to inflate and deflate the peristaltic cuff balloon based on pressure sensor feedback and to also provide a user interface with a touch-sensitive display. The following software functions were utilised in the cuff controller.

UFTF Touch Screen Software Library

The UFTF touch screen software library *(#include <UTFT_Buttons.h>*) is a prewritten set of code that allows the creation of the user interface for the EACD. The touch screen interface embedded in the EACD software uses two open source libraries for the visual interface of the touch screen to interact with the buttons. EACD software code was written to initiate, display and take in touch response of the screen. The program displayed and responded to the touch buttons for initiating or terminating operation of the four linear drives, and displayed the sensor reading, calculated position of the linear drive, absolute pressure and sensor voltage as shown in Figure 5.45.

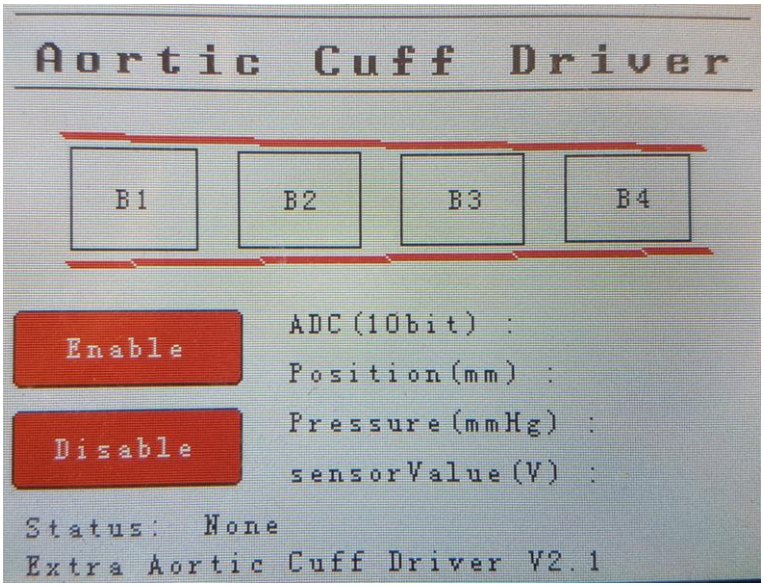

Figure 5.45: The graphical user interface of the cuff controller showing functional enable and disable buttons.

BED Software Library

The BED software library (*#include <AccelStepper.h>*) has sets of functions that allow programming functions to drive the linear drive. This library was used to assign the 3 connection pins each of the four linear drives between the BED and the cuff controller. All of the GND pins of each linear drive were assigned to pin 1 of the Arduino mega 2560. The STEP and DIR pins were assigned to available digital input pins. For example, *AccelStepper stepper1(1, 9, 8)* assigns pin 1 as GND pin, pin 9 as STEP pin and pin 8 as DIR pin. The two major BED software functions that were utilised for actuating the linear drives were *stepper.moveTo()* and *stepper.run()* function. The *stepper.moveTo* function sets the target position and moves the linear drive one step per function call from the current position to the target position that's set by the most recent call to this function. The *stepper.run()* function polls the linear drive and steps it if a step required based on the set speed *stepper.setMaxSpeed()* and acceleration *stepper.setAcceleration()* assigned to achieve the target position.

Setup Function

The setup function of the EACD software is where the initial setup and non-animating UTFT touch screen user interface is drawn, the four stepper motor's speed and

acceleration values are defined, and the pins assigned to the inputs and outputs. The speed and acceleration settings for the BED software are assigned to the setup function for all four linear drives. The initialization of the FIR filter's relevant variables is also defined in this function.

Run Motor Function

This function is responsible for defining the linear drive's calculated position based on the calling of the *stepper.moveTo()* and *stepper.run()* BED software functions. The distance to be moved is calculated from the pressure sensor in the main EACD loop.

Sensor Reading Function

This is a function that calculates and displays the analogue pressure signals. The Arduino Mega 2560's analogue pin has the capability to read the signal at 10,000 samples/second, i.e. the ADC can read a sample every 100µs under the following conditions:

Clock speed = 16MHz

13 clock cycles per second.

Pre-scale = 1

However, the practical sampling rate that was observed – using a sample rate software function – was 9600 samples/second (116µs). This means that the ADC calculation takes 116µs to perform one reading. The sample rate calculated was an important factor in the development of the FIR filter. The MPX5100AP sensor transfer function to convert the analogue signal into absolute pressure in mmHg units is shown in Equation 5.1.

$$V_{out} = V_s(P \times 0.009 - 0.095)$$

$$\pm(Pressure\ Error \times Temp.Mult. \times 0.009 \times V_s$$

Equation 5.1

$$V_s = 5.0V \pm 5\%\ P\ kPa$$

The digital value from pin A14 (*pressureSensor*) is converted into a voltage value (*sensorVoltage*) based on the reference voltage of 5VDC and the 10-bit resolution of the analogue pin (see Equation 5.2).

$$sensorVoltage = sensorValue \times (5.0 \div 1023) \qquad \textit{Equation 5.2}$$

The derived sensor voltage is then used to calculate the pressure – measured in kPa – from the sensor using the transfer function in Equation 5.3.

$$sensorPressure = 4.444 \times ((5 \times sensorVoltage) + 1) \qquad \textit{Equation 5.3}$$

To obtain the pressure readings in mmHg units (*absolutePressure*) a unit conversion from kPa (see Equation 5.4).

$$absolutePressure = 7.50061561303 \times sensorPressure \qquad \textit{Equation 5.4}$$

The pressure range was observed to be between 76 – 120 mmHg during operation of the cardiovascular simulation platform. This was mapped to the linear drive's travel of 38.1mm with 0.0508mm of movement per step count. Thus the total step count was 1415.61 steps, rounded to 0 to 1400. The software code that was implemented for assigning the position of the linear actuator from the pressure that was sensed was:

pos = map(absolutePressure,78,120, 1400, 0)

This mapping is inverted to extend the linear drive as the absolute pressure decreases and retract when the absolute pressure increases, and thus implements counterpulsation.

For debugging purposes, calculated variables were displayed on the UTFT touch screen. However, during operation display was disabled to maintain the speed of the motor control loop.

Main loop

The main loop of the EACD software continuously executed component functions. The sensor reading function was first obtained and derived variables calculated. This was followed by a series of condition statements that check for touch input from the UTFT touch screen to see if the enable button or disable button was pressed. For the case that a motor is enabled, the FIR function performs the calculations that phase shifts the motor actuations for that motor and the motor is driven.

5.2.4.4 Software Programming

The programming and debugging of the Arduino Mega 2560 board were performed using the Arduino Integrated Development Environment (Arduino IDE) on a computer running Windows 10. The programming language that the EACD software was written in was C and made use of the software libraries mentioned previously in section 5.2.4.3. The code was uploaded to the Arduino Mega 2560 via USB interface (see Figure 5.46).

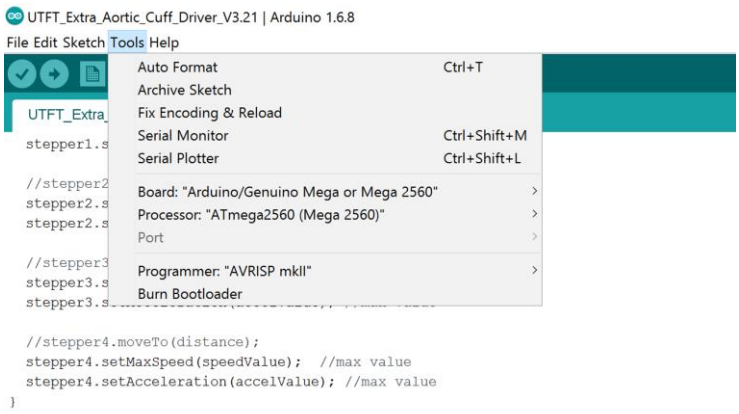

Figure 5.46: Arduino IDE software tool. Drop down menu used for selecting the communication ports and processors.

5.2.4.5 Testing

The cuff controller was tested to ensure functionality with the assembled hardware and EACD software. The initial test was to make sure that all connector wirings were assigned to the correct pins using a multimeter to check the connectivity. The next test

was powering up the cuff controller with 12VDC and testing the reset button. The reset button was found to be useful during development as, occasionally, the uploading process of the EACD software code to the Arduino Mega 2560 resulted in the UTFT touch screen being non-responsive. The UTFT LCD touch screen interface was then tested for functionality whereby pressing the enable button would display a message 'running' and display 'stopped' when disable button is pressed. Testing display of the correct sensor value from the pressure sensor was also performed. This involved connecting the 3 pin pressure sensor to the cuff controller and performing voltage measurements across the sensor and comparing it with the value displayed on the touch screen. The voltage measured across the ground and signal pin of the pressure sensor was observed to be 0.24VDC, whereas the cuff controller displayed 0.22VDC. The difference was found to be due to the difference between actual sensor supply voltage of 4.6VDC and nominal 5VDC used to convert the sensor value into sensor voltage. The last test that was performed for the cuff controller involved connecting all four linear drives to test the run motor function in the EACD software. This test was to check that the linear drives operate at optimal speed and acceleration with the change in analogue signal from the pressure sensor. The pressure change to step movement calibration that was code into the EACD software mentioned previously in section 5.2.4.3 was defined by this test. The values that were derived from the linear drives' speed and acceleration profiles were found by trial and error, as initially the values for both profiles were set too high resulting in a slip in position causing the motion to become out of synchronisation with pressure readings.

It was also found that the Arduino development board used as a controller could not display the pressure readings from the pressure sensor and run the four pneumatic drivers at the same time. The lack of processing power was the cause of the problem, although better optimisation could have alleviated this. With this lack of processing power, the controller was not able to also perform peristalsis movement of inflating and deflating each balloon within the initial cardiac cycle time of 0.8 seconds and subsequent tests were run at 60 bpm.

Three major versions of the EACD software were created for testing of the PEABC system. The first software version drove all four linear drives without peristaltic motion. The second software version was the implementation of the peristaltic model – using the equations created on the Matlab® (MathWorks®, United States) simulation based on basic delay timing to actuated each balloon. The third software version was an alternative delay timing method – using FIR filters – to implement a peristaltic model using the linear

drives. Testing of the PEABC device attached to the cardiovascular simulation platform is explained in Chapter 6 and Chapter 7.

Chapter 6

Result of System Tests

This chapter presents results obtained when all of the components of this research were tested together, i.e. when the PEABC device is attached to the cardiovascular simulation platform. Two main focal data – pressure and flow characteristics – are documented and analysed against related studies, and discussed later in Chapter 7.

6.1 PEABC Prototype and Pressure Characteristics

With the same testing equipment – pressure catheters and flow sensors – used for obtaining the results for cardiovascular simulation platform, both pressure and flow waves and values were acquired under three conditions. The first condition was the PEABC device attached, but not actuating, to the descending aorta (directly after the aortic arch) with the cardiovascular simulation platform operating. The second condition was setting the PEABC device to actuate all four air chambers (non-peristaltic) in counterpulsation to the cardiovascular simulation platform pumping rhythm. The third condition was setting the PEABC device to perform both peristalsis and counterpulsation operation on the cardiovascular simulation platform.

With the cardiac cycle set on the cardiovascular simulation platform for 2sec, the pressure waveforms at the aortic arch acquired from the three testing conditions are shown in Figure 6.1. The pressure waveforms at the descending aorta were also acquired from the three testing condition and are shown in Figure 6.2. It is observed that for the ascending pressures that the end diastolic pressure at point C increased by ~8 mmHg for non-peristaltic and counterpulsation operation, and ~6 mmHg for peristaltic and counterpulsation operation. In the descending aorta, the end-diastolic pressure increased by ~2.5 mmHg for both non-peristaltic and counterpulsation operation, and peristaltic and counterpulsation operation. In both locations, the peak systolic pressures (shown as point A) are highest when the PEABC device was not operating. At points B in both locations the pressure with peristaltic and counterpulsation operation drops by as much as ~10 mmHg when compared to the normal pressure.

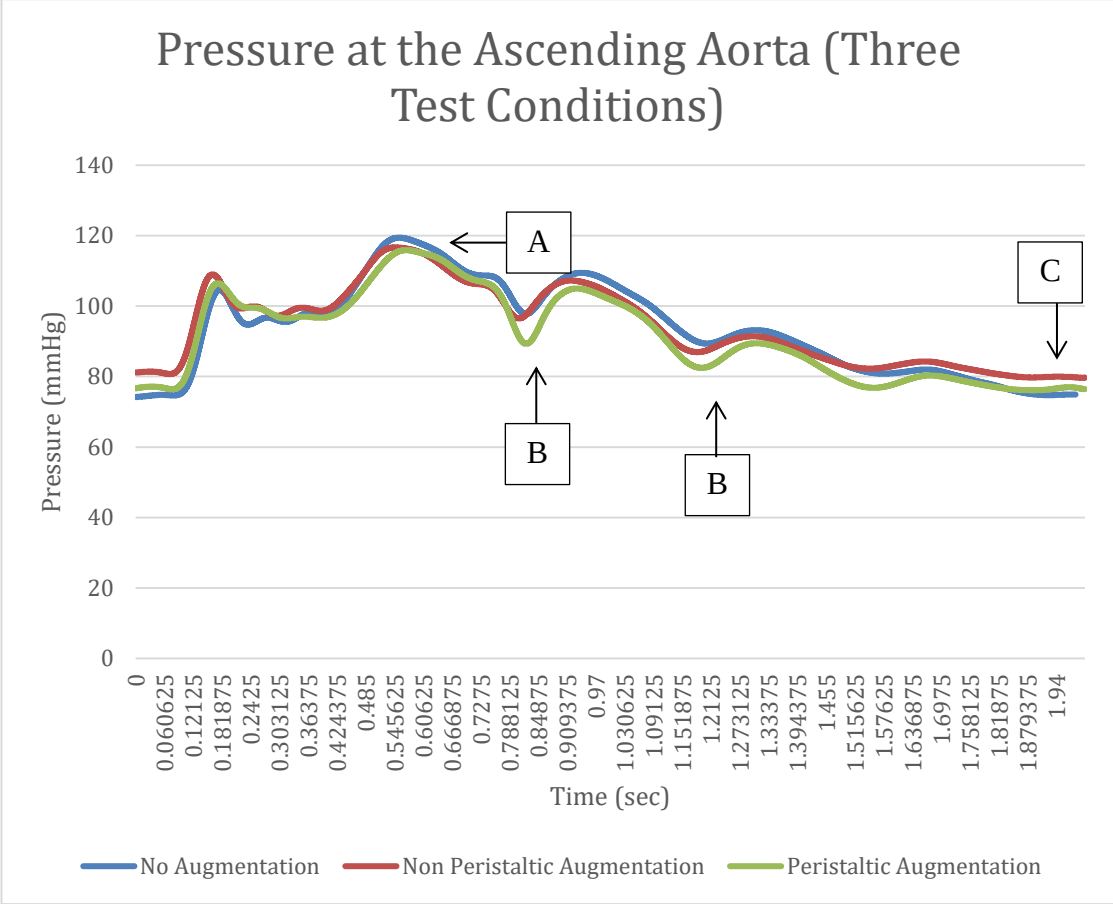

Figure 6.1: Pressure waveforms at the ascending aorta. (A): Peak systolic pressures. (B): Pressure drops when comparing to normal pressure. (C): End-diastolic pressures.

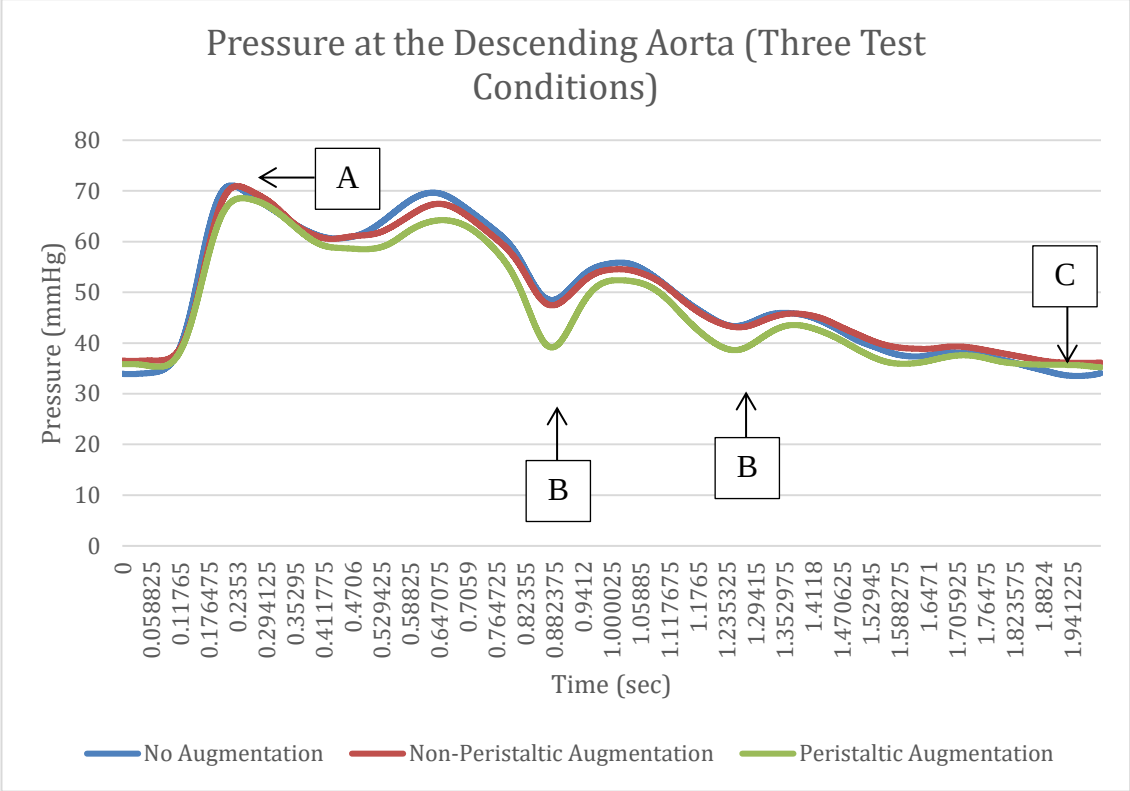

Figure 6.2: Pressure waveforms at the descending aorta. (A): Peak systolic pressures. (B): Pressure drops when comparing to normal pressure. (C): End-diastolic pressures.

The before, during and after effects of operating the PEABC device with both non-peristaltic and peristaltic, and counterpulsation attached to the descending aorta were sampled for 2 min on the LabChart 8 software (see Figure 6.3). The sampling rate was set at 40,000 samples/second.

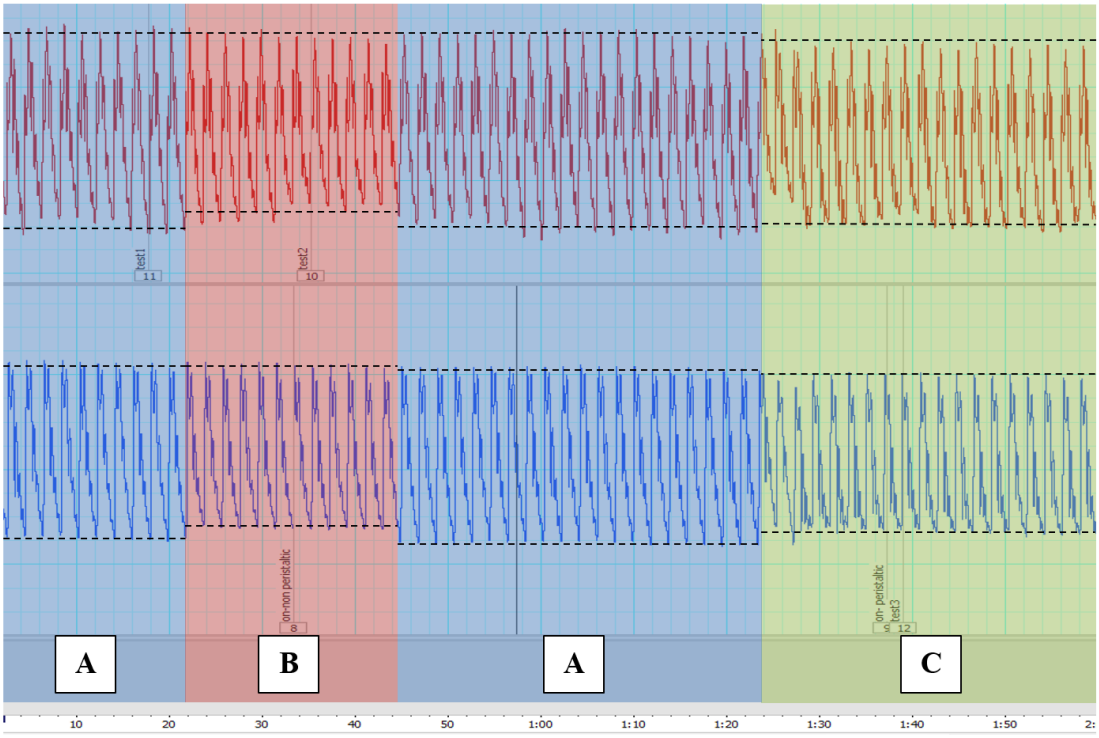

Figure 6.3: Aortic arch pressure (red waveform). Descending aortic pressure (blue waveform). The area highlighted blue (A): PEABC prototype not operating. The area highlighted red (B): non-peristaltic and counterpulsation from PEABC prototype. The area highlighted green (C): peristaltic and counterpulsation from PEABC prototype.

5 cardiac cycle samples of each testing condition were extracted from Figure 6.3 and are shown in Figure 6.4 and Figure 6.5.

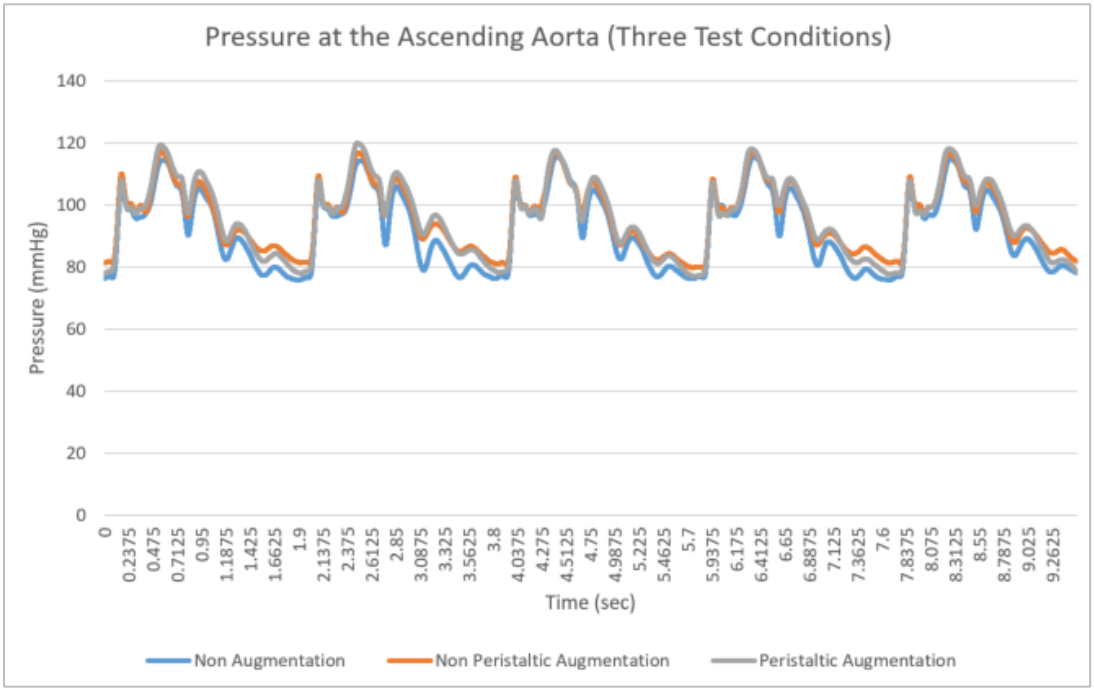

Figure 6.4: 5 cardiac cycle samples of the pressure extracted at the ascending aorta – showing three pressure wave that represents the three testing conditions.

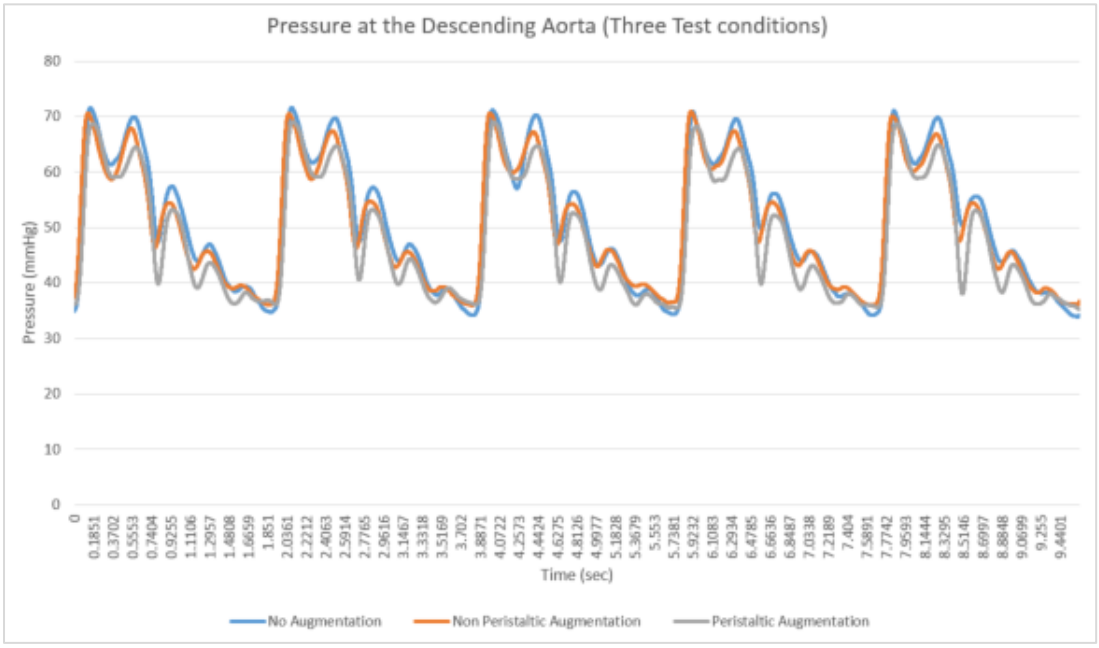

Figure 6.5: 5 cardiac cycle samples of the pressure extracted at the descending aorta – showing three pressure wave that represents the three testing conditions.

The mean pressures at the ascending aorta and the descending aorta from the two testing conditions (PEABC not operating and PEABC operating with counterpulsation and peristaltic augmentation) were calculated based on sampling the 5 cardiac cycles.

A Students T-test – two-sample assuming equal variances – was performed and found a significant difference ($\alpha = 0.05$) in mean pressure between the no augmentation test condition and peristaltic augmentation test condition, for pressures at both the ascending aorta and descending aorta (see Table 15).

Table 15: Mean aortic pressure comparisons between PEABC off and on.

Pressure Comparison A (PEABC off) vs B (PEABC on)	**N**	**Mean (±SD) A mmHg**	**Mean (±SD) B mmHg**	**Difference (B – A) mmHg**	**P-Value**
Mean ascending aorta pressure PEABC off vs on	5	92.1 (SD ± 0.22)	95.7(SD ± 0.72)	4.6	**$6.84e^{-6}$**
Mean descending aorta pressure PEABC off vs on	5	51.4 (SD ± 0.27)	48.6 (SD ± 0.28)	-2.8	**$2.83e^{-7}$**
Mean ascending aorta pressure (diastolic pressure) PEABC off vs on	5	87.3 (SD ±0.75)	91.4 (SD ±1.27)	6.8	**$5.0e^{-5}$**
Mean descending aorta pressure (diastolic pressure) PEABC off vs on	5	45.6 (SD ±1.07)	43.7 (SD ±0.47)	-1.9	**$8.83e^{-3}$**

6.2 PEABC Prototype and Flow Characteristics

The flow characteristics and parameters under the operation of the PEABC device were measured using the ACUSON Sequoia 512 (Siemens, Germany) ultrasound machine. Peak flow velocities in both the ascending aorta and brachiocephalic artery were measured with the ultrasound transducer under two conditions - PEABC device off and PEABC device operating with peristalsis and counterpulsation. The ascending aorta waveforms are shown in Figure 6.6 and Figure 6.7 and brachiocephalic artery waveforms are shown in Figure 6.8 and Figure 6.9. The ultrasound measurements obtained show both the distribution of fluid particles with both forward and backwards flow velocities. The top half of the readings indicate the forward flow velocity, and the bottom half indicates the backwards flow velocity. A student T-test was performed for comparing the differences between PEABC off and PEABC on states (refer to Table 16).

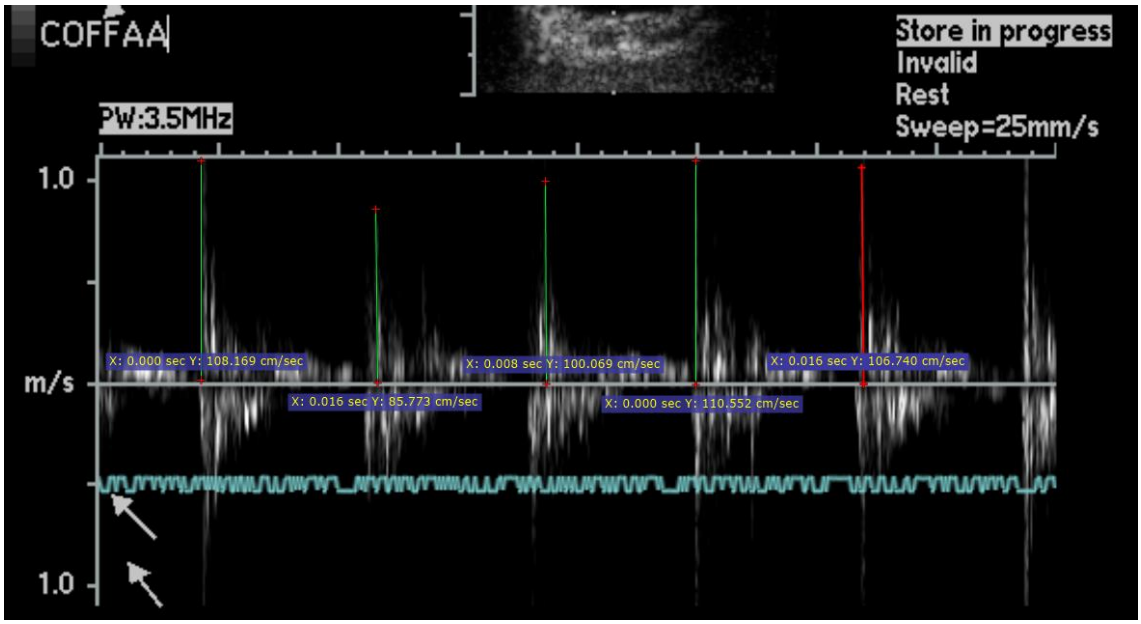

Figure 6.6: Peak forward flow velocity measured at the ascending aorta with the PEABC prototype off.

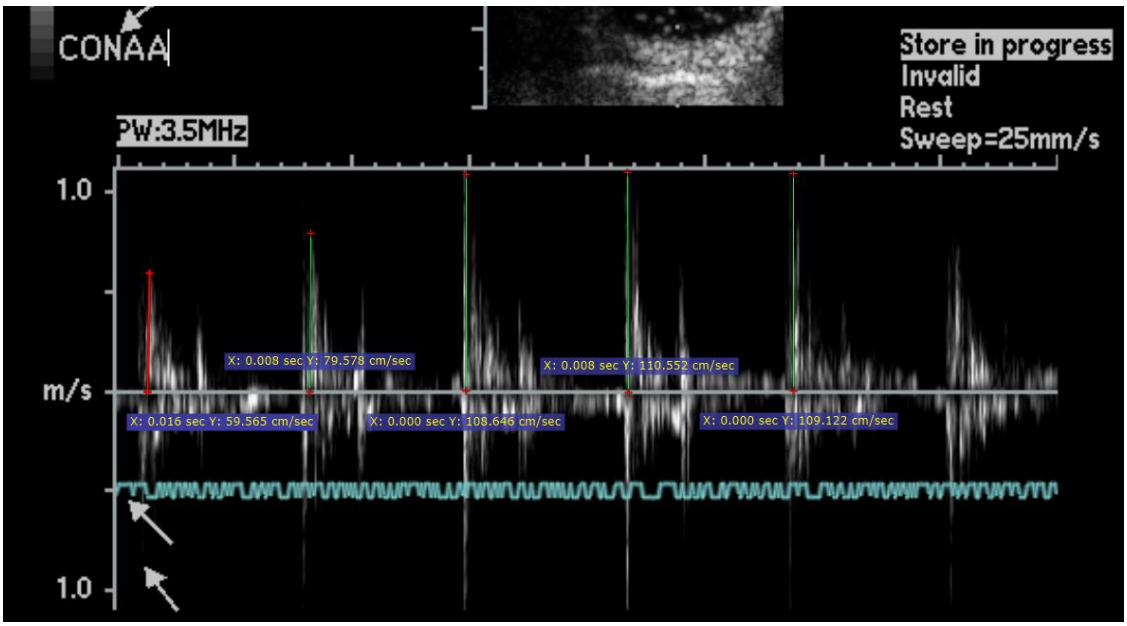

Figure 6.7: Peak forward flow velocity measured at the ascending aorta with the PEABC prototype on.

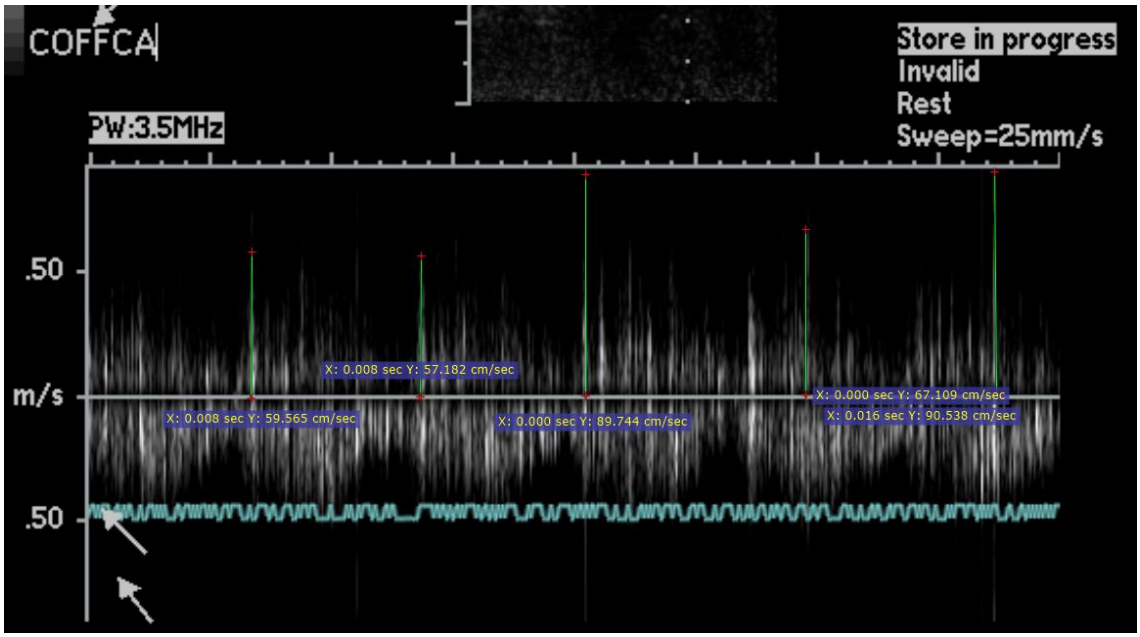

Figure 6.8: Peak forward flow velocity measured at the brachiocephalic artery with the PEABC prototype off.

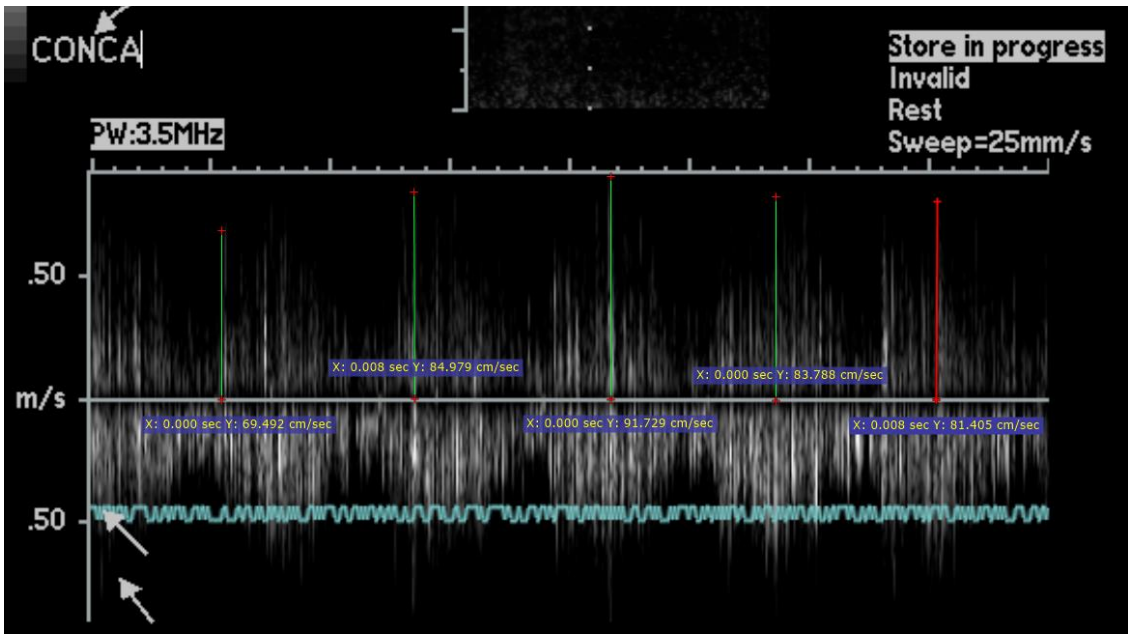

Figure 6.9: Peak forward flow velocity measured at the brachiocephalic artery with the PEABC prototype on.

Mean flow velocities for the 5 cycles were also obtained for both PEABC off and PEABC on conditions and Student's T-test used to evaluate the differences (refer to Table 16). The flow velocities samples – ascending aorta and brachiocephalic artery – are shown in Figure 6.10 and Figure 6.11.

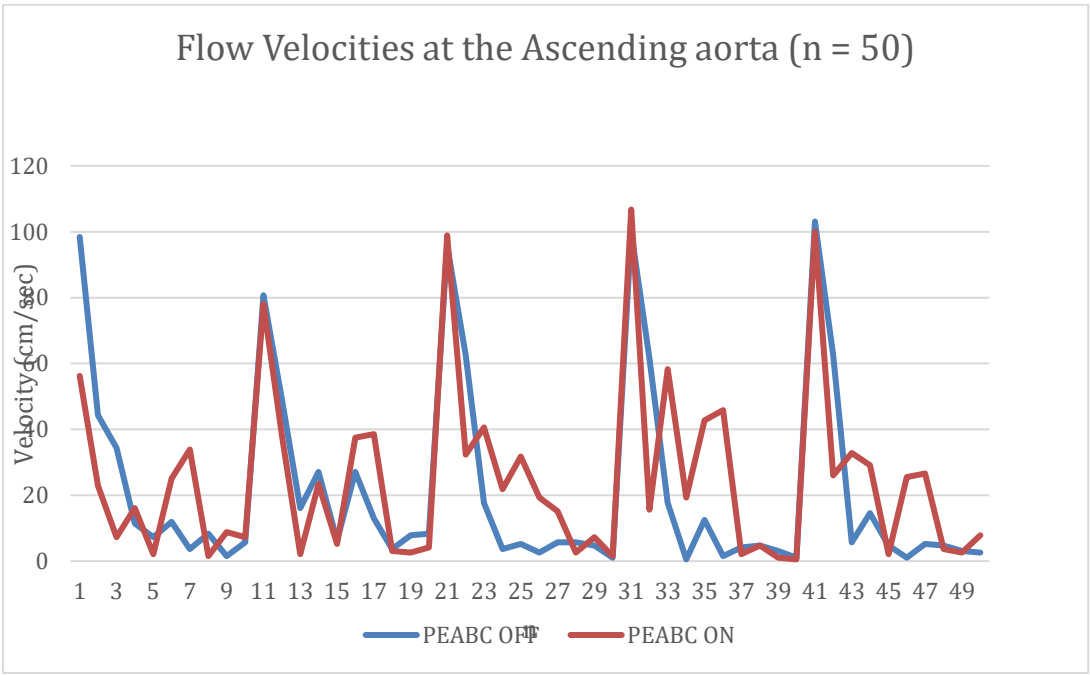

Figure 6.10: Flow velocities in the ascending aorta.

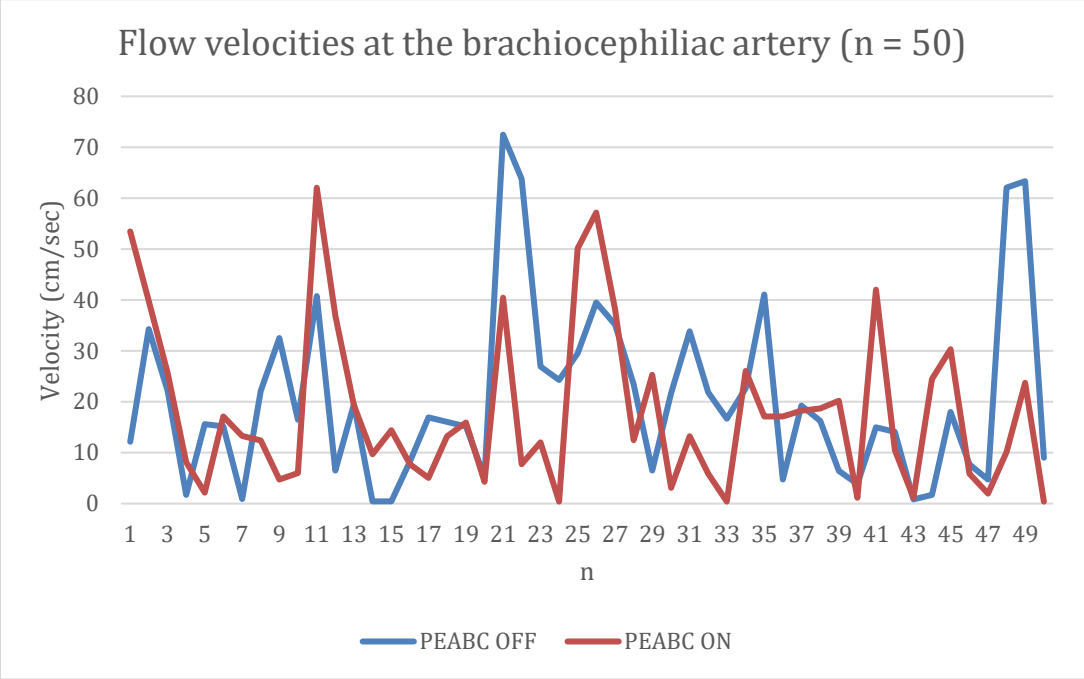

Figure 6.11: Flow velocities in the brachiocephalic artery.

A forward and backwards flow velocity of the ascending aorta sample of the PEABC off and on was measured and compared (see Figure 6.12 and Figure 6.13). The mean flow velocity and P-value are shown in Table 16.

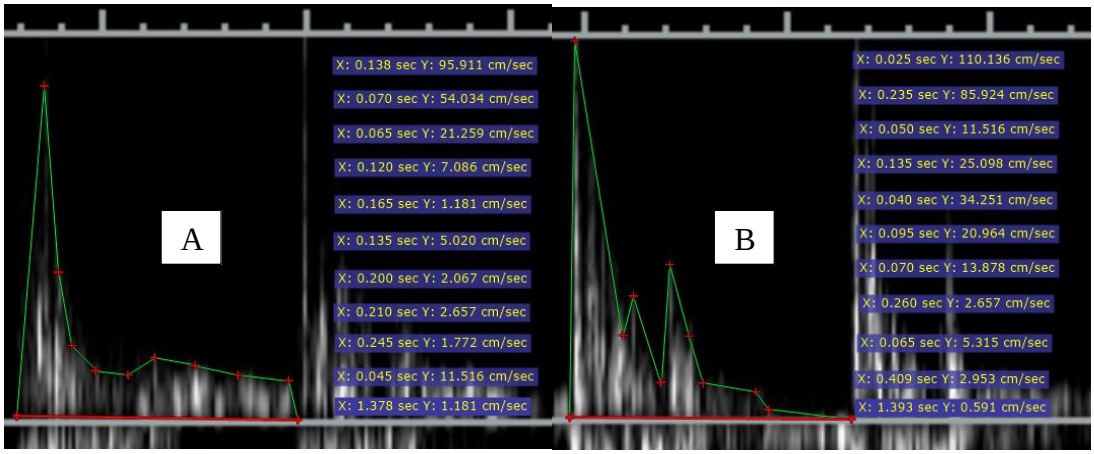

Figure 6.12: (A): Forward flow velocity with PEABC off, (B): Forward flow velocity with PEABC on.

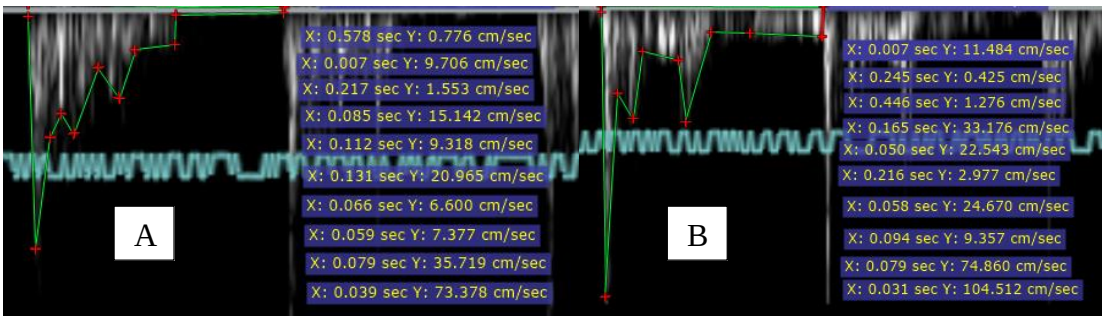

Figure 6.13: (A): Backwards flow velocity with PEABC off, (B): Backwards flow velocity with PEABC on.

Table 16: Flow velocity comparison at the ascending and descending aorta with the PEABC off and PEABC on.

Flow Velocity Comparison A (off) vs B (on)	N	Mean (SD) A cm/s	Mean (SD) B cm/s	Difference B – A cm/s	P-Value
Mean peak forward flow velocity, ascending aorta, off vs on	5	102	93	-9	0.22
Mean peak forward flow velocity, brachiocephalic aorta, off vs on	5	72.8	82.3	1.5	0.13
Mean flow velocity, ascending aorta (whole phase), off vs on	5	21.7	24.8	3.1	0.08
Mean flow velocity, ascending aorta (diastolic phase), off vs on	5	13.5	17.7	4.2	**0.01**
Mean flow velocity, brachiocephalic artery (whole phase), off vs on	5	20.6	18.2	-2.4	0.28
Mean flow velocity, brachiocephalic artery (diastolic phase), off vs on	5	19.0	15.5	-3.5	0.18
Mean forward flow velocity, ascending aorta, off vs on	10	20.0	31.3	11.3	**0.02**
Mean backward flow velocity, ascending aorta, off vs on	10	18.1	28.5	10.4	**0.04**

Chapter 7

Discussion Summary

Examining the pressure wave that was sampled at the descending aorta, the pressure had similar augmentation characteristics as the pressure that was sampled at the ascending aorta. However, the amount of amplitude augmentation at the end-diastolic phase was smaller. This signifies that by visual inspection, the PEABC resulted in more pressure augmentation in the ascending aorta than the descending aorta at the beginning and the end of the cardiac cycle. Referring back to Figure 6.1 and Figure 6.2, inspection to the both the ascending and descending aorta pressures show that the amount of diastolic pressure wave augmentation – as a result of PEABC operation – is small. However, when analysing the significant differences ($\alpha = 0.05$) based on the mean ascending aortic pressures during whole phase obtained from the Student T-Test the P-Value ($P=6.84e^{-6}$) for the ascending aorta pressure and ($P=6.84e^{-6}$) for the descending aorta pressure indicate that are significant differences of pressure augmentation with the operation of the PEABC prototype. The ascending and descending aortic aorta pressure data during diastolic phase only was also seen to have significant differences – ($P=5.0e^{-5}$) and ($P=8.83e^{-3}$) respectively. The results also show that the mean ascending aorta pressure (whole phase) was increased by 4.6 mmHg due to PEABC operation, on the other hand, the mean descending aorta pressure was reduced by 2.8 mmHg. The mean ascending aorta pressure (diastolic phase only) on the other hand, had a larger increase of 6.8mmHg due to PEABC operation. A decrease in mean descending aorta pressure was also seen during diastole (-1.9 mmHg).

Table 17: Comparing the amount of pressure augmentation created by the PEABC in both the ascending and descending aorta.

Aortic Pressure Comparisons	PEABC Augmentation (Off Vs On)
Ascending Aorta (full phase)	3.94% ▲
Descending Aorta (full phase)	5.39% ▼
Ascending Aorta (diastolic phase only)	4.58% ▲
Descending Aorta (diastolic phase only)	4.24% ▼

Examining the amount of augmentation that PEABC has on the normal aortic pressures shown in Table 17, it is observed that both pressure data – at the ascending aorta (whole phase) and ascending aorta (diastolic phase only) – show some percentage increase. Since the location of the PEABC prototype was attached near the aortic arch (closer to the ascending aorta than the descending aorta), it would be expected that the mean ascending aorta pressure would increase (see Figure 7.1).

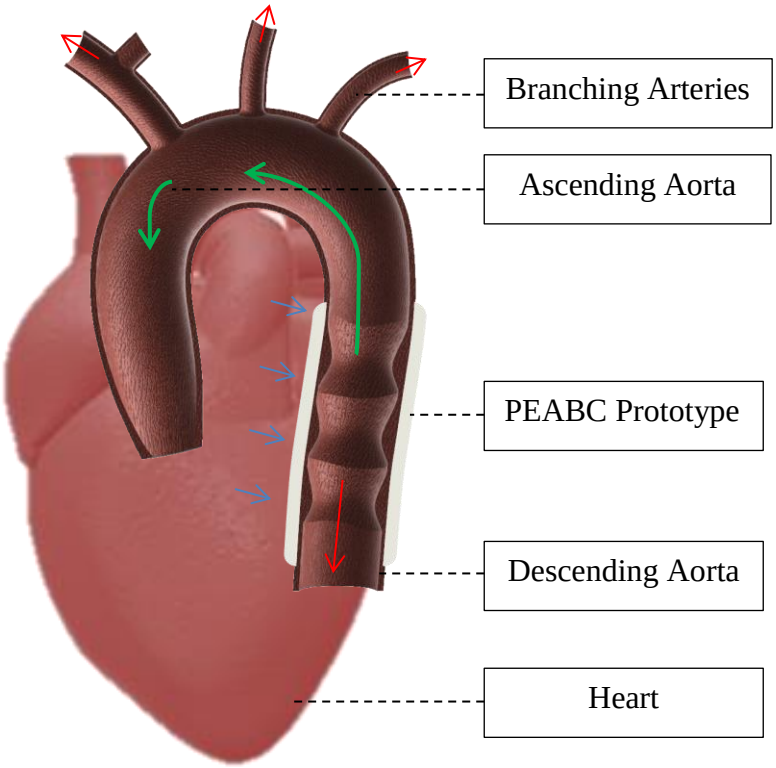

Figure 7.1: Visual illustration of the increase (green arrow) and decrease (red arrow) in pressure and flow velocity during the operation of the PEABC prototype.

An increase in the mean flow velocity at the ascending aorta of 3.07 cm/s was also experienced under the operation of the PEABC prototype. However, the mean brachiocephalic artery flow velocity was reduced by 2.4 cm/s. Furthermore, when investigating the effects of the PEABC prototype only during the diastolic phase of the cardiac cycle, the mean flow velocities of the ascending aorta and brachiocephalic artery – derived from averages of 5 cycles – show similar trends. T-Tests were also used to determine the statistical significance of the differences. Both test conditions – systolic and diastolic, and diastolic only phases – were tested for. It is noted that the diastolic mean flow velocity at the ascending aorta was the only set of flow velocity data that showed significant differences when comparing the results from PEABC off and PEABC on. Although there was no significant difference in mean flow velocities obtained in the ascending aorta when considering both systolic and diastolic phases (P=0.08) when only diastolic phase was considered statistically significant differences were found (P=0.01). Moreover, a significant difference was calculated and found in mean ascending aortic forward and backwards flow velocity augmentation under the influence of the PEABC prototype (P=0.02 and P=0.04 respectively).

This shows that the PEABC does augment mean aortic flow velocity during the diastolic phase of the cardiac cycle (see Table 18). No significant differences were found in the brachiocephalic artery. However, it was observed that the brachiocephalic artery flow velocities obtained from the ultrasound were not clear (a lot of noise in the waveform), whereas the ascending aorta ultrasound signals were clearer. These T-Test outcomes of the mean flow velocities indicate that the PEABC prototype is more effective at augmenting the diastolic phase of the cardiac cycle – predominantly in the ascending aorta, for both pressure and flow.

Table 18: Comparing the amount of flow velocity augmentation created by the PEABC in both the ascending and descending aorta.

Flow Velocity Comparisons	PEABC Augmentation (Off Vs On)
Mean Flow Velocity at the Ascending aorta (diastolic phase only)	31.6%▲
Mean Flow Velocity at the Brachiocephalic artery (diastolic phase only)	18.5%▼
Mean Flow Velocity at the Ascending aorta (whole phase)	14.1%▲
Mean Flow Velocity at the Brachiocephalic artery (whole phase)	11.8%▼

7.1 Comparison to Simulation

The results obtained from testing the PEABC prototype on the cardiovascular simulation platform showed some level of evidence that the PEABC can augment both pressure and flow waveforms. Examining the effects of the PEABC prototype on the ascending aorta pressure shown previously in Chapter 6, it is noticed that pressure is augmented throughout the whole cardiac cycle with the largest increase at the beginning of systole and end diastolic phase. The largest reduction in ascending aorta pressure was observed to occur during the beginning of the diastolic phase. With the PEABC prototype set to apply an external peristaltic movement to the descending aorta in counterpulsation to the pressure waveform generated by the cardiovascular simulation platform, it was found that the timing of when each balloon inflates and deflates is reflected in the augmentation profile of the pressure wave in the ascending and descending aorta.

It is recognised that the pressure increase due to PEABC operation is fairly small. A similar outcome was observed in the pulse wave simulation software. The 1-D pulse wave simulation software can simulate the implementation of 4 external cuffs that induce peristaltic movement in the aortic wall. The pressure waveforms from the 1-D pulse wave simulation and the cardiovascular simulation platform are shown in Figure 7.2.

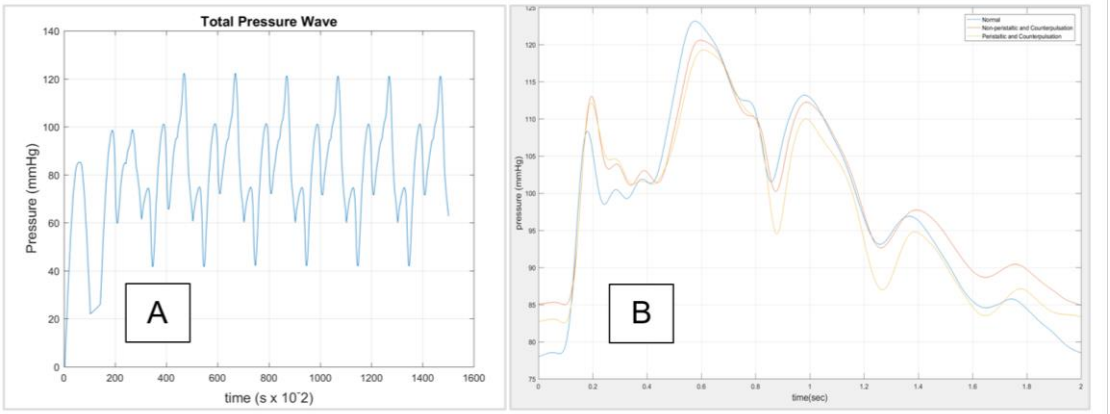

Figure 7.2: (A[9]): Comparison between the total pressure waveform from the pulse wave simulation and (B[10]): the pressure waveform from the cardiovascular simulation platform.

Comparing the peristaltic augmentation of the total pressure waveform from the pulse wave simulation against the PEABC prototype pressure augmentation to the phantom aorta 2 on the cardiovascular simulation platform shows that the pulse wave simulation's peristatic augmentation reduces the diastolic pressure as opposed to the PEABC prototype experimentation which increases the diastolic pressure. It is expected that these discrepancies are due to some parameters from the pulse wave simulation that do not match with the PEABC prototype experimentation. Some of the assumed key parameters include the following:

- Cuff wave profile from pulse wave simulation doesn't match the cuff wave profile created by the PEABC system.
- Aortic valve open/close profile created on the pulse wave simulation differs from the prosthetic aortic valve installed in the cardiovascular simulation platform.

However, in both the simulation and experimentation, there was very little change in systolic pressures, which is expected as the counterpulsation occurs in the diastolic phase. The relevant pressure waveforms are shown in Figure 7.3.

[9] Simulated data from 8 cycles

[10] Experimentation data obtained from 1 cycle

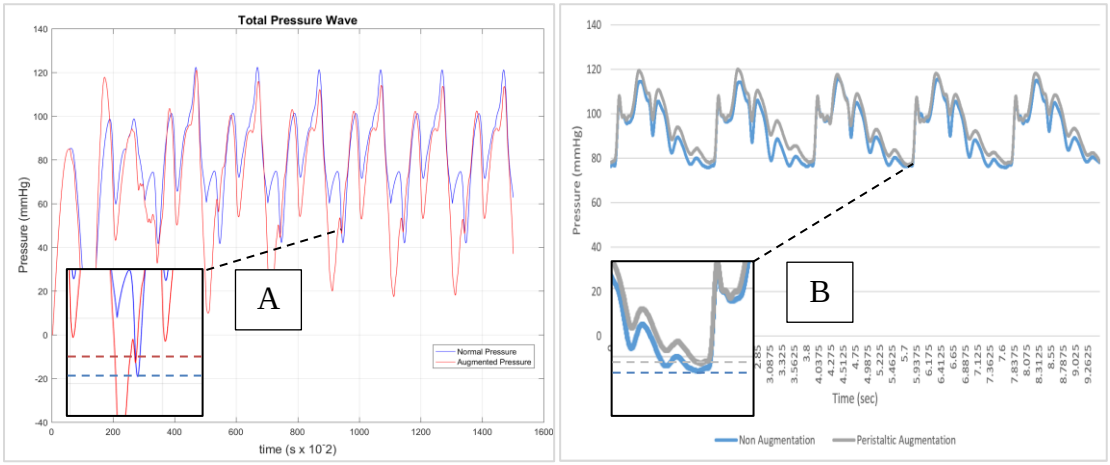

Figure 7.3: (A): An analysis of the differences of the peristaltic augmentation of the pulse wave simulation Vs. (B): Cardiovascular simulation platform.

The results from the PEABC prototype that tested three conditions – normal, non-peristaltic and peristaltic augmentation – indicate that non-peristaltic augmentation caused a larger increase in diastolic and end-diastolic pressures than the peristaltic augmentation. This result was also seen in the pulse wave simulation whereby a significant augmentation to the total pressure wave was shown as an outcome of all four balloon cuffs inflating and deflating at the same time – non-peristaltic augmentation simulated for 0.8 seconds and 2 seconds cardiac cycles.

7.2 Comparison to C-Pulse

Comparison of the effects of the C-Pulse® counterpulsation inflation on the pressure wave tested by Sunshine Heart [49] and the PEABC show an increase in end diastolic pressure (see Figure 7.4) in both non-peristaltic and peristaltic operations of the PEABC.

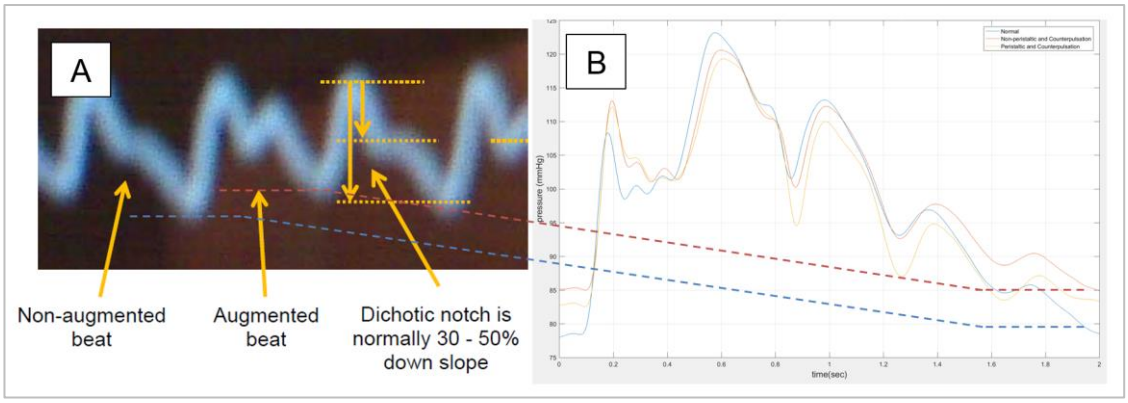

Figure 7.4: Pressure wave comparison between the effects of (A): C-Pulse® and (B): PEABC.

The PEABC increased pressure from 0 to 0.4 seconds, and from 1.5 to 2 sec and reduced pressure between 0.4 to 1.5 sec. The reduction in pressure during diastole was not present in Sunshine Heart's case; in fact, the C-Pulse® increases the dicrotic notch pressure [49]. This is likely due to differences in timing of the counterpulsation.

Studies documented by Sunshine Heart on the hemodynamics of C-Pulse® [47] obtained using ultrasound shows an increase in diastolic carotid flow velocity when the C-Pulse® is active. Sunshine Heart's average increase in carotid flow velocity was stated to be 30% [47] compared to the increase of the mean flow velocity in the ascending aorta of 14.1%. Results of operating the PEABC prototype showed an average increase in diastolic flow velocity in the ascending aorta of 31.62% ($P < 0.05$). This increase in flow velocities in the ascending aorta, along with C-Pulse results solidly indicate flow velocities in the carotid artery and the coronary flow could also increase. Further development of the cardiovascular simulation platform would be needed to validate this.

The C-Pulse® device has been designed to increase the diastolic arterial blood pressure, as well as increasing the coronary flow [40] using the counterpulsation system applied to a pneumatic balloon cuff attached to the ascending aorta to assist heart function. The results obtained lead to the conclusion that the PEABC prototype – with its corresponding ability to increase mean diastolic and end-diastolic pressure, and mean diastolic flow

velocities in the ascending aorta - should also be able to assist heart function. However, the amount diastolic arterial pressure augmentation of the C-Pulse® device is greater than that demonstrated by the PEABC prototype. In comparing the singular balloon cuff design of the C-Pulse® and the multi-chamber balloon cuff design of the PEABC, it is obvious that a large single balloon cuff design is significantly more effective at indenting the aortic wall than the PEABC smaller multi-balloon cuff (see Figure 7.5). Future adaptations of the PEABC system could address this issue, and it is of note that the PEABC system is located on the descending aorta, whereas the C-Pulse is located on the ascending aorta, which is more restricted in terms of space available. In addition, the multi-cuff system also has the potential for more nuanced control of pressure and flow in the aorta.

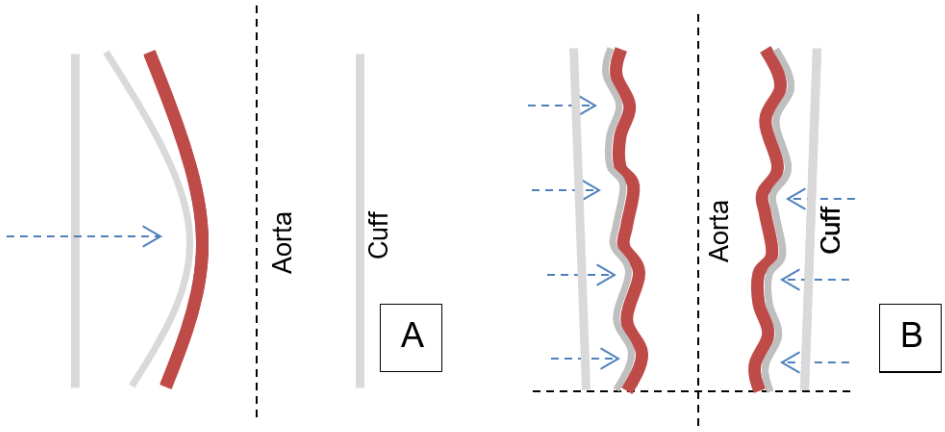

Figure 7.5: (A): Cross-sectional diagram of an aorta with the C-Pulse® inflated, and (B): PEABC with all balloon inflated.

The results obtained from testing the PEABC prototype on the cardiovascular simulation platform showed some level of evidence that the PEABC can augment both pressure and flow waveforms. Examining the effects that the PEABC prototype on the ascending aorta pressure shown previously in Chapter 6, it is noticed that the pressure is augmented throughout the whole cardiac cycle and the largest increase is at the beginning of systole and end diastolic phase. The biggest reduction in ascending aorta pressure was observed to occurring during the start of the diastolic phase. With the PEABC prototype set to apply an external peristaltic movement to the descending aorta in counterpulsation to the pressure waveform generated by the cardiovascular simulation platform, one can state that the timing of when each balloon inflates and deflates will reflect on the augmentation

profile of the pressure wave in the ascending and descending aorta. If we were to compare the effects of the C-Pulse® counterpulsation inflation on the pressure wave tested by Sunshine Heart [49] and the PEABC, both show an increase in end diastolic pressure (refer to Figure 7.4).

Chapter 8

Conclusion and Future Work

The objective of this research was to establish whether an extra-aortic balloon cuff operating with counterpulsation and peristaltic movement at the descending aorta has the potential to increase both diastolic pressure and flow. Both numerical simulation and physical simulations were created to investigate the pulse wave under the influence of an external augmentation.

It has been shown with both numerical and physical simulation that applying an external peristaltic movement to the walls of the descending aorta can augment the diastolic ascending aortic pressure and the diastolic brachiocephalic peak flow velocity (which can be considered as a surrogate of coronary flow). These results are qualitatively similar to those achieved by the existing C-Pulse system which also increases coronary flow. It is plausible that the PEABC system can also be effective in increasing coronary flow as a response to the increased diastolic pressure and flow velocity in the ascending aorta, which can be expected to drive flow into the coronary arteries during diastole (i.e. the heart's relaxed phase). This can assist heart function in the same way that C-Pulse® was designed to do – to help ensure perfusion of the weakened heart muscle by pumping more blood back to the walls of the heart muscle.

In comparing peristaltic and non-peristaltic motion being applied to the PEABC system, it was observed that the mean pressure measured at both the ascending and descending aorta was smaller when the PEABC system was operating with peristaltic motion. For the experimentation that was carried out in this study, an extra-aortic balloon cuff operating with counterpulsation and non-peristaltic motion had a better effect on augmenting pressure and flow to potentially assist heart function in a similar operation to the C-Pulse® system. However, it would be expected that with further modifications, future studies of an extra-aortic balloon cuff that performs counterpulsation and peristaltic motion could also potentially assist heart function.

This study provides a contribution to research into the novel concept of applying an external peristaltic movement with counterpulsation to the walls of the descending aorta to augment the pressure and flow in the aorta that can assist heart function. Both the pulse

wave simulation and the PEABC system has provided an understanding of the effects of waveform augmentation due to counterpulsation with and without peristaltic motion. The fabrication of the extra-aortic balloon cuff with multiple cavity chambers designed to produce peristaltic motion was achieved and has the potential to be adapted to future developments in healthcare devices. Development of the cardiovascular simulation platform has provided a hardware system that does not require a pump system to maintain mean pressure but instead naturally produce similar physiological pressure values and waveforms that would be expected in a human body using a single bellows actuation system. The manufacturing techniques developed for reliably producing the phantom aortas for the cardiovascular simulation platform will guide the development of arterial phantoms in other research sector. Together, the research presented in this thesis has the potential to assist and guide other studies related to phantom aorta development, 1-D pulse wave simulation and experimental cardiovascular and haemodynamic simulation for both research and teaching.

During the course of this research, a number of aspects of future investigation and development have been identified. They are mentioned below:

Pulse Wave Simulation

- Refining the pulse wave profile to produce closer to physiological pressure waveforms.
- Considering the development of a pulse wave simulation that factors in the change in aortic wall thickness, and the stiffness.

  Refining the peristaltic augmentation modelling by means of improving the balloon cuff augmentation waveform, timing of each balloon and increasing/decreasing the number of balloon cuffs being modelled.

Cardiovascular Simulation Platform

- Modifying the cardiovascular simulation platform to be stable when operated at a faster cardiac cycle, which will require larger interconnecting tubes between reservoirs.
- Further develop the phantom aorta– alternative materials, more anatomically representative phantom size, add coronary arteries.
- Obtain flow velocity under non-peristaltic movement from the PEABC prototype.

PEABC Prototype

- Further experimentation of changing the peristaltic inflation and deflation timing of each balloon cuff.
- Develop another balloon cuff with more air chambers to possibly improve peristaltic movement.
- Investigate the effect of cuff volume on flow augmentation.
- Minimising the prototype to a smaller footprint.
- Refine the EACD software to a more robust control system.
- Explore with programming other balloon cuff movements (e.g. reversed peristaltic motion).

Experimentation

- Explore the adaptation of the 2:1 ratio augmentation test that was performed by Sunshine Heart (extra-aortic cuff activated every 2^{nd} cardiac cycle)
- Utilise more flow/pressure probes to obtain more accurate data from the cardiovascular simulation platform. Furthermore, the flow rate at various points of the phantom aorta 2 could be explored to provide a better understanding of the effects that the PEABC prototype produces

Appendix A

Journal Paper Published in ICSPS 2016

Feasibility of a Novel Extra-Aortic Balloon Cuff with Peristaltic Motion and Counterpulsation to Assist Heart Function

Parn N. W. Jones[1], Dr. Andrew Lowe[1], Jeffrey Kilby[2]

[1]Institute of Biomedical Technologies, [2]Auckland University of Technology, Auckland, New Zealand

Abstract—**This paper scopes on how peristaltic model and counterpulsation system can be applied to an extra-aortic cuff to alter aortic flow and pressure waveforms. The system is similar to the application and technology of an existing clinical treatment – C-Pulse by Sunshine Heart - for patients with New York Heart Association (NYHA) class III and ambulatory class IV heart failure. The topics that are relevant to this paper involves the knowledge of counterpulsation, peristaltic model, aortic physiology and hemodynamics that was implemented into a device that resulted in augmentation of blood flow and pressure during a cardiac cycle. The investigation on these topics reflect on the how the concepts from coherent sources assist in the development of functional prototypes for future heart assisting devices. From the findings, an increase in ascending aortic pressure and flow velocity was present as result of the device operating on simulation platform.**

Keywords—**Peristaltic movement; Extra-aortic balloon cuff; Counterpulsation; Hemodynamics; Heart failure; Ascending aorta, Descending aorta, Phantom aorta, Cardiovascular simulation platform.**

I. INTRODUCTION

Congestive heart failure (CHF) remains one of the biggest unsolved healthcare issue encountering medical experts worldwide. According to statistics, CHF affects more that 5 million people in America alone with approximately 550,000 of new case diagnosed each year [1]. The fundamental foundation of this paper is based on exploring the feasibility of applying peristaltic model and counterpulsation to an extra aortic balloon cuff (EAB), to augment aortic flow and pressure that would result in reducing cardiac afterload. The outcome from this paper is aimed towards producing a functional prototype that is capable of assisting heart function compelled by these four main themes that will outline the context of the discussion towards alternative treatment for CHF:

- Extra-Aortic Balloon Cuff (C-Pulse)
  Current technology that uses counterpulsation developed by Sunshine Heart Inc. (under clinical trials)[2].

- Peristaltic Model
  The understating of peristaltic movement to transport viscous fluid in an elastic tube.

- Hemodynamic Pressure and Flow Modelling
  Knowledge of normal and abnormal hemodynamics and modelling of waveforms within the aorta.

- Counterpulsation
  Adapting the proven effectiveness of the existing counterpulsation system.

The importance of this paper points towards developing an alternative method of assisting heart function with a novel peristaltic balloon cuff, other than cardiopulmonary bypass surgery [3] or a full heart transplant with donor organs to treat CHF. An innovative device called C-Pulse developed by Sunshine Heart Inc. – an international medical device company – is a heart assisting system designed to clinically treat patients with Class III and ambulatory Class IV heart failure. Patients with Class III and ambulatory Class IV heart failure are usually incompetent to participate in normal activities and often have to compromise their quality of life (QoL) [4]. The C-Pulse Heart Assist System applies the concept of counterpulsation technology to reduce the workload of the weakened left ventricle by inflating and deflating a balloon cuff that is wrapped around the ascending aorta [3].

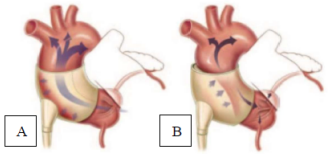

Figure 1: Extra-aortic balloon cuff (C-Pulse) attached to the ascending aorta. (A): deflated, (B): inflated).

The C-Pulse device was proven by Sunshine Heart that the clinical device is able to improve heart function in three different ways:

- *"Increase coronary blood flow with more oxygenated blood flowing to the blood vessels and heart muscle."*[2]

- *"Decrease cardiac afterload reducing how hard the heart has to work to pump blood through the body."* [2]

- *"Increase cardiac function with more blood being pumped from the heart to the rest of the body."* [2]

The C-Pulse device has been clinically tested on certain patients with CHF through which Sunshine Heart's finding confirms that the C-Pulse can increase the carotid diastolic flow velocity by an average of 30% with a marked increase net flow of (+57%) [5]. An investigation by Legget et al. on testing the C-Pulse verifies that the coronary flow is also increased by 67% - more blood flow transported back to the heart muscle walls to aid healing of the already damaged heart muscles walls [2][6].

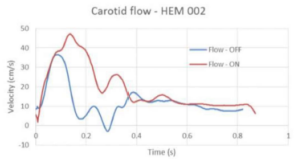

Figure 2: Carotid flow velocity. Blue: C-Pulse off, Red: C-Pulse on [5].

The effects of the C-Pulse in altering the blood flow in the aorta also directly alters the pressure waveform in the aorta through which the cardiac afterload is reduced and the cardiac output is increased as a result.

II. METHODOLOGY

With the implementation of exploring the additional concept of a peristaltic movement to the adaptation of extra-aortic balloon cuff with counterpulsation, a Peristaltic Extra-Aortic Balloon Cuff (PEABC) Prototype was developed. The prototype consists of three main components – extra aortic balloon cuff, pneumatic balloon cuff driver and the cuff controller.

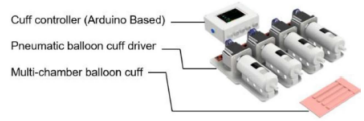

Figure 3: Components of the PEABC Prototype.

Multi chamber balloon cuff

The extra aortic balloon cuff is made up of four air chambers that are designed to squeeze the aorta when inflated. The balloon cuff is made up two layered materials – Silicone rubber (inner layer) and Pemotex (outer layer) – through which it is designed to be attached to the descending aorta.

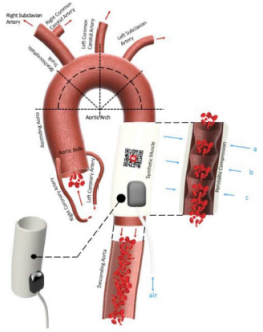

Figure 4: Balloon cuff attached to the descending aorta.

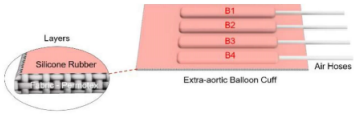

Figure 5: The compositions of the balloon cuff.

Pneumatic Cuff Driver

The multi chamber balloon cuff is inflated and deflated with four pneumatic cuff driver that uses an air tight bellows system. The compression and decompression of the bellows in driven by a linear actuator that operates at different timing to create a peristaltic movement of the multi chamber balloon cuff.

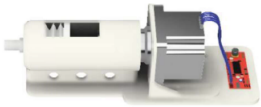

Figure 6: Assembled pneumatic cuff driver

Cuff Controller

The operation of the pneumatic cuff driver that inflates and deflates the multi chamber balloon cuff is performed by the cuff controller – powered by Arduino Mega 2560 – that takes in the pressure readings from the ascending aorta through which drives the position of the linear actuators at different times based on finite impulse response FIR filtering implementation.

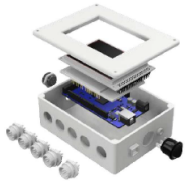

Figure 7: Exploded view of the cuff controller

The PEABC Prototype was designed to be attached to the descending aorta of which a phantom aorta with an experimentation platform – cardiovascular simulation platform – that could produce similar physiological pressure and flow outputted from left ventricle was created and utilized (see Figure 8).

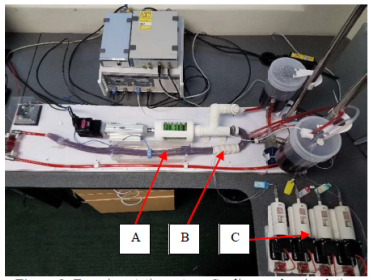

Figure 8: Experimentation setup. Cardiovascular simulation platform used for testing the PEABC prototype. (A): Phantom aorta made from Dragon Skin 10 (Silicone Rubber) (B): Balloon cuff, (C): Pneumatic cuff drivers.

III. RESULTS

Both pressure and flow velocities were obtained from the experimentation setup through which two conditions were performed – PEABC off and PEABC on – to examine the effectiveness of the PEABC prototype. The pressure at the ascending aorta shows an increase in both diastolic and end-diastolic pressure (see Figure 9). The mean ascending aorta pressure was increased by 3.94% ($P<0.05$).

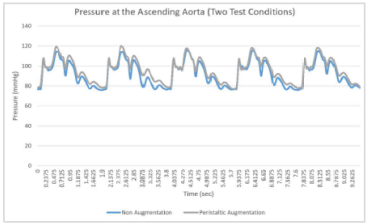

Figure 9: Comparison of the ascending aorta pressure with the PEABC off (Blue), PEABC on (Grey).

T Test: Two-Sample Assuming Equal Variances (n=5)		
	PEABC off	PEABC On
Mean	92.0657	95.6924
Variance	0.0905	0.6572
t Stat	9.3779	
P(T<=t) one-tail	6.84078E-06	
t Critical one-tail	1.8595	

Table 1: Student T-Test of the mean ascending aorta pressures obtained from the two test conditions.

The flow velocities in the ascending aorta were obtained using an ultrasound through which – in the same outcome – an increase in mean diastolic flow velocities were observed. With the same testing conditions, the effectiveness of the PEABC on increases mean diastolic flow velocity at the ascending aorta by 31.6% ($P<0.05$).

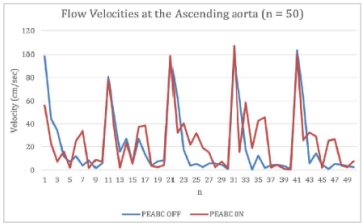

Figure 10: Comparison of the ascending aorta pressure with the PEABC off (Blue), PEABC on (Grey).

T Test: Two-Sample Assuming Equal Variances (n=5)		
	PEABC Off	PEABC On
Mean	13.4793	17.7398
Variance	6.4327	7.1784
t Stat	-2.5822	
P(T<=t) one-tail	0.0162	
t Critical one-tail	1.8595	

Table 2: Student T-Test of the mean diastolic flow velocities at the ascending aorta obtained from the two test conditions.

IV. DISCUSSION

The function of the PEABC prototype has been proven to augment both pressure and flow parameters in the ascending aorta based on the utilization of the cardiovascular simulation platform. Although the experimentation platform was able to create similar pressure values to physiological, more improvements can be done to eliminate some unwanted artifacts on the pressure waveform. However, the experimentation platform is able to demonstrate basic outputs that the PEABC prototype can be tested and validated on through which some aspects can be compared to the C-Pulse.

The extent data comparison in this paper is limited to the information about the C-Pulse that was published by Sunshine Heart Inc. of which the device is classified as an investigational device that is only being tested in clinical trials and thus limited data is obtainable. However, analyzing the augmentation profile of both pressure and flow velocities of the PEABC prototype, somewhat points to the assumption that with an increase in both of these parameters in the ascending aorta can result in an increase in both coronary flow and the carotid flow velocities (like the C-Pulse). Moreover, with the acquisition that an increase in mean pressure and flow velocity in the ascending aorta – similar to Sunshine Heart Inc. findings of augmenting the pressure and flow in the ascending aorta – assist heart function by transporting more blood back to heart muscle walls and reduce cardiac afterload [6].

The augmentation of the flow velocities in the carotid artery (with C-Pulse) when compared to the augmentation of the flow velocities in the ascending aorta (with PEABC), show similar diastolic augmentation characteristics (see Figure 2 and Figure 10). It is noticed that the PEABC's effectiveness of altering the mention parameters is not as great as the P-Pulse but the concept of combining the peristaltic model with counterpulsation is practicable.

V. CONCLUSION

The feasibility of this study lies towards further experimentations of both software and hardware aspects through which the current results somewhat indicate some level of heart assistance. Further studies are possible for execution of which many parts can be altered for obtaining more results. This study has the potential to not only provide knowledge of modelling hemodynamics with peristaltic augmentation and counterpulsation, but to also introduce a novel medical device that could assist heart function for patients with CHF in the near future.

VI. REFERENCE

[1] K. Franco, V. H. Thouram, and M. S. Slaughter, "Counterpulsation Devices for Myocardial Support."
[2] "C-Pulse - Sunshine Heart | C-Pulse Heart Assist System | Heart Failure | Counter HF." [Online]. Available: http://www.sunshineheart.com/c-pulse/. [Accessed: 07-Dec-2014].
[3] W. T. Abraham *et al.*, "Ambulatory Extra-Aortic Counterpulsation in Patients With Moderate to Severe Chronic Heart Failure," *JACC Heart Fail.*, vol. 2, no. 5, pp. 526–533, Oct. 2014.
[4] Redfield, M. M., Roger, V. L., & Weston, S. A., *Heart Failure*. 2015.
[5] "Hemodynamics of C-Pulse | Sunshine Heart." [Online]. Available: http://www.sunshineheart.com/hemodynamics-of-c-pulse/. [Accessed: 02-Jun-2016].
[6] M. E. Legget *et al.*, "Extra-Aortic Balloon Counterpulsation An Intraoperative Feasibility Study," *Circulation*, vol. 112, no. 9 suppl, p. I–26, 2005.

Appendix B

Abstract Published to Queenstown Research Week 2016

Feasibility of a Novel Extra-Aortic Balloon Cuff with Peristaltic Motion and Counterpulsation to Assist Heart Function.

Wangdee Jones, P.N.[1], Lowe, A.[1], Kilby, J.[2]

[1]Institute of Biomedical Technologies, Auckland University of Technology, NZ, [2]Department of Electrical and Electronics, School of Engineering, Auckland University of Technology, NZ.

The development of an extra-aortic balloon cuff with peristaltic motion and counterpulsation is explored to investigate the practicality for future treatments for chronic heart failure (CHF). This concept is an extension of existing heart assisting technology marketed as C-Pulse by Sunshine Heart[1] which is used to treat patients with New York Heart Association (NYHA) class III and ambulatory class IV heart failure.

This study incorporates experiments of both software simulation and hardware aspects. The software experiment simulated the aortic pressure and flow waveform under the influence of external peristaltic augmentation using a 1 dimensional wave propagation mode. The data was obtained from the simulation and a prototype device was constructed using the parameters from the simulation to test the overall feasibility of a novel extra-aortic balloon cuff. The hardware prototype was developed using Arduino base controller that drives multiple pneumatic pumps that inflate and deflate the cuff according to the rhythm of the heartbeat. A devised left ventricle mechanism with an attached phantom aorta was used as a testing platform for the functionality of the prototype.

Preliminary results from both simulation and experiment show that the system can augment the pressure waves in the descending aorta. Further testing is planned and will be compared with the C-Pulse system and other CHF devices in the efficacy of modulating coronary flow and cardiac afterload. This research has the potential to not only provide knowledge of modelling hemodynamic with peristaltic augmentation, but to also introduce a novel medical device that could assist heart function for patients with CHF in the near future.

1. *"C-Pulse Heart Assist System | Heart Failure Products," Sunshine Heart. [Online]. Available: http://www.sunshineheart.com/c-pulse-technology/. [Accessed: 01-Jun-2016].*

Appendix C

Big Easy Driver V1.1 Schematic

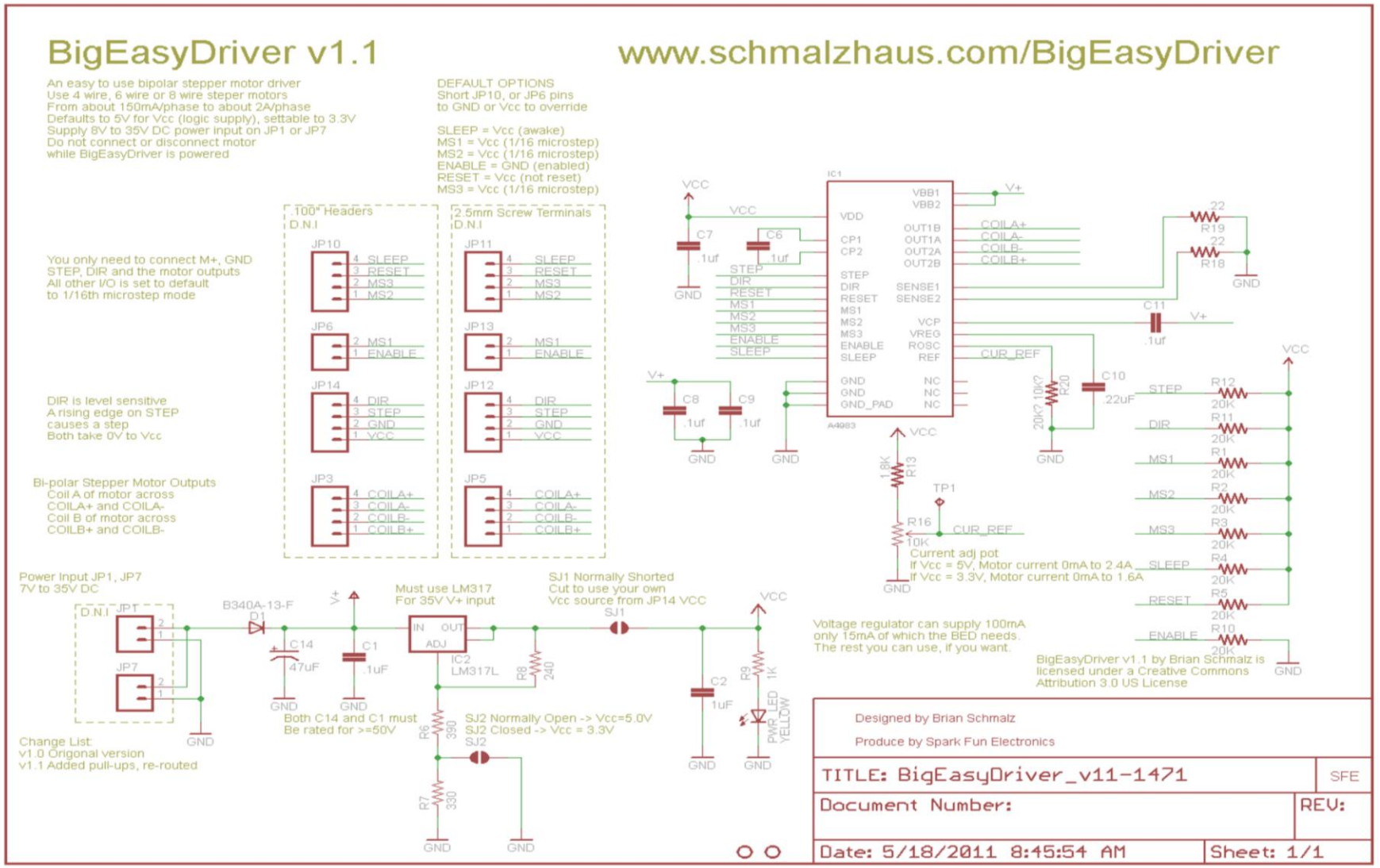
BigEasyDriver v1.1
www.schmalzhaus.com/BigEasyDriver
An easy to use bipolar stepper motor driver
Use 4 wire, 6 wire or 8 wire steper motors
From about 150mA/phase to about 2A/phase
Defaults to 5V for Vcc (logic supply), settable to 3.3V
Supply 8V to 35V DC power input on JP1 or JP7
Do not connect or disconnect motor
while BigEasyDriver is powered
DEFAULT OPTIONS
Short JP10, or JP6 pins
to GND or Vcc to override
SLEEP = Vcc (awake)
MS1 = Vcc (1/16 microstep)
MS2 = Vcc (1/16 microstep)
ENABLE = GND (enabled)
RESET = Vcc (not reset)
MS3 = Vcc (1/16 microstep)
.100" Headers
D.N.I
2.5mm Screw Terminals
D.N.I
You only need to connect M+, GND
STEP, DIR and the motor outputs
All other I/O is set to default
to 1/16th microstep mode
JP10
JP11
JP6
JP13
JP14
JP12
JP3
JP5
SLEEP
RESET
MS3
MS2
MS1
ENABLE
DIR
STEP
GND
VCC
COILA+
COILA-
COILB-
COILB+
DIR is level sensitive
A rising edge on STEP
causes a step
Both take 0V to Vcc
Bi-polar Stepper Motor Outputs
Coil A of motor across
COILA+ and COILA-
Coil B of motor across
COILB+ and COILB-
IC1
A4983
VDD
VBB1
VBB2
CP1
CP2
OUT1B
OUT1A
OUT2A
OUT2B
SENSE1
SENSE2
VCP
VREG
ROSC
REF
GND_PAD
NC
C7
C6
C8
C9
C10
C11
.1uf
.22uF
R19
R18
R20
R13
R16
R12
R11
R1
R2
R3
R4
R5
R10
22
20K
10K
1.8K
CUR_REF
TP1
Current adj pot
If Vcc = 5V, Motor current 0mA to 2.4A
If Vcc = 3.3V, Motor current 0mA to 1.6A
Voltage regulator can supply 100mA
only 15mA of which the BED needs.
The rest you can use, if you want.
BigEasyDriver v1.1 by Brian Schmalz is
licensed under a Creative Commons
Attribution 3.0 US License
Power Input JP1, JP7
7V to 35V DC
D.N.I
JP1
JP7
B340A-13-F
D1
C14
47uF
C1
.1uF
Must use LM317
For 35V V+ input
IC2
LM317L
IN
OUT
ADJ
R8
240
SJ1 Normally Shorted
Cut to use your own
Vcc source from JP14 VCC
SJ1
C2
1uF
R9
1K
PWR_LED
YELLOW
Both C14 and C1 must
Be rated for >=50V
R6
390
SJ2 Normally Open -> Vcc=5.0V
SJ2 Closed -> Vcc = 3.3V
SJ2
R7
330
Change List:
v1.0 Origonal version
v1.1 Added pull-ups, re-routed
Designed by Brian Schmalz
Produce by Spark Fun Electronics
TITLE: BigEasyDriver_v11-1471
SFE
Document Number:
REV:
Date: 5/18/2011 8:45:54 AM
Sheet: 1/1

Appendix D

Arduino Mega 2560 Schematic

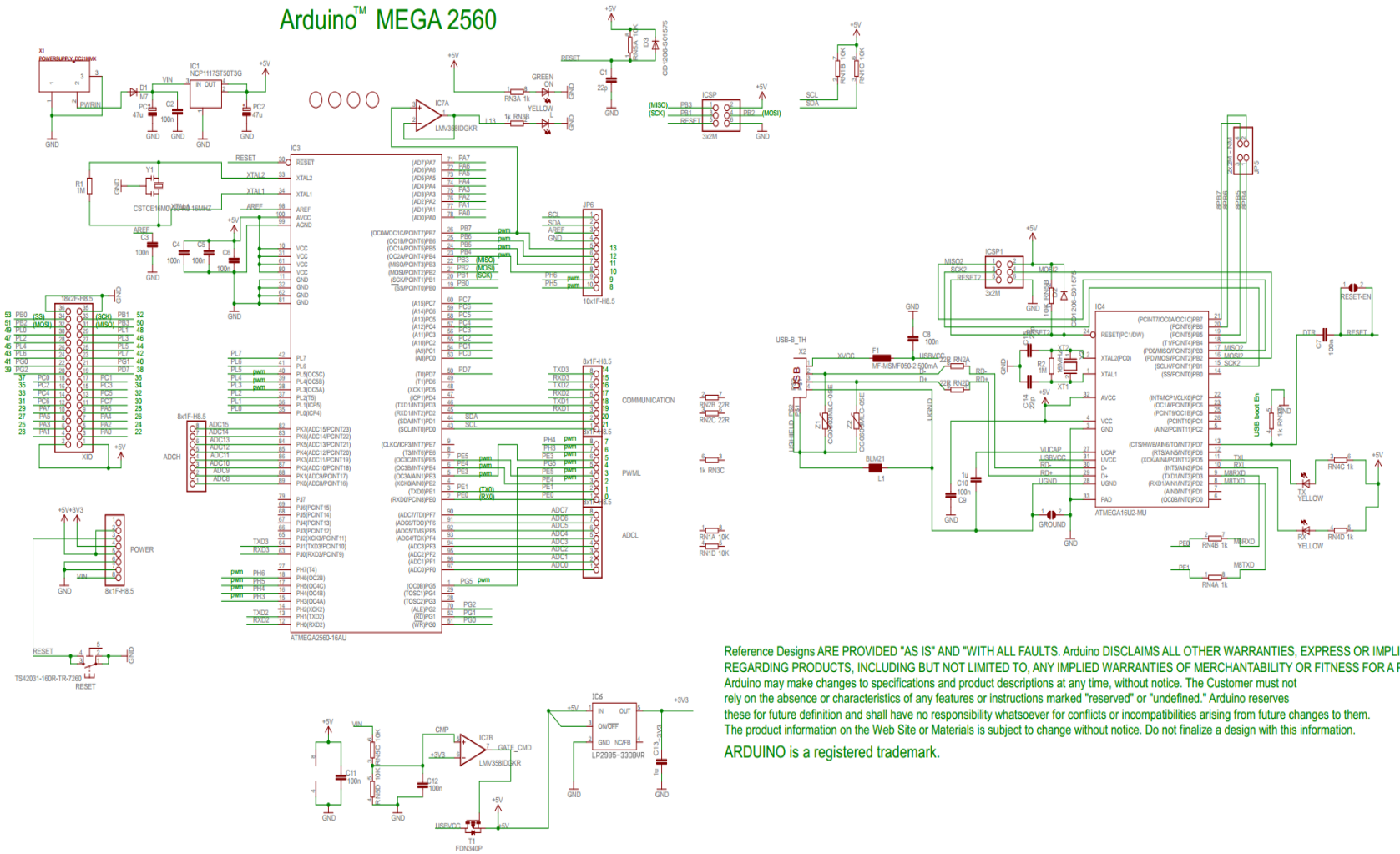

Appendix E

3.2” TFT LCD with SD and Touch for Arduino Mega with adjustable TFT shield Datasheet


Quickstart Guide
3.2" TFT LCD with SD and Touch for Arduino Mega with adjustable TFT shield
Product Name
—SKU 20-011-045
QUICK SPECS:
Brief Description
Getting Started:
sainLABS
engineering

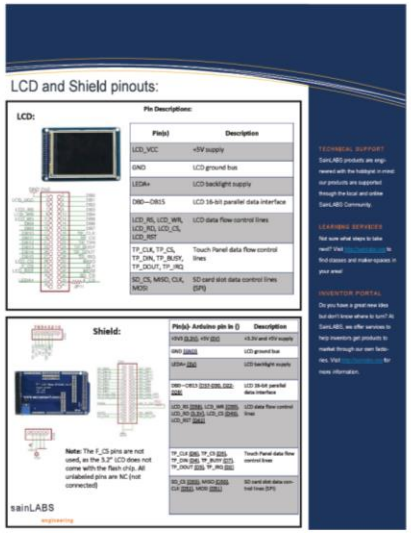
LCD and Shield pinouts:
LCD:
Pin Descriptions:
Pin(s)
Description
LCD_VCC
+5V supply
GND
LCD ground bus
LEDA+
LCD backlight supply
DB0—DB15
LCD 16-bit parallel data interface
LCD_RS, LCD_WR, LCD_RD, LCD_CS, LCD_RST
LCD data flow control lines
T_CLK, T_CS, T_DIN, T_BUSY, T_DOUT, T_IRQ
Touch Panel data flow control lines
SD_CS, MISO, CLK, MOSI
SD card slot data control lines (SPI)
Shield:
Note: The F_CS pins are not used, as the 3.2" LCD does not come with the flash chip. All unlabeled pins are NC (not connected)
sainLABS
engineering


Assembling the shield and LCD to the Mega:
Begin by carefully starting the rear connector of the TFT shield onto the Arduino Mega. Go slowly and ensure that all pins are inserted correctly and are straight.
Press down on the shield to seat all three connectors fully onto the Arduino Mega. Check to ensure all pins are seated fully.
Start the LCD display connector into the 40-pin header on the TFT shield, ensuring that all pins are properly aligned.
While applying pressure to the underside of the TFT shield, fully seat the LCD connector onto the TFT shield header using a slight rocking motion.
Finished! Your LCD is now ready to use.
To adjust the backlight: using a non-conductive tuning wand or screwdriver, turn the potentiometer screw on the TFT shield while the unit is powered to achieve the desired brightness level.
sainLABS
engineering

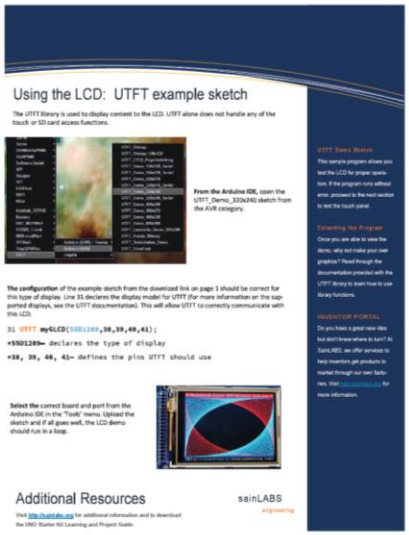
Using the LCD: UTFT example sketch
The UTFT library is used to display content to the LCD. UTFT alone does not handle any of the touch or SD card access functions.
From the Arduino IDE, open the UTFT_Demo_320x240 sketch from the AVR category.
The configuration of the example sketch from the download link on page 1 should be correct for this type of display. Line 31 declares the display model for UTFT (for more information on the supported displays, see the UTFT documentation). This will allow UTFT to correctly communicate with this LCD.
31 UTFT myGLCD(SSD1289,38,39,40,41);
•SSD1289– declares the type of display
•38, 39, 40, 41– defines the pins UTFT should use
Select the correct board and port from the Arduino IDE in the "Tools" menu. Upload the sketch and if all goes well, the LCD demo should run in a loop.
Additional Resources
sainLABS
engineering

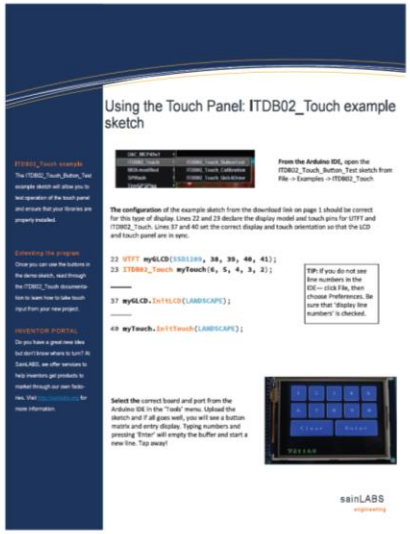
Using the Touch Panel: ITDB02_Touch example sketch
From the Arduino IDE, open the ITDB02_Touch_Button_Test sketch from File -> Examples -> ITDB02_Touch
The configuration of the example sketch from the download link on page 1 should be correct for this type of display. Lines 22 and 23 declare the display model and touch pins for UTFT and ITDB02_Touch. Lines 37 and 40 set the correct display and touch orientation so that the LCD and touch panel are in sync.
22 UTFT myGLCD(SSD1289, 38, 39, 40, 41);
23 ITDB02_Touch myTouch(6, 5, 4, 3, 2);
37 myGLCD.InitLCD(LANDSCAPE);
40 myTouch.InitTouch(LANDSCAPE);
TIP: If you do not see line numbers in the IDE -- click File, then choose Preferences. Be sure that 'display line numbers' is checked.
Select the correct board and port from the Arduino IDE in the "Tools" menu. Upload the sketch and if all goes well, you will see a button matrix and entry display. Typing numbers and pressing 'Enter' will empty the buffer and start a new line. Tap away!
sainLABS
engineering


Reading from SD: UTFT_SDRaw example
NOTE: SD card access can be achieved with the standard SDFat Arduino library alone. UTFT_SDRaw allows an easy way to also load bitmap images directly to the LCD from SD card. Images must be in "565" raw format. The UTFT library includes an image converter in the "Tools" folder within the library. Images must be uploaded to a FAT formatted SD card prior to inserting into the LCD card slot.
Prepare your SD card for this demo by ensuring that is formatted with the FAT file system. Then copy the contents of the "Image Files" folder from the library download to the SD card. This will allow the demo sketch access
With the SD contacts facing up, carefully insert the SD card into the slot on the back of the LCD and ensure that it is fully seated.
From 'Examples' in the Arduino IDE, open the SdRaw_320x240 test sketch.
The configuration of the example sketch from the download link on page 1 should be correct for this type of display. Lines 33 and 50 declare the display model and touch pins for UTFT and ITDB02_Touch. Line 81 sets the correct touch orientation.
33 UTFT myGLCD(SSD1289, 38, 39, 40, 41);
50 ITDB02_Touch myTouch(6, 5, 4, 3, 2);
81 myTouch.InitTouch(LANDSCAPE);
Select the correct board and port from the Arduino IDE in the "Tools" menu. Upload the sketch and if all goes well you will see the demo play, loading images from the SD card.
sainLABS
engineering

Appendix F

Marbocote® 277CEE Technical Bulletin

MARBOCOTE

Technical Data Sheet
227
Mold Release Agent

Product Description:

Marbocote 227 is an all purpose, semi-permanent release agent designed to release epoxy, polyester, vinyl-ester, phenolic, thermoplastics and most thermosetting resins. Marbocote 227 is an advanced polymeric resin system in a non-chlorinated organic solvent blend. **It does not contain any CFC's, chlorinated, aromatic or toxic solvents and was formulated to meet all of the regulations for solvent use in North America.** The polymeric resin in Marbocote 227 provides the highest slip and the most durable coating available, capable of providing maximum number of multiple releases per application. Like all other Marbocote release agents, Marbocote 227 will not contaminate the released surface. This product also excels as a silicone rubber mold sealant and is also great for adhesive fixtures as well.

Product Benefits:

- Easy application
- Fast curing at room temperature
- Thermally stable to 900°F
- Non-contaminating
- Non-chlorinated, ecologically friendly solvents
- Low odor
- Minimal mold build-up
- Durable; provides multiple releases per application
- Broad capabilities, releases most resins from all types of tooling

Physical Properties:

Appearance – Clear, colorless liquid
Odor – Slight Hydrocarbon
Specific Gravity – 0.762 g/cc
Solvents – Aliphatic Hydrocarbon
Coverage – 800-1000 sq. ft. /gal.
Shelf life – One year
Storage – Appropriate for flammable liquids (see MSDS for details)

Application Guidelines:

For safe handling of this product, please read MSDS prior to use.

Note: The polymeric resin used in Marbocote 227 reacts with moisture. Please ensure can is resealed after each use. Product is supplied ready to use, no shaking or mixing is required. Do not mix with other products or solvents. Mold cleaning and release agent application should always be performed in a well-ventilated area.

New/Repaired Molds: For best results, always insure that all molds and mold repairs are completely cured prior to applying release agents. For new, porous or damaged molds, RS415 ECO should be used prior to applying the Marbocote 227. This sealer may be used for all types of tooling. See RS415 ECO technical data sheet for application details. If necessary, polish mold to desired level of gloss. If a wax or silicone based release agent has been used previously, remove all traces of previous product using Marbocote Mold Cleaner MC. Marbocote 227 can be applied over existing semi-permanent release agents without a further cleaning step. However, the mold should be clean and dry before use.

Marbocote 227

Application:

1. Apply Marbocote 227 to a clean, dry cotton cloth.
2. Gently wipe over mold surface covering an area of approximately 2-3 sq/ft. and allow it to dry. Vigorous rubbing or polishing is not required.
3. Repeat steps 1 and 2 on the adjacent area. Ensure a good overlap with the previous area to provide complete coverage.
4. Repeat until mold is completely coated.
5. When dry, allow a further 15 minutes between coats for the film to cure. Note: If it takes 10-15 minutes to apply one coat to the entire mold, then you can go back to the starting point and proceed with the next coat.
6. Repeat Steps 1-5 above for a further 3 coats (4 in total).
7. When dry, allow final film to cure for at least 30 minutes at room temperature before molding. Allowing a longer cure or heat curing (15 minute @ 150°F) will improve film durability.

Touch-ups:

Maximum number of multiple releases can be achieved by applying a touch-up coat after the first couple of releases to break in the mold. When release becomes hesitant, reapply one coat of Marbocote 227 in the same manner as described above. Spot touch-ups can also be done on high wear or abrasive areas of the mold.

Tips To Achieve Optimum Results:

- Always apply following our application instructions.
- Always completely cure green/new molds and repairs per supplier's instructions.
- Do not over-apply the release agent. Best results will be obtained by applying light and uniform coats.
- Users of closed mold systems must make sure that all solvents have been completely dried and all residual solvent vapors have been evacuated from the mold cavity prior to closing the mold.
- If you choose to spray the release agent, you must use a dry and moisture free air source. Hold the spray nozzle 8-10 inches from the mold surface and apply a uniform film following the application instructions above. As always, use in a well ventilated area.

1/17/11 AI

Marbo America Inc. 5210-B South Orange Ave Orlando FL 32809
Tel: 407-857-1330 Fax: 407-857-1340

Appendix G

Rebound® 25 Technical Bulletin

Rebound® 25 and Rebound® 40

Brushable Platinum Silicone Rubbers

www.smooth-on.com

PRODUCT OVERVIEW

Rebound® 25 and Rebound® 40 are easy-to-use platinum-cure silicone rubbers which self-thicken for making brush-on molds of almost any model. Mixed 1A:1B by volume (no scale necessary), **Rebound®** rubber can be applied with a brush or spatula to vertical surfaces without sagging and will cure with negligible shrinkage to a flexible rubber.

Rebound® 25 is soft, flexible and is good for making molds of models with deep undercuts. Depending on model configuration, **Rebound® 25** can be inverted as a glove molds. **Rebound® 40** is harder and less flexible. These products are compatible. For example, you can apply two coats of **Rebound® 25** and back it up with two coats of **Rebound® 40**.

Advantages Over Urethane Brush-On® Rubber: (a) **Rebound®** will not stick to most surfaces, so surface preparation is minimal, (b) Two liquids that mix easily together, (c) stands up better to production casting of resins and low temperature melt metal alloys and (d) has a long library life.

4 thin layers are all that is necessary to make a flexible, strong and durable production mold for casting wax, gypsum, concrete or resins (urethane, polyester, etc.). And because **Rebound®** is a platinum silicone, it will last for many years in your mold library. Applications include reproducing sculpture, architectural restoration, making candle molds, casting pewter, etc.

Note: These products will not work with modeling clays containing sulfur under any circumstances.

TECHNICAL OVERVIEW

	Specific Gravity (g/cc) (ASTM D-1475)	Specific Volume (cu. in./lb.) (ASTM D-1475)	Pot Life (ASTM D-2471)	Cure Time	Color	Shore A Hardness (ASTM D-2240)	Tensile Strength (ASTM D-412)	Elongation at Break % (ASTM D-412)	Die B Tear Strength (ASTM D-624)	Shrinkage (in./in.) (ASTM D-2566)
Rebound® 25	1.14	23.5	20 min.	6 hours	Orange	25A	515 psi	690%	102 pli	<.001 in./in.
Rebound® 40	1.14	23.5	20 min.	6 hours	Green	40A	486 psi	324%	106 pli	<.001 in./in.

*All values measured after 7 days at 73°F/23°C

Mix Ratio: 1A:1B by volume or weight ***Mixed Viscosity:*** Brushable

PROCESSING RECOMMENDATIONS

PREPARATION...Safety - Use in a properly ventilated area ("room size" ventilation). Wear safety glasses, long sleeves and rubber gloves to minimize contamination risk. Wear vinyl gloves only. Latex gloves will inhibit the cure of the rubber.

Store and use material at room temperature (73°F/23°C). Warmer temperatures will drastically reduce working time and cure time. Storing material at warmer temperatures will also reduce the usable shelf life of unused material. These products have a limited shelf life and should be used as soon as possible.

Cure Inhibition - Addition cured silicone rubber may be inhibited by certain contaminants in or on the pattern to be molded resulting in tackiness at the pattern interface or a total lack of cure throughout the mold. Latex, sulfur clays, certain wood surfaces, newly cast polyester, epoxy or urethane rubber my cause inhibition. If compatibility between the rubber and the surface is a concern, a small-scale test is recommended. Apply a small amount of rubber onto a non-critical area of the pattern. Inhibition has occurred if the rubber is gummy or uncured after the recommended cure time has passed. To prevent inhibition, one or more coatings of a clear acrylic lacquer applied to the model surface is usually effective. Allow any sealer to thoroughly dry before applying rubber.

Important: Even with a sealer, Rebound® will not work with modeling clays containing sulfur. If you are not sure if your clay contains sulfur, do a small compatibility test before using for an important project.

Applying A Release Agent - Although not usually necessary, a release agent will make demolding easier when casting into most surfaces. Ease Release® 200 is a proven release agent for releasing silicone from silicone or other surfaces.Mann Ease Release® products are available from Smooth-On or your Smooth-On distributor. **Because no two applications are quite the same, a small test application to determine suitability for your project is recommended if performance of this material is in question.**

Safety First!

The Material Safety Data Sheet (MSDS) for this or any Smooth-On product should be read prior to use and is available upon request from Smooth-On. All Smooth-On products are safe to use if directions are read and followed carefully.

Keep Out of Reach of Children

BE CAREFUL - Avoid contact with eyes. Silicone polymers are generally non-irritating to the eyes however a slight transient irritation is possible. Flush eyes with water for 15 minutes and seek medical attention. Remove from skin with waterless hand cleaner followed by soap and water. Children should not use this product without adult supervision.

IMPORTANT - The information contained in this bulletin is considered accurate. However, no warranty is expressed or implied regarding the accuracy of the data, the results to be obtained from the use thereof, or that any such use will not infringe upon a patent. User shall determine the suitability of the product for the intended application and assume all risk and liability whatsoever in connection therewith.

MEASURING & MIXING...

Before you begin, pre-mix Part A and Part B separately. After dispensing required amounts of Parts A and B into mixing container (1A:1B by volume or weight), **mix thoroughly** making sure that you **scrape the sides and bottom of the mixing container several times.** The rubber should be a uniform color with no streaks.

APPLYING, CURING & PERFORMANCE...

Applying The Rubber - This product must be applied in layers. Mold makers generally find that four thin layers (minimum 3/8" thickness) is suitable for a strong, working mold. Using a stiff brush, the first coat of rubber should be applied in a very thin layer to capture intricate detail. Use dabbing strokes, especially around undercuts, to reduce entrapped air. Subsequent coats will add strength to the mold. Let the first coat dry for 60 minutes at room temperature until it becomes "tacky" before adding the next coat. "Tacky" is defined as sticky to the touch, but does not come off onto your gloved finger. Once "tacky", you are ready to apply the next layer. Tack-time can be reduced with mild heat (hair dryer or heat gun). Repeat until the necessary mold thickness is achieved.

Coverage: 1 gal. unit=7 sq.ft. (0.65 sq.m) - **5 gal. unit**=35 sq.ft. (3.25 sq. m)

Note: Although not necessary, adding a small amount of Silc-Pig® color pigment to every other mix of rubber will help you distinguish one layer from the next. Ensures that you apply a thorough coating each time and help build uniform layers.

Option: Add Thi-Vex® thickener for greater thixotropy—adding a small amount of Thi-Vex® will thicken the rubber for filling deep undercuts and detail. Amount to add? 1% of the total volume of your mix will increase thixotropy substantially.

Option: Add Smooth-On Silicone Thinner to your initial mix to lower the viscosity of your "print coat".

Apply A Support Shell - Once the mold is fully cured, a rigid support shell (mother mold) is necessary to support the rubber mold during casting. Plasti-Paste® II is a trowelable plastic is ideal as a mother mold material.

Curing - Allow the mold to cure at least 6 hours at room temperature (77°F/25°C) before demolding. Do not cure rubber where temperature is less than 65°F /18°C. You can cure the mold faster by applying mild heat (150°F/60°C) for 2 hours.

Using The Mold - When first cast, silicone rubber molds exhibit natural release characteristics. Depending on what is being cast into the mold, mold lubricity may be depleted over time and parts will begin to stick. No release agent is necessary when casting wax or gypsum. Applying a release agent such as Ease Release® 200 (available from Smooth-On) prior to casting polyurethane, polyester and epoxy resins is recommended to prevent mold degradation.

Mold Performance & Storage - The physical life of the mold depends on how you use it (materials cast, frequency, etc.). Casting abrasive materials such as concrete can quickly erode mold detail, while casting non-abrasive materials (wax) will not affect mold detail. Before storing, the mold should be cleaned with a soap solution and wiped fully dry. Two part (or more) molds should be assembled. Molds should be stored on a level surface in a cool, dry environment.

Call Us Anytime With Questions About Your Application.

Toll-free: **(800) 381-1733** Fax: **(610) 252-6200**

The new **www.smooth-on.com** is loaded with information about mold making, casting and more.

111816-JR

Appendix H

Dragon Skin® Series Technical Bulletin

Dragon Skin® Series

Addition Cure Silicone Rubber Compounds

Cured Material Certified Skin Safe!

www.smooth-on.com

PRODUCT OVERVIEW

Dragon Skin® silicones are high performance platinum cure liquid silicone compounds that are used for a variety of applications ranging from creating skin effects and other movie special effects to making production molds for casting a variety of materials. Because of the **superior physical properties** and flexibility of Dragon Skin® rubbers, they are also used for medical prosthetics and cushioning applications. Dragon Skin® rubbers are also used for a variety of industrial applications and have a service temperature range of a constant -70°F to +400°F (-21°C to + 205°C).

Great for Making Molds for a Variety of Applications - Available in **Shore 10A, 20A and 30A,** Dragon Skin® silicones can be used to make exceptionally strong and tear resistant molds for casting plaster, wax, concrete (limited production run), resins and other materials.

Time Tested, Versatile Special Effects Material – Soft, super-strong and stretchy, Dragon Skin® 10 (**Very Fast, Fast, Medium and Slow speeds**) is used around the world to make spectacular skin and creature effects. An infinite number of color effects can be achieved by adding Silc Pig® silicone pigments or Cast Magic® effects powders. Cured rubber can also be painted with the Psycho Paint® system. Cured material is skin safe and certified by an independent laboratory to ISO 10993-10, Biological evaluation of medical devices, Part 10: Tests for irritation and skin sensitization.

Easy To Use – Dragon Skin® silicones are mixed 1A:1B by weight or volume. Liquid rubber can be thinned with Silicone Thinner® or thickened with THI-VEX®. Rubber cures at room temperature (73°F/23°C) with negligible shrinkage. ***Vacuum degassing is recommended to minimize air bubbles in cured rubber.***

TECHNICAL OVERVIEW

	Mixed Viscosity (ASTM D-2393)	Specific Gravity (g/cc) (ASTM D-1475)	Specific Volume (cu. in./lb.) (ASTM D-1475)	Pot Life (ASTM D-2471)	Cure Time	Shore A Hardness (ASTM D-2240)	Tensile Strength (ASTM D-412)	100% Modulus (ASTM D-412)	Elongation at Break % (ASTM D-412)	Die B Tear Strength (ASTM D-624)	Shrinkage (in./in.) (ASTM D-2566)
Dragon Skin® 10 Very Fast	23,000 cps	1.07	25.8	4 min.	30 min.	10A	475 psi	22 psi	1000%	102 pli	< .001 in./in.
Dragon Skin® 10 Fast	23,000 cps	1.07	25.8	8 min.	75 min.	10A	475 psi	22 psi	1000%	102 pli	< .001 in./in.
Dragon Skin® 10 Medium	23,000 cps	1.07	25.8	20 min.	5 hours	10A	475 psi	22 psi	1000%	102 pli	< .001 in./in.
Dragon Skin® 10 Slow	23,000 cps	1.07	25.8	45 min.	7 hours	10A	475 psi	22 psi	1000%	102 pli	< .001 in./in.
Dragon Skin® 20	20,000 cps	1.08	25.6	25 min.	4 hours	20A	550 psi	49 psi	620%	120 pli	< .001 in./in.
Dragon Skin® 30	30,000 cps	1.08	25.7	45 min.	16 hours	30A	500 psi	86 psi	364%	108 pli	< .001 in./in.

Mix Ratio: 1A:1B by volume or weight
Color: Translucent
Useful Temperature Range: -65°F to +450°F (-53°C to +232°C)
Dielectric Strength (ASTM D-147-97a)**:** >350 volts/mil

*All values measured after 7 days at 73°F/23°C

PROCESSING RECOMMENDATIONS

PREPARATION... Safety – Use in a properly ventilated area ("room size" ventilation). Wear safety glasses, long sleeves and rubber gloves to minimize contamination risk. Wear vinyl gloves only. Latex gloves will inhibit the cure of the rubber.

Store and use material at room temperature (73°F/23°C). Warmer temperatures will drastically reduce working time and cure time. Storing material at warmer temperatures will also reduce the usable shelf life of unused material. These products have a limited shelf life and should be used as soon as possible.

Cure Inhibition – Addition-cure silicone rubber may be inhibited by certain contaminants in or on the pattern to be molded resulting in tackiness at the pattern interface or a total lack of cure throughout the mold. Latex, tin-cure silicone, sulfur clays, certain wood surfaces, newly cast polyester, epoxy, tin cure silicone rubber or urethane rubber may cause inhibition. If compatibility between the rubber and the surface is a concern, a small-scale test is recommended. Apply a small amount of rubber onto a non-critical area of the pattern. Inhibition has occurred if the rubber is gummy or uncured after the recommended cure time has passed.

Because no two applications are quite the same, a small test application to determine suitability for your project is recommended if performance of this material is in question.

Safety First!

The Material Safety Data Sheet (MSDS) for this or any Smooth-On product should be read prior to use and is available upon request from Smooth-On. All Smooth-On products are safe to use if directions are read and followed carefully.

Keep Out of Reach of Children

Be careful. Use only with adequate ventilation. Contact with skin and eyes may cause irritation. Flush eyes with water for 15 minutes and seek immediate medical attention. Remove from skin with waterless hand cleaner followed by soap and water.

Important: The information contained in this bulletin is considered accurate. However, no warranty is expressed or implied regarding the accuracy of the data, the results to be obtained from the use thereof, or that any such use will not infringe upon a patent. User shall determine the suitability of the product for the intended application and assume all risk and liability whatsoever in connection therewith.

Cure Inhibition – To prevent inhibition, one or more coatings of a clear acrylic lacquer applied to the model surface is usually effective. Allow any sealer to thoroughly dry before applying rubber. Note: Even with a sealer, platinum silicones will not work with modeling clays containing heavy amounts of sulfur. Do a small scale test for compatibility before using on your project.

Applying A Release Agent - Although not usually necessary, a release agent will make demolding easier when pouring into or over most surfaces. Ease Release® 200 is a proven release agent for making molds with silicone rubber. Mann Ease Release® products are available from Smooth-On or your Smooth-On distributor.

IMPORTANT: To ensure thorough coverage, lightly brush the release agent with a soft brush over all surfaces of the model. Follow with a light mist coating and let the release agent dry for 30 minutes.

If there is any question about the effectiveness of a sealer/release agent combination, a small-scale test should be made on an identical surface for trial.

MEASURING & MIXING...

Before you begin, pre-mix Part B thoroughly. After dispensing required amounts of Parts A and B into mixing container (1A:1B by volume or weight), **mix thoroughly for 3 minutes making sure that you scrape the sides and bottom of the mixing container several times.** After mixing parts A and B, vacuum degassing is recommended to eliminate any entrapped air. Vacuum material for 2-3 minutes (29 inches of mercury), making sure that you leave enough room in container for product volume expansion.

POURING, CURING & MOLD PERFORMANCE...

For best results, pour your mixture in a single spot at the lowest point of the containment field. Let the rubber seek its level up and over the model. **A uniform flow will help minimize entrapped air.** The liquid rubber should level off at least 1/2" (1.3 cm) over the highest point of the model surface.

Curing / Post Curing - Allow rubber to cure as prescribed at room temperature (73°F/23°C) before demolding. Do not cure rubber where temperature is less than 65°F/18°C. **Optional:** Post curing the mold will aid in quickly attaining maximum physical and performance properties. After curing at room temperature, expose the rubber to 176°F/80°C for 2 hours and 212°F/100°C for one hour. Allow mold to cool to room temperature before using.

If Using As A Mold - When first cast, silicone rubber molds exhibit natural release characteristics. Depending on what is being cast into the mold, mold lubricity may be depleted over time and parts will begin to stick. No release agent is necessary when casting wax or gypsum. Applying a release agent such as Ease Release® 200 (available from Smooth-On) prior to casting polyurethane, polyester and epoxy resins is recommended to prevent mold degradation.

Thickening Dragon Skin® Silicones - **THI-VEX®** is made especially for thickening Smooth-On's silicones for vertical surface application (making brush-on molds). Different viscosities can be attained by varying the amount of THI-VEX®. See the **THI-VEX® technical bulletin** (available from Smooth-On or your Smooth-On distributor) for full details.

Thinning Dragon Skin® Silicones - Smooth-On's **Silicone Thinner®** will lower the viscosity of Dragon Skin® for easier pouring and vacuum degassing. **A disadvantage** is that ultimate tear and tensile are reduced in proportion to the amount of **Silicone Thinner®** added. ***It is not recommended to exceed 10% by weight of total system (A+B).*** See the **Silicone Thinner® technical bulletin** (available from Smooth-On or your Smooth-On distributor) for full details.

Mold Performance & Storage - The physical life of the mold depends on how you use it (materials cast, frequency, etc.). Casting abrasive materials such as concrete can quickly erode mold detail, while casting non-abrasive materials (wax) will not affect mold detail. Before storing, the mold should be cleaned with a soap solution and wiped fully dry. Two part (or more) molds should be assembled. Molds should be stored on a level surface in a cool, dry environment.

Call Us Anytime With Questions About Your Application.
Toll-free: **(800) 381-1733** Fax: **(610) 252-6200**

The new **www.smooth-on.com** is loaded with information about mold making, casting and more.

072516-JR

Appendix I

Pulse Wave Simulation Matlab®

Code

```
AValv = zeros(nt,nx);
%Aortic valve
PRFCoe  = zeros(nt,nx);
%Foward Reflection coefficient matrix
PTFCoe  = zeros(nt,nx);
%Foward Transmission coefficient matrix
PRBCoe = zeros(nt,nx);
%Backwards Reflection coefficient matrix
PTBCoe = zeros(nt,nx);
%Backwards Transmission coefficient matrix
Y   = zeros(nt,nx);
%Admittance matrix
Pf  = zeros(nt,nx);
%Foward Pressure Matrix
Pb  = zeros(nt,nx);
%Backwards Pressure Matrix
Pt  = zeros(nt,nx);
%Transmitted Pressure Matrix

%%%%%%%%%%%%%%%%%%%%%%%%%%%%%%%%%% Wave Initialization %%%%%%%%%%%%%%%%%%%%%%%

dr   = ri-rt;
%difference in radidus
grad = dr/nx;
%gradiance of radius along aorta
N    = 2/dt;
%wave shape
n    = 1:cc*N;
%wave shape
n0   = 2*N;
%wave shape
xL   = nx/dx;
%x segment
xL0  = 1:xL/10;
%x segment scale
t(:,1) = (0:nt-1)*dt;
%time domain scale
AValvCloseCoe = 1;
%aortic valve closing coefficient

[b,a]=butter(2,0.085);
AValv = AValvCloseCoe*filtfilt(b,a,double(mod(t,2)>0.6));
%aortic valve profile
PresWave=Ampl*(max(0,sin(2*pi*1/2*t)));
%pressure wave profile

InflateTime1 = 0.5;
InflateTime2 = 0.6;
InflateTime3 = 0.7;
InflateTime4 = 0.8;
%inflation time for each cuff (sec)

InflateLocation1 = 0.015;
InflateLocation2 = 0.035;
InflateLocation3 = 0.055;
InflateLocation4 = 0.075;
%inflation location for each cuff (m)
```

```
%%%%%%%%%%%%%%%%%%%%%%%%%%%%%%%%%% Main Code %%%%%%%%%%%%%%%%%%%%%%%%%%%%%%%%

for m = 2:nt
  for n = 1:nx
        CuffWave1(:,n)=-0.005*max(0,sin(2*pi*1/2*(t-InflateTime1))*exp(-((n-
InflateLocation1*N)/(N/40)).^6));
        CuffWave2(:,n)=-0.005*max(0,sin(2*pi*1/2*(t-InflateTime2))*exp(-((n-
InflateLocation2*N)/(N/40)).^6));
        CuffWave3(:,n)=-0.005*max(0,sin(2*pi*1/2*(t-InflateTime3))*exp(-((n-
InflateLocation3*N)/(N/40)).^6));
        CuffWave4(:,n)=-0.005*max(0,sin(2*pi*1/2*(t-InflateTime4))*exp(-((n-
InflateLocation4*N)/(N/40)).^6));
        %cuff wave propagation
        dR(m,n) = (ri-(n*grad));
        AortaRad(m,n) =
dR(m,n)+CuffWave1(m,n)+CuffWave2(m,n)+CuffWave3(m,n)+CuffWave4(m,n);
        %calulating differnce in radius over aortic length
        C(m,n)  = sqrt(E*h/(2*Roh*(AortaRad(m,n))*(1-v^2)));
        %calulating pwv
        A(m,n)  = pi*((AortaRad(m,n)^2));
        %calculating area of aorta
        Y(m,n)  = A(m,n)/Roh*C(m,n);
        %calculating admittance
  end

  for n = 1:nx-1
        PRFCoe(m,n) = (Y(m,n) - Y(m,n+1)) / (Y(m,n) + Y(m,n+1));
        %calulating forward reflecting pressure coefficient
        PTFCoe(m,n) = 2 * Y(m,n) / (Y(m,n)+(Y(m,n+1)));
        %calulating forward total pressure coefficient
  end

  for n = 2:nx
        PRBCoe(m,n) = (Y(m,n) - (Y(m,n-1))) / (Y(m,n) + (Y(m,n-1)));
        %calulating backwards reflecting pressure coefficient
        PTBCoe(m,n) = 2 * Y(m,n) / (Y(m,n) + (Y(m,n-1)));
        %calulating backwards total pressure coefficient
  end

  for n = 1:nx
      if n == 1
          PFLeft    = PresWave(m);
          TfCoeLeft = 1;
          RbCoeLeft = AValv(m);
          %initialise wave from start of aortic length
      else
          PFLeft    = Pf(m,n-1);
          TfCoeLeft = PTFCoe(m,n-1);
          RbCoeLeft = PRBCoe(m,n);
      end

      if n == nx
          PbRight    = 0;
          TbCoeRight = 0.5;
          RfCoeRight = 0.5;
          %bifucation ratio at end of aortic length
```

```
        else
            PbRight    = Pb(m,n+1);
            TbCoeRight = PTBCoe(m,n+1);
            RfCoeRight = PRFCoe(m,n);
        end

        Pf(m+1,n) = PFLeft * TfCoeLeft + Pb(m,n) * RbCoeLeft;
        %calculating and update forwards pressure wave
        Pb(m+1,n) = PbRight * TbCoeRight + Pf(m,n) * RfCoeRight;
        %calculating and update backwards pressure wave
        Pt(m+1,n) = Pf(m,n) + Pb(m,n);
        %calculating and update total pressure wave
    end
end

%%%%%%%%%%%%%%%%%%%%%%%%%%%%%%%%% Wave Plotting %%%%%%%%%%%%%%%%%%%%%%%%%%%%%%

figure(1)
mesh(Pf);
xlabel('x(mm)','FontSize',14), ylabel('t(s)','FontSize',14),
zlabel('Ampl','FontSize',14)
title(' {Pressure Wave - Forward}', 'FontSize',14)
%mesh plotting forwards pressure

figure(2)
mesh(Pb);
xlabel('x(cm)','FontSize',14), ylabel('t(s)','FontSize',14),
zlabel('Ampl','FontSize',14)
title(' {Pressure Wave - Backward}', 'FontSize',14)
%mesh plotting backwards pressure

figure(3)
mesh(Pt);
xlabel('x(cm)','FontSize',14), ylabel('t(s)','FontSize',14),
zlabel('Ampl','FontSize',14)
title(' {Pressure Wave - Total}', 'FontSize',14)
%mesh plotting total pressure

figure(4)
plot(Pt(:,1));
grid on;
title1 = ['Total Pressure Wave'];
title(title1 ,'fontsize',14);
xlabel('time (s x 10^-2)','fontSize',14);
ylabel('Pressure (mmHg)','fontSize',14);
fh = figure(4);
set(fh, 'color', 'white');
%plotting total pressure

figure(5)
plot(C(2,:))
grid on;
title1 = ['PWV of the Descending Aorta'];
title(title1 ,'fontsize',14);
xlabel('X-Segment (m x 10^-1)','fontSize',14);
ylabel('PWV (m/s)','fontSize',14);
fh = figure(5);
```

```
set(fh, 'color', 'white');
%plotting pwv waveform

figure(6)
plot(AortaRad(2,:))
grid on;
title1 = ['Change in Aortic Radius'];
title(title1 ,'fontsize',14);
xlabel('X-Segment (m x 10^-1)','fontSize',14);
ylabel('Radius (m)','fontSize',14);
fh = figure(6);
set(fh, 'color', 'white');
%plotting aortic radius profile

figure(7)
plot(AValv(:,1))
grid on;
title1 = ['Aortic Valve Open/Cose'];
title(title1 ,'fontsize',14);
xlabel('time','fontSize',14);
ylabel('AV Coefficient','fontSize',14);
fh = figure(7);
set(fh, 'color', 'white');
%plotting aortic valve profile

figure(8)
for m = 1:nt
  plot(xL0 ,Pf(m,:), 'b', xL0 ,Pb(m,:), 'r', xL0 ,Pt(m,:), 'g');
  grid on;
  legend('Forward wave','Backwards wave', 'Total wave')
  xlabel('X-Segment (m)','fontSize',14);
  ylabel('Pulse Wave Amplitude','fontSize',14);
  title1 = ['TIME STEP = ',num2str(m), '   TIME = ',num2str(t(m)),' (s)'];
  title(title1 ,'fontsize',14);
  ylim([-AmpLim AmpLim]);
  h = gca;
  get(h,'FontSize');
  set(h,'FontSize',14);
  fh = figure(8);
  set(fh, 'color', 'white');
  F = getframe(fh);
  %animation plotting of pressure waves
end

%%%%%%%%%%%%%%%%%%%%%%%%%%%%%%%%%%%%%%%%%%%%%%%%%%%%%%%%%%%%%%%%%%%%%%%%%%%%%%%%%%%%%%%%%%%%%%%%%%%%%%%%%%%%%%%%%%%%%%%%%%%%%%%%%%%%%%%%%%%%%%%%%%%
```

Appendix J

EACD Software Arduino Code

```
//    Parn Naruenart Wangdee Jones
//    Auckland University of Technology
//    EACD_Software
//    Code for controlling the Cuff controller to inflated and deflate a
multichamber balloon cuff.
//    Version 3.51
//    25/11/2016

#include <AccelStepper.h>
#include <UTFT_Buttons.h>
#include <TimerOne.h>

#define pressureSensor A14
#define FILTERTAPS 1
#define HISTORY 1000

AccelStepper stepper1(1, 9, 8);   //(GND, STEP, DIR)
AccelStepper stepper2(1, 11, 10); //(GND, STEP, DIR)
AccelStepper stepper3(1, 13, 12); //(GND, STEP, DIR)
AccelStepper stepper4(1, 16, 17); //(GND, DIR, STEP)

unsigned long start_times[100];
unsigned long stop_times[100];
unsigned long readvalues[100];

bool motorFlag;
byte n = 0;
extern uint8_t SmallFont[];
extern uint8_t BigFont[];
extern uint8_t Dingbats1_XL[];
float posadc;
float absolutePressure;
float sensorPressure;
float sensorVoltage;
float aorticPressure;
float sensorValue;
int pos, pos1, pos2, pos3, pos4;
int coef[FILTERTAPS];
int values[HISTORY];
int outs[HISTORY];
int button1, button2, pressed_button;
int i = 0;
int gain = 1;
long previousMillis = 0;
long interval = 2000;
int k = 0;

UTFT          myGLCD(ITDB32S, 38, 39, 40, 41);
UTouch        myTouch(6, 5, 4, 3, 2);
UTFT_Buttons  myButtons(&myGLCD, &myTouch);

void setup(void)
{
  Serial.begin(250000);

  boolean default_colors = true;
  int speedValue = 600;
  int accelValue = 5000;

  pinMode(pressureSensor, INPUT);
```

```
button1 = myButtons.addButton( 10,  130, 90,  30, "Enable");
//x-axis, y-axis, but length, but height
button2 = myButtons.addButton( 10, 170, 90,  30, "Disable");
myGLCD.InitLCD();
myGLCD.clrScr();
myGLCD.setFont(SmallFont);
myGLCD.setColor(VGA_BLACK);
myGLCD.fillScr(VGA_WHITE);
myTouch.InitTouch();
myTouch.setPrecision(PREC_MEDIUM);
myButtons.setTextFont(SmallFont);
myButtons.setSymbolFont(Dingbats1_XL);
myGLCD.setColor(VGA_BLACK);
myGLCD.setBackColor(VGA_WHITE);
myGLCD.setFont(BigFont);
myGLCD.print("Aortic Cuff Driver", 16,  20);
myGLCD.setFont(SmallFont);
myButtons.setButtonColors(VGA_WHITE, VGA_GRAY, VGA_BLACK, VGA_RED,
VGA_RED);
myButtons.drawButtons();
myGLCD.setColor(0, 0, 0);
myGLCD.print("  Status:", 0, 210);
myGLCD.print("  Extra Aortic Cuff Driver V2.1", 0, 225);
myGLCD.print("  None    ", 70, 210);
//headline
myGLCD.drawLine(10,10,310,10);
myGLCD.drawLine(10,40,310,40);
//redlines
myGLCD.setColor(255, 0, 0);
myGLCD.drawLine(30,60,290,65);
myGLCD.drawLine(29,59,289,64);
myGLCD.drawLine(28,58,288,63);
myGLCD.drawLine(30,110,290,105);
myGLCD.drawLine(31,111,291,106);
myGLCD.drawLine(32,112,292,107);
myGLCD.setColor(0, 0, 0);
//b1-b4 boxes
myGLCD.print("B1", 50,  79);
myGLCD.print("B2", 118,  79);
myGLCD.print("B3", 186,  79);
myGLCD.print("B4", 254,  79);
myGLCD.drawRect(32,64,82,105); // B1
myGLCD.drawRect(99,65,149,104); // B2
myGLCD.drawRect(166,66,216,103); // B3
myGLCD.drawRect(233,67,283,102); // B4
myGLCD.setColor(0, 0, 0);
myGLCD.setFont(SmallFont);
myGLCD.print("ADC(10bit) :", 120, 130);
myGLCD.print("Position(mm) :", 120, 150);
myGLCD.print("Pressure(mmHg) :", 120, 170);
myGLCD.print("sensorValue(V) :", 120, 190);

//max value for speed
stepper1.setMaxSpeed(speedValue);
stepper1.setSpeed(600);
//max value for acceleration
stepper1.setAcceleration(4000);
stepper1.setAcceleration(accelValue);
stepper2.setMaxSpeed(speedValue);
stepper2.setSpeed(600);
```

```
stepper2.setAcceleration(4000);
stepper2.setAcceleration(accelValue);
stepper3.setMaxSpeed(speedValue);
stepper3.setSpeed(600);
stepper3.setAcceleration(4000);
stepper3.setAcceleration(accelValue);
stepper4.setMaxSpeed(speedValue);
stepper4.setSpeed(600);
stepper4.setAcceleration(4000);
stepper4.setAcceleration(accelValue);

// initialise coefficient array
for(i=0;i<FILTERTAPS;i++)
{
coef[i]=1;
}
// initialise filtertap history array and outs
for(i=0;i<HISTORY;i++)
{
values[i]=0;
outs[i]=0;
}
}

int fir(int offset)
{
int out = outs[(k - offset + HISTORY) % HISTORY];
// out is the return variable. It is set to 0 every time we call the
filter!
return out;
}

void firFilter(void)
{
values[k] = pos;
outs[k] = 0;
for (i = 0; i < FILTERTAPS; i++)
{
outs[k] += coef[i % FILTERTAPS] * values[(i + k) % HISTORY];
}
}

void sensorReading(void)
{
unsigned long currentMillis = millis();
//reading analog signal from sensor
sensorValue = analogRead(pressureSensor);
//analog sensor to voltage conversion
sensorVoltage = sensorValue*(5.0/1023);
//pressure sensor transfer function
sensorPressure = 4.444*((5*sensorVoltage)+1);
//kpa to mmHg conversion
absolutePressure  = 7.50061561303*sensorPressure;
//calibrated distance of driver over sensor pressure
//38.1mm = stroke
//0.0508mm = per step
//total steps = 1415.61 steps
pos = map(absolutePressure,78,120, 1500, 300);


}
```

```
void runMotor1(void)
{
//assign position from sensor to motor
stepper1.moveTo(pos1);
//moving motor position
stepper1.run();
}

void runMotor2(void)
{
stepper2.moveTo(pos2);
stepper2.run();
}

void runMotor3(void)
{
stepper3.moveTo(pos3);
stepper3.run();
}

void runMotor4(void)
{
stepper4.moveTo(pos4);
stepper4.run();
}

void loop(void)
{
while(1)
{
//run sensor reading function
sensorReading();
//conditions for touch responce from user
if (myTouch.dataAvailable() == true)
{
pressed_button = myButtons.checkButtons();
//check for enable button press
if (myButtons.buttonEnabled(button1))
{
motorFlag = true;
}
else if (myButtons.buttonEnabled(button2))
{
motorFlag = false;
}
else
{
motorFlag = false;
}
//check for start button condition
if (pressed_button == button1)
{
myGLCD.setColor(0, 204, 0);
myGLCD.print(" Running", 70, 210);
}
//check for stop button condition
if (pressed_button == button2)
{
myGLCD.setColor(255, 0, 0);
myGLCD.print(" Stopped", 70, 210);
}
```

```
//check for no button pressed condition
if (pressed_button == -1)
{
myGLCD.print("None           ", 70, 210);
}
}
//operate fir filter fucntion for all four motors
if ( motorFlag == true && pressed_button == button1)
{
firFilter();
pos1=fir(5);
runMotor1();
pos2=fir(105);
runMotor2();
pos3=fir(205);
runMotor3();
pos4=fir(305);
runMotor4();
k=(k+1) % (HISTORY);
}
else
{
motorFlag == false;
}
}
}
```

Appendix K

SmartMotor™ Program Code

```
EIGN(W,0)
ZS
CTE (1)
CTA (23,100)
CTW (0)
CTW (2664)
CTW (4995)
CTW (6993)
CTW (8658)
CTW (9990)
CTW (10822)
CTW (11389)
CTW (11655)
CTW (9000)
CTW (7500)
CTW (6000)
CTW (4500)
CTW (3500)
CTW (2400)
CTW (1600)
CTW (1100)
CTW (700)
CTW (400)
CTW (150)
CTW (75)
CTW (40)
CTW (0)
SRC (2)
MCE (2)
MCW (1,0)
MC
MCMUL = 2
MCDIV = 1
MFMUL = 1
MFDIV = 7
MFA (0)
MFD (0)
MFSDC (0,0)
G
END
```

Appendix L

CAD Drawings

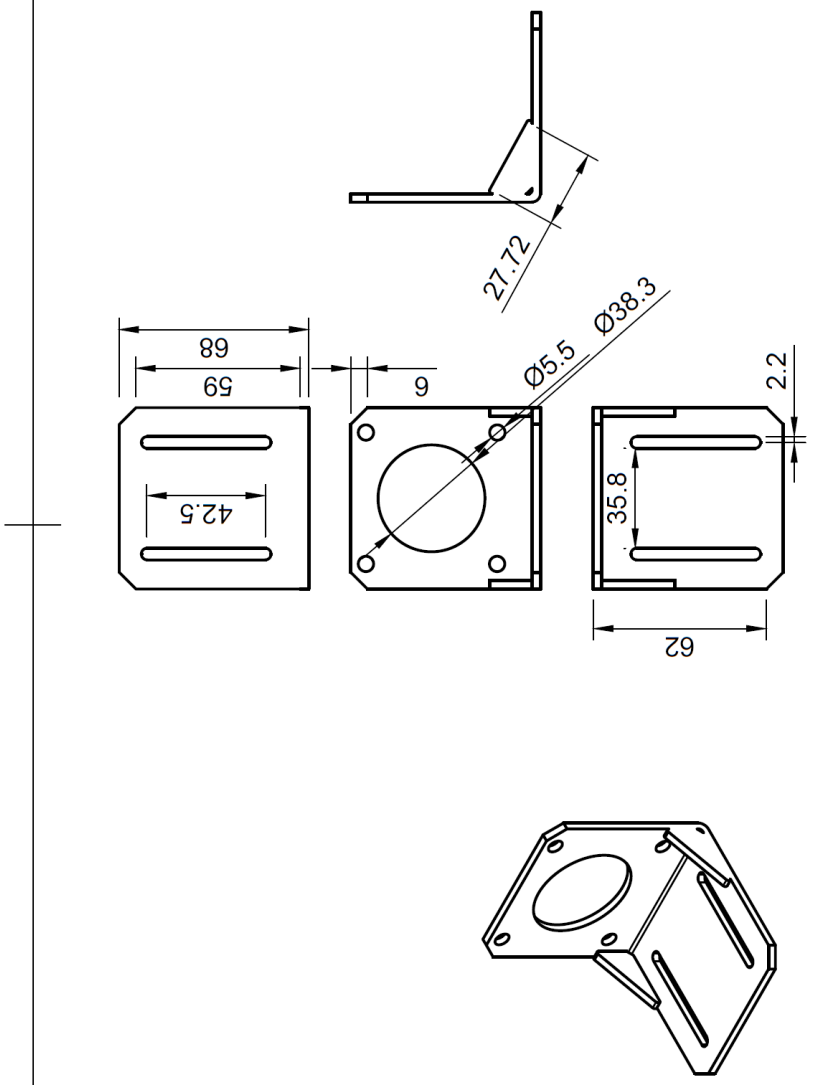
27.72
Ø38.3
Ø5.5
68
59
6
2.2
42.5
35.8
62
Dept.
Technical reference
Created by
Parn Jones
9/02/2017
Document type
Approved by
Document status
DWG No.
Title
Nema 23 Mount
Rev.
Date of issue
Sheet
1/1

Ø14
Ø10
2
A
4
14
A
A-A (2:1)
Dept.
Technical reference
Created by
Parn Jones
9/02/2017
Document type
Approved by
Document status
DWG No.
Title
Luer Lock Fitting M6
Rev.
Date of issue
Sheet
1/1

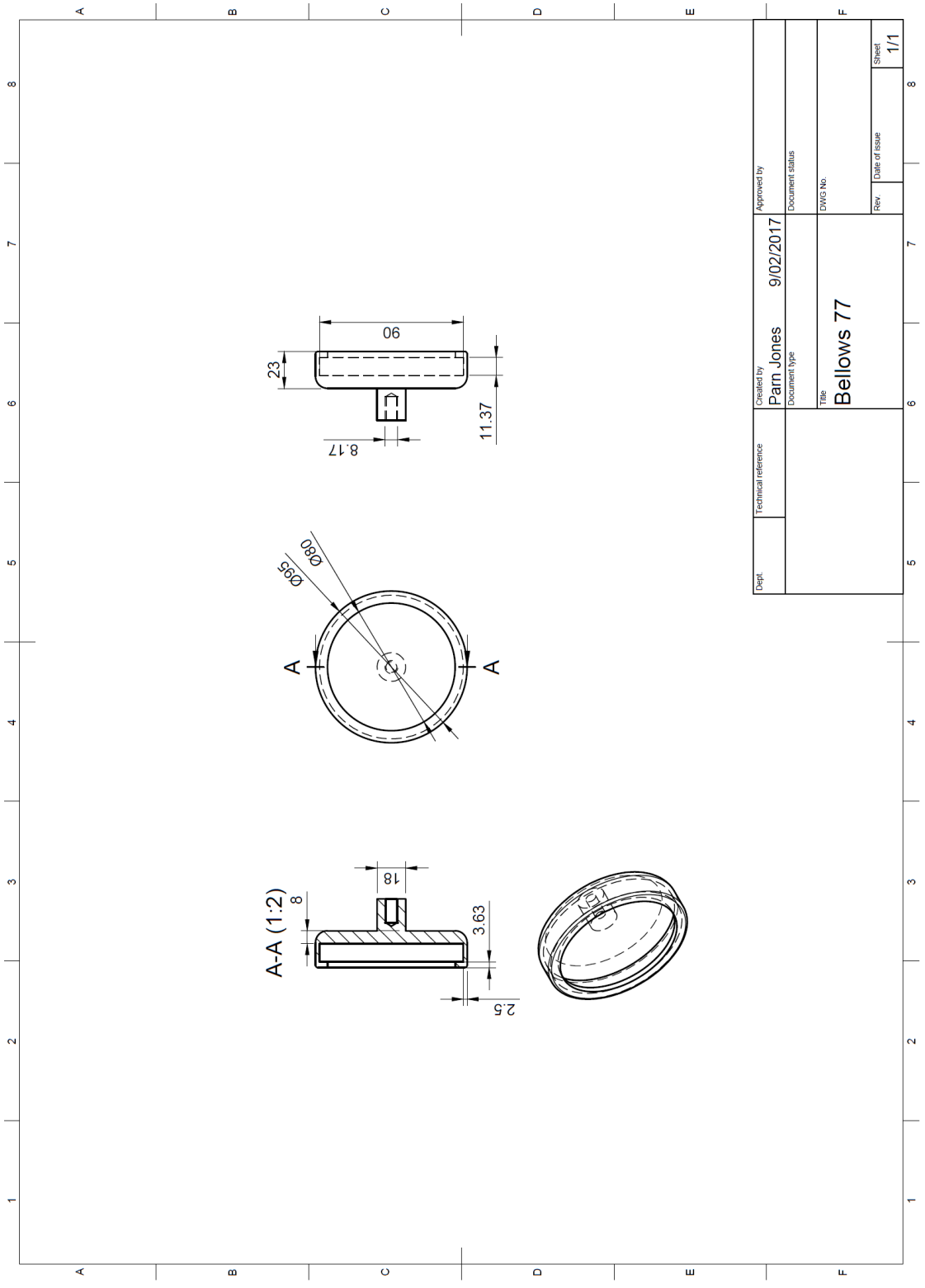
90
23
11.37
8.17
Ø80
Ø95
A
A
A-A (1:2)
18
8
3.63
2.5
Dept.
Technical reference
Created by
Parn Jones
9/02/2017
Approved by
Document type
Document status
Title
Bellows 77
DWG No.
Rev.
Date of issue
Sheet
1/1

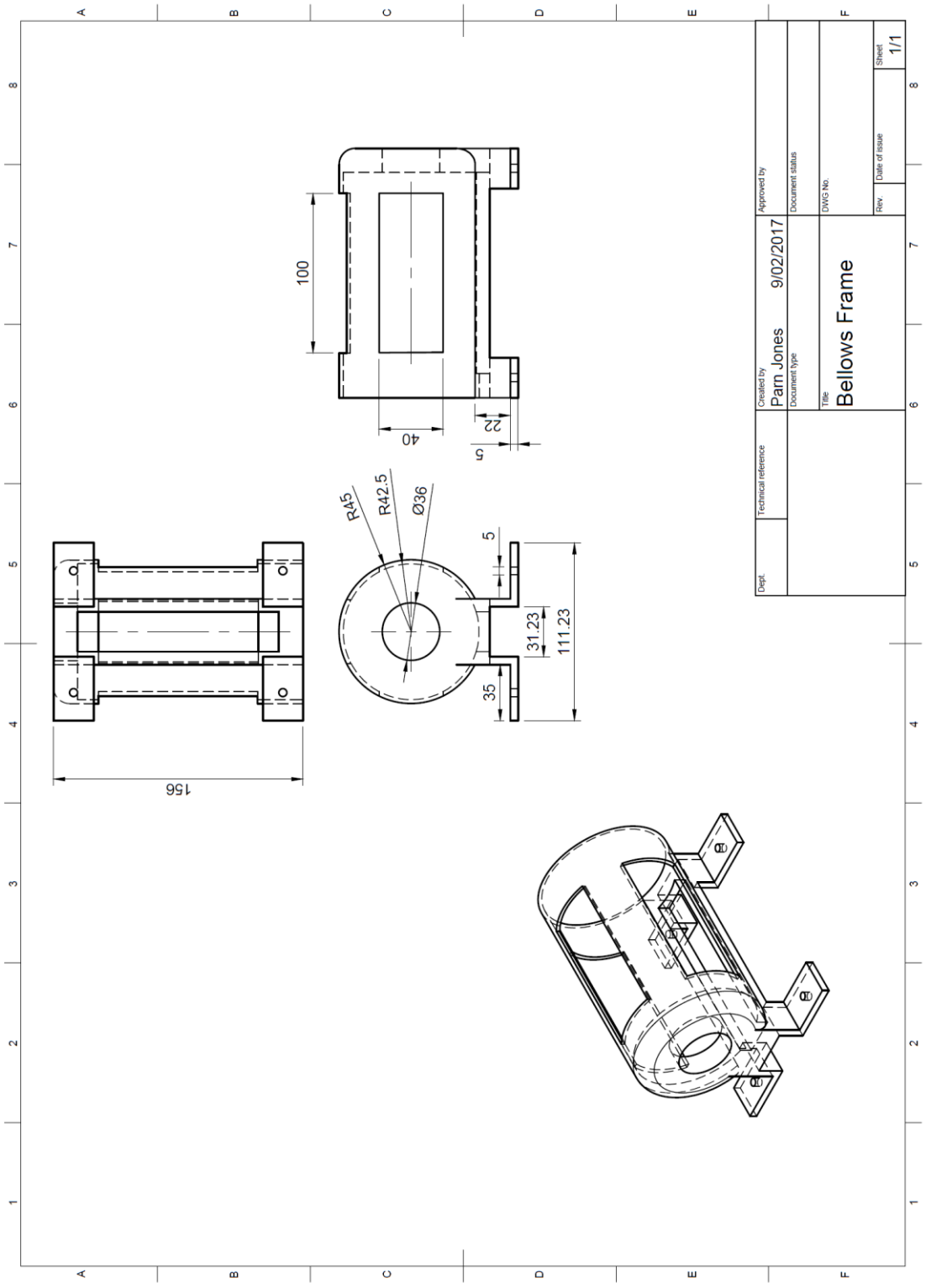
100
40
22
5
R45
R42.5
Ø36
5
31.23
111.23
35
156
Dept.
Technical reference
Created by
Parn Jones
9/02/2017
Document type
Approved by
Document status
Title
Bellows Frame
DWG No.
Rev.
Date of issue
Sheet
1/1

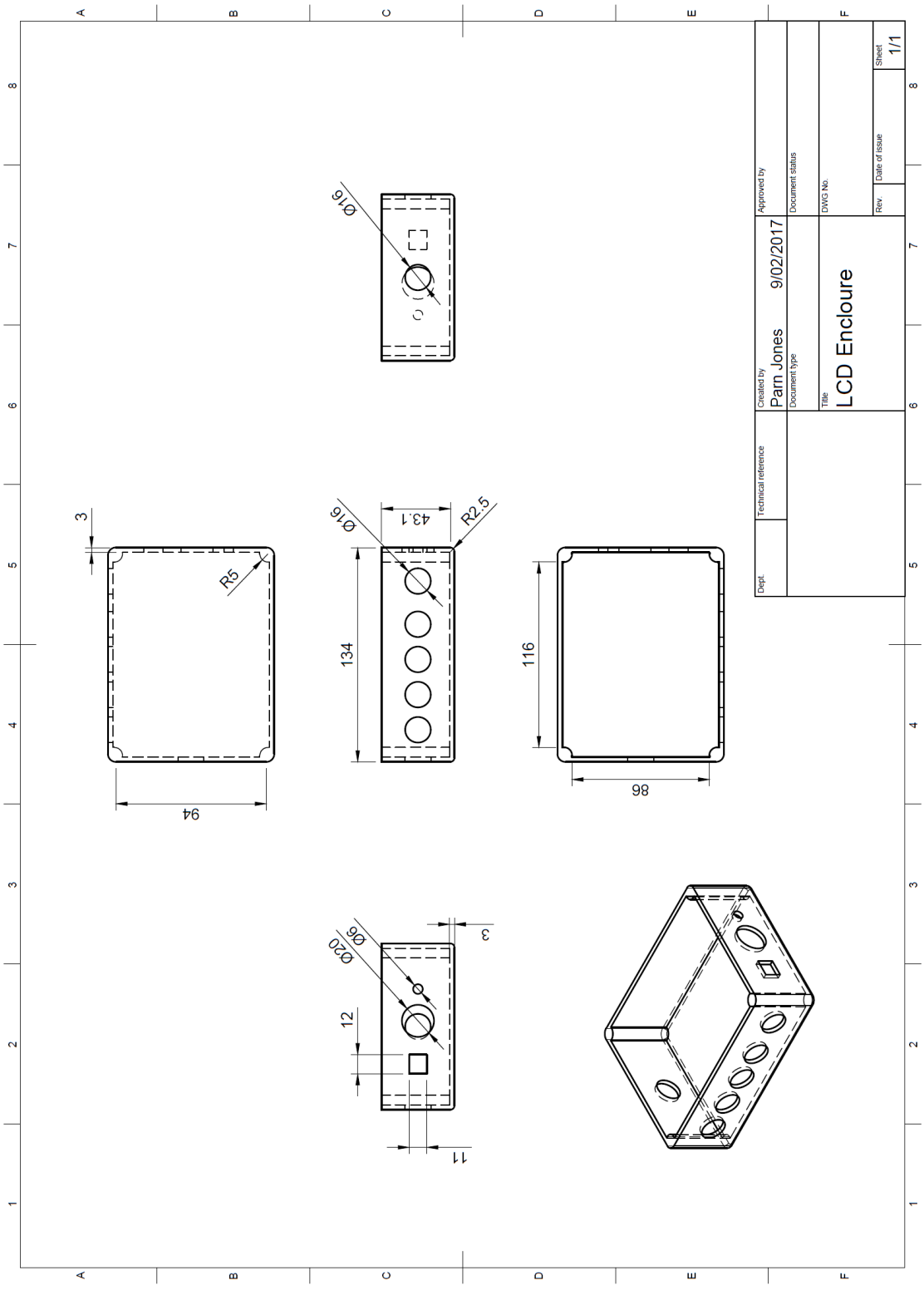
Ø16
Ø16
43.1
R2.5
3
R5
134
116
94
98
Ø20
Ø6
12
3
11
Dept.
Technical reference
Created by
Parn Jones
9/02/2017
Approved by
Document type
Document status
Title
LCD Encloure
DWG No.
Rev.
Date of issue
Sheet
1/1

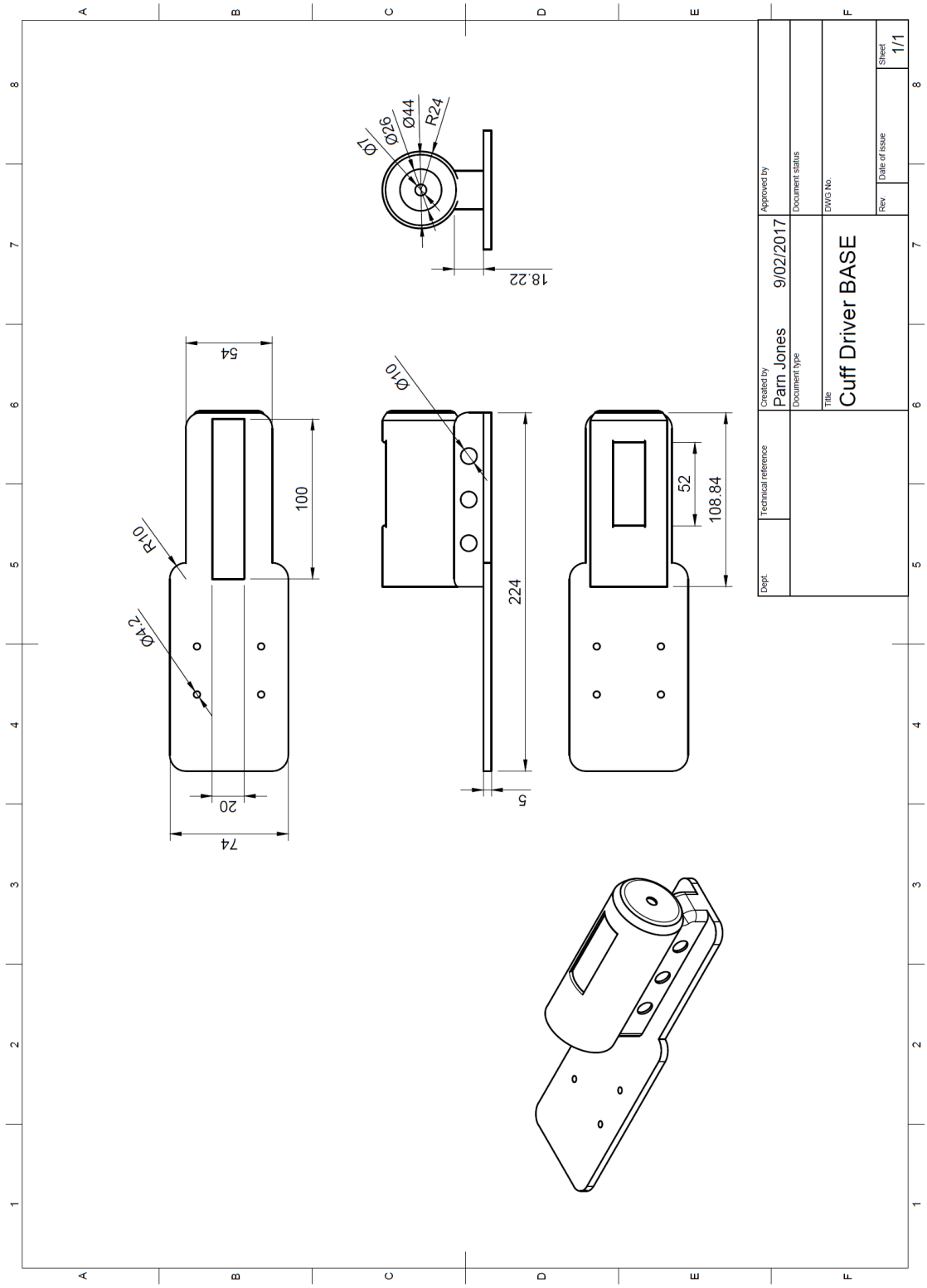
Ø7
Ø26
Ø44
R24
18.22
54
100
R10
Ø4.2
20
74
Ø10
224
5
52
108.84
Dept.
Technical reference
Created by
Parn Jones
9/02/2017
Approved by
Document type
Document status
Title
Cuff Driver BASE
DWG No.
Rev.
Date of issue
Sheet
1/1

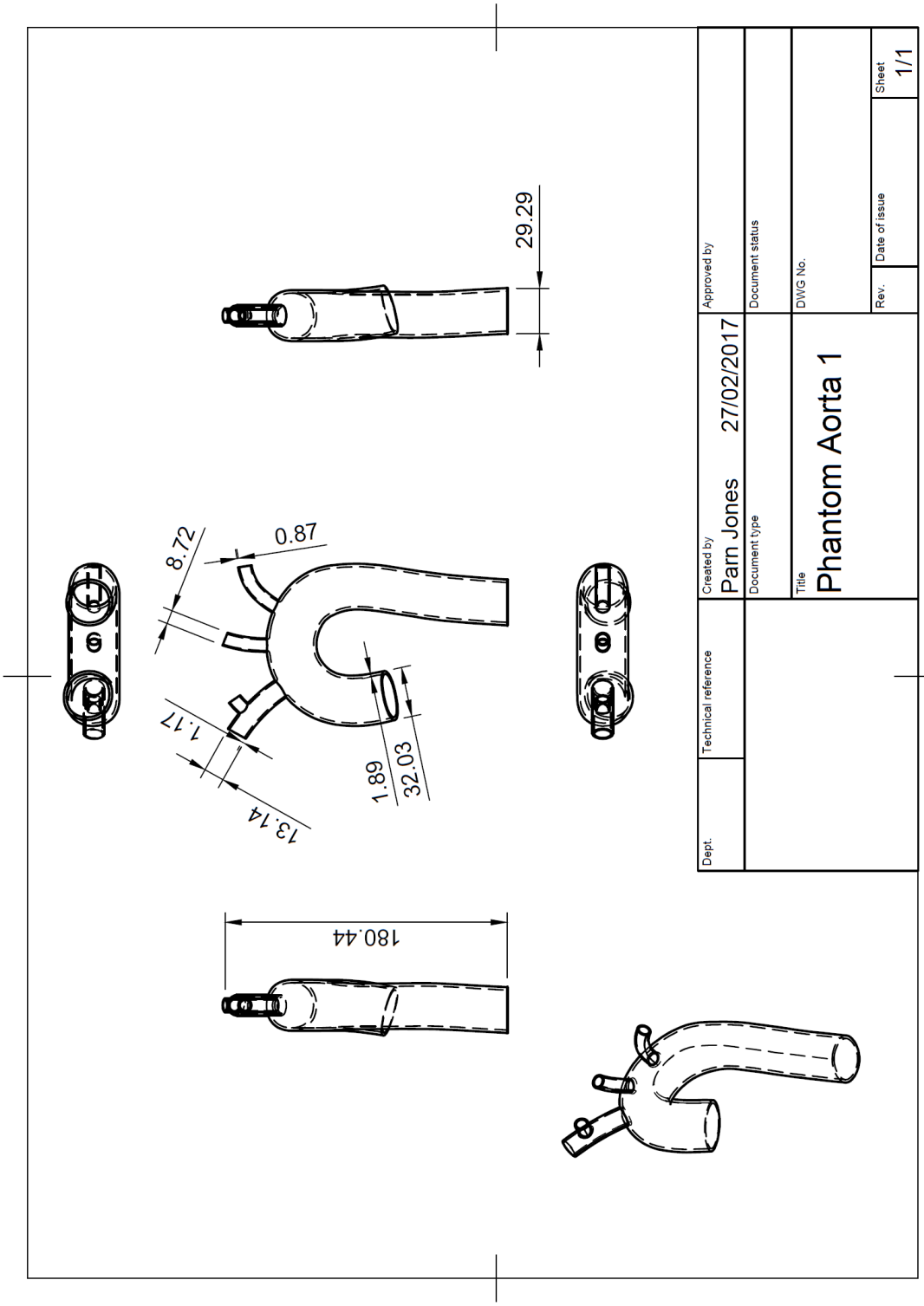
29.29
8.72
0.87
1.17
13.14
1.89
32.03
180.44
Dept.
Technical reference
Created by
Pam Jones
27/02/2017
Approved by
Document type
Document status
Title
Phantom Aorta 1
DWG No.
Rev.
Date of issue
Sheet
1/1

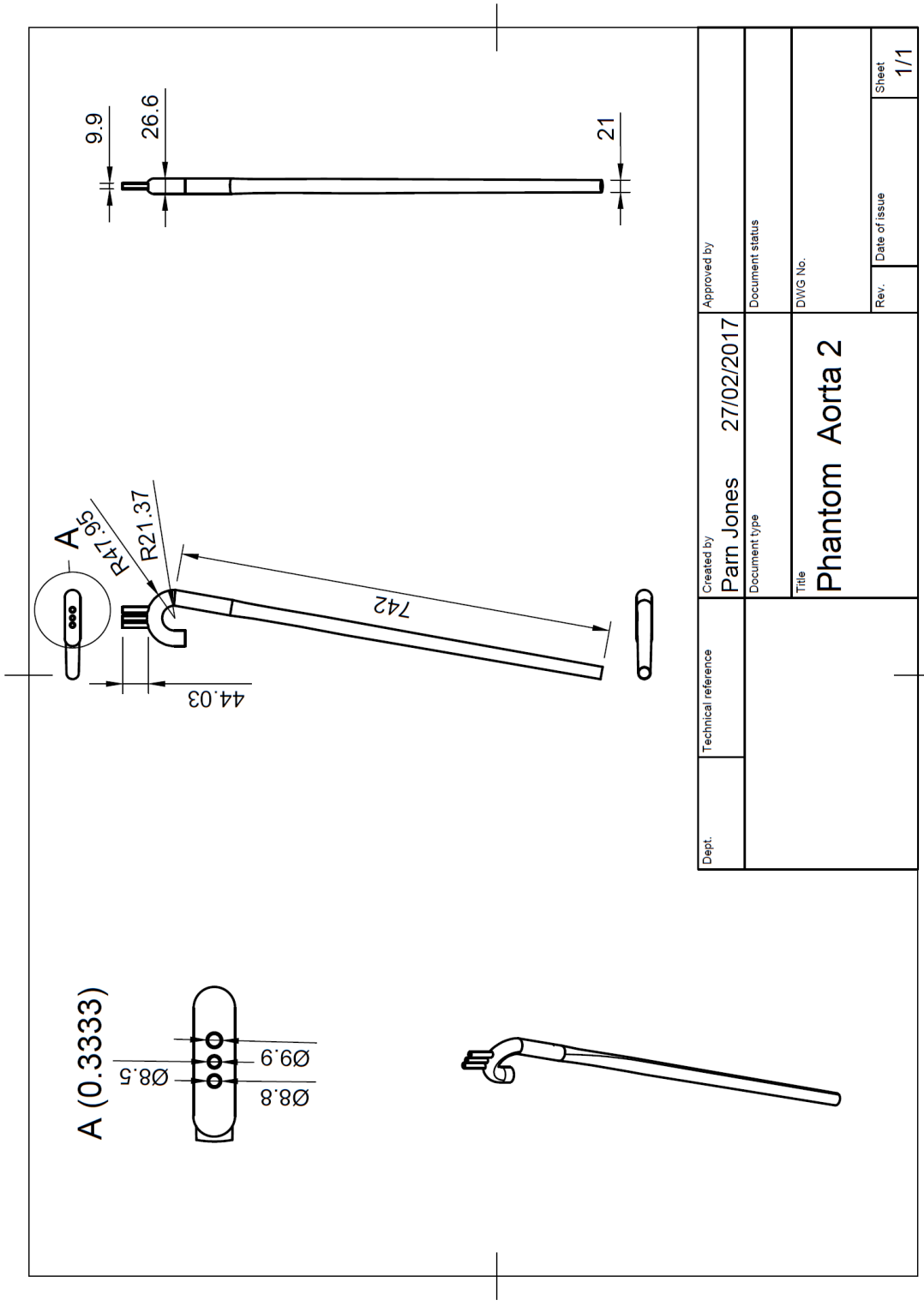
9.9
26.6
21
A
R47.95
R21.37
742
44.03
A (0.3333)
Ø8.5
Ø9.9
Ø8.8
Dept.
Technical reference
Created by
Parn Jones
27/02/2017
Approved by
Document status
Document type
DWG No.
Title
Phantom Aorta 2
Rev.
Date of issue
Sheet
1/1

References

[1] “WHO | About cardiovascular diseases,” *WHO*. [Online]. Available: http://www.who.int/cardiovascular_diseases/about_cvd/en/. [Accessed: 22-Nov-2015].

[2] “Heart Disease.” [Online]. Available: http://www.heartfoundation.org.nz/know-the-facts/conditions/heart-disease. [Accessed: 23-Nov-2015].

[3] K. Franco, V. H. Thouram, and M. S. Slaughter, “Counterpulsation Devices for Myocardial Support.”

[4] “Innovative C-Pulse Heart Assist Technology | Heart Failure Products,” *Sunshine Heart*. .

[5] W. T. Abraham *et al.*, “Ambulatory Extra-Aortic Counterpulsation in Patients With Moderate to Severe Chronic Heart Failure,” *JACC Heart Fail.*, vol. 2, no. 5, pp. 526–533, Oct. 2014.

[6] “Cardiovascular System Anatomy: Overview, Gross Anatomy, Natural Variants.” [Online]. Available: http://emedicine.medscape.com/article/1948510-overview. [Accessed: 07-Dec-2015].

[7] “Cardiac Output-Topic Overview,” *WebMD*. [Online]. Available: http://www.webmd.com/heart-disease/tc/cardiac-output-topic-overview. [Accessed: 07-Dec-2015].

[8] “Five Amazing Facts About the Human Heart,” *WebMD*. [Online]. Available: http://www.webmd.com/heart/features/amazing-facts-about-heart-health-and-heart-disease_. [Accessed: 22-Nov-2015].

[9] “Heart Disease: Definition and Facts About Symptoms,” *MedicineNet*. [Online]. Available: http://www.medicinenet.com/heart_disease_coronary_artery_disease/article.htm. [Accessed: 22-Nov-2015].

[10] "The Aorta (Human Anatomy): Picture, Function, Location, and Conditions," *WebMD*. [Online]. Available: http://www.webmd.com/heart/picture-of-the-aorta. [Accessed: 17-May-2016].

[11] "Anatomy of the Aorta and Heart - Cedars-Sinai." [Online]. Available: http://www.cedars-sinai.edu/Patients/Programs-and-Services/Heart-Institute/Centers-and-Programs/Aortic-Program/Anatomy-of-the-Aorta-and-Heart.aspx. [Accessed: 22-May-2016].

[12] R. Erbel and H. Eggebrecht, "Aortic dimensions and the risk of dissection," *Heart*, vol. 92, no. 1, pp. 137–142, Jan. 2006.

[13] "Aorta." [Online]. Available: http://america.pink/aorta_433701.html. [Accessed: 17-May-2016].

[14] "heart | anatomy," *Encyclopedia Britannica*. [Online]. Available: http://www.britannica.com/science/heart. [Accessed: 07-Dec-2015].

[15] T. Lewis, "Human Heart: Anatomy, Function & Facts," *LiveScience.com*. [Online]. Available: http://www.livescience.com/34655-human-heart.html. [Accessed: 22-Nov-2015].

[16] "Circulatory System," *Pinterest*. [Online]. Available: https://www.pinterest.com/ArtInBiology/circulatory-system/. [Accessed: 02-Dec-2015].

[17] "What Are Congenital Heart Defects? - NHLBI, NIH." [Online]. Available: http://www.nhlbi.nih.gov/health/health-topics/topics/chd. [Accessed: 02-Dec-2015].

[18] "Heart disease | World Heart Federation." [Online]. Available: http://www.world-heart-federation.org/cardiovascular-health/heart-disease/. [Accessed: 02-Dec-2015].

[19] "Cardiovascular disease terms | World Heart Federation." [Online]. Available: http://www.world-heart-federation.org/heart-facts/fact-sheets/cardiovascular-disease-terms/. [Accessed: 02-Dec-2015].

[20] "Heart Failure - The Heart Foundation." [Online]. Available: http://www.heartfoundation.org.nz/know-the-facts/conditions/heart-failure. [Accessed: 02-Dec-2015].

[21] “Heart Failure Statistics,” *Emory Healthcare*. [Online]. Available: http://www.emoryhealthcare.org/heart-failure/learn-about-heart-failure/statistics.html. [Accessed: 31-Aug-2015].

[22] “Types of Heart Failure.” [Online]. Available: http://www.heart.org/HEARTORG/Conditions/HeartFailure/AboutHeartFailure/Types-of-Heart-Failure_UCM_306323_Article.jsp#.Vl6WVeOGRHw. [Accessed: 02-Dec-2015].

[23] H. F. F. Sheet, “Heart Failure in the United States.”

[24] “Ageing,” *UNFPA - United Nations Population Fund*. [Online]. Available: http://www.unfpa.org/ageing. [Accessed: 30-Nov-2015].

[25] “The Future Is Here: Ventricular Assist Devices for the Failing Heart,” *Medscape*. [Online]. Available: http://www.medscape.com/viewarticle/709956. [Accessed: 30-Nov-2015].

[26] “C-Pulse - Sunshine Heart | C-Pulse Heart Assist System | Heart Failure | Counter HF.” [Online]. Available: http://www.sunshineheart.com/c-pulse/. [Accessed: 07-Dec-2014].

[27] “Meritus Health Maryland | Congestive Heart Failure Program.” [Online]. Available: http://www.meritushealth.com/Our-Services/Meritus-Medical-Center/Heart-Stroke/Cardiac-Services/Congestive-Heart-Failure-Program.aspx. [Accessed: 01-Dec-2015].

[28] “Classes of Heart Failure.” [Online]. Available: http://www.heart.org/HEARTORG/Conditions/HeartFailure/AboutHeartFailure/Classes-of-Heart-Failure_UCM_306328_Article.jsp#.VlvjAd8rKMI. [Accessed: 30-Nov-2015].

[29] M. M. Givertz, “Ventricular Assist Devices Important Information for Patients and Families,” *Circulation*, vol. 124, no. 12, pp. e305–e311, Sep. 2011.

[30] “Adult Cardiothoracic Surgery - Ventricular Assist Devices (VAD).” [Online]. Available: http://adultct.surgery.ucsf.edu/conditions--procedures/ventricular-assist-devices-(vad).aspx. [Accessed: 01-Dec-2015].

[31] “Left Ventricular Assist Device: Guidelines, Complications,” *MedicineNet*. [Online]. Available: http://www.medicinenet.com/left_ventricular_assist_device_lvad/article.htm. [Accessed: 02-Dec-2015].

[32] J. B. Shea and M. O. Sweeney, “Cardiac Resynchronization Therapy A Patient’s Guide,” *Circulation*, vol. 108, no. 9, pp. e64–e66, Sep. 2003.

[33] “Bundle branch block - Mayo Clinic.” [Online]. Available: http://www.mayoclinic.org/diseases-conditions/bundle-branch-block/basics/definition/con-20027273. [Accessed: 04-Dec-2015].

[34] “Pacemaker for Heart Failure (Cardiac Resynchronization Therapy).” [Online]. Available: https://myhealth.alberta.ca/Health/medications/pages/conditions.aspx?hwid=zm6382. [Accessed: 04-Dec-2015].

[35] M. Landolina *et al.*, “Long-Term Complications Related to Biventricular Defibrillator Implantation Rate of Surgical Revisions and Impact on Survival: Insights From the Italian ClinicalService Database,” *Circulation*, vol. 123, no. 22, pp. 2526–2535, Jun. 2011.

[36] “Intra-Aortic Balloon Pump-Topic Overview,” *WebMD*. [Online]. Available: http://www.webmd.com/heart-disease/tc/intra-aortic-balloon-pump-topic-overview. [Accessed: 05-Dec-2015].

[37] “5MinuteConsult | Counterpulsation (Aortic).” [Online]. Available: http://5minuteconsult.com/collectioncontent/1-151346/diseases-and-conditions/counterpulsation-aortic. [Accessed: 06-Dec-2015].

[38] “C-Pulse Extra-Aortic Balloon Counter Pulsation Device Technology,” *Sunshine Heart.* .

[39] “Safety Information,” *Sunshine Heart.* .

[40] “C-Pulse Extra-Aortic Balloon Counter Pulsation Therapy + Treatment,” *Sunshine Heart.* .

[41] D. Takagi and N. J. Balmforth, “Peristaltic pumping of viscous fluid in an elastic tube,” *J. Fluid Mech.*, vol. 672, pp. 196–218, Apr. 2011.

[42] S. Maiti and J. C. Misra, “Peristaltic transport of a couple stress fluid: some applications to hemodynamics,” *J. Mech. Med. Biol.*, vol. 12, no. 3, p. 1250048, 2012.

[43] “Adrian Kantrowitz: ventricular assists…Philip Liebson.” [Online]. Available: http://www.hektoeninternational.org/index.php?option=com_content&view=article&id=28%3Aadrian-kantrowitz-the-iaba-and-the-lvad&catid=66&Itemid=544. [Accessed: 10-Nov-2015].

[44] M. E. Legget *et al.*, “Extra-Aortic Balloon Counterpulsation An Intraoperative Feasibility Study,” *Circulation*, vol. 112, no. 9 suppl, p. I–26, 2005.

[45] “Heart Failure Clinical Evidence,” *Sunshine Heart*. [Online]. Available: http://www.sunshineheart.com/c-pulse-technology/clinical-evidence/. [Accessed: 01-Jun-2016].

[46] V. L. Sales and P. M. McCarthy, “Understanding the C-Pulse Device and Its Potential to Treat Heart Failure,” *Curr. Heart Fail. Rep.*, vol. 7, no. 1, pp. 27–34, Mar. 2010.

[47] “Hemodynamics of C-Pulse | Sunshine Heart.” [Online]. Available: http://www.sunshineheart.com/hemodynamics-of-c-pulse/. [Accessed: 02-Jun-2016].

[48] M. Capoccia, C. T. Bowles, J. R. Pepper, N. R. Banner, and A. R. Simon, “Evidence of clinical efficacy of counterpulsation therapy methods,” *Heart Fail. Rev.*, vol. 20, no. 3, pp. 323–335, May 2015.

[49] Sunshine Heart, “Use of Plethysmography to Confirm C-Pulse Timing.” Sunshine Heart, 24-Feb-2010.

[50] “Intra-aortic Balloon Counterpulsation: Overview, Indications, Contraindications,” Sep. 2015.

[51] MAQUET Group, “MECHANISMS OF COUNTERPULSATION.” MAQUET, 2012.

[52] “peristalsis | successive waves of involuntary contraction passing along the walls of a hollow muscular structure (as the esophagus or intestine) and forcing the contents onward compare SEGMENTATION 2.” [Online]. Available: http://www.merriam-webster.com/medical/peristalsis. [Accessed: 05-Nov-2015].

[53] P. Hariharan, V. Seshadri, and R. K. Banerjee, “Peristaltic transport of non-Newtonian fluid in a diverging tube with different wave forms,” *Math. Comput. Model.*, vol. 48, no. 7–8, pp. 998–1017, Oct. 2008.

[54] “Phys GI - Physician Assistant 2014 with Lockwood at University of Bridgeport,” *StudyBlue*. [Online]. Available: https://www.studyblue.com/notes/note/n/phys-gi-/deck/3159802. [Accessed: 05-Nov-2015].

[55] K. A. Daltorio, A. S. Boxerbaum, A. D. Horchler, K. M. Shaw, H. J. Chiel, and R. D. Quinn, “Efficient worm-like locomotion: slip and control of soft-bodied peristaltic robots,” *Bioinspir. Biomim.*, vol. 8, no. 3, p. 35003, Sep. 2013.

[56] J. D. Glenn, J. G. King, and J. F. Hillyer, “Structural mechanics of the mosquito heart and its function in bidirectional hemolymph transport,” *J. Exp. Biol.*, vol. 213, no. 4, pp. 541–550, Feb. 2010.

[57] “The mosquito circulatory system.” [Online]. Available: http://www.vanderbilt.edu/hillyerlab/Research__Circulation.html. [Accessed: 05-Nov-2015].

[58] A. K. Singh and D. P. Singh, “Peristaltic flow of blood through artery with a wave of small amplitude travelling down its wall,” *Int. J. Math. Trends Technol.*, vol. 2, pp. 1–3, 2011.

[59] S.Maiti, S.K.Tiwari, and J.C.Misra, “Peristaltic Transport if Blood: Wave Propagation in Small Blood Vessel.” ICFM, 26-Mar-2015.

[60] J. S. Martin, A. R. Borges, and D. T. Beck, “Peripheral conduit and resistance artery function are improved following a single, 1-h bout of peristaltic pulse external pneumatic compression,” *Eur. J. Appl. Physiol.*, vol. 115, no. 9, pp. 2019–2029, 2015.

[61] Nicholas Kiefer, Judith Theis, Gabriele Putensen-Himmer, and Andreas Hoeft, “Peristaltic Pneumatic Compression of the Legs Reduces Fluid Demand and Improves Hemodynamic Stability during Surgery.” American Society of Anesthesiologist, 2011.

[62] C.-J. Thore, “Pressure Estimation in the Systemic Arteries Using a Transfer Function,” 2007.

[63] R. Rhoades and D. R. Bell, *Medical Physiology: Principles for Clinical Medicine*. Lippincott Williams & Wilkins, 2009.

[64] "CV Physiology: Arterial Blood Pressure." [Online]. Available: http://www.cvphysiology.com/Blood%20Pressure/BP002.htm. [Accessed: 10-Nov-2015].

[65] "CV Physiology: Hemodynamics (Pressure, Flow, and Resistance)." [Online]. Available: http://www.cvphysiology.com/Hemodynamics/H001.htm. [Accessed: 10-Nov-2015].

[66] "LiDCO - Normal Hemodynamic Parameters." [Online]. Available: http://www.lidco.com/clinical/hemodynamic.php. [Accessed: 27-Sep-2016].

[67] F. Drummond, "Design and Analysis of Left Ventricular Pump Mechanism," AUT University, Oct. 2014.

[68] G. M. London and B. Pannier, "Arterial functions: how to interpret the complex physiology," *Nephrol. Dial. Transplant.*, vol. 25, no. 12, pp. 3815–3823, Dec. 2010.

[69] A. L. Wentland, T. M. Grist, and O. Wieben, "Review of MRI-based measurements of pulse wave velocity: a biomarker of arterial stiffness," *Cardiovasc. Diagn. Ther.*, vol. 4, no. 2, pp. 193–206, Apr. 2014.

[70] F. N. van de Vosse and N. Stergiopulos, "Pulse Wave Propagation in the Arterial Tree," *Annu. Rev. Fluid Mech.*, vol. 43, no. 1, pp. 467–499, Jan. 2011.

[71] J. Vappou, J. Luo, and E. E. Konofagou, "Pulse Wave Imaging for Noninvasive and Quantitative Measurement of Arterial Stiffness In Vivo," *Am. J. Hypertens.*, vol. 23, no. 4, pp. 393–398, Apr. 2010.

[72] C. Russ, M. Gessat, V. Falk, and G. Székely, "Rapid prototyping of silicone-based phantom models for stent simulation validation," *Proc. MICCAI-Stent*, vol. 12, 2012.

[73] G. V. Savrasov, A. F. Batanov, and S. G. Gusarov, "A Model of the Human Arterial System," *Biomed. Eng.*, vol. 45, no. 3, pp. 77–81, 2011.

[74] A. Evangelista *et al.*, "Echocardiography in aortic diseases: EAE recommendations for clinical practice," *Eur. Heart J. - Cardiovasc. Imaging*, vol. 11, no. 8, pp. 645–658, Sep. 2010.

[75] P. Vasava *et al.*, “Finite Element Modelling of Pulsatile Blood Flow in Idealized Model of Human Aortic Arch: Study of Hypotension and Hypertension, Finite Element Modelling of Pulsatile Blood Flow in Idealized Model of Human Aortic Arch: Study of Hypotension and Hypertension,” *Comput. Math. Methods Med. Comput. Math. Methods Med.*, vol. 2012, 2012, p. e861837, Feb. 2012.

[76] N. Shahcheraghi, H. A. Dwyer, A. Y. Cheer, A. I. Barakat, and T. Rutaganira, “Unsteady and Three-Dimensional Simulation of Blood Flow in the Human Aortic Arch,” *J. Biomech. Eng.*, vol. 124, no. 4, p. 378, 2002.

[77] B. Mensel, J.-P. Kühn, T. Schneider, A. Quadrat, and K. Hegenscheid, “Mean thoracic aortic wall thickness determination by cine MRI with steady-state free precession: validation with dark blood imaging,” *Acad. Radiol.*, vol. 20, no. 8, pp. 1004–1008, Aug. 2013.

[78] U. of W. H. and C. Authority, “Types of Aortic Aneurysms,” *UW Health*. [Online]. Available: http://www.uwhealth.org/heart-cardiovascular/types-of-aortic-aneurysms/10973. [Accessed: 24-May-2016].

[79] R. S. of N. A. (RSNA) and A. C. of R. (ACR), “Computed Tomography (CT) Angiography (Angiogram).” [Online]. Available: http://www.radiologyinfo.org/en/info.cfm?pg=angioct. [Accessed: 26-May-2016].

[80] A. D. Caballero and S. Laín, “A Review on Computational Fluid Dynamics Modelling in Human Thoracic Aorta,” *Cardiovasc. Eng. Technol.*, vol. 4, no. 2, pp. 103–130, Jun. 2013.

[81] C. Stefanadis *et al.*, “Aortic Function in Arterial Hypertension Determined by Pressure-Diameter Relation Effects of Diltiazem,” *Circulation*, vol. 96, no. 6, pp. 1853–1858, Sep. 1997.

[82] N. Alessandri *et al.*, “Elasticity/distensibility of the ascending aorta: basal conditions and simulated conditions from space flights,” *Eur. Rev. Med. Pharmacol. Sci.*, vol. 14, no. 5, pp. 421–426, May 2010.

[83] “Elasticity & Young’s Modulus for Tissue Analysis - Lesson,” *www.teachengineering.org*. [Online]. Available: https://www.teachengineering.org/lessons/view/van_floppy_lesson02. [Accessed: 31-May-2016].

[84] A. Atieh, “Design, Modeling, Fabrication and Testing of a Piezoresistive-Based Tactile Sensor for Minimally Invasive Surgery Applications,” Concordia University, 2012.

[85] U. Gülan, B. Lüthi, M. Holzner, A. Liberzon, A. Tsinober, and W. Kinzelbach, “Experimental Investigation of the Influence of the Aortic Stiffness on Hemodynamics in the Ascending Aorta,” *IEEE J. Biomed. Health Inform.*, vol. 18, no. 6, pp. 1775–1780, Nov. 2014.

[86] D. Bia, R. Armentano, Y. Zócalo, J. Grignola, and F. Ginés, “Aortic and pulmonary arterial distensibility, elastic modulus, and pulse wave velocity, during active and passive systemic and pulmonary acute hypertension.”

[87] J. Lantz, J. Renner, and M. Karlsson, “WALL SHEAR STRESS IN A SUBJECT SPECIFIC HUMAN AORTA — INFLUENCE OF FLUID-STRUCTURE INTERACTION,” *Int. J. Appl. Mech.*, vol. 3, no. 4, pp. 759–778, Dec. 2011.

[88] J. Urbina *et al.*, “Realistic aortic phantom to study hemodynamics using MRI and cardiac catheterization in normal and aortic coarctation conditions,” *J. Magn. Reson. Imaging*, vol. 44, no. 3, pp. 683–697, Sep. 2016.

[89] “Award for team behind cardiac device test system - E & T Magazine.” [Online]. Available: http://eandt.theiet.org/news/2012/aug/ni-awards.cfm. [Accessed: 14-Sep-2016].

[90] “Mold-A-Wax.” [Online]. Available: http://www.freemanwax.com/mold-a-wax.html. [Accessed: 07-Jun-2016].

[91] “Rebound® 25 Product Information,” *Smooth-On, Inc.* [Online]. Available: https://www.smooth-on.com/products/rebound-25/. [Accessed: 07-Jun-2016].

[92] “Marbocote 227CEE Archives,” *Marbocote Release Technology*. [Online]. Available: http://www.marbocote.co.uk/tag/marbocote-227cee/. [Accessed: 07-Jun-2016].

[93] M. Johnson, “Creating a synthetic aorta for the means to study arterial pulse wave velocity,” N/A, Jun. 2016.

[94] M. Willemet and J. Alastruey, “Arterial Pressure and Flow Wave Analysis Using Time-Domain 1-D Hemodynamics,” *Ann. Biomed. Eng.*, vol. 43, pp. 190–206, 2015.

[95] “Venous Air Embolism: Background, Pathophysiology, Etiology,” Jul. 2016.

[96] A. Swillens *et al.*, “Effect of an abdominal aortic aneurysm on wave reflection in the aorta,” *IEEE Trans. Biomed. Eng.*, vol. 55, no. 5, pp. 1602–1611, May 2008.

[97] Y. Watanabe, T. Asada, and P.-Y. Lagrée, “One-Dimensional Model for Propagation of a Pressure Wave in a Model of the Human Arterial Network: Comparison of Theoretical and Experimental Results.”